Dissertation

submitted to the

Combined Faculties for the Natural Sciences and for Mathematics

of the Ruperto-Carola University of Heidelberg, Germany

for the degree of

Doctor of Natural Sciences

Put forward by:

Diplom-Physiker Patrick Weise

Born in Bremen

Oral examination: October 13, 2010

Search for planets around young stars with the radial velocity technique

Referees: Prof. Dr. Thomas Henning

Prof. Dr. Immo Appenzeller

Suche nach Planeten um junge Sterne mit der Radialgeschwindigkeitsmethode

Zusammenfassung

Riesenplaneten entstehen in zirkumstellaren Scheiben um junge Sterne. Es existieren zwei verschiedene theroretische Beschreibungen, wonach Riesenplaneten durch gravitative Instabilität oder Kern-Akkretion entstehen. Beide Modelle können auch zusammen unter bestimmten Bedingungen zutreffen, aber die Kern-Akkretion scheint der dominante Prozess zu sein. Bisher wurde jedoch die Planetenentstehung noch nicht direkt beobachtet. Aus diesem Grund soll in dieser Arbeit nach sub-stellaren Begleitern um junge Sterne (1–100 Mjahre) gesucht werden, da die Eigenschaften junger Planeten wichtige Hinweise auf die Prozesse der Planetenentstehung geben können. In dieser Arbeit wurden echelle Spectren von 100 jungen Sternen aufgenommen und deren Eigenschaften charakterisiert. Thie Radialgeschwindigkeit wurde durch Kreuz-Korrelation der Spektren mit Vorlagen in MACS gewonnen. Weiterhin wurde die stellare Aktivität durch die Analyse des Linien Bisektors und anderer Indikatoren, charakterisiert. FÃijr 12 der untersuchten Sterne ist die Variation der Radialgeschwindigkeit durch die Modulation der stellaren Aktivität mit der Rotationsperiode gegeben. Weiterhin wurden sechs Riesenplaneten und ein Brauner Zwerg im Orbit um junge Sterne (2–90 Myr) gefunden. Dennoch ist die Anzahl der gefundenen sub-stellaren Begleiter zu wenig und das Alter der Sterne zu ungenau um Aussagen zu der Entstehung von Planeten zu treffen. Allerdings ist die Häufigkeit von Riesenplaneten und Brauner Zwerge um junge Sterne ähnlich derer um sonnenähnliche Sterne.

Search for planets around young stars with the radial-velocity technique

Abstract

Giant planets form in circumstellar disks around young stars. Two alternative theoretical formation concepts, disk instability and core accretion, may both apply under certain conditions, but core accretion is believed to be the main mechanism. No observational proof of the dominant process has been found thus far. Therefore, this thesis aims to detect sub-stellar companions orbiting young stars (1–100 Myr), because characteristics of young planets give input on formation processes involved. For this thesis, echelle spectra of 100 young stars have been obtained and analysed for $v \sin i$ and basic stellar parameters. The radial-velocity has been calculated by cross-correlation of the spectra with templates using MACS. Stellar activity has been characterized by the analysis of the line bisector and other indicators. For 12 of the analysed stars, the radial-velocity variation is most likely caused by rotational modulation of stellar activity. Furthermore, one brown dwarf and six giant planets orbiting stars with ages of 2–90 Myr have been found. However, the ages of the stars are ill constraint and the number of found sub-stellar companions is too low to draw serious conclusions for formation processes. The frequency of giant planets and brown dwarfs around young stars is comparable to the frequency around solar-like stars.

This thesis is dedicated to
Sabrina,
thanks for being there
&
Joey and Elliot,
thanks for the
Greyhound-way of life

Contents

List of Figures

List of Tables

1 Introduction

More than 460 planets have been found to date, mainly by the radial velocity (RV) technique [Schneider, 2010], since the first discovery of a giant planet of jovian mass orbiting a sun-like star in 1995 [Mayor & Queloz, 1995]. This technique is most sensitive to giant planets in close-in orbits because of the large RV variations induced by such planets, whereas planets orbiting on larger orbits induce smaller RV variations and can only be discovered with a long observation time line. However, most RV planet-search surveys monitor solar-like main-sequence stars because the RV of the host star is less affected by stellar activity than that of, e.g., young stars or giants. To be able to identify a RV signal induced by a planet around a young star (age < 100 Myr), a careful analysis of all stellar activity indicators is needed (e.g., Setiawan *et al.* [2007]). Active magnetic regions on the star, like plagues and star spots, can change the shape of spectral lines, which in turn affects the measured effective RV and can thus mimic a planetary reflex motion with a period that is equal to the rotational period of the host star (e.g., Saar & Donahue [1997]). It is a challenge to disentangle such signals from the RV variation induced by a planet. This difficulty is the main reason why young planets discovered with the RV method are still rare [Setiawan *et al.*, 2007, 2008a], or as in the cases of TW Hya and BD+20 1790, are still under debate [Figueira *et al.*, 2010; Hernán-Obispo *et al.*, 2010; Huélamo *et al.*, 2008].
Nevertheless, revealing planets orbiting young stars and their characteristics is important because they can give valuable constraints on the questions of how and when giant planets form and how they evolve. Giant planets form in turbulent circumstellar disks around young stars by two alternative mechanisms, 'top-down' (disk instability) or 'bottom-up' (core accretion), which may both apply under certain circumstances. However, the observation of planets orbiting solar-like stars can give only indirect constraints on the dominant model of giant planet formation via statistical comparison of the planets characteristics with predictions of planet formations models (e.g., Mordasini *et al.* [2009]). With current results, the core accretion model can explain the characteristics of the majority of the detected planets better than the gravitational instability model. In addition to differences in characteristics of planets orbiting solar-like stars, both models differ in time-scales of giant planet formation, at which the 'top-down' model is faster.

The scientific motivation for this thesis is to detect planets around young stars and to put observational constraints on the time-scales of planet formation. Setiawan *et al.* [2008a] showed for the first time that planet formation indeed occurs in circumstellar disks. However, even younger planets than the 8 Myr old TW Hya b are needed to put

constraints on planet formation time-scales. However, because young stars are mainly active and rapidly rotating stars, this thesis is also dedicated to the identification of the limits set by stellar activity and rotation, in which high precision RV measurements are still possible and can lead to the identification of a planetary signal.
The aim of this thesis is to start a long-term (longer than the time-span of this thesis) program to monitor the RV of very young stars. For this purpose, a new cross-correlation tool has been developed which can handle spectra of young and active stars. In addition to the RV, the stellar activity is characterized in order to identify the source of the RV variation. The goal is to find giant planets and brown dwarfs around very young stars, although the number of detections will probably be too low to draw significant conclusions for planet formation theories. However, the field of young extrasolar planets is just beginning to emerge and the detection of the first young planets might reveal characteristics of the planets that can not be explained by current formation theories, like the detection of the first extrasolar planet in 1995 did. Furthermore, a lot of young planet detections is needed for a statistical comparison of both young and old planets and their characteristics, which can also reveal the dominant formation process and the evolution of planets.

This thesis is structured as follows. In Chapter 2, I briefly summarize the scientific and technical background important in this study. This includes the formation of stars and planets, as well as the principles of the radial velocity technique, and the definition of stellar activity and its influence on radial velocity measurements. In Chapter 3, the selection criteria to create the target list, the observing strategy, as well as the instrumentation and data reduction is described. In Chapter 4, the data analysis methods are described. These involve the measurement of radial velocities and bisectors with the new tool MACS, and the measurement of stellar activity indicators. Furthermore, the methods used to derive stellar parameters, like effective temperature and age, as well as $v \sin i$ and accretion signatures are presented. In Chapter 5, the analysis of the stellar spectra is presented. The results include the distribution of stellar age, metallicity, evolutionary stage and $v \sin i$ of the targets. For this analysis, I added a sample of other SERAM stars to the targets of this study to have a larger sample to be able to do statistics and to yield stronger conclusions. In Chapter 6, the analysis of radial velocities and stellar activity for 26 stars with more than 5 observations is presented. Here, the RV and stellar activity is analysed for each star individually. Finally, the results are summarized, compared with statistics of companions around solar-like stars, and preliminary concluded in Chapter 7.

2 Scientific and technical background

In this chapter, I present the astronomical and technical background for this study. The general concepts of star and planet formation are reviewed and the theories of planet formation compared with respect to the aim of this study (Section 2.1). In addition, the RV method is described in Section 2.2. RV measurements are mainly affected by variations in the stellar atmosphere, called stellar activity. The processes and the influences of stellar activity on RV measurements are described in Section 2.3.

2.1 Star and planet formation

2.1.1 Star formation

Stars form from cold molecular clouds, mainly made up of H_2, which are on average 200 times denser than the uniformly distributed atomic gas in the Milky Way disk. These clouds are believed to be build by density waves induced by the spiral arms of the galaxy, which swept up and compress the atomic gas into molecular clouds (e.g., [Lada & Kylafis, 1999]). The column density of the dust in molecular clouds is high enough to cool down the interior of the cloud down to 10–30 K. Considering thermal and gravitational effects alone, the requirement that the cloud be self-graviting leads to the determination of a critical mass and density, the well-known Jeans criterion. The critical Jeans mass and density is proportional to the temperature of the gas and gets smaller with decreasing temperature. Furthermore, the thermal pressure of the gas is proportional to the temperature of the gas and therefore, it can no longer balance gravity when the critical mass is reached in the cold cloud. Thus, the cloud has to collapse within the free-fall time (typical $\sim 10^5$ yr). In this simple picture, the whole cloud must have been converted into stars within 1 Myr (e.g., Palla [2002]). However, the observed rate of star formation is much lower than the rate expected by this scenario. Therefore, two alternative processes of star formation have been proposed to explain that only 10–15% of the cloud mass is converted into stars. The first model of ambipolar diffusion predicts that star formation is slowed down by magnetic fields intrinsic to molecular clouds. These magnetic fields prevent the fast formation of stars by friction between the infalling atomic gas and ionic gas trapped by the magnetic fields (e.g., Palla [2002]). The second model of turbulence predicts that star formation is a fast, but ineffective process, because only a small number of massive cores can survive for a time sufficient enough to form stars in a turbulent cloud (e.g., Mac Low & Klessen [2004]). Observations show that both models probably apply under certain

circumstances, but turbulence is most likely the dominant process on larger scales in star formation.
However, clumps massive enough against destruction by thermal pressure and outer turbulence, slowly contract according to the model of ambipolar diffusion until the nearly free-fall collapse starts when the gravitational force is higher than thermal and magnetic pressure (e.g., Palla [2002]). A hydrostatic core forms at the center of these clumps, the mass of which is still much smaller than that of the final star it will become, while the envelope material is still falling down on this core. These objects are called Class 0 protostars and are still hidden behind a thick envelope of gas and dust, such that they are only visible at longer wavelengths, i.e. radio wavelengths. After some 10^5 years, the collapsing core gets dense enough that it can no longer be cooled by the emission of thermal radiation. Thus, it gets heated and enters a phase of quasi-hydrostatic equilibrium. At this stage, the proto-star has accumulated more than half of its final mass, but is still hidden in a gaseous and dusty envelope. These objects are called Class I young stellar objects.
An important aspect of star formation is the preservation of angular momentum. Stars forming in rotating molecular cloud cores preserve only a very minor fraction of their initial angular momentum (e.g., Lamm *et al.* [2005]; Palla [2002]), otherwise the centrifugal force will disrupt the forming cores. The initial angular momentum of rotating molecular cloud cores is about 4–5 orders of magnitude higher than that of the stars that eventually form in this cloud core (e.g., Bodenheimer [1989]). Stellar formation models must account for that and several mechanisms are discussed, e.g., magnetic braking or magnetocentrifugally driven outflows (bipolar jets). However, there is still no consens as on whether there is one dominant process for dispersing angular momentum during the entire star formation process or which process dominates at what evolutionary stage after the formation of a star-disk system (e.g., Palla [2002]). Furthermore, redistribution of angular momentum by the creation of a circumstellar disk and probably planet formation play also an important role [Hogerheijde, 2010].
After most of the material in the envelope has been accumulated in the star and the rest settled down in a circumstellar disk, the young star becomes visible in the optical light as a Pre-Main-Sequence (PMS) star or Class II object. In this thesis, such PMS stars which often still have a disk and may be in a stage of planet formation, are observed and analysed for RV variations.
The PMS stars evolve further and undergo a phase of contraction and mass accretion from the surrounding disk, although at a accretion rate 2–3 orders of magnitude lower than at the previous stages. The time spent in this evolutionary stage can be estimated to $\sim 10^7$ years. After this phase, the star reaches the Zero-Age-Main-Sequence (ZAMS) [Palla, 2002].

2.1.1.1 Characteristics of very young stars

PMS stars with an age<10 Myr and mass $M_\star < 3M_\odot$ are named T Tauri stars [Appenzeller & Mundt, 1989; Joy, 1945]. The spectrum of this type of star shows a strong Li I feature that confirms the youth of the star. Some T Tauri stars show an emission feature of photospheric and chromospheric lines that points towards ongoing mass accretion and high magnetic activity of these stars [Herbig, 1962]. Such stars are named *classi-*

cal T Tauri stars (cTTs), whereas stars of similar age but showing no sign of ongoing accretion are named *weak-lined* T Tauri stars (wTTs) (e.g., Herbst *et al.* [1994]). Note that these stars also show signs of high magnetic activity. However, wTTs are still surrounded by a circumstellar disk, either with an inner hole or as a nearly gas-free debris disk. In both cases only small amounts of accretion of gas material onto the star is possible.

2.1.2 Circumstellar disks

All low-mass (T Tauri type) stars form surrounded by a disk, with typical masses of 0.001–0.3 $M_\odot$ and up to several AU in size (e.g, Hogerheijde [2010]). Observations of molecular emission lines arising from the disk show that the gas is in Keplerian rotation with dust grains in the cold and dense disk interior.

Circumstellar disks around young stars can be identified and characterized by analysing the spectral energy distribution (SED) of the star. Stars with disks show a strong emission from the infrared (IR) between 2 μm and 25 μm to millimetre wavelengths, as compared to the single-temperature blackbody SED of a disk-less star. Over this wavelength range, dust of different temperatures at certain distances to the star can be traced. Therefore, the structure and size of the disk can be estimated from the analysis of the SED [Hogerheijde, 2010].

Disk masses can be inferred from the (sub-)millimetre thermal emission of the dust. This requires knowledge of the gas-to-dust ratio, dust temperature, and its emissivity κ_ν, which is still ill constrained and significantly changes during the evolution of dust grains growing from μm-size to cm-size. Initially the gas-to-dust ratio of the disk material is 150:1, as measured in the interstellar medium. However, the ratio may evolve subsequently throughout the disks' life-time. The gas is predominantly made up of H (80%) and He I (20%). Other elements are present in trace amounts. The gas is molecular, although material at the upper layers and close to the star may be photo-ionized [Hogerheijde, 2010]. The inferred disk masses are in the range of 0.001–0.3 $M_\odot$ with an uncertainty of a factor of 2–3 [Hogerheijde, 2010].

The circumstellar disk transports angular momentum due to its viscosity that has its source in turbulence. The viscosity is parametrized as $\nu = \alpha H c_s$, with H as the hydrostatic scale height of the disk, c_s as sound-speed and α as a describing parameter <1. This formulation describes an accretion disk with material flowing inwards and the outer edge of the disk spreading outwards, carrying with it the excess angular momentum of the star-disk system. The surface density profile of such a disk is

$$\Sigma \propto R^{-1} \quad . \tag{2.1}$$

The vertical structure of the disk, parametrized by H, varies with the radius, thus resulting in a flared disk that is no longer perfectly thin (e.g., Dullemond *et al.* [2009]).

The life-time of circumstellar disks can be inferred from the observations of infrared excess emission of stars in different clusters of known age. It has been found that the disk fraction (stars with circumstellar disks) decreases from more than 80% in clusters less than 1 Myr old to less than 10% in clusters older than 10 Myr. For the inner disk, the typical life expectancy is 2–3 Myr [Hogerheijde, 2010]. This means that after this time ~50% of the stars have a cleared inner disk and accretion stops. This is the small

population of so-called cold or transitional disks around wTTs. The inner hole or gap in transitional disks develops either due to photo-ionization of the disk surface or by rapid grain growth and planetesimal formation. In the first case, the material cannot flow inward and disperse through photo-evaporation as well. In the latter case, a proto-planet of sufficient mass would open a gap in the disk. The only direct detection so far of a disk with a cleared out inner hole and a planet is TW Hya [Setiawan *et al.*, 2008a].
Further observations support the idea that the inner and outer disk disappear simultaneously and that the disk dispersal mechanisms are fast (<0.5 Myr) compared to the typical time before dispersal starts [Hogerheijde, 2010].

2.1.3 Planet formation

In this section, I briefly summarize the theories of planet formation. For a detailed description of planet formation, I refer to, e.g., Papaloizou & Terquem [2006].

A planet is, according to the official definition of a planet by the IAU (International Astronomical Union), a celestial body in hydrostatic equilibrium with a mass lower than the deuterium-burning limit (<13 M_{Jup}). This definition can further be divided into *terrestrial* planets, which are rocky planets like the earth, and *giant* planets, which have a rocky core of several earth-masses and a gaseous envelope.

The theory of *terrestrial* planet formation can be traced back into the 19th century in which the formation of planets via solid body accretion has been proposed. However, it was Safronov [1969], who calculated in detail the different stages of planet formation. As far as *giant* planets are concerned, two theories have been proposed. The first one states that giant planets are formed through the fragmentation and collapse of circumstellar disk material, the *disk instability model*. This was first proposed by Laplace in 1796, picked up by Kuiper in the 1950's and is still being studied today (e.g., Boss [2008]). The second model is called *core accretion model* [Cameron, 1973; Pollack *et al.*, 1996]. A solid core is first assembled in the same way terrestrial planets are formed and once the core becomes massive enough, a gaseous envelope is gravitationally bound to the core. The core accretion model is believed to be the dominant mechanism during the formation of a planet. However, under certain circumstances, both models can apply [Ida, 2010].

2.1.3.1 The core accretion model

The dust is distributed within the gaseous circumstellar disk with a surface density given in Equation 2.1. The velocity of the dust particles is Keplerian, whereas the relative velocity among the particles depends strongly on gas pressure and turbulence. Dust particles are conglomerating in the disk midplane due to gravity (e.g., Henning [2008]). During this process they are going to increase in size and mass due to sticking, which occurs when relative collision velocities are ~1 ms^{-1}. With this process, meter-sized particles can be formed.
However, meter-sized particles spiral into the host star within ~100 years due to *head-wind* by the slower rotating gas or they can be fragmented by collisions (e.g., Johansen *et al.* [2007]). Thus, growth by collisions to larger particles is very inefficient because the collision velocities are too high. However, several processes have been proposed to

overcome this *meter-barrier*. These processes include the growth of km-sized particles behind the *snow-line*, where water is no longer vaporized by the star-light and ice sticks to the dust particles, allowing a faster growth to km-size within a few thousand years [Brauer *et al.*, 2008]. Another process that is probably involved is that km-sized bodies can grow in local turbulent vortices of high pressure. In these vortices, cm-sized particles are accumulated. Thus, the local mass density rises and collisional velocities get damped. Therefore, the growth by collision is effective in these dense clumps and particles of km-size can be built.
For the further growth of km-sized particles, so-called *planetesimals*, several different stages can be identified from numerical n-body simulations [Ida, 2010]. First, the planetesimals enter a stage, which is dominated by rapid growth, so-called *runaway growth* (e.g., Papaloizou & Terquem [2006]). In this phase, slightly larger particles can grow faster than other, smaller particles because they have an increased cross-section for the accretion of other planetesimals. As runaway growth proceeds, the larger bodies become detached from the continuous mass distribution of the planetesimals and they become the scattering center. This transition to the next stage occurs when the total mass of the runaway bodies is still much smaller than the sum of all small bodies. In this phase, so-called *oligarchic growth*, the growth of the largest bodies slows down, whereas the mass ratio between the large bodies and the smaller planetesimals still increases (e.g., Papaloizou & Terquem [2006]). This results in a bimodal population consisting of a small number of similar-sized protoplanets and a large number of planetesimals. Furthermore, dynamical frictions from the gas in the disk damps eccentricities of the protoplanets so efficiently that the orbits of the protoplanets are kept isolated. This results in an isolation mass of the protoplanets which is ~3–7 $M_\oplus$ at 5-10 AU and 0.1–0.2 $M_\oplus$ at ~1 AU. Therefore, terrestrial planets can only be formed inside 5 AU by giant impacts among the protoplanets when the gas is dissipated. Giant gas planets can only be formed behind the snow-line (e.g., Raymond *et al.* [2009]).
At the end of the oligarchic growth phase, protoplanetary cores with a mass >3 $M_\oplus$ are able to gravitationally bind gas from the circumstellar disk. This process turns into a very rapid process once the core and the accreted atmosphere reach a critical mass of 5–15 $M_\oplus$. This critical mass is reached by additional capturing of planetesimals that enter the atmosphere of the proto-gas-planet. When this mass is reached, runaway gas accretion occurs, such that the time-scale of gas accretion is comparable to the disk life-time at a certain distance to the star (e.g., Ida [2010]). The gaseous envelope of a giant planet has to be accreted within the life-time of the gaseous disk.

2.1.3.2 The disk-instability model

According to this theory, giant gas planets are formed by fragmentation of the circumstellar disk and self-gravitation of the dense clumps (e.g., Boss [2008]). Condensation may appear in high density areas in the spiral arms that form out in a rotating disk. The core with a mass of ~12 $M_\oplus$ of the giant gas planet would then form out of accumulation of dust grains within such dense clumps [Boss, 2008]. However, simulations yield that these clumps are not long-lived enough to form planets and that It may be unlikely that a disk can get massive enough to fragment because a disk mass >0.1 $M_\odot$ is needed [Papaloizou & Terquem, 2006]. Terrestrial planets are believed to form by

TABLE 2.1 : Time-scales of planet formation

Model	Stage	Time
Core accretion model	Core accretion	$\sim 10^6$ years
	Envelope accretion	$\sim 10^6$ years
	Migration	$\sim 10^3 - 10^5$ years
Disk instability model	Core accretion	$\sim 10^3$ years
	Migration	$\sim 10^3 - 10^5$ years

the same slow process as the core accretion model.

2.1.3.3 Disk-Planet interactions

Since the first discovery of a close-in giant gas planet in 1995 around 51 Peg at a distance of 0.05 AU, disk-planet interactions play a crucial role during planet formation. Giant planets can only form outside of the snow-line (distances larger than ~5 AU around a solar-like star) and have not been expected to be found close to the star. Thus, disk-planet interaction, like *migration*, have to occur to move giant planets in orbits close to the host star. Migration occurs through angular momentum exchange between the protoplanet and the gaseous disk. By loosing angular momentum, the planet migrates inwards toward the host star (see, e.g., Papaloizou & Terquem [2006]). Three types of migration can be distinguished from theoretical calculations (e.g., Papaloizou & Terquem [2006]). Type I migration applies to an embedded protoplanet of smaller mass (~2 $M_\oplus$), in type II migration, the protoplanet is massive enough to open a gap, and type III migration is a runaway migration applicable only in massive disks. The main difference between the three types of migration is the way the angular momentum is exchanged. Type I migration is induced by wave excitation which transfer angular momentum from the planet to the disk. For type II migration the angular momentum exchange occurs through wave excitation and shock dissipation at the shock-front of the planet and the disk material. Therefore, a planet undergoing type II migration opens a gap in the disk. The runaway migration of type III is due to direct exchange of angular momentum with the material in the planets' orbit [Terquem, 2010]. During migration, the giant planet sweeps up additional material and grows further in mass.
However, after $\sim 10^3 - 10^5$ years, migration has to stop before the planet spirals into the host star. Supposed stopping mechanisms involve the dissipation of the gaseous disk during the migration of the planet that causes the planet to stop at a certain distance. This distance is given by the outer rim of a possible inner hole of the circumstellar disk which has been produced by photo-evaporation [Papaloizou & Terquem, 2006]. In addition, planets very close to their host stars have most likely been stopped by a magnetospheric cavity, such that no further exchange of angular momentum is possible, or they have been trapped by tidal forces of the rotating host star [Hogerheijde, 2010].

2.1.3.4 Planet formation time-scales

The time-scales for giant gas planet formation by both models are presented in Table 2.1. According to the core accretion model, the time needed to form a protoplanetary core massive enough to accrete gas is $\sim 10^6$ years when runaway and oligarchic growth is considered [Ida, 2010]. The gaseous envelope gets accreted in additional $\sim 10^6$ years. In contrast, the time-scale for giant planet formation in the disk instability model is much shorter with $\sim 10^3$ years [Boss, 2008]. However, in both models the formation of giant gas planets is possible within the life-time of circumstellar disks. Nevertheless, the time-scales needed is a significant difference between both models. Thus, searching for planets around young stars with an age around 1–10 Myr can give constraints on the dominant formation model of giant gas planets.

2.1.4 The brown dwarf desert

Brown dwarfs are bodies massive enough to burn deuterium ($M \geq 13\,M_{Jup}$), but not massive enough to burn hydrogen ($M \leq 80\,M_{Jup}$), such that they have masses between the planetary and stellar regime (e.g., Burrows *et al.* [1997]). The formation of brown dwarfs in circumstellar disks may have elements of the star and planet formation models or some new mechanism [Burrows *et al.*, 1997]. The mass boundaries of brown dwarfs should not necessarily correspond to transitions in the mode of formation. The physics of gravitational collapse, fragmentation, accretion disk stability, and transfer of angular momentum should be responsible for the relative abundances of objects of different masses, not fusion onset limits. However, there seems to be a brown dwarf desert, a deficit in the frequency of brown dwarf companions relative to the frequency of either less massive planetary companions or more massive stellar companions to solar-like hosts [Grether & Lineweaver, 2006]. Of the solar-like stars that have a close companion ($P \leq 5$ yr), 11 ± 3% have stellar, <1% have brown dwarf companions, and 5±2% have planetary companions [Grether & Lineweaver, 2006], despite brown dwarfs being the easiest objects to detect by the radial velocity technique (see Section 2.2).
The constraints for the companions to solar-like stars indicate that close-orbiting brown dwarfs are very rare. The fact that there is a close-orbiting brown dwarf desert but no free-floating brown dwarf desert suggests that post-collapse migration mechanisms may be responsible for this relative dearth of observable brown dwarfs rather than some intrinsic minimum in fragmentation and gravitational collapse in the brown dwarf mass regime [Grether & Lineweaver, 2006]. A suggestion is that the kinematic viscosity of a massive circumstellar disk could cause brown dwarfs to spiral into the host star. The prediction is that young stars should have an order of magnitude more brown dwarfs in close orbits, since the time-scale for the migration is ~1 Myr [Armitage & Bonnell, 2002]. This prediction can be tested during this study.

2.2 The radial velocity technique

The *radial velocity technique*, also called *Doppler spectroscopy*, is an indirect detection method which uses the starlight to measure the gravitational influence of an orbiting planet on its host star. In a star-planet system, both orbit their common center of mass

(barycenter) according to the laws of gravity and motion. Thus, the star is also in motion and according to the Doppler effect, the light emitted by a source approaching the observer is shifted towards shorter wavelengths and for a receding source, the light is shifted to longer wavelengths. Thus, the radial velocity technique consists of monitoring potential Doppler shifts in the spectra of stars and convert these shifts into radial velocity variations (see review of Eggenberger & Udry [2010]). These shifts can be interpreted as the reflex motion of the star due to an orbiting companion. Such a companion on a Keplerian orbit induces on its parent star a perturbation in the form of

$$V_r(t) = K[\cos(v(t) + \omega) + e\cos(\omega)] + \gamma \tag{2.2}$$

where K is the velocity semi-amplitude

$$K = \frac{2\pi a_\star \sin i}{P\,(1-e^2)^{1/2}} \quad , \tag{2.3}$$

ω is the longitude of periastron, and γ is the systemic velocity (barycentric velocity). Since $v(t)$, the true anomaly, depends on the orbital period (P), eccentricity (e), and time of periastron (T_0), fitting a radial velocity time series with a Keplerian model yields six parameters: $K, e, \omega, T_0, P,$ and γ. For a planetary system, K is related to the masses of the two components through the mass function

$$\frac{(m_p \sin i)^3}{(M_\star + m_p)^2} = \frac{P}{2\pi G} K^3 \left(1-e^2\right)^{3/2} \tag{2.4}$$

(G as the gravitational constant) by which the minimum mass of the planet can be inferred as

$$m_p \sin i \simeq \left(\frac{P}{2\pi G}\right)^{1/3} K\, M_\star^{2/3} \left(1-e^2\right)^{1/2} \tag{2.5}$$

and the semimajor axis of the orbit as

$$a \simeq \left(\frac{G}{4\pi^2}\right)^{1/3} M_\star^{1/3} P^{2/3} \quad . \tag{2.6}$$

Therefore, fitting radial velocity data with a Keplerian model to account for a planetary companion gives all orbital elements, except the orbital inclination i. When the mass of the host star is known or can be estimated by other means, the minimum mass and the orbital distance of the companion can be inferred. The inclination i can be calculated from the projected rotational velocity, rotation period and the radius of the star, when assuming that the planet orbits in the rotation plane of the star.

2.2.1 Instrumentation

Since the probability of detecting a planetary signal depends essentially on the value of the velocity semi-amplitude, it indicates that the radial velocity technique is sensitive to the detection of massive and short-period companions. In the solar system, Jupiter induces a radial velocity perturbation on the sun of $K = 12.3\,\mathrm{ms}^{-1}$, while the earth induces a perturbation of $K = 9\,\mathrm{cms}^{-1}$ (e.g., Eggenberger & Udry [2010]). To

achieve such high-precision measurements of spectral line shifts, highly stable *echelle* spectrographs have to be used. Such spectrographs are built with optical fibres to convey the starlight from the telescope to the spectrograph, which produce a nearly uniformly illuminated disk at the spectrograph entry. This technique accounts for moving of the incoming light at the spectrograph slit due to guiding errors, seeing fluctuations and atmosphere refraction. This moving produces errors in the order of a few kms^{-1}. Furthermore, modern spectrographs are stabilized in temperature and pressure with variations below 0.1 K (e.g., for HARPS) because variations of the air refractive index and thermomechanical flexures within the spectrograph can produce motions of the spectrum relative to the detector in the order of $\sim$400 ms^{-1} [Eggenberger & Udry, 2010]. Yet, small wavelength shifts can not be avoided, such that some kind of wavelength calibration to monitor these shifts and correct for them, has to be applied. The commonly used techniques are the simultaneous wavelength calibration and the use of a cell with a well-characterized gas in the path of the starlight. In this gas-cell method, a composition of the stellar spectrum and a static reference spectrum is recorded. These both must be deconvolved to be able to obtain the stellar spectra and to use the reference spectrum for wavelength calibration. In the simultaneous wavelength method, the light of a reference lamp is fed into the spectrograph via a second fibre. This reference light takes the same path through the spectrograph, such that it experience the same internal drifts as the stellar light, which can be corrected for internal drifts with the reference light. As a reference lamp, Th Ar +Ne is often used and for the gas-cell method, a cell filled with Hg is used.
For this study, the observations have been carried out with the echelle spectrographs FEROS and HARPS at the 2.2m MPG/ESO and 3.6m telescope in La Silla, Chile, which use the simultaneous wavelength calibration method (see Section 3.2) [Kaufer *et al.*, 1999; Mayor *et al.*, 2003].

2.3 Stellar activity and its influence on RV

Stellar activity is used throughout this study as a synonym for activity in the stellar chromosphere and photosphere induced by the stars' magnetic field and accretion process. Thus, activity in this sense encompasses diverse phenomena that all produce emission in excess of that expected from an atmosphere in radiative equilibrium. It is linked to changes in the stellar magnetic field, whether periodic or irregular and is therefore tied to the structure of the subsurface convection zone, the star's rotation and the regeneration of the magnetic field via a self-sustaining dynamo (e.g., Hall [2008]). Stars of spectral type F–M inhibit such a convection zone and magnetic field, such that stellar activity is crucial for the targets of this study. For a complete review of stellar atmospheres, I refer to Reid & Hawley [2005] and Unsöld & Baschek [2002].
The magnetic phenomena on the stellar surface induce radial-velocity variation through the temporal and spatial evolution of spots, plaques, and convective inhomogeneities. These perturbations of the radial velocity are referred to as *stellar jitter* or *RV jitter*. This jitter depends on effective temperature, activity and $v \sin i$. Typical values are $<5\,\mathrm{ms}^{-1}$ for quiet, slowly rotating stars with an age of a few Gyr (e.g., Hall [2008]) and $\sim$50–1 000 ms^{-1} for young and active F5–M2 dwarfs [Desort *et al.*, 2007]. This RV

jitter is induced because the stellar activity alters the shape of the spectral lines and therefore, affects the RV computetion (see Section 4.1). Note that solar-like oscillations of the surface produce amplitudes in the order of several cms^{-1} and are therefore not detectable in highly active (young) stars.

2.3.1 The stellar magnetic field as the source of activity

The magnetic field of the star is produced and regenerated by the differential rotation of the star and the convection zone below the photosphere (e.g., Reid & Hawley [2005]). Because of this so-called $\alpha - \Omega$ process, magnetic flux tubes break through the stellar surface creating bipolar groups of stellar surface spots. These spots appear black compared to the photosphere because the temperature of the spots is ~2000 K colder than that of the photosphere [Reid & Hawley, 2005]. In addition, magnetic flux tubes heat the chromosphere and corona of the star. However, the chromosphere must be cooled down by some processes, because a rapid increase in temperature is not measured in contrast to the corona. These processes involve the cooling of the plasma by collisional encounters of e^-, which can be identified by emission in stellar spectral lines which have their origin in the chromosphere [Reid & Hawley, 2005]. These indicators of stellar activity are presented in Section 2.3.2.

2.3.2 Stellar activity indicators

There are several possibilities to quantify stellar activity by measuring spectral lines that are sensitive to changes in the stellar photosphere and chromosphere. These indicators are listed in Table 2.2.

The source functions of the Mg II and Ca II lines are dominated by collisional encounters of e^-, reflecting the local plasma conditions in the chromosphere because collisional processes are tied to the local electron temperature [Hall, 2008]. This manifest in the emission reversal in the line cores which are formed in the chromosphere [Vaughan *et al.*, 1978]. The increase of the electron temperature occurs due to the acceleration along magnetic field lines breaking through the chromosphere. Thus, these lines are good indicators for magnetic activity. In order to see an emission reversal in the line core of the Hα and Hβ lines, which are also formed in the chromosphere, a much hotter and denser environment than for the Mg II and Ca II lines is needed because the source function for these lines is dominated by the photoelectric effect and the collisional term becomes important only under hot and dense conditions [Hall, 2008]. These conditions are reached during flares, for very active stars, or during the accretion process at the shock front of the infalling material. Similar conditions have to be satisfied for the emission reversal of the He I line at λ 5876 Å. Therefore, this line is a good indicator for an ongoing accretion process.
In order to measure the effect of cold spots on the surface (which are also induced by magnetic activity) the line-depth ratio (LDR) of temperature sensitive and insensitive lines can be used [Gray, 1992]. With the LDR of two temperature sensitive and insensitive lines, changes in the surface temperature due to changes of the area covered by a colder spot can be traced. The presence of a dark spot would affect the depth of the temperature sensitive line because of the lower temperature in the spot. Therefore, the LDR of temperature sensitive and insensitive lines changed. The amount of depth

ratio variation should depend on the sensitivity to the temperature variation of the specific lines considered, and the fraction of surface covered by the spot [Catalano *et al.*, 2002]. The LDR of V I/Fe I has been chosen for this analysis because this ratio is sensitive to temperature changes over the full range of spectral types analysed in this study (see Section 4.2).
In addition, the decrease in the continuum induced by the presence of a cold spot also affects the line shape because only the part of the spectral line arising from the location of the spot is affected, whereas the rest of the line is not [Gray, 1992]. This sums up to an asymmetric profile of the spectral line, which can be measured with the bisector. The bisector connects the mid-points of lines joining both sides of the spectral lines at equal heights (see Section 4.1.2).

These indicators of stellar activity have to be measured when analysing the radial velocity data. However, the Mg II lines lie outside of the wavelength range of both FEROS and HARPS spectrographs, consequently no observations of this lines are possible. A description of the measuring methods for the other stellar activity indicators is given in Section 4.2.

TABLE 2.2 : Stellar activity indicators.

Indicator	Measurement of	Caused by	Origin	Tracer for	Analysis
Bisector span	bisector of the CCF	asymmetric shape of the spectral lines	photosphere	cold spots on stellar surface	- time analysis for periodicity - correlation with RV
Ca II K index	ratio of central emission to wings	magnetic heating	chromosphere	hot spots on surface	- time analysis for periodicity
Ca II IRT lines	equivalent width	magnetic heating	chromosphere	hot spots on surface	- time analysis for periodicity
Hα, Hβ	equivalent width	magnetic heating and shock front of infalling material	chromosphere	flares, accretion	- time analysis for periodicity
Mg II index	ratio of central emission to wings	magnetic heating	chromosphere	hot spots on surface	- time analysis for periodicity
He I	equivalent width	heating by shock front of infalling material	chromosphere	accretion	- time analysis for periodicity
V I/Fe I	line depth ratio	temperature change	photosphere	cold spots on stellar surface	- time analysis for periodicity

3 Observations and data reduction

3.1 Target list

The purpose of this study is to search for giant planets around young stars with the RV technique. In order to obtain precise RV measurements, the targets have to be selected carefully. The selection criteria for the targets are summarized in Table 3.1. The selection criteria are:

- The first selection criteria is the age of the targets. In order to find observational constraints for planet-formation time-scales, I selected stars with ages of 1–100 Myr. To be able to determine the age of the targets, Li I measurements should be available.
- From previous observations [Setiawan *et al.*, 2007, 2008b; Weise, 2007], I concluded that the accuracy of the RV measurements is coupled to the projected rotational velocity $v \sin i$ of the target, with higher accuracy for slowly rotating stars. Therefore, I selected stars with $v \sin i < 30\,\mathrm{kms}^{-1}$. The correlation between $v \sin i$ and the accuracy of the RV measurement is presented in Section 5.2.3.
- The precision of the RV measurements is also limited by the signal-to-noise ratio (SNR) of the stellar spectrum (see Section 5.2.3). For the 2.2m MPG/ESO telescope in La Silla, Chile, where FEROS is located, the execution time for a V=11.5 mag star is 40 minutes to obtain a spectrum with a SNR of 50–70. However, observing time is limited by the amount of time allocated for this study. Therefore, I selected stars with $V \leq 11.5$ mag.
- Furthermore, the targets should be single or SB1 stars and of spectral type F5–M2 in order to be correctly cross-correlated with the appropriate template (see Section 4.1).

I selected targets from Torres *et al.* [2006] and other sources [Guenther *et al.*, 2007; James *et al.*, 2006; Lahuis *et al.*, 2007; Padgett *et al.*, 2006; Rodmann *et al.*, 2006; Schegerer *et al.*, 2006; Silverstone *et al.*, 2006], by applying these selection criteria. For all stars, Li I measurements or age estimations, $v \sin i$ measurements, and the spectral type are given in the source catalogues. For some stars, information about the evolutionary stage of the circumstellar disks is also available.

Overall, 200 stars have been selected, 100 of which have been observed with FEROS at the 2.2m MPG/ESO telescope between February 2008 and May 2010 on 14 MPG GTO

TABLE 3.1 : Selection criteria for the targets in this study. Observations for $v \sin i$, multiplicity status, and spectral type are taken from Torres *et al.* [2006].

Criterion	Based on	Reason
Age 1–100 Myr	Li I measurements	planet formation time-scales
$v \sin i < 30\,\mathrm{kms}^{-1}$	observations	RV accuracy
V < 11.5 mag	from SIMBAD	integration time at the telescope, sets SNR
Single or SB1 stars	observations	RV accuracy
Dwarf stars of type F5–M2	observations	match the template for cross-correlation

(*Max-Planck Gesellschaft Guaranteed Time Observations*) observing runs and 2 HARPS runs. The target list of all 200 stars is shown in Table A.1 in Appendix A. The 100 targets observed are listed in Table B.1 in Appendix B.

3.1.1 Observing strategy

To be able to identify the period of a RV variation, a good phase coverage is needed. Therefore, the observing strategy was to observe 10–15 targets for 2–3 times each night during an observing block with different time intervals between the observations. The time intervals between the observations have to be variable because constant spacing between individual observations can lead to false detections in the period analysis. In that case, the most significant periods derived correspond to the interval between the observations. Furthermore, large uneven spacing has to be avoided because this can disturb the period analysis. In this case, only short periods are found to be significant, independent of the real period of the variation [Zechmeister & Kürster, 2009].
However, observing the star more than once each night gives a good coverage of a short-term variation and observations on subsequent nights covers long-term variability. The number of stars observed during each observing block has been set according to the amount of time allocated for this project in the particular observing run.
After the first three runs, the strategy has been changed in order to obtain more spectra for stars that show a significant RV variation. Because of this, other stars have been observed less often than planed at the beginning of this project. Thus, at the end of the observations in May 2010, 18 stars have more than 10 observations, 9 stars have 5–10 observations, and 73 stars have less than 5 observations.

3.2 Observations and Data reduction

For the 100 observed targets, high-resolution echelle spectra have been obtained with FEROS at the 2.2m MPG/ESO (*Max-Planck-Gesellschaft/European Southern Observatory*) telescope at La Silla, Chile, between February 2008 and May 2010 during MPG guaranteed time. FEROS (*Fibre-fed Extended Range Optical Spectrograph*) is a high-resolution ($(\lambda/\Delta\lambda) = \mathrm{R} = 48\,000$) fibre-fed spectrograph with a wavelength coverage of 3600 - 9200 Å in 39 echelle orders [Kaufer *et al.*, 1999], and a long-term RV precision of better than $10\,\mathrm{ms}^{-1}$ [Setiawan *et al.*, 2007]. The spectrograph has two fibers (Section 2.2.1) and can be operated in both "object-sky" (OS)-mode for spectral analysis, and in "object calibration" (OC)-mode for precise RV measurements [Kaufer *et al.*, 2000]. In the

OS-mode, the first fiber is fed with the stellar spectrum, while the second fiber observes the sky background. The OC-mode is used for the simultaneous calibration technique, where a ThAr+Ne emission spectrum from a calibration lamp is observed simultaneously in the second fiber during the object's exposure to monitor the intrinsic velocity drift of the instrument [Baranne *et al.*, 1996]. All observations of the targets presented here have been carried out in the OC-mode. A mean signal to noise ratio (SNR) of 100 in the continuum at 6690 Å has been reached with an exposure time of 10 min for a 7 mag star. All calibration files have been obtained following the standard ESO calibration plan. The reduction of all data presented here has been done by using the FEROS Data Reduction System (DRS) available at the telescope. This package does the bias subtraction, flatfielding, traces and extracts the echelle orders, computes and applies the wavelength calibration, and puts all data in the barycentric frame. Special care has been taken of the wavelength calibration, which was repeated if the residuals deviated more than 1 σ from the last calibration made.
In addition to the FEROS observations, high-resolution spectra for 32 targets have been observed with HARPS (*High Accuracy Radial velocity Planet Searcher*; Mayor *et al.* [2003]) at the 3.6m telescope in La Silla, Chile, in May 2008 and February 2009 (081.C-0779 and 082.C-0390). HARPS spectra span a wavelength range from 3780–6910 Å, somewhat smaller than FEROS, but at a much higher resolution (R = 115 000). The stability of HARPS is about 1 ms^{-1} [Mayor *et al.*, 2003]. The data have been reduced using the online DRS for HARPS at the telescope.

4 Data analysis methods

4.1 Measuring radial velocities with MACS

In order to have a reliable and adaptable tool to measure precise radial velocities from spectra of young and active stars, I developed a new cross-correlation tool for the analysis of FEROS and HARPS data, called MACS, *Max-Planck Institute for Astronomy Cross-correlation and Spectral analysis tool*. This tool comes with a graphical user interface and is written in JAVA. Therefore, it can be used with any operating system. It is used to calculate radial velocities by cross-correlation of stellar spectra obtained with FEROS and HARPS, with a box-shaped binary template [Baranne *et al.*, 1996] which matches the spectral type of the target. MACS makes use of the JAVA scientific library of T.M. Flanagan[1]. In this Section, I describe the scientific background of MACS. In Appendix F, a more technical description in the user guide is given.

4.1.1 Cross-correlation of stellar spectra

The spectral data have to be reduced using the standard DRS available at the telescopes before the data can be analysed with MACS. After this, the science spectrum and the spectrum used for simultaneous calibration can be analysed with MACS. MACS starts with the normalization of the flux in each echelle order to remove the curvature of the flux over the wavelength range of the order. This curvature of the flux is due to the use of an image slicer in FEROS. The normalization is based on the IRAF task `continuum` and the algorithm of Zhao *et al.* [2006]. MACS extracts the continuum of the spectrum and fits this by a low order polynomial to remove the curvature. The continuum is extracted by fitting a low order polynomial to the spectrum and replacing residuals which differ more than 1σ from the fit by the calculated value of the fit, like in IRAFs `continuum` task. However, this does not extract a completely line-free continuum. Thus, MACS further selects the local high points, following Zhao *et al.* [2006], by defining derivatives of the left and right subsequent pixels to pixel i by

$$\begin{aligned} s'_{+}(\mathrm{i}) &= s(\mathrm{i}) - s(\mathrm{i}-1), \\ s'_{-}(\mathrm{i}) &= s(\mathrm{i}+1) - s(\mathrm{i}). \end{aligned} \tag{4.1}$$

A local high point is given when $s'_{-}(\mathrm{i}) < 0$ and $s'_{+}(\mathrm{i}) > 0$ are fulfilled. These points allow MACS to get an interpolation of the now nearly line-free continuum, which

[1] Available at `http://www.ee.ucl.ac.uk/~mflanaga`

is then fitted to remove the curvature of the flux in the echelle order. The described algorithm works fine for spectra without broad emission features. To account for broad emission lines, e.g., to be able to normalize spectra of T Tauri like stars, MACS removes emission features which deviate more than a user-defined threshold from the mean of the spectral data before the normalization starts.

After normalization, each echelle order is cross-correlated with an adequate box-shaped, binary template. For this, MACS follows Baranne *et al.* [1996] by using

$$C(v) = \sum_{l} \sum_{x} t_{l,x}(v) f_x, \tag{4.2}$$

where $t_{l,x}$ is the value of the lth line on pixel x and f_x is the value of the spectrum at pixel x. The CCF is thus minimal when the spectral lines and the box-shaped line in the template are aligned. The CCF can be fitted by a Gaussian and the minimum yields the RV of the star (e.g., Griffin [1967]; see review by Eggenberger & Udry [2010]).
The range for v and the step-size Δv of this calculation can be adjusted by the user. For the calculations in this study, Δv has been set to $0.8\,\mathrm{kms}^{-1}$. MACS then fits a Gaussian to the cross-correlation function (CCF) $C(v)$ to obtain the radial velocity for each echelle order. The regression is done by a Nelder-Mead-Simplex method.
For each individual science order and simultaneous calibration order the RV is obtained separately. The RV measured for the calibration order is subtracted from the RV of the science order to account for internal instrumental shifts, which is a commonly used method (e.g., Setiawan *et al.* [2007]). Before the RV for the whole spectrum is computed, outliers in the individual RV measurements are removed by a interquartile-filter (Tukey filter), which rejects outliers Y falling outside of the interquartile range by

$$Y < (Q_1 - 1.5\,\mathrm{IQR}) \text{ or } Y > (Q_3 + 1.5\,\mathrm{IQR}) \qquad , \tag{4.3}$$

with IQR as the interquartile range $Q_3 - Q_1$ [Hoaglin *et al.*, 1983].
From the corrected RV measurements of each echelle order, the RV for the whole spectrum is calculated by taking the weighted mean of the individual RV measurements. The weight of the individual RV measurement i is $1/\sigma^2_{\mathrm{RV}_i}$. The error σ_{RV_i} of an individual RV measurement is given by the accuracy of the Gaussian fit.

HARPS data are normalized using the same algorithm as for FEROS data, but the full wavelength range of HARPS data is divided into smaller sections of equal length and each section is normalized separately. Side effects at the edges of the defined sections have not been observed while using this algorithm for HARPS data. Furthermore, the HARPS spectrum is cross-correlated as a whole. Thus, only a single RV measurement per observation is calculated.

4.1.2 Calculation of the bisector

The CCF also represents the mean shape of the spectral lines used in the cross-correlation [Benz & Mayor, 1984]. Thus, the line shape (bisector) can be inferred from the CCF.
MACS is able to compute the bisector velocity span (BVS), bisector curvature (BC), and bisector velocity displacement (BVD) of the CCF automatically or the range of the CCF is entered by the user. For the calculation of the bisector, MACS first normalize

each echelle order and calculates the CCF according to Equation 4.9. Thereafter, points of the same height at the left and right wing of the CCF are connected. The bisector itself is defined as the connection of the midpoints of these lines [Gray, 1992]. The BVS is calculated by following Queloz *et al.* [2001]:

$$\mathrm{BVS} = \frac{1}{N}\left(\sum_t v_t - \sum_b v_b\right), \tag{4.4}$$

where v_t is a velocity at a specified height at the top of the bisector and v_b is a velocity in the lower half. Thus, the BVS gives the velocity over which the bisector spans. MACS has several built-in functions to calculate the BVS at different heights of the bisector, like the definition by Queloz *et al.* [2001] or Martínez Fiorenzano *et al.* [2005]. Throughout this thesis, the definition of Martínez Fiorenzano *et al.* [2005] has been used to calculate the BVS. By this definition, v_t is at 87% and v_b at 25% of the height of the CCF.
The BVD is a variant of the BVS and is more sensitive to changes in line profile. I defined the bisector velocity displacement following Povich *et al.* [2001] as:

$$\mathrm{BVD} = \frac{1}{3}\left(\frac{1}{N}\left(\sum_t v_t + \sum_b v_b\right) + v_5\right) - \mathrm{RV}, \tag{4.5}$$

with v_5 as the velocity at 50% height of the CCF. The BVD measures the displacement of the midpoint at 50% height of the CCF.
The BC is the second moment of the line bisector. It measures the curvature along the bisector and gives an estimate how strong the asymmetry of the CCF is. Formally the BC is the difference between the span and the midpoint at half height of the CCF [Queloz *et al.*, 2001],

$$\mathrm{BC} = \frac{v_9 - v_1 + h_5 - \left(h_1 - v_1 \frac{h_9 - h_1}{v_9 - v_1}\right)}{h_9 - h_1} - v_5. \tag{4.6}$$

In this case, h_x and v_x denote the absolute height and velocity of the CCF at the specified point of 90%, 10% and 50%.

The bisector is an important indicator for stellar activity because activity changes the shape of the spectral lines (see Section 2.3). Therefore, the shape of the CCF and the RV measurement are also affected. In this case, the BVS (and BVD, BC) and the RV are simultaneously changed and, therefore, correlated. This correlation of the BVS on RV has a negative slope because light from the star is missing due to a colder spot (e.g., Martínez Fiorenzano *et al.* [2005]; Queloz *et al.* [2001]). On the other hand, the spectral line shape can also be changed by pollution with light from a stellar companion. In this case, the correlation of the BVS on RV shows a positive slope [Martínez Fiorenzano *et al.*, 2005].

4.1.3 Adjustments available in MACS

MACS is very user-friendly and the most important adjustments to the calculations can be easily set in the GUI. To improve the accuracy of the fitting process of the CCF,

a Savitzky-Golay filter [Savitzky & Golay, 1964] has been implemented, which flattens the noise next to the CCF. This comes from noise imposed on the stellar spectra due to photon-noise, order extraction, SNR, and mismatch of the used template, and can be filtered out by the Savitzky-Golay filter. This filter can be used when the peak of the CCF is distinguishable from the noise. The Savitzky-Golay filter acts as a high-frequency band filter, thus it cleans the CCF from noise. As a result, the CCF peak can be fitted with higher accuracy and precision.
Further special features of MACS are several fitting functions that have been implemented, e.g., a rotationally broadened Gaussian [Hirano *et al.*, 2010] and a Voigt profile, and MACS is able to fit multiple Gaussians to the CCF. In addition, MACS is able to correlate of a stellar spectrum with itself or that of a template star. It is also possible to correlate the stellar spectrum with a theoretical spectrum (saved as an ascii-file). For this calculation both spectra are normalized and cross-correlated as described in Section 4.1.1.

4.1.4 Testing MACS

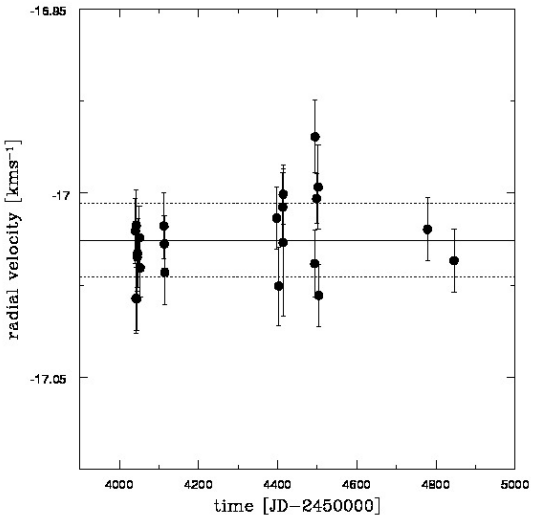

FIGURE 4.1 : Testing MACS - MACS measurements of the RV of τ Cet.

As a first test of the capabilities of MACS, I measured the RV of one of the standard stars in the SERAM program, τ Cet, which has been observed since 2004. The measurements are presented in Figure 4.1. I derived mean RV of -17.01 kms^{-1}. Note that the absolute RV depends on the starting conditions of the cross-correlation and can differ when using different algorithms. The accuracy of the mean RV is 10 ms^{-1}, which is similar to the long-term stability derived by Setiawan *et al.* [2007]. This result shows that MACS is able to calculate high-precision RV measurements from stellar spectra. I find that the differences between the individual measurements of τ Cet come from different SNR of the spectra analysed.

4.2 Measuring stellar activity indicators

In Section 2.3.2, I described the stellar activity indicators that can be analysed in the stellar spectra. In this Section, I describe the methods of measurement for these stellar activity indicators.
To estimate the chromospheric activity, a flux-index S_{FEROS} of the Ca II K line, analogous to Vaughan *et al.* [1978], has been calculated. The Ca II H line has been excluded from this analysis because of a possible contamination by the Hϵ line [Wilson, 1976]. Note that S_{FEROS} cannot be directly compared to the flux index used by Vaughan *et al.* [1978] because of slightly different spectral ranges used. However, for the purpose of this study, only relative measurements between the individual FEROS observations are needed. S_{FEROS} is the ratio of the flux of the Ca II K central emission to that in two nearby pseudo-continuum reference bandpasses (blue and red, see Equation 4.7) [Vaughan *et al.*, 1978], which are in this analysis located at 3930–3933 Å and 3935–3938 Å.

$$S_{\mathrm{FEROS}} = \frac{F_{\mathrm{emission}}}{F_{\mathrm{blue}} + F_{\mathrm{red}}} \quad . \tag{4.7}$$

This ratio has the advantage of being independent of an absolute flux calibration of the spectrum. However, because no absolute flux calibration is made, S_{FEROS} cannot be compared among the target stars, since it depends on the effective temperature of an individual star. To obtain a temperature-independent index of the chromospheric activity, I followed Noyes *et al.* [1984] to calculate R'_{FEROS}. First, the index S_{FEROS} has to be corrected for the photospheric flux in the line wings by

$$R_{\mathrm{FEROS}} = 1.34 \cdot 10^{-4} \cdot C_{cf} \cdot S_{\mathrm{FEROS}} \quad , \tag{4.8}$$

with the factor $1.34 \cdot 10^{-4}$ to compensate for $\sigma_{\mathrm{Boltzmann}}$ and a correction factor C_{cf}, which depends on stellar temperature and therefore on $(b - v)$ [Noyes *et al.*, 1984],

$$\log C_{cf} = 1.13\,(b-v)^3 - 3.91\,(b-v)^2 + 2.84\,(b-v) - 0.47 \quad . \tag{4.9}$$

This correction factor has been found by Noyes *et al.* [1984] by the analysis of Main-Sequence stars, but in Weise [2007], it is shown that this factor is also applicable to young stars. Finally, the photospheric flux of the central emission has to be removed by $\log R_{\mathrm{phot}} = -4.02 - 1.4\,(b - v)$ [Noyes *et al.*, 1984], such that

$$R'_{\mathrm{FEROS}} = R_{\mathrm{FEROS}} - R_{\mathrm{phot}} \quad . \tag{4.10}$$

The values of R'_{FEROS} are now comparable among the target stars because this index is independent from the stellar temperature. Note that young stars show a higher value of R'_{FEROS}, expressing their high stellar activity (e.g., Mamajek [2009]). Results of R'_{FEROS} for the target stars are listed in Table B.2 in Appendix B.

The infrared-triplet (IRT) of Ca II can also be used as a tracer of chromospheric activity [Linsky *et al.*, 1979]. From these 3 lines, only the Ca II lines at 8498 Å and 8662 Å are included in the FEROS spectra due to a gap in wavelength between 2 echelle orders. Of these, the Ca II line at 8498 Å is contaminated by atmospheric water vapour [Larson *et al.*, 1993], such that only the λ8662 line has been considered. For this activity indicator, the equivalent width (EW) of the central emission has been measured

after normalization of the spectrum [Larson *et al.*, 1993]. Note that no analysis for the Ca II IRT lines is possible for the HARPS data due to the smaller wavelength coverage of HARPS.
The Hα line is also an indicator of activity in the chromosphere (see Section 2.3.2). To search for variations of this line, the EW of Hα has been measured after normalization of the spectrum. As an indicator of photospheric activity, the LDR of the V I (at 6252 Å) and Fe I (at 6253 Å) lines has been measured, analogous to Catalano *et al.* [2002]. Changes in this V I/Fe I LDR show a linear relation to temperature over a large temperature range [Catalano *et al.*, 2002]. Thus, changes of the mean surface temperature due to changes in the area covered by cooler spots can be identified.

4.2.1 Radial velocity variation induced by stellar surface spots

Surface inhomogeneities, like surface spots, can live longer than the rotational period of the star and produce a variation in radial velocity because the shape of the spectral lines is altered by surface spots (see Sections 2.3 and 4.1.2). Thus, this RV variation can be interpreted as caused by an orbiting companion. To account for this *RV jitter*, the influence of surface spots has been studied in detail by, e.g., Desort *et al.* [2007] and Saar & Donahue [1997]. The equations derived by them can be used to estimate the expected RV jitter when the configuration of the spot pattern is known, or, vice-versa, can be used to estimate the size of the surface spot from the RV jitter or photometric variation (when assuming a single equatorial spot) [Desort *et al.*, 2007].
Saar & Donahue [1997] estimate the amplitude A_{tot} of the RV jitter caused by stellar activity to

$$A_{\mathrm{tot}} = \sqrt{A_{\mathrm{s}}^2 + A_{\mathrm{c,max}}^2} \quad , \tag{4.11}$$

with A_{s} as the semi-amplitude of the RV jitter induced by spots,

$$A_{\mathrm{s}} \approx 6.5\, f_{\mathrm{s}}^{0.9}\, v \sin i \quad . \tag{4.12}$$

Here, A_{s} depends on $v \sin i$ and the spot-filling factor f_{s} expressed in percent, which can be estimated by $f_{\mathrm{s}} \approx 0.4\,\Delta V$, with ΔV as the amplitude of the photometric variation. The second factor in Equation 4.11 is caused by inhomogeneous convection [Saar & Donahue, 1997] and is given by

$$A_{\mathrm{c,max}} = (\mathrm{BVS}_{\mathrm{max}} - \mathrm{BVS}_{\mathrm{min}})\,/4 \quad , \tag{4.13}$$

with the maximum and minimum values of the measured bisector velocity span (BVS).

Desort *et al.* [2007] gives the expected RV amplitude caused by a single equatorial spot as

$$A_{\mathrm{D}} = C_{\mathrm{D}}\, f_{\mathrm{r}}\, v \sin i^{1.1} \quad , \tag{4.14}$$

with $C_{\mathrm{D}} = 15.4$ for F6V type stars, $C_{\mathrm{D}} = 16.0$ for G2V type stars, and $C_{\mathrm{D}} = 18.3$ for K2V type stars. The factor f_{r} is the fraction of the visible hemisphere covered by the spot [Desort *et al.*, 2007]. Note that $f_{\mathrm{r}} = f_{\mathrm{s}}/2$.
With these equations, the RV jitter caused by stellar activity can be estimated and compared to the measured amplitude of the RV variation.

4.3 Obtaining stellar parameters

4.3.1 Basic stellar parameters

The effective temperature $T_{\rm eff}$, surface gravity $\log g$, metallicity [Fe/H] and microturbulence of the stellar surface v_t describe fully the stellar atmosphere. Therefore, I name these parameters the *basic stellar parameters*. These parameters can be measured by different methods, like photometric observations to obtain the effective temperature. In this study, the basic stellar parameters will be derived directly from the stellar spectrum itself. This has the advantage of being independent from extinction, in contrast to photometric observations. The basic stellar parameters have been calculated by measuring EWs of suitable spectral lines of a single element, e.g., Iron, because the abundance A of an element in the stellar atmosphere depends on $T_{\rm eff}$ and $\log g$, and affects directly the opacity of the spectral lines and, therefore, the shape, depth, and EW of the lines [Gray, 1992]. To obtain the basic stellar parameters from EW measurements of Fe I and Fe II, the method described by Takeda *et al.* [2002] has been used. According to this method, the stellar parameters are determined by minimizing the differences between the measured EWs and a grid of theoretical EWs taken from artificially created spectra. The grid of theoretical EWs ranges from 4750 K to 6750 K (~ K2 to F5). Thus, $T_{\rm eff}$, $\log g$, [Fe/H], and v_t can be determined directly from the measured equivalent widths. The Fe I and Fe II lines of which the EWs have been measured are listed in Table 4.1. For each target, 41 Fe I and 6 Fe II lines in the spectrum with the highest SNR have been measured and the best fitting values for $T_{\rm eff}$, $\log g$, and [Fe/H] have been obtained by using *TGV*, developed by Takeda *et al.* [2002]. The results agree well within the errorbars with the results of other studies, thus, confirming the validity of this approach. I discuss the results in Chapter 5) and list them in Table B.2 in Appendix B.

4.3.2 Measurement of $v \sin i$

To measure the radial and rotational velocities of the target stars, the stellar spectra have been cross-correlated with appropriate numerical templates for the respective stellar spectral type (see Sections 2.2 and 4.1.1). The half width at half maximum $\sigma_{\rm CCF}$ of the CCF, derived from a Gaussian fit, corresponds to a mean spectral line width broadened due to intrinsic (thermal, natural), instrumental, and rotational effects [Benz & Mayor, 1984; Melo *et al.*, 2001; Queloz *et al.*, 1998]:

$$\sigma^2_{\rm CCF} = \sigma^2_{\rm rot} + \left(\sigma^2_{0,\star} + \sigma^2_{\rm inst}\right), \tag{4.15}$$

where $\sigma_{\rm rot}$ is the broadening due to stellar rotation and $\sigma^2_0 = \sigma^2_{0,\star} + \sigma^2_{\rm inst}$ is the effective line width of the non-rotating star. In this latter variable, all intrinsic line-broadening effects, like thermal and gravitational broadening, turbulence (all in $\sigma_{0,\star}$), and the instrumental profile, $\sigma_{\rm inst}$, are convolved.

Thus, the projected rotational velocity, $v \sin i$, is proportional to $\sigma_{\rm rot}$, such that

$$v \sin i = A \sqrt{\sigma^2_{\rm CCF} - \sigma^2_0}, \tag{4.16}$$

where A is a coupling constant.

TABLE 4.1 : Fe I and Fe II used in TGV with their excitation potential χ and $\log gf$ (f is the oscillator strength of the electron transition). Lines marked with * can be used for stars with $20 < v \sin i < 75\,\mathrm{kms}^{-1}$. All other lines also for stars rotating slower than $20\,\mathrm{kms}^{-1}$. From Takeda *et al.* [2002]

λ [Å]	χ [eV]	$\log gf$		λ [Å]	χ [eV]	$\log gf$	
Fe I lines				Fe I lines			
4445.476	0.087	-5.441		6271.283	3.330	-2.703	*
5247.059	0.087	-4.946		6297.801	2.223	-2.740	
5250.217	0.121	-4.938		6311.505	2.830	-3.141	
5326.145	3.570	-2.071		6322.694	2.588	-2.426	
5491.835	4.190	-2.288		6481.878	2.279	-2.984	
5600.227	4.260	-1.420		6498.946	0.958	-4.699	
5661.348	4.280	-1.756		6518.374	2.830	-2.450	
5696.093	4.550	-1.720		6574.233	0.990	-5.004	
5701.553	2.560	-2.216		6593.880	2.433	-2.422	
5705.468	4.300	-1.355		6609.119	2.559	-2.692	*
5778.458	2.590	-3.440		6625.027	1.010	-5.336	
5855.080	4.610	-1.478		6750.160	2.424	-2.621	
5909.978	3.210	-2.587		6752.711	4.640	-1.204	
5956.700	0.859	-4.605	*	6837.009	4.590	-1.687	*
6082.715	2.223	-3.573	*	6945.214	2.424	-2.482	
6137.000	2.198	-2.950		6971.936	3.020	-3.340	
6151.622	2.176	-3.299	*	7401.689	4.190	-1.599	
6173.343	2.223	-2.880	*	Fe II			
6180.208	2.730	-2.586	*	4576.339	2.844	-2.900	*
6200.320	2.609	-2.437	*	4620.520	2.828	-3.190	
6219.289	2.198	-2.433	*	5234.630	3.221	-2.220	*
6232.649	3.650	-1.223	*	5414.075	3.221	-3.480	
6240.652	2.220	-3.233	*	6432.683	2.891	-3.510	*
6265.141	2.176	-2.550	*	7711.731	3.903	-2.450	

This coupling constant has already been calibrated for FEROS by Melo *et al.* [2001]. However, it depends not only on the instrument, but also on the cross-correlation method used to calculate the CCF. Therefore, A had to be recalibrated for measurements with MACS. Furthermore, σ_0 has only been calibrated for FEROS at the 1.52m telescope in La Silla, Chile. However, FEROS moved to the 2.2m telescope in 2003, such that a new calibration for this study was needed.

Measurements of $v \sin i$ using HARPS data have often been calibrated by the calibration by Santos *et al.* [2002]. This calibration was built from CORALIE data. Therefore, in order to have a self-consistent analysis in this study, a new calibration similar to the one for FEROS has been calculated from the HARPS data.

The details of these calibrations are described in Appendix E. I derive and use in this study:

$$A_{\mathrm{FEROS}} = 1.8 \pm 0.1$$

$$A_{\mathrm{HARPS}} = 1.88 \pm 0.05$$

and

$$\log \sigma_{0,\mathrm{FEROS}} = 0.641 + 0.043 \cdot (\mathrm{b} - \mathrm{v})$$

$$\log \sigma_{0,\mathrm{HARPS}} = 0.574 + 0.032 \cdot (\mathrm{b} - \mathrm{v}).$$

For the 16 stars, which were observed with FEROS and HARPS, I compared the $v \sin i$ calculated by both calibrations and found that both measurements diverge no more than $0.4\,\mathrm{kms}^{-1}$, which is within the measurement accuracy. The accuracy for $v \sin i$ of both instruments is also similar.

4.3.3 Age estimation

In the convective envelopes of F–M type stars, primordial lithium (Li I) is depleted as the star ages (e.g., Palla [2002]). The amount of depletion depends also on the effective temperature of the star, which means that the EW of Li I can only be compared among stars with the same effective temperatures, i.e., spectral type. To derive the dependency of Li I EW on age and spectral type, the measured mean Li I EW for different stellar associations with known age have been used. These associations are UMa (300 Myr), Pleiades (90 Myr), IC 2602 (30 Myr), TucHor (30 Myr), βPic (30 Myr), TWA (8 Myr), ηCha (8 Myr), and NGC 2264 (4 Myr) and the EW of Li I has been taken from [Zuckerman & Song, 2004]. These data points have been triangulated, interpolated and combined on a regular grid to obtain a contour plot in Figure 5.1. The effect of the rotational velocity on Li I depletion is negligible for the stars in the sample [Bouvier, 1995].
The age of the individual targets has then been derived by comparing the EW of Li I at 6708 Å with this grid. For stars that are members of young stellar associations with known age range, the age derived by the Li I EW has been compared to the mean age of the associations. I find that the age estimates agree very well in all cases, confirming the validity of this approach. The Li I feature is a good indicator of stellar age, but the accuracy of the stellar age is typically 10–50%.

In addition to the Li I EW measurements, the ages for some stars have been inferred from evolutionary tracks calculated by Siess *et al.* [2000]. For this, the position of the star in the Hertzsprung-Russell-Diagram (HRD) has to be known and for this, the effective temperature or color $(b - v)$ and the distance to the star, to derive the absolute magnitude, have to be known. The accuracy of T_{eff} and distance determine the error of the age inferred by this approach. The distance to the young open clusters is known to only 5–20% and distances to individual field stars are unknown and hard to measure. Therefore, the accuracy of the age inferred from evolutionary tracks is also limited to 20%. A further concern of systematic error for the age determination by evolutionary tracks is that pre-main-sequence evolutionary tracks are poorly constrained and the resulting stellar age depends significantly on model assumptions and these models seem to under-predict stellar ages by 30–100% [Hillenbrand *et al.*, 2008].

4.3.4 Veiling

For accreting stars, veiling produces an additional continuum overlayed on the intrinsic stellar spectrum due to hot accretion spots on the stellar photosphere. This additional continuum alters the EW of spectral lines, as it changes the relative line depth (e.g., Appenzeller & Mundt [1989]). Therefore, the veiling has to be determined in order to derive the pure photospheric EW of Li I.

In order to determine the veiling, theoretical spectra have been computed for the respective stellar spectral types by using the SPECTRUM package [Gray & Corbally, 1994] together with Kurucz atmosphere files [Kurucz, 1993]. These theoretical spectra have been broadened to the $v \sin i$ of the star and veiled by adding a flat continuum. The veiling of the target stars has then been determined using spectral lines other than Li I in a 50 Å window centred on the Li I feature (6708 Å) by minimising the difference between the simulated and the observed stellar spectrum. The EW of Li I was then corrected by

$$\mathrm{EW}_{\mathrm{corrected}} = \mathrm{EW}_{\mathrm{measured}} \cdot (V + 1)\,, \tag{4.17}$$

where V is the measured veiling [Johns-Krull & Basri, 1997], to measure the photospheric EW of Li I.

Veiling also affects the colours of accreting stars, such that they appear to be of earlier spectral type than they actually are. This is because the boundary layer of the circumstellar disk, where the accreted material is originating from, emits more light in the blue part of the stellar spectrum [Hartigan *et al.*, 1989]. Thus, due to an apparent shift to an earlier spectral type, this will underestimate σ_0 in the calibration of $v \sin i$ (Equation E.6). The width of the CCF remains unchanged. With an unchanged CCF and underestimation of σ_0 due to a wrong (b − v), we therefore slightly overestimate the $v \sin i$ for accreting stars.
The maximum change in $v \sin i$ due to veiling can be estimated by using Equation (E.6) and a shift in spectral type from M0 to G0 (as an example of the effect of veiling). I found this maximum effect on $v \sin i$ to be 0.7 kms^{-1}, which is smaller than the uncertainty of the $v \sin i$ measurements, and, therefore, does not affect the results.

4.3.5 Signatures of accretion and disk presence

In order to analyse the measured $v \sin i$ for disk-braking mechanisms (in Section 5.2), I have to know the evolutionary state of the circumstellar disks of the target stars. Furthermore, I have to distinguish between accreting and non-accreting stars.
To identify stars which are still accreting, the EW and full width at 10% height ($\mathrm{W}_{\mathrm{H}\alpha}$) of the H$\alpha$ emission, as well as the EW of He I at 5876 Å have been measured. All criteria have to be fulfilled, because high stellar rotation broadens also the Hα emission line.
To distinguish between Hα emission due to chromospheric activity and due to accretion of disk material, the criteria by Appenzeller & Mundt [1989], and Jayawardhana *et al.* [2006] have both been investigated. According to Appenzeller & Mundt [1989] a star is assumed to accrete when the EW of Hα exceeds 10 Å. In contrast, Jayawardhana *et al.* [2006] use $\mathrm{W}_{\mathrm{H}\alpha}$ and determine a value of 200 kms^{-1} (4.4 Å) as the accretion threshold.

The EW of Hα has been widely used to identify accreting stars, but chromospherically active stars can produce a comparable increase of the Hα EW. During accretion, Hα emission also arises from "hot spots" on the stellar surface produced by accreting disk material. The EW in both cases can be comparable, because for late-type stars, the chromospheric Hα emission is more prominent due to a diminished photosphere as compared to hotter stars (e.g., White & Basri [2003]). This means that the EW of Hα due to chromospheric activity is much higher for cool stars and depends on the spectral type of the stars. Therefore, no clear statement can be made at which Hα EW a star accretes.

A better discrimination between accreting and chromospherically active stars can be made by measuring the $W_{H\alpha}$ of the emission feature. Emission due to an active chromosphere is limited in amount by the saturation of the chromosphere and in width by stellar rotation and non-thermal velocities of the chromosphere. White & Basri [2003] found that accreting stars tend to have $W_{H\alpha}$ broader than 270 kms^{-1} (5.9 Å), whereas Jayawardhana *et al.* [2006] used a less conservative threshold at 200 kms^{-1} (4.4 Å). For the purpose of this study, the threshold from Jayawardhana *et al.* [2006] has been used to avoid missing accretors in this selection process.

In addition, He I at 5876 Å has been investigated, because stellar rotation also affects the $W_{H\alpha}$. The He I feature can be directly linked to the accretion process of the star, because the luminosity of He I correlates with the accretion luminosity (Fang *et al.* [2009, and references herein]). Other features, like [O I] at 8446 Å cannot be used to identify the accretion process, since it can be contaminated by the [O I] feature of the circumstellar disk [Fang *et al.*, 2009]. All stars identified as accretor candidates by the Hα criteria of Jayawardhana *et al.* [2006], have also been searched for presence of He I. We identified only those stars as accretors that fulfil both criteria, $W_{H\alpha} > 4.4$Å [Jayawardhana *et al.*, 2006] and the presence of He I. This results in 12 accretors in this sample, which are listed in Table 5.1.
Accretion rates were then derived by computing the luminosity of Hα, Hβ, and He I, which correlates with the accretion luminosity and applying Equation (2) in Fang *et al.* [2009].

4.4 Determine periods of RV and stellar activity data

To identify the periods of the radial velocity variations, the tool GLS (*Generalized Lomb-Scargle Periodogram*) by Zechmeister & Kürster [2009] has been used. The computation of a generalized Lomb-Scargle (LS) periodogram is superior to the standard LS periodogram, as it provides more accurate frequencies (periods) and is less susceptible to aliasing [Zechmeister & Kürster, 2009]. The normalized power $z = \frac{N-2}{2}\frac{p}{1-p_b}$, with N as the number of measurements, p as the computed power per period, and p_b as the power of the best fitting period, is used for plotting [Zechmeister & Kürster, 2009]. The accuracy for the periods is typically 5–10%. However, GLS searches for frequencies (periods) with the Fourier technique, which is susceptible for false detections when the data is unevenly spaced over a large time-span [Zechmeister & Kürster, 2009]. Therefore, I adopt a special observing strategy (see Section 3.1.1).
GLS is not only able to search for frequencies by a sine-fit to the data, but also to obtain periods by fitting a Keplerian model (see Section 2.2) to the data. Thus, it is able to obtain the parameter P, T_0, e, ω, K, and RV_0 from the fit. Both fits, sine and Keplerian, are obtained by minimising χ^2.

5 Characterization of the targets

In this section, I present the results of the spectral analysis. The methods used are described in Section 4.3.
The goal of this study is to find sub-stellar companions around young stars. However, I am able to study the evolution of $v \sin i$ for young stars in different evolutionary stages. For this, I added stars from an additional SERAM sample, from hereof sub-sample (b), to the stars observed for this study, now sub-sample (a). The additional stars have been observed between 2004 and 2007 with FEROS at the 2.2m MPG/ESO telescope in La Silla, Chile, as an initial sample for the planet search program at the MPIA and analysed in Weise [2007]. These stars are listed in Table C.1 in Appendix C. The analysis of stellar age, metallicity, evolutionary state of the stars, and $v \sin i$ in this chapter has been done both on each sub-sample individually and on all 260 stars in a larger sample.

5.1 Stellar parameters

The effective temperature, surface gravity, and metallicity obtained for sub-sample (a) are presented in Table B.2. A similar analysis has been done for sub-sample (b) in Weise [2007].

5.1.1 Age

Almost all of the target stars show the Li I feature at 6708 Å, thus confirming their youth. I find a typical detection limit for the Li I feature of 2 mÅ in spectra with a SNR>10 around 6700 Å. In spectra with a SNR<10, I was not able to measure the EW of Li I. The EW of Li I was not corrected for the possible blend with a nearby Fe I feature, because the correction would be smaller than our measurement accuracy [Soderblom *et al.*, 1993].
The measured EW of Li I are listed in columns (10) and (11) of Table C.1 and were used to derive the age of the individual stars as described in Section 4.3.3. The accuracy of this method is typically 10–50%.
The resulting age distributions are shown in Figure 5.2. The histogram for sub-sample (b) (the additional SERAM targets) in the left panel of Figure 5.2 has a strong peak at 30 Myr, which is due to the selection effect towards stars in associations with these ages (from Zuckerman & Song [2004]). In sub-sample (b), 5 stars are most likely older than the Hyades (age $\approx$ 600 Myr). For the stars in sub-sample (a), two peaks can be

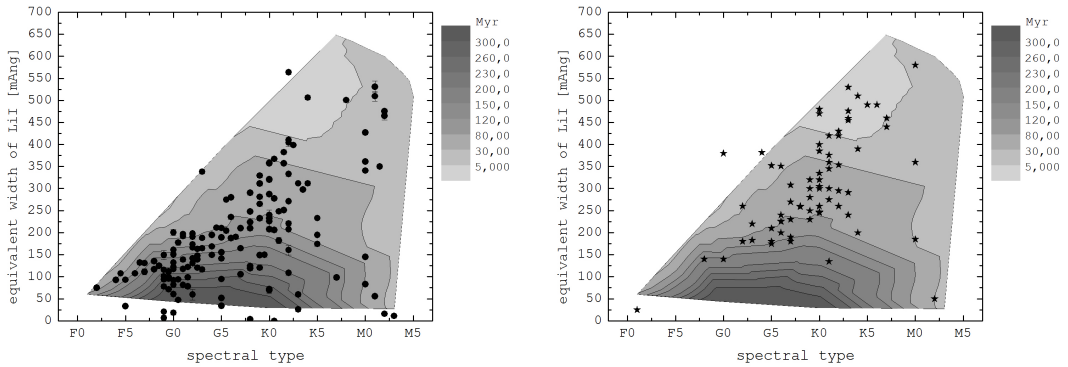

FIGURE 5.1 : Li I measurements for the observed target stars - **Left:** Lithium measurements of sub-sample (b). **Right:** Lithium measurements for sub-sample (a). These targets show higher EW of Li I and are therefore younger on average than sub-sample (b). The shaded contours have been derived from Li I measurements for young stellar associations with known mean age (Section 4.3.3).

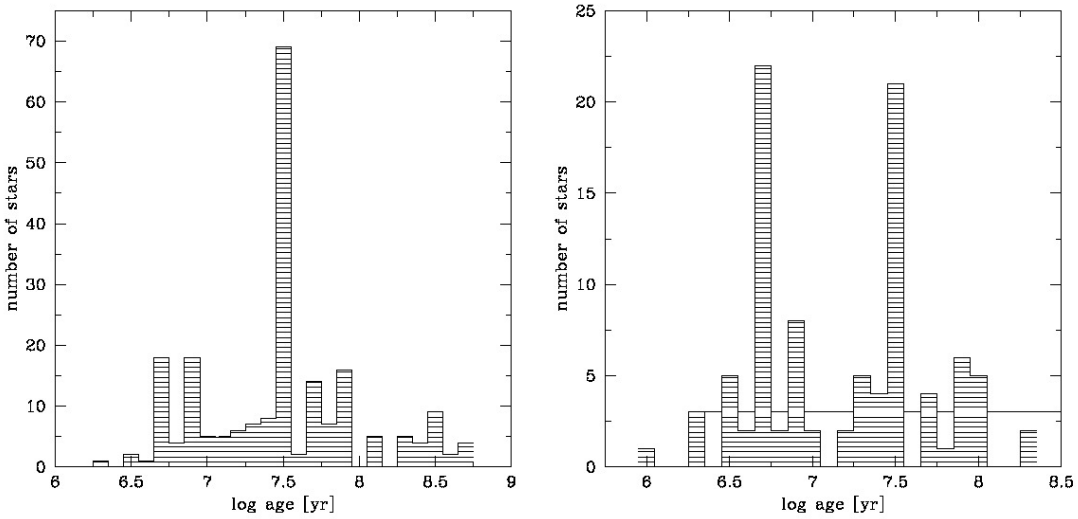

FIGURE 5.2 : Distribution of stellar ages - **Left:** Distribution for sub-sample (b). The highest peak is at 30 Myr. **Right:** Age distribution for sub-sample (a). The two peaks are at 5 Myr and 30 Myr. (see Sections 4.3.3 and 5.1.1).

identified in the histogram (right panel of Figure 5.2), one at 5 Myr and the second at 30 Myr. This shows that the targets of sub-sample (a) are on average younger than the targets of sub-sample (b). In total, 47 stars are younger than 10 Myr and 3 stars are older than 100 Myr.
In 12 stars, I could not detect the Li I feature. Of these, 2 stars (TYC 9129-1361-1 and HD 21411) have a sufficient SNR, but the Li I feature is below the detection limit of 2 mÅ. The spectra of 10 stars (LX Lup, EM* SR 21, HD 43989, HD 201219, HD 201989, HD 205905, HD 209253, HD209779, HD 212291, and HD 225213) have an insufficient SNR < 10, and no lithium feature could be identified and measured. These 8 stars are marked with "n/a" in Table C.1 (column 10).

5.1.2 Metallicity

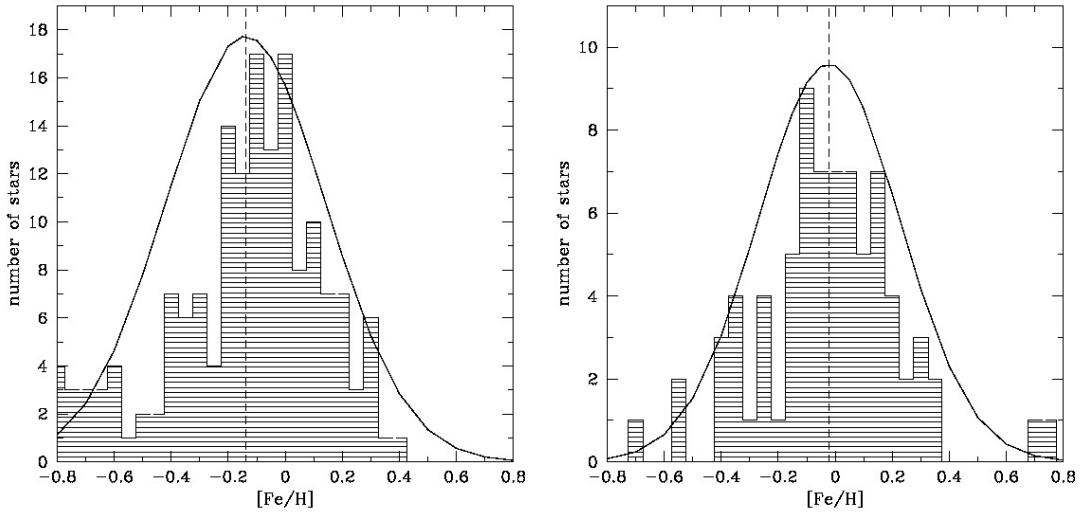

FIGURE 5.3 : Distribution of metallicity - **Left:** distribution of metallicity for the sub-sample (b), the SERAM sample. Marked is the mean metallicity of -0.14±0.02 dex. **Right:** Distribution of metallicity for sub-sample (a), the targets of this study. This sub-sample has a higher mean metallicity of -0.02±0.03 dex than sub-sample (b).The mean metallicity is marked by the dashed line.

The metallicity of the stars in both sub-samples has been measured as described in Section 4.3. The resulting distributions are shown in Figure 5.3. I derived the mean metallicites of both sub-samples by fitting a Gaussian distribution to the histograms using a χ^2 minimization algorithm. The mean metallicity of sub-sample (a) is -0.02 ± 0.03 dex, which is nearly solar-like, and the mean metallicity of sub-sample (b) is -0.14 ± 0.02 dex. Thus, the targets of sub-sample (a) are slightly more enriched in Fe I compared to the stars of sub-sample (b). However, both mean metallicities agree well with the mean metallicities derived for young stellar associations, which range from -0.15 dex to 0.1 dex (e.g., Viana Almeida *et al.* [2009]). I also analysed the correlation of metallicity and stellar age, but no significant correlation is found for the stars of this sample. The spread in stellar age in this sample is to small to see an effect in the metallicity of the stars.

In both sub-samples, a clear dependence of metallicity with T_{eff} (and stellar mass)

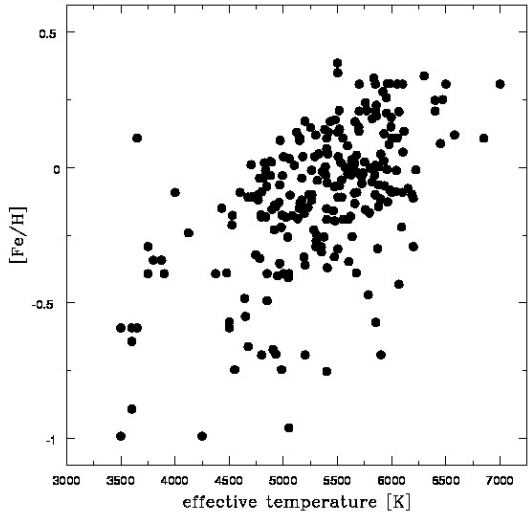

FIGURE 5.4 : Metallicity dependence on effective temperature - T_{eff} vs. [Fe/H] plot for sub-samples (a) and (b). A dependence of [Fe/H] on temperature can be identified.

is given (see Figure 5.4). This trend contradicts the standard idea that stars originated within the same cloud will show a similar abundance pattern. However, the whole sample consists of field stars and stars from different young stellar associations. A similar trend is also found by Viana Almeida *et al.* [2009], who believed that this trend is caused by systematic errors because atmospheric parameters can be modulated by stellar surface spots which are prominent in Pre-Main-Sequence stars [Morel *et al.*, 2004; Viana Almeida *et al.*, 2009]. However, no physical justification can be found to apply a correction for this trend because stellar surface spots should affect the atmospheric parameters at random and independent of effective temperature. Therefore, no correction is applied.

5.1.3 Evolutionary state of the stars

In order to investigate the dependence of $v \sin i$ on the evolutionary state of the stars (in Section 5.2.2.2), I subdivided the large sample (both sub-samples (a) and (b) together) into five subgroups, using the presence or absence of accretion indicators as well as the nature of the circumstellar disks (from Carpenter *et al.* [2009]) as tracers of evolutionary state (see Section 4.3.5). I derive the following five subgroups: (i) stars that still accrete from their circumstellar disk (12 stars), (ii) stars with non-accreting, optically thick disks (12 stars), (iii) stars with debris disks (23 stars), (iv) stars which have no circumstellar disks left (81 stars), and (v) stars with no disk-relevant information available, but with the same mean age and age spread as group (iv). Finally, 72 stars could not be classified this way, because neither their disk status is known, nor could we derive a reliable age. These stars are not further considered in this discussion. In Table 5.2, I list the 5 sub-samples and their details, including the number of low-mass stars ($n_{\mathrm{M-stars}}$) in each

TABLE 5.1 : EW of Hα, $W_{H\alpha}$, EW of He I, accretion rates $\dot{M}_{acc}$, and $v \sin i$ for accretor candidates. Close binary or multiple stars are marked with †.

Identifier	EW(Hα) Å	$W_{H\alpha}$ Å	EW of He I Å	$\dot{M}_{acc}$ $10^{-8} M_{\odot}$/yr	$v \sin i$ kms^{-1}	Notes
HD 3221	2.0	10.2	...	...	146.6	chromospheric activity
TWA 6	3.6	5.1	...	...	94.7	chromospheric activity
V* IM Lup	5.7	5.5	0.03	n/a	13.4	accretor
V* HT Lup†	7.0	11.0	...	...	44.8	chromospheric activity
TWA 5†	8.5	8.8	...	...	63.2	chromospheric activity
CP−72 2713	12.5	2.3	...	...	6.4	chromospheric activity
V 2129 Oph	14.6	6.5	0.25	1.2	13.5	accretor
HBC 603	16.1	7.7	0.1	0.75	6.7	accretor
EM* SR 9	20.4	7.8	0.3	19.3	14.3	accretor
V* GW Ori†	20.8	9.9	0.05	17.1	43.7	accretor
V 1121 Oph	20.8	8.3	0.3	0.5	9.3	accretor
DoAr 44	22.9	9.9	0.6	35.6	15.7	accretor
V* DI Cha	26.1	9.8	0.03	2	38.1	accretor
V* CR Cha	26.9	10.6	0.06	0.2	38.5	accretor
V* GQ Lup	39.5	13.2	0.6	13.6	9.2	accretor
V* MP Mus	42.1	10.5	0.5	0.7	13.0	accretor
V* TW Hya	116.8	9.5	1.94	0.3	6.2	accretor

sub-sample to show that no sub-sample is dominated by low-mass stars and, therefore, a low $\langle v \sin i \rangle$ is not the result of the mass-dependence of $v \sin i$ (Section 5.2.2.1).

All stars with EW of He I > 20 mÅ (detection threshold in the spectra) *and* $W_{H\alpha} > 4.4$ Å (Section 4.3.5) are classified here as accretors. The accretors in this sub-group are DI Cha, TW Hya, GW Ori, CR Cha, V2129 Oph, GQ Lup, IM Lup, DoAr 44, EM* SR 9, HBC 603, V1121 Oph, and MP Mus. For the analysis, we excluded GW Ori because it is a close binary star [Ghez *et al.*, 1997]. The accretion rates have been calculated following Fang *et al.* [2009] with a typical computational accuracy of 15%. For IM Lup, I was not able to derive an accretion rate because the measured EW of Hα, Hβ and He I could not be fitted by the assumed accretion model. In addition to the accretors, 5 more stars also show $W_{H\alpha}$ over the threshold of 4.4 Å, but no He I has been found in the spectra of these stars. For these stars, the Hα emission is likely due to chromospheric activity and broadened by fast rotation or an undiscovered close binary. These 5 stars are HT Lup, HD 3221, CP-72 2713, TWA 6, and TWA 5. I list all 17 stars with a $W_{H\alpha} > 4.4$ Å, accretors and non-accretors, in Table 5.1.

5.2 $v \sin i$

5.2.1 Introduction

Rotation is one of the most important kinematic properties of stars, giving rise to stellar magnetism and mixing of chemical elements. The mechanisms believed to be responsible for efficient loss of stellar angular momentum after the formation of a star-disk system involve transfer of angular momentum along magnetic field lines that connect the stellar surface with the disk, either onto the disk (so-called 'disk-locking', e.g. Camenzind [1990]; Koenigl [1991]) or into stellar winds originating at that boundary [Matt & Pudritz, 2005, 2008]. Both models predict that the stellar magnetic field threads the circumstellar disk, accretion of disk material onto the star occurs along the field lines, and magnetic torques transfer angular momentum away from the star. In the disk-locking model, the angular velocity of the star is then locked to the Keplerian velocity at the disk boundary. For reasonable magnetic field strengths and accretion rates $\sim 10^{-9}$ $M_\odot$/yr, both models account for the observed rotational periods of classical T Tauri stars (e.g., Armitage & Clarke [1996]). Both models can be observationally distinguished only by the absence or presence of stellar winds originating from the boundary. When the accretion process ends and there is no longer an efficient way to disperse angular momentum, the star can spin-up during the contraction phase (see, e.g., Bouwman *et al.* [2006]; Lamm *et al.* [2005]). Once arrived on the ZAMS, stars undergo additional rotational braking by magnetic winds, irrespective of whether they arrived as slow or fast rotators (e.g., Palla [2002]; Skumanich [1972]; Wolff *et al.* [2004]).

If this picture holds true, very young stars are expected to rotate slower than slightly older stars that have already decoupled from their disks. Three different classes of young stars are expected to be distinguishable, which can be interpreted as a kind of evolutionary sequence: (i) slow rotating stars which still accrete, (ii) slow to intermediate rotating stars which do not longer accrete and are about to gradually spin-up due to contraction and (iii) fast rotators without disks. However, one has to keep in mind that all star forming regions show an enormous spread in rotation periods and that differences in rotation velocities between different star forming regions can also be caused by the initial conditions of star formation and the braking time-scale of the star-disk system (e.g., Herbst *et al.* [2007]; Lamm *et al.* [2005]; Nguyen *et al.* [2009]).

Several surveys of stellar rotation periods and projected rotational velocities of very young stars indeed found relatively slow rotators (e.g., Herbst *et al.* [2002]; Rebull *et al.* [2004, 2006]; Sicilia-Aguilar *et al.* [2005]), which points to effective braking mechanisms, whereas other surveys did not find evidence for rotational braking of very young stars (e.g., Makidon *et al.* [2004]; Nguyen *et al.* [2009]). Nevertheless, rotational velocity measurements of stars with circumstellar disks and ongoing accretion in associations

such as η Cha, TW Hydrae, and NGC 2264 support a disk-locking mechanism for the removal of angular momentum from the star [Bouwman *et al.*, 2006; Fallscheer & Herbst, 2006; Jayawardhana *et al.*, 2006; Lamm *et al.*, 2005]. This rotational braking due to disk-locking is mainly visible in very young clusters with an age < 3 Myr. These stars are expected to spin-up by a factor of ≈ 3 due to contraction after being magnetically disconnected from the circumstellar disk. In fact, a large fraction of PMS stars have been observed that evolve at nearly constant angular velocity through the first 4 Myr [Rebull *et al.*, 2004]. In clusters at the age of ~ 10 Myr, signs of stellar velocity spin-up can be seen [Rebull *et al.*, 2006].

5.2.2 Results

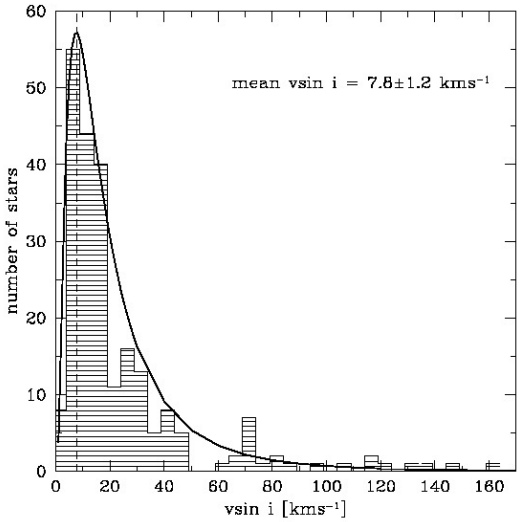

FIGURE 5.5 : Distribution of $v \sin i$ for the target stars - The fit of a log-normal distribution function to the histogram is also shown and peaks at $7.8 \pm 1.2\,\mathrm{kms}^{-1}$ and 70% of the stars have $v \sin i < 30\,\mathrm{kms}^{-1}$.

The $v \sin i$ derived from the FEROS and HARPS spectra for all stars of sub-samples (a) and (b) together are listed in column (3) of Table C.1. The lower limit of the $v \sin i$ measurements has been calculated by using artificially broadened theoretical spectra to be $2\,\mathrm{kms}^{-1}$ for the data. Thus, for all stars in the sample, the line broadening due to rotation exceeds the instrumental broadening. Figure 5.5 shows the distribution of $v \sin i$ for all stars in the sample. I fitted all histograms with a log-normal distribution function using a χ^2 minimization algorithm. The fit to the $v \sin i$ distribution of all stars peaks at $7.8 \pm 1.2\,\mathrm{kms}^{-1}$ with a width of $9\,\mathrm{kms}^{-1}$. I find that 70% of the stars have $v \sin i < 30\,\mathrm{kms}^{-1}$. However, the sub-sample (a) of 100 stars was biased towards slow rotators due to the selection (see Section 3.1). For the analysis of $v \sin i$ as function of stellar mass (Section 5.2.2.1), I therefore excluded those 100 stars which have been

initially chosen to have $v \sin i < 30\,\mathrm{kms}^{-1}$. However, I have to include them again in Section 5.2.2.2 for the analysis of $v \sin i$ as a function of the evolutionary state, because these stars are the youngest in the sample. The analysis also revealed that 8 of these 100 stars have in fact $v \sin i > 30\,\mathrm{kms}^{-1}$. These stars are CD-78 24, GW Ori, HD 42270, CR Cha, Di Cha, T Cha, HT Lup, and HD 220054. The $v \sin i$ measurements for the stars in the sample are important to select target stars for radial velocity planet searches around young stars, since sufficient RV accuracy can only be achieved for slow rotators with $v \sin i < 25$–$30\,\mathrm{kms}^{-1}$ (see Section 5.2.3).

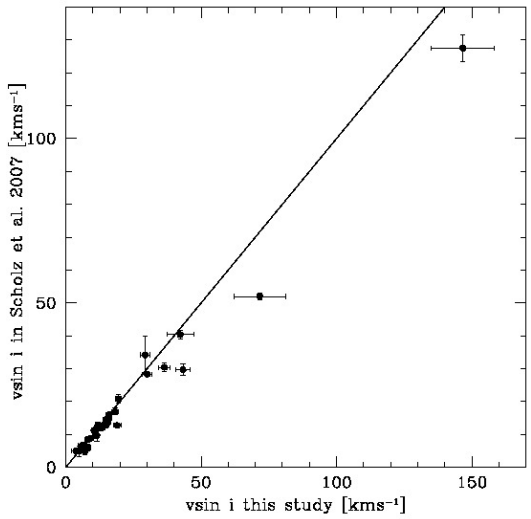

FIGURE 5.6 : $v \sin i$ of this study compared to literature - $v \sin i$ values obtained in this study compared to $v \sin i$ values presented in Scholz *et al.* [2007] for stars that have been analysed in both studies.

I compare in Figure 5.6 the $v \sin i$ values obtained here with the results from Scholz *et al.* [2007], because 29 stars have been analysed in both studies. In Scholz *et al.* [2007] the $v \sin i$ of the stars have been obtained by the comparison with broadened template stars of similar spectral-type, which is different to this study. As a result, both methods of measurement for $v \sin i$ yield similar values for stars rotating slower than $50\,\mathrm{kms}^{-1}$. This agreement supports the validity of my approach. However, the overestimation for stars rotating faster than $50\,\mathrm{kms}^{-1}$ by the $v \sin i$ calculation from the CCF is because the CCF can no longer be fitted by a Gaussian (see Section E.1).

5.2.2.1 $v \sin i$ as a function of stellar mass

The rotational evolution of a star depends on its magnetic activity, which is coupled to the stellar mass (e.g., Attridge & Herbst [1992]; Palla [2002], and references herein). Lower-mass stars tend to have higher magnetic activity due to the deeper convection zones than higher-mass stars, because the stellar magnetic field is driven by the con-

TABLE 5.2 : Sub-samples used to investigate the dependence of $v \sin i$ on the evolutionary state of the stars. I list the selection criteria for the sub-sample, the number of stars and M-type lower-mass stars, mean age, $v \sin i$, and the width of the Gaussian fit to the distribution $\sigma_{v \sin i}$.

sub-sample	description	$n_{\rm stars}$	$n_{\rm M-stars}$	$\langle$Age$\rangle$ Myr	$\langle v \sin i \rangle$ kms^{-1}	$\sigma_{v \sin i}$ kms^{-1}	Results
(i)	accreting stars	11	3	5	10 ± 1	3 ± 1	small $\langle v \sin i \rangle$ no fast rotators
(ii)	non-accreting stars, thick disks	12	4	7	15 ± 2	8 ± 2	larger $\langle v \sin i \rangle$ fast rotators
(iii)	stars with debris disks	23	2	33	10 ± 1	5 ± 1	small $\langle v \sin i \rangle$ fast rotators
(iv)	stars without disks	81	1	90	11 ± 1	4 ± 1	small $\langle v \sin i \rangle$ tail of fast rotators
(v)	no disk info, same age as (iv)	81	3	90	7 ± 1	2 ± 1	similar to (iv)
(iv)+(v)	combined (iv)+(v)	162	4	90	8 ± 1	2 ± 1	small $\langle v \sin i \rangle$ tail of fast rotators

vective zone. Thus, due to the higher magnetic activity, lower-mass stars are therefore expected to rotate slower than higher-mass stars. To examine this dependency, I followed Nguyen *et al.* [2009] and divided the sample into two sub-samples of spectral types F–K (higher mass) and M (lower mass). In order to be not affected by possible age effects, I selected for this test only stars which are younger than 20 Myr, resulting in sub-samples of 21 F–K type stars and 12 M-type stars. For the F–K type stars, we find a weighted mean of $\langle v \sin i \rangle = 13.7 \pm 0.1\,\mathrm{kms}^{-1}$ and for M-type stars $\langle v \sin i \rangle = 11.3 \pm 0.4\,\mathrm{kms}^{-1}$. This difference is small, but significant and confirms the finding of Nguyen *et al.* [2009], that late-type, lower-mass stars rotate on average slower than earlier-type, higher-mass stars. Note that all stars in the sample have $M \geq 0.25 M_{\odot}$, such that I am not able to probe the higher rotation rates of stars with $M < 0.25 M_{\odot}$ as found in the Orion Nebular Cluster [Attridge & Herbst, 1992].

5.2.2.2 $v \sin i$ as a function of evolutionary state

To search for evidence of disk-braking and rotational spin-up in our sample, I analysed the $v \sin i$ distributions of the 5 sub-samples described in Section 5.1.3. Note that these sub-samples have been created independently of the mass of the individual stars and I only compare different evolutionary stages. The $v \sin i$ distributions of the sub-samples have been fitted with a log-normal distribution function. The resulting mean $\langle v \sin i \rangle$ and widths $\sigma_{v \sin i}$ are listed in columns 6 and 7 of Table 5.2. Since sub-samples (iv) and (v) represent similar evolutionary states, I combined them for further analysis. The distribution histograms together with the fits are shown in Figure 5.7.

As a result, I find that accretors are slow rotators. Furthermore, stars in sub-sample (ii) with non-accreting and optically thick disks rotate on average faster compared to accreting stars and stars at later evolutionary stages. However, the $v \sin i$ distribution

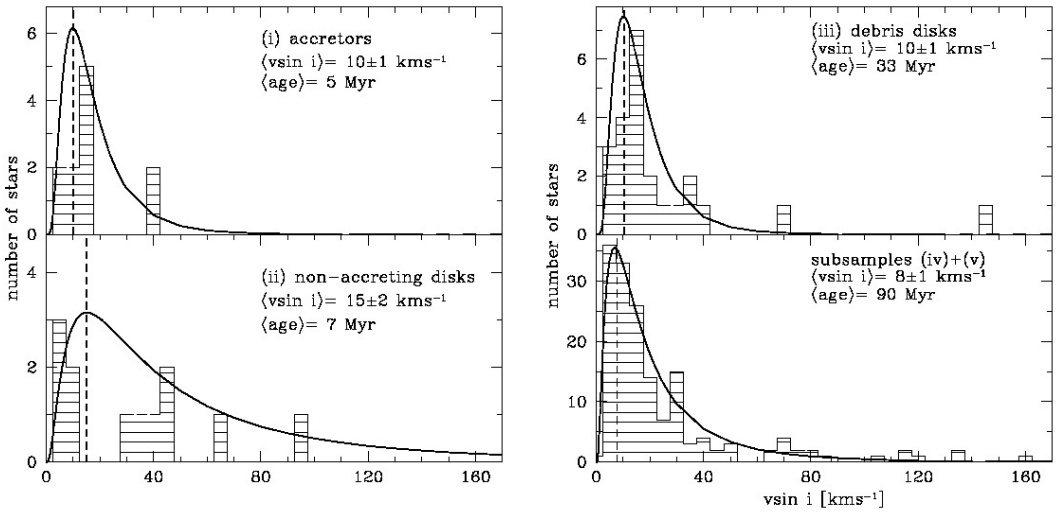

FIGURE 5.7 : Distribution of $v \sin i$ for the 4 sub-samples of stars - (i) accretors, (ii) stars with non-accreting, thick disks, (iii) stars with debris disks, (iv)+(v) stars without disks and stars without information of circumstellar disks. The mean $v \sin i$ of the log-normal distribution function fits to the histograms are shown by dashed lines.

for these stars shows a large spread of rotation velocities. Stars older than 30 Myr rotate again slower on average, but with a long tail in the distribution towards individual fast rotators. This general trend conforms with the well-known picture that rotational spin-up of contracting Pre-Main-Sequence stars is compensated by efficient braking mechanisms during the accretion phase. At the end of the accretion phase, there is no or less efficient braking, such that a rotational spin-up occurs. In later evolutionary stages on the ZAMS, other braking mechanisms are efficient. These mechanisms depend on different disk-braking and contraction times of the individual stars, thus leading to several individual fast rotators. Note that other surveys of stellar rotation in young open clusters found a larger spread in rotation of stars with an age of 30 Myr than I found in the data and rotational spin-down has been found for stars older than 30 Myr (e.g., Allain [1998]). This difference is possibly due to a lower number of stars in sub-sample (iii) and the error in age estimation. However, the general trend in the data is consistent with the findings of other surveys (e.g., Lamm *et al.* [2005]; Sicilia-Aguilar *et al.* [2005]).

To search for indications of disk-braking, I compared the $v \sin i$ of stars in sub-sample (i) with the accretion rates listed in Table 5.1. Disk-braking mechanisms depend on a magnetic connection between the star and its circumstellar disk and therefore on the accretion rate of the star. Furthermore, stellar age and disk lifetimes are expected to have an impact on disk-braking, since the amount of time spent for rotational braking by the disk (disk-braking time; e.g., Nguyen *et al.* [2009]) determines the resulting stellar

rotation velocity. However, this also depends on the initial rotational conditions of the star-forming region. The $v \sin i$ distribution for accretors in sub-sample (i) can be due to a combination of these effects, in which the amount of time spent for disk-braking is dominant, because the two youngest accretors (DI Cha and CR Cha) rotate faster than the other accretors independent of their accretion rate. This is also supported by other surveys (e.g., Jayawardhana *et al.* [2006]; Joergens & Guenther [2001]; Lamm *et al.* [2005]; Nguyen *et al.* [2009]; Sicilia-Aguilar *et al.* [2005]). A larger survey of stars in different star-forming regions, measuring the age and accretion rates, would be necessary to study the dependence of stellar rotation on $\dot{M}_{\rm acc}$ further.

5.2.3 Influence of $v \sin i$ on radial velocity measurements

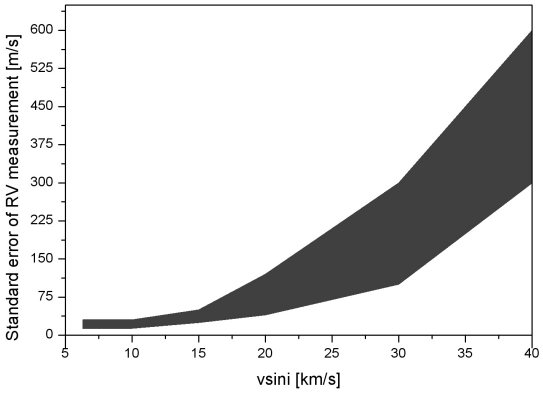

FIGURE 5.8 : Error on radial velocity against $v \sin i$ of the targets - The error on an individual radial velocity measurement is higher for faster rotating stars.

To investigate the influence of stellar rotation on the radial velocity (RV) measurements, I measured the standard error of the RV with respect to the $v \sin i$ of the target. The result is presented in Figure 5.8. The error of an individual RV measurement is higher for faster rotating stars. The reason for this correlation is that the rotationally broadened CCF can no longer be fitted by a Gaussian (see Section E.1). Therefore, the determination of the minimum of the CCF and its width get inaccurate. The scatter in the standard error of RV measurements with $v \sin i$ (shaped area in Figure 5.8) is caused by a mismatching template, bad SNR, and stellar activity. These effects also change the CCF and also lead to inaccurate RV measurements.
The accuracy of an individual RV measurement sets a limit on the minimum mass of a (sub)-stellar companion that can be detected because the amplitude of the RV variation must be significantly larger than the error of a single RV measurement. The amplitude is significant when it is larger than $3\sigma_{\rm RV}$. Thus, for a star with $v \sin i = 30\,{\rm kms}^{-1}$ the minimum mass of a sub-stellar companion that can be detected is 6–10 $M_{\rm Jup}$. Therefore, I selected stars rotating slower than $30\,{\rm kms}^{-1}$ for this planet search survey to be

able to detect companions with masses below 6–10 M_{Jup}.

5.2.4 Stellar rotation periods

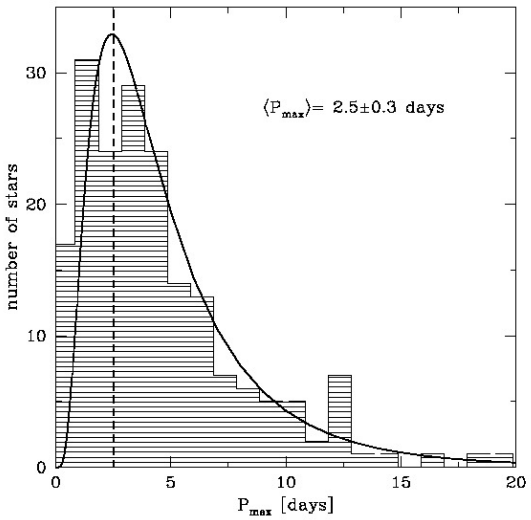

FIGURE 5.9 : Distribution of the stellar rotation period $P_{\max}$ for the whole sample - The mean $\langle P_{\max} \rangle$ = 2.5 ± 0.3 days, derived by fitting a log-normal distribution function, is marked by the dashed line.

For stars for which accurate measurements of T_{eff}, absolute magnitude, and bolometric correction are available (e.g., from Flower [1996]; Weise [2007]), I estimated the stellar radius $R/R_{\odot}$ following Valenti & Fischer [2005]. An upper limit to the rotational period of the star can then be derived from the estimated radius by using:

$$P_{\max} = 50.6 \frac{R/R_{\odot}}{v \sin i} \qquad [d]. \tag{5.1}$$

The resulting distribution of rotational periods for the whole sample is shown in Figure 5.9. The distribution of $P_{\max}$ for all our target stars peaks at at $\langle P_{\max} \rangle$ = 2.5±0.3 days, derived by fitting a log-normal distribution function. This compares well to the result derived by Cieza & Baliber [2007], that young stars show rotational periods around 2–3 days (in the ONC and NGC 2264).
However, because of the uncertainties introduced by the assumptions used to calculate the radii of the stars, no further analysis of $P_{\max}$ has been done, like, e.g. for $v \sin i$ in Section 5.2.2.2.

6 Analysis of radial velocity data

In this Section, I present the analysis of the radial velocity (RV) data. The analysis is done for stars with more than 5 observations to be able to identify a variation of the RV and derive its period. The analysis is done for each of the 26 stars individually. I present a detailed analysis for 13 stars with an interesting RV variation. For the remaining 13 stars, the analysis is summarized here because for these stars either more observations are needed in order to draw a significant conclusion, or stellar activity is most likely the source of the RV variation.
For each star, the RV variation, the stellar activity indicators and photometric observations (if available) are analysed with GLS. The accuracy of the derived periods is in the range of 5–10%. In addition, the bisector is analysed (see Section 4.1.2). I only show the correlation of the BVS with RV because the other derivatives of the bisector, BC and BVD, show a similar behaviour with RV. Furthermore, I compute the correlation coefficient r (also in percent) for the correlation of BVS on RV and the probability T that both data sets do not correlate. For the probability T, I use the threshold of 0.5% to distinguish between un-correlated and correlated data [Bevington & Robinson, 2003]. In addition, the slope of a linear regression to the BVS vs. RV data is used to identify whether the RV variation is induced by stellar activity (negative slope) or a stellar companion (positive slope) as described in Section 4.1.2.
The results for the RV analysis with GLS are presented in Table B.3 and the results for the stellar activity indicators in Table B.4, both in Appendix B.

6.1 1RXS J153328.4-665130

1RXS J153328.4-665130 is a young K2-3 V star with V=11 mag [Torres *et al.*, 2006] that has been analysed in detail by Viana Almeida *et al.* [2009]. They derived basic stellar parameters and allocated the target as a member of the Upper Scorpius group. Following them, I adopt a distance of 145 pc. The stellar parameters derived by Viana Almeida *et al.* [2009] agree well with my own stellar parameter estimation within the error-bars (Table 6.1). However, I derive a slightly lower temperature of 4770 K instead of 4955 K as Viana Almeida *et al.* [2009], which might result from a different fitting method for

TABLE 6.1 : Parameters for 1RXS J153328.4-665130.

Parameter	Value	Method/Reference
Identifier	1RXS J153328.4-665130	...
Optical counterpart	TYC 9034-968-1	Voges *et al.* [1999]
Coordinates	15 33 27.49 -66 51 24.8	SIMBAD
Spectral type	K2–3V	Torres *et al.* [2006]
V magnitude	11 mag	Torres *et al.* [2006]
Young Stellar Association	Upper Scorpius	Viana Almeida *et al.* [2009]
Distance	145 pc	Makarov [2007]
$M_\star$	1.1±0.1 $M_\odot$	evolutionary tracks, Siess *et al.* [2000]
$R_\star$	1.0±0.1 $R_\odot$	evolutionary tracks, Siess *et al.* [2000]
$T_{\rm eff}$	4770±50 K	*TGV*, this study
$\log g$	4.4±0.2 cms^{-2}	*TGV*, this study
[Fe/H]	-0.10±0.08	*TGV*, this study
EW of Li I	295±1 mÅ	this study
Age	30±15 Myr	Li I measurements, this study
Age	15±7 Myr	evolutionary tracks, Siess *et al.* [2000]
$v \sin i$	9.1±1.1 kms^{-1}	this study
$R'_{\rm FEROS}$	-4.1±0.2	this study
Number of observations	63	...

the measured EWs of Fe I and Fe II. It is worth noting that 1RXS J153328.4-665130 has nearly solar metallicity.

The age of 1RXS J153328.4-665130 has been determined as described in Section 4.3.3 by measuring the EW of Li I and by using evolutionary tracks. I adopt the range of 15–30 Myr as the most likely age of 1RXS J153328.4-665130. Furthermore, I have been able to derive the stellar mass $M_\star = 1.1 \pm 0.1 M_\odot$ and radius of $R_\star = 1.0 \pm 0.1 R_\odot$ from the evolutionary track, although with the same systematic concern as for the age determination (see Section 4.3.3).

Unfortunately, nothing is known about the evolutionary state of a possible circumstellar disk around 1RXS J153328.4-665130 because no observations with, e.g., *Spitzer* are available.

6.1.1 Radial velocity data

I measured the RV as described in Section 4.1 and show the resulting RV over observing time in Figure 6.1 (left panel). I find a peak-to-peak amplitude of 550 ms^{-1} over the time-span of the observations (898 days). This variation is significantly larger than the accuracy of a single measurement (6 to 42 ms^{-1}).

The GLS periodogram (see Section 4.4) reveals one strong peak at 292±4 days with a False Alarm Probability (FAP) of <0.1%. I also applied the *bootstrap* method to the data, which yields the same FAP. I conclude that this is a significant detection of the 292±4 days period.

In Figure 6.1 (right panel), I also show the RV data phase-folded with the 292±4 days

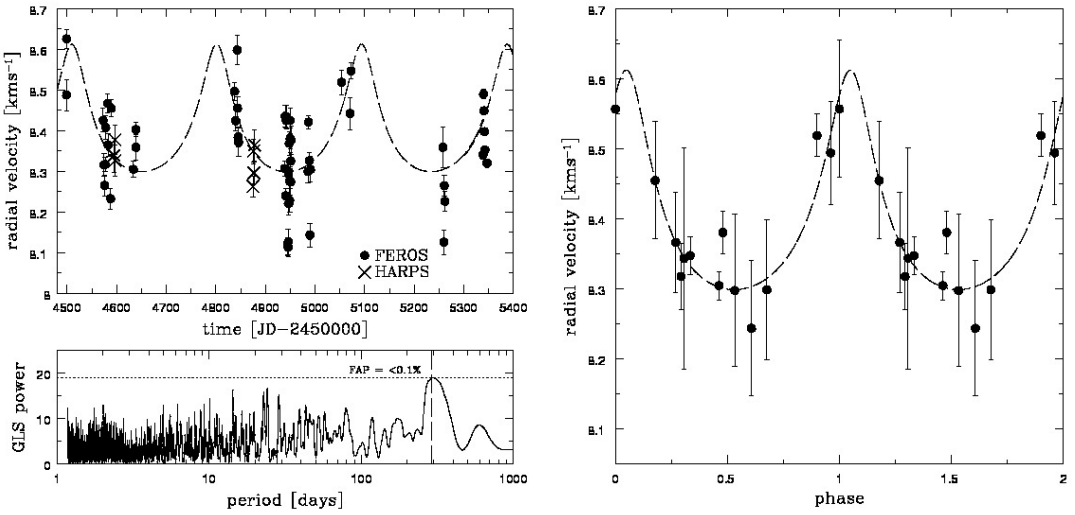

FIGURE 6.1 : Radial velocity variation for 1RXS J153328.4-665130 - **Left:** RV variation and the corresponding GLS periodogram. Marked is the peak at 292±4 days. **Right:** RV data phase-folded with the 292±4 days period. For this plot, the mean RV for each observation run has been calculated. In both figures, the best fit to the data with the orbital parameters listed in Table 6.3 is shown.

period. To create the phase-folded diagram, I calculated the mean RV for each observing run, such that the short-term variations (Section 6.1.2) average out and the long-term variation can be seen better. The errors of mean RV values are higher than the errors of the individual RV measurements due to the short-term scatter in each observing run (Section 6.1.2).

I also computed the residuals after subtracting the 292 days period from the RV data and analysed them for periodicity. The GLS periodogram for the residuals yields a peak at a period of 11.2 days with a FAP of 20%. In Section 6.1.2, I will show that these short-term variations are probably due to stellar activity and rotational modulation. Note that after subtracting the short-term period of 11.2 days from the whole data set, the FAP of the 292 days period is reduced to 10^{-3}%, which strengthens the significance of the long-term period.

6.1.2 Photometric variation and stellar activity indicators

After deriving periods for the RV variation, I still have to verify whether this variation is caused by an orbiting companion or by rotational modulation due to photospheric and chromospheric activity. Therefore, I also derive the photometric period, analyse the bisector and other stellar activity indicators, and list the results in Table 6.2. The results are shown in Figure 6.2 for the photometric data, Figure 6.3 for the bisector

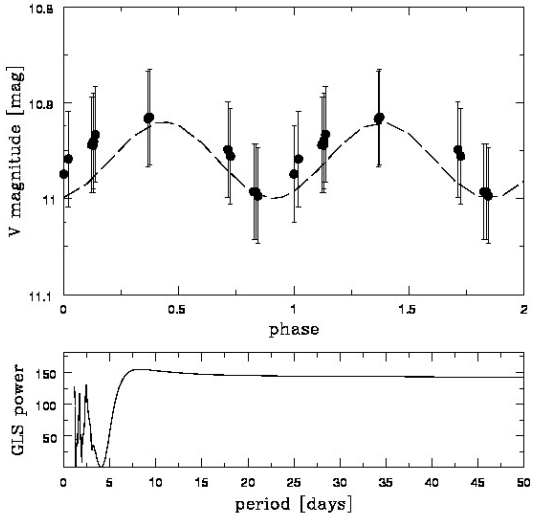

FIGURE 6.2 : Photometric data obtained for 1RXS J153328.4-665130 - phase-folded with a period of 8.5 days. A sine-fit to the data is plotted. In the lower panel, the GLS periodogram for the data is shown.

TABLE 6.2 : Periods of stellar activity indicators, photometric data, RV, the FAP of the period, and the amplitude. I list further the accuracy of a single measurement $\sigma_{\rm meas}$ and mark the significant periods.

Activity indicator	Period [days]	FAP	Significance	Semi-amplitude	$\sigma_{\rm meas}$
Stellar activity					
BVS	7.5±0.5	0.7%	significant	69 $\rm ms^{-1}$	13–40 $\rm ms^{-1}$
V I/Fe I LDR	25	12%	...	0.13	0.005
Hα	8.8±1.7	0.2%	significant	41 mÅ	5 mÅ
$S_{\rm FEROS}$	~2	60%	...	0.3	0.05
Ca II λ 8662	11.8±1.4	1%	significant	36 mÅ	2 mÅ
Photometric variation	8.5±2.5	<0.1%	significant	0.03 mag	0.02 mag
Radial Velocity	292±4	<0.1%	significant	157 $\rm ms^{-1}$	16–42 $\rm ms^{-1}$
RV residuals	11.2	20%	...	85 $\rm ms^{-1}$	16–42 $\rm ms^{-1}$

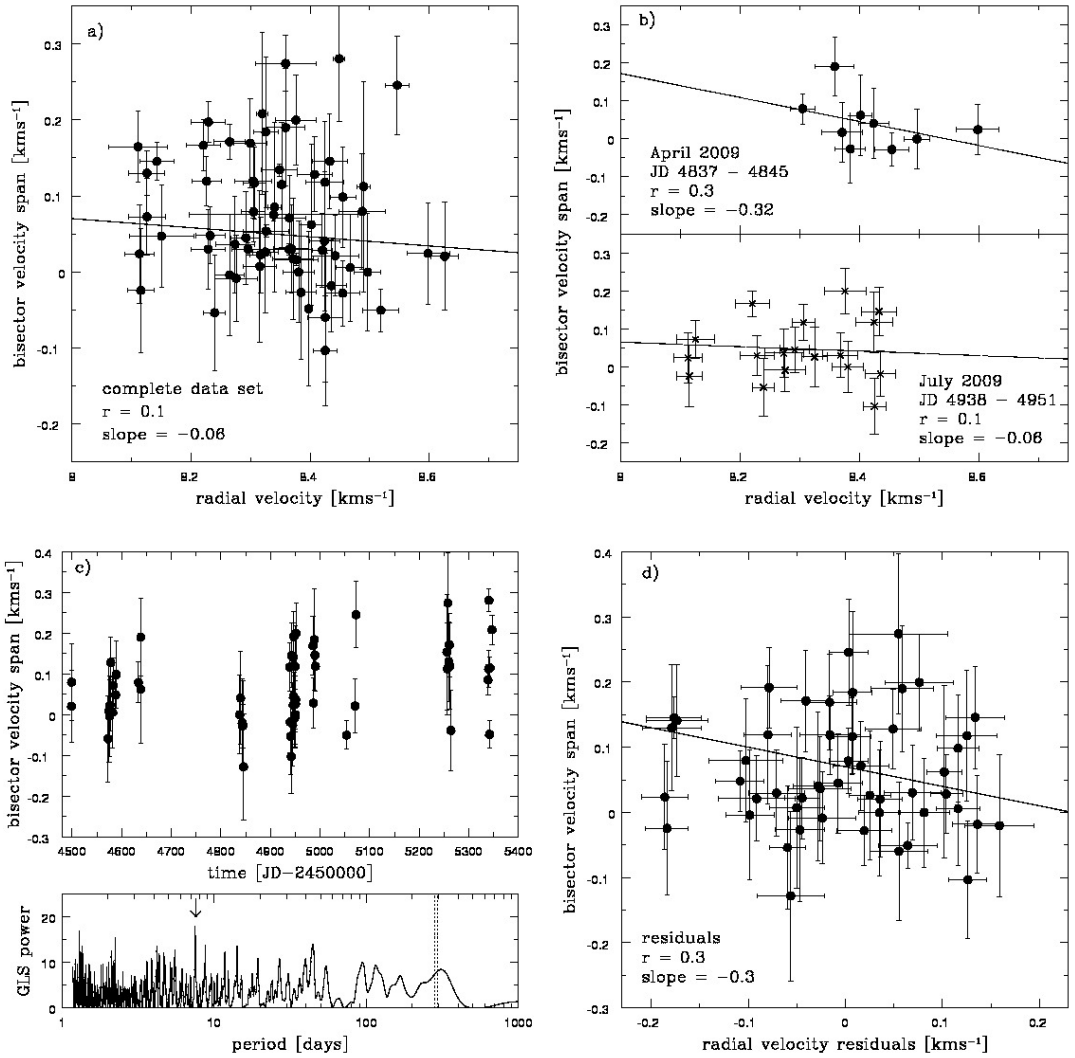

FIGURE 6.3 : Bisector analysis for 1RXS J153328.4-665130 - Panel a): I plot BVS and RV for all observations. The correlation coefficient $r = 0.1$ for all data obtained and the slope of linear correlation is -0.06. Panel b): Plot of BVS and RV for two shorter time-intervals. The correlation coefficient and the slope of the linear correlation are more significant when analysing short time-intervals that last shorter than 8 days as compared to longer time-intervals of 13 days. Panel c): Variation over time of BVS. The BVS varies with a period of 7.5 days. In the GLS periodogram, we marked the identified period with an arrow and the RV period (292±4 days, see Figure 6.1) with dotted lines. Panel d): BVS vs. RV residuals. For the correlation of BVS with RV residuals r equals 0.3 and the slope is also more significant with -0.3.

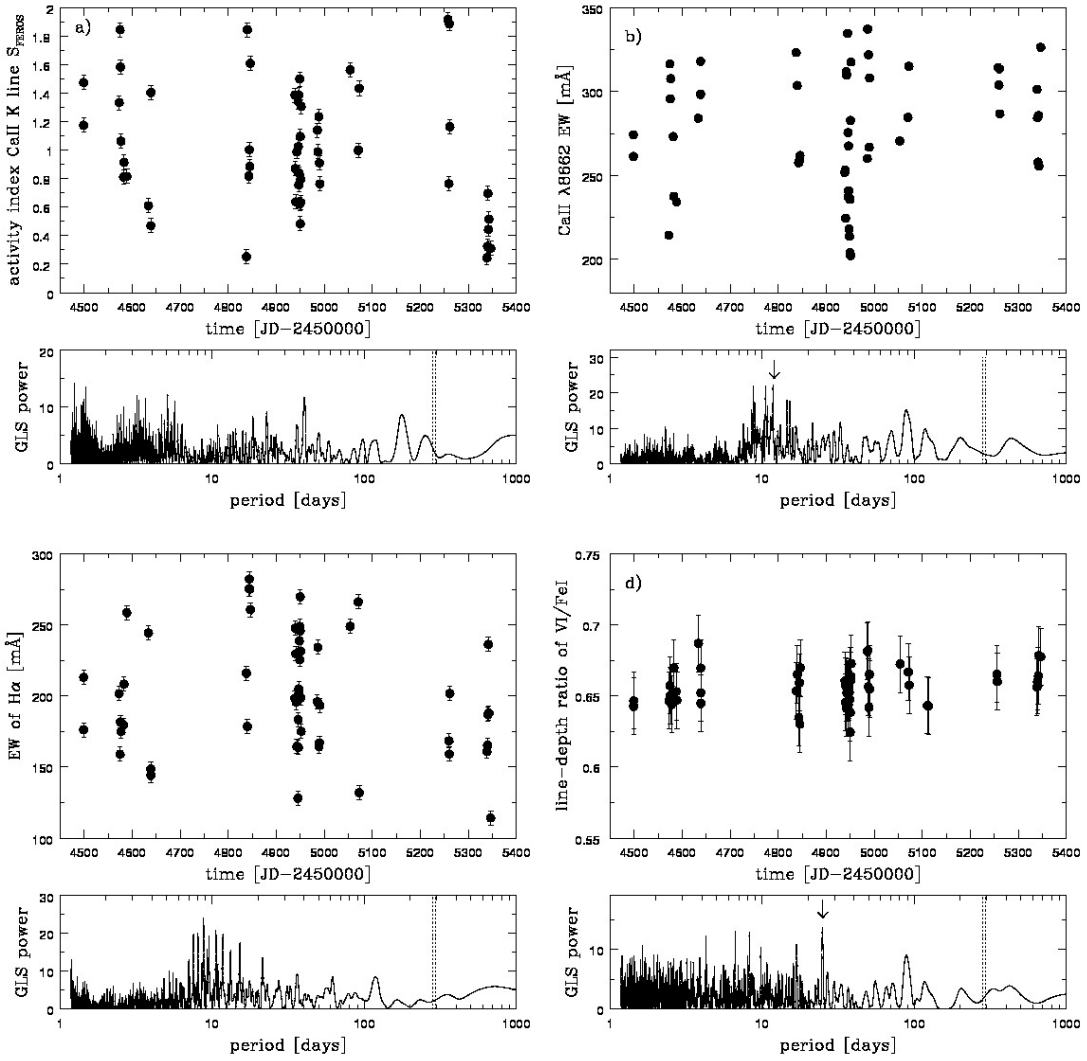

FIGURE 6.4 : Other stellar activity indicators for 1RXS J153328.4-665130 - Panel a): S_{FEROS}, panel b): EW of Ca II λ8662, panel c): Hα, and panel d): LDR of V I/Fe I. I show also the GLS periodogram for each activity indicator and mark the period of the indicator by an arrow and the 292±4 days RV period by dotted lines.

analysis, and Figure 6.4 for the other activity indicators.

6.1.2.1 Photometric variation

Photometric observations of 1RXS J153328.4-665130 have been carried out with WFI (*Wide Field Imager*; Baade *et al.* [1998]) at the 2.2m MPG/ESO telescope in La Silla, Chile, in August 2009, to determine the stellar rotation period. The pixel-scale of WFI is 0.238''per pixel. To avoid saturation of our target and simultaneously increase the SNR of the image, 4 integrations in V-band with a duration of 0.7 sec have been obtained and combined to a single image. The individual frames have been reduced and combined using standard routines of the *ESO-ECLIPSE* package [Devillard, 1997]. In total, I obtained 13 combined images over a time-span of 9 days, with seeing ranging from 0.7'' to 2.2''. The stellar sources in the images have been extracted and aperture photometry has been done by using IDL. The aperture size has been changed according to the FWHM of the targets airy disk on each image (mean FWHM: 10 pixel) to include the stellar flux down to sky-level. The sky annulus has been set to a radius spreading 15 pixels further than the aperture size to subtract the contribution of the sky to the total flux. From the measured flux of 8 stars with known V-magnitudes on the same WFI-chip on which 1RXS J153328.4-665130 was located, the zero-point for the magnitude has been calculated for each observation separately. With this method, an accuracy of 0.02 mag per observation has been achieved.
I searched for periodicities in the photometric data set using the GLS periodogram. This yielded a strong peak at 8.5 days with an amplitude of 0.06 mag, corresponding to a variation of 0.55%. However, the time-span of the observation was 9 days and the sampling of the data is not sufficient to identify longer periods. But the data suggest that one full cycle of a sinusoidal period of 8.5 days has just been fully covered (Figure 6.2). Therefore, I adopt the 8.5 days period for the photometric variation.

6.1.2.2 Bisector analysis

The relationship of the bisector of stellar spectral lines with the RV is a powerful tool to determine whether the RV variation is induced by stellar activity or not (see Section 2.3). I computed the BVS, BC and BVD (see Section 4.1.2) and found a correlation coefficient $r = 0.1$, corresponding to a correlation of 1% between BVS and RV data (panel a in Figure 6.3). The slope of the linear correlation is -0.07 and, therefore, not significant. The BC and BVD show a similar behaviour with respect to the RV, i.e., there is no significant correlation. In addition, I computed the probability that RV and BVS do *not* correlate by following Bevington & Robinson [2003]. This probability T is high with T = 46%, which shows that changes in spectral line shape are unlikely to be the cause for the RV variation. In this analysis, a threshold of 0.5% is commonly used to distinguish

between correlation and no correlation (e.g., Bevington & Robinson [2003]).
In addition, I investigated the time-dependence of the BVS and found a significant peak (FAP = 0.7%) in the GLS periodogram at 7.5±1.5 days with an semi-amplitude of 70 ms^{-1} (panel c in Figure 6.3). With this result at hand, I independently analysed the dependence of BVS on RV in a time window of 8 nights during the observing run in April 2009 (panel b in Figure 6.3). I found a much stronger correlation coefficient $r = 0.3$ (correlation of 10% and a slope of -0.3) and a small probability, T<0.1%, that both do not correlate. In contrast to this, the correlation of BVS and RV in a longer time-interval of 13 nights is less strong with $r = 0.1$ and a slope of -0.07, which resembles that of the whole data set. This result shows that the short-term jitter in the RV data is most likely caused by stellar surface features, but over longer time-scales this effect averages out. The analysis of BVS with respect to the RV residuals (after subtracting the 292 days period) yields a correlation coefficient of $r = 0.3$ (panel d in Figure 6.3). This also shows that the variation of the RV residuals (P=11.2 days) is most likely caused by rotational modulation due to stellar activity.

With the amplitude of the photometric variation of 0.06 mag and the BVS variation, I can estimate the expected amplitude in RV due to stellar surface spots by following Desort *et al.* [2007] and Saar & Donahue [1997] (see Section 4.2.1). I find an expected RV semi-amplitude of 115 ms^{-1} and 125 ms^{-1}, respectively. Both expected semi-amplitudes are smaller than the observed RV semi-amplitude of 157±15 ms^{-1}.

6.1.2.3 Other activity indicators

I also analysed the activity index S_{FEROS} of the Ca II K line, the EW of Ca II λ 8662, the LDR of V I/Fe I, and the EW of Hα (see Section 4.2). The time dependence of these stellar activity indicators and the corresponding GLS periodograms is shown in Figure 6.4.
For S_{FEROS}, I do not find a significant period in the data set, but the highest peaks in the GLS periodogram are in the 2 and 5 days range, although with FAP> 60%. The reason for the missing periodicity is most probably the short life-time of the chromospheric activity. This behaviour results in a quasi-periodic activity that changes phases between the individual observing runs and no clear period can be identified (e.g., Setiawan *et al.* [2008a]).
From the mean $S_{\mathrm{FEROS}} = 1.1 \pm 0.3$, I computed the corrected activity index $\log R'_{\mathrm{FEROS}} = -4.1 \pm 0.2$ following Noyes *et al.* [1984] (see Section 4.2). The derived activity index is typical for a highly active star (e.g., Mamajek [2009]). For such stars, the rotational modulation due to chromospheric plaques is not always detectable, which can also explain the lack of significant periods in the S_{FEROS} data.
The EW of Ca II λ 8662 is variable with a significant period of 11.8±1.4 days (FAP of

1%; see Figure 6.4, panel b). This period is similar to the period identified in the RV residuals. This gives additional evidence that the variation of the RV residuals is caused by stellar activity (in this case, chromospheric activity). The Hα line is in absorption in the spectra of 1RXS J153328.4-665130, although the line core is filled, which is also due to the high magnetic activity in the chromosphere of this star. In the Hα EW data, a period of 8.8±1.7 days with a low FAP=0.2% is present. This period is comparable to the period of the photometric and BVS variation. For the period of the V I/Fe I LDR, I found periods of 8 and 25 days with a FAP of 12%, but the latter can be an alias of the shorter Period of 8 days. However, the period of the V I/Fe I LDR is not significant, which might be because of irregular and short-lived star spot patterns on the surface of 1RXS J153328.4-665130 that smear out a clear period for this activity indicator.
However, I can deviate the stellar rotation period from the analysis of the stellar activity indicators and the photometric variation. For this, I calculated the weighted mean of the periods of the photometric variation, BVS, Hα, and Ca II λ8662 line, which have the most significant periods with FAP <1%. This yields 8.1±0.5 days for the stellar rotation period.

Unfortunately, I was not able to obtain NIR spectroscopic data of 1RXS J153328.4-665130. As shown by e.g., Prato *et al.* [2008], the analysis of bisector and the other stellar activity indicators in the optical part of the spectra are not sufficient alone to rule out the possibility of an activity induced RV variation. NIR spectroscopy can be a complementary indicator for stellar activity because the contrast between spot and photosphere is smaller in the near-IR, hence the amplitude of the RV variation will be smaller. For RV variation due to a planet, the amplitude should be the same (e.g., Prato *et al.* [2008]). The total decrease in amplitude of the RV variation in the NIR depends on the surface spot configuration and composition and can vary from 20% to 50%. With the current precision of 20–30 ms^{-1} of *CRIRES* [Seifahrt & Käufl, 2008] and the need of excellent phase coverage for reliable amplitude measurements, this decrease in amplitude would be hard to identify for this target and no conclusive result could probably be drawn from such an analysis.

6.1.2.4 Stellar surface spots as the origin of the RV variation

In Section 6.1.2.2, I already showed that the measured RV variation amplitude is larger than the expected amplitude due to stellar activity, calculated with our measurements of photometric and bisector variations. In order to check whether the measured RV variation can be described in total by stellar activity, I calculated the spot-filling factor and photometric variation needed to produce the peak-to-peak amplitude of 550 ms^{-1}.

TABLE 6.3 : The planetary companion

Parameter	Value	Method
Period	292±4 days	GLS
FAP	<0.1%	GLS
Amplitude K	157±15 ms^{-1}	GLS
Eccentricity e	0.38±0.09	GLS
Periastron passage	4511±20 HJD	GLS
Longitude of periastron ω	4±20°	GLS
Offset RV	8396±30 ms^{-1}	GLS
$m_p \sin i$	5.1±0.9 M_{jup}	GLS
$\sin i$	$0.98^{+0.01}_{-0.07}$	rotation period, $v \sin i$
True m_p	5.2±1.0 M_{jup}	
a $\sin i$	0.92±0.03 AU	GLS
rms of residuals	87 ms^{-1}	GLS

For this, I used the Equations (4.11) and (4.14) from Section 4.2.1. I calculated that an equatorial surface spot with a filling factor f_s = 5.3% can produce such a RV variation for an edge-on star. 1RXS J153328.4-665130 is a nearly edge-on star (see Section 6.1.3). On the other hand, a spot-filling factor of f_s = 5.3% would produce a photometric variation of 1.33 mag, which is more than twice the measured photometric variation of 0.06 mag for 1RXS J153328.4-665130.

Nevertheless, there are spot-configurations that can produce such a RV variation, show nearly no correlation of the BVS with RV, and produce a smaller amplitude of the photometric variation. Therefore, the lack of a correlation between the bisector and the RV as well as of the other activity indicators is a necessary but not sufficient argument to rule out stellar spots as the source of the RV variation. Such configurations can be found for pole-on stars with high-latitude spots (e.g., Desort *et al.* [2007]). In this case, 1RXS J153328.4-665130 is an edge-on star with i = 80°. These analyses support the hypothesis that the long-term (292 days) RV variation is not caused by rotational modulation due to surface stellar spots.

In addition, I found that the RV residuals (after subtracting the 292 days period) vary with a period (11.2 days) similar to the periods of most activity indicators (7.5–12 days; see Table 6.2), while no activity indicator shows a long-term periodicity. The total RV signal is thus a combination of a strictly periodic long-term (P=292 days) planetary signal with K=157±15 ms^{-1} *and* a quasi-periodic short-term (P~8 days) stellar activity jitter with K=85±20 ms^{-1}.

6.1.3 The planetary companion

I have shown by the analysis of the stellar activity indicators (Section 6.1.2) that the stellar rotation period is most likely 8.1±0.5 days and that the observed long-term RV variation is very unlikely to be induced by stellar activity, so that I can assume a

sub-stellar companion orbiting around 1RXS J153328.4-665130 in 292±4 days.
Using GLS, I computed an amplitude K = 157 ± 15 ms^{-1}, a longitude of periastron $\omega = 4 \pm 20°$, a periastron passage $t_0 = 4511 \pm 20$ HJD, and a RV offset of 8.4 kms^{-1} as the orbital parameters from a fit with P=292±4 days to the RV data. I list these results in Table 6.3.
From these parameters and the stellar mass of $M_\star = 1.1 \pm 0.1$, I can derive the minimum mass $m_p \sin i = 5.1 \pm 0.9 M_{\rm jup}$ of the planetary companion. With the calculation of $\sin i = 0.98^{+0.01}_{-0.07}$ from the rotation period, $v \sin i$, and radius, I find the true mass of the planet to be 5.2±1.0 $M_{\rm jup}$. This is within the mass-regime of giant planets. The orbit of the planet is eccentric with $e = 0.38 \pm 0.09$ at a distance $a = 0.92 \pm 0.03$ AU, which can be due to the young age of the system because the circularization time-scale for such disks is up to a few Gyr [Hernán-Obispo *et al.*, 2010]. Another explanation of the higher e is that the orbit is altered due planet-planet interactions after the disk has dissipated (e.g., Papaloizou *et al.* [2004]). However, the characteristics of the planetary orbit are not unusual compared to other orbits of extrasolar planets [Schneider, 2010]. The analysis of the RV data and stellar activity of 1RXS J153328.4-665130 has been submitted to A&A.

TABLE 6.4 : Basic parameters for CD-78 24.

Parameter	Value	Method/Reference
Identifier	CD-78 24	...
Coordinates	00 42 20.0 -77 47 40.0	SIMBAD
Spectral type	K2–3V	Torres *et al.* [2006]
V magnitude	10.2 mag	Torres *et al.* [2006]
Distance	69 pc	Chauvin *et al.* [2010]
$M_\star$	$0.95\pm0.1\,M_\odot$	evolutionary tracks, Siess *et al.* [2000]
$R_\star$	$0.97\pm0.1\,R_\odot$	evolutionary tracks, Siess *et al.* [2000]
$T_{\rm eff}$	4845±120 K	*TGV*, this study
$\log g$	5.2 ± 0.3 cms^{-2}	*TGV*, this study
[Fe/H]	-0.07±0.08	*TGV*, this study
EW of Li I	291±8 mÅ	this study
Age	30±10 Myr	Li I measurements, this study
Age	30±5 Myr	evolutionary tracks, Siess *et al.* [2000]
$v \sin i$	30.7 ± 2.3 kms^{-1}	this study
$R'_{\rm FEROS}$	-4.65	this study
Number of observations	13	...
single star	...	Chauvin *et al.* [2010]

6.2 CD-78 24

CD-78 24 is a young K2–3V type star of V = 10.2 mag and a member of the Tucana-Horologium association [Torres *et al.*, 2006]. Because of this, I adopt a distance of 69 pc [Chauvin *et al.*, 2010]. For CD-78 24 no basic stellar parameters have been derived so far, thus the results obtained in this study are the first measurements. The results for the stellar parameters are consistent with the spectral type of K2 and are summarized in Table 6.4. CD-78 24 has, like 1RXS J153328.4-665130, solar-like metallicity.
The age of CD-78 24 has been calculated from Li I EW measurements to be 30±10 Myr. Furthermore, the age, stellar mass, and radius have been derived from evolutionary tracks (although with the systematic concerns described in Section 4.3.3) to be 30±5 Myr, $0.95\pm0.1\,M_\odot$, and $0.97\pm0.1\,R_\odot$, respectively. In this case, both methods of measurement of the stellar age yield a similar result, such that I adopt 30±7 Myr as the age of CD-78 24.
Unfortunately, no observations of the evolutionary stage of a possible circumstellar disk are available for CD-78 24.

6.2.1 Radial velocity variation

The RV has been measured as described in Section 4.1 and is shown in Figure 6.5 (left panel). The RV shows a peak-to-peak variation of 1 150 ms^{-1}. The period of the RV variation obtained by using GLS is 65.18 days (with an accuracy of 5%), although with a FAP of 23%. This higher FAP for this period is due to the lower number of observations as compared to 1RXS J153328.4-665130. Therefore, more observations are needed to

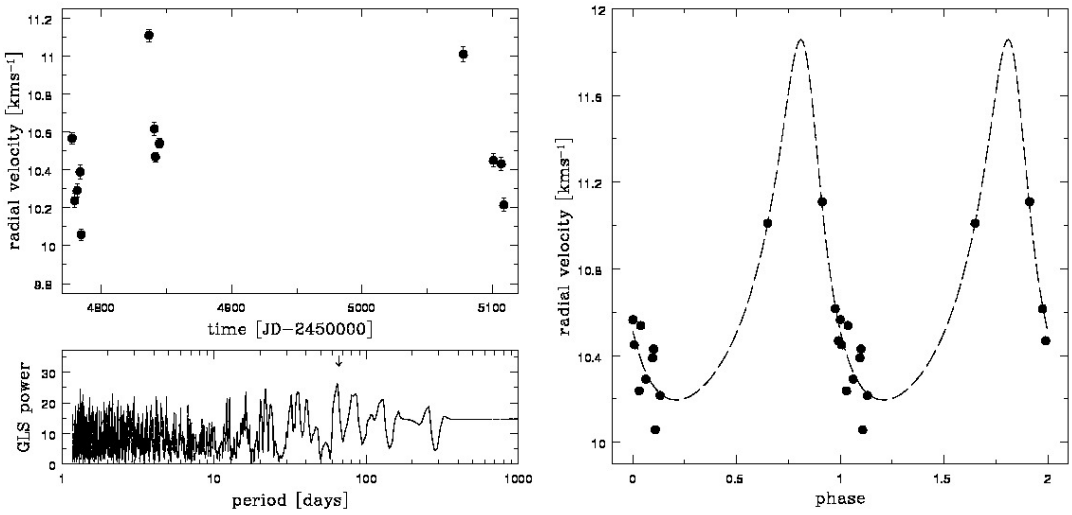

FIGURE 6.5 : Radial velocity variation of CD-78 24 - variation over time and phase-folded with 65.18 days.

TABLE 6.5 : Periods of stellar activity indicators, photometric data, RV, the FAP of the period, and the amplitude for CD-78 24. I list further the accuracy of a single measurement σ_{meas} and mark the significant periods.

Activity indicator	Period [days]	FAP	Significance	Semi-amplitude	σ_{meas}
Stellar activity					
BVS	2.14	57%	...	467.36 ms^{-1}	13–36 ms^{-1}
V I/Fe I LDR	39.99	12%	...	0.03	0.008
Hα	1.45	16%	...	70.95 mÅ	1.3 mÅ
S_{FEROS}	2.88	0.6%	significant	0.29	0.07
Ca II λ 8662	4.31	56%	...	46.65 mÅ	2 mÅ
Radial Velocity	65.18	23%	...	831.52 ms^{-1}	25–36 ms^{-1}

verify the 65.18 days period. However, I adopt this period for the RV variation and present the RV data phase-folded with the 65.18 days period in Figure 6.5 (right panel). Also shown is the best Keplerian fit to the data with the parameters in Table 6.6.

6.2.2 Analysis of stellar activity

Although the period of the RV variation is not significant due to the low number of observations, the analysis of the stellar activity indicators can show whether the RV variation is caused by rotational modulation due to stellar activity or by an orbiting companion. Unfortunately, no photometric observations are available for CD-78 24; as a consequence, the rotational period can not be derived.

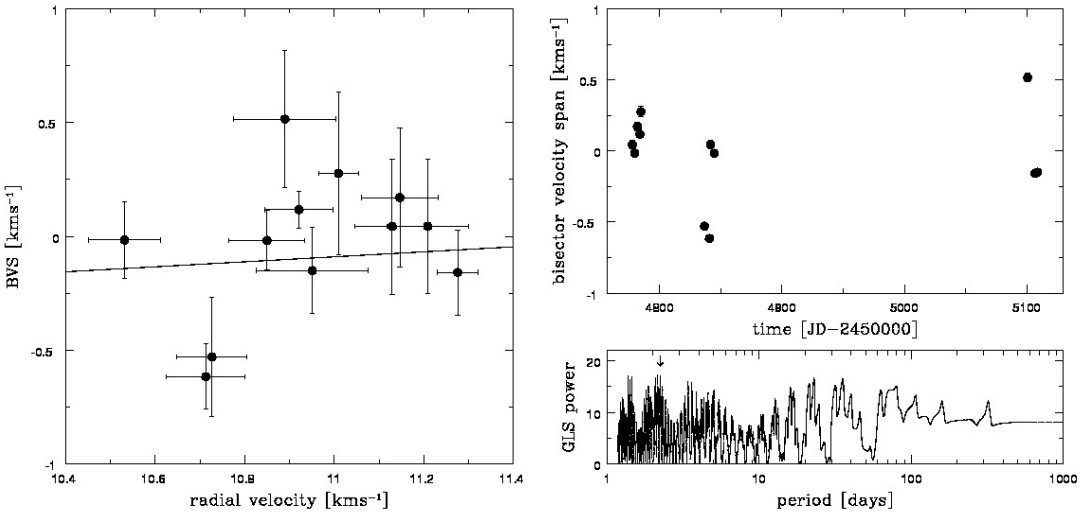

FIGURE 6.6 : Bisector velocity span for CD-78 24 - BVS vs. RV and time variance

6.2.2.1 Bisector analysis

I measured the BVS, BC and BVD as described in Section 4.1.2 and present the correlation of the BVS with RV in Figure 6.6 (left panel). The BC and BVD show a similar behaviour, and are therefore not presented here. The correlation coefficient of the BVS with RV is r=0.05 (0.25%). The slope of the linear regression to the BVS vs. RV data is 0.11, which is positive. Therefore, a (sub-)stellar companion, rather than stellar activity, is most likely the source of the RV variation (see Section 4.1.2). Nevertheless, further observations are needed to get a significant conclusion on the BVS data. However, calculating the probability T that the BVS is not correlated with RV, yields T=87% (see Section 6.1.2.2). Furthermore, I analysed the variation of the BVS over time (Figure 6.6, right panel) with GLS and found a period for the variation of 2.14 days, although with a FAP of 57%. However, this period is shorter than the 65.18 days period of the RV data.
As a result, I found that the bisector velocity span does not correlate with the radial velocity data and shows a variability on a much shorter time-scale.

6.2.2.2 Other activity indicators

In addition to the bisector analysis, I also analysed the variation over time of the other stellar activity indicators S_{FEROS} of the Ca II K line, the EW of Ca II λ 8662, the LDR of V I/Fe I, and the EW of Hα (see Section 4.2). The variation over time of these stellar activity indicators and the corresponding GLS periodograms are shown in Figure 6.7. Nearly all activity indicators show a periodicity in the range of 1.45–4.31 days, except the LDR of V I/Fe I which has a variability of 39.99 days (see Table 6.5). However,

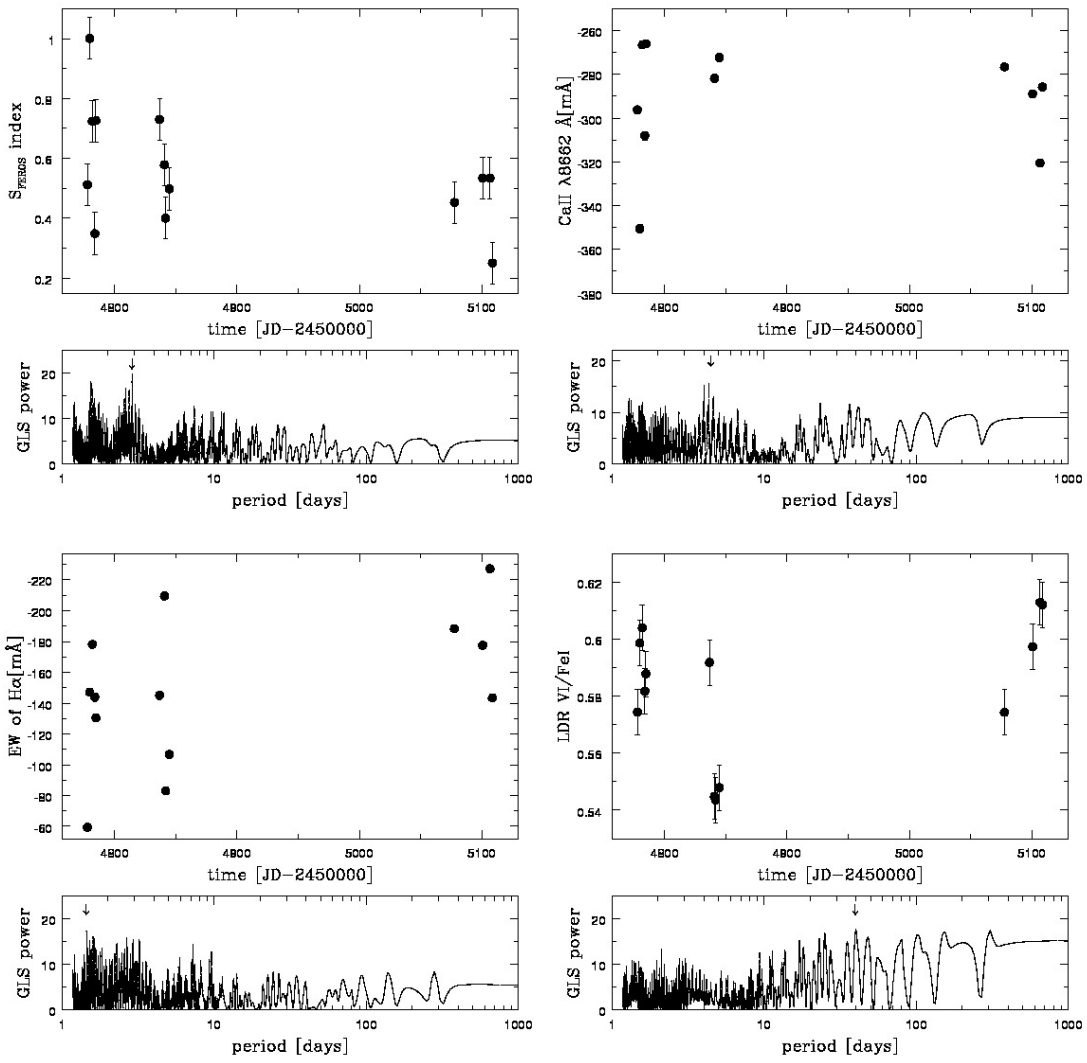

FIGURE 6.7 : Activity indicators for CD-78 24 - $S_{\rm FEROS}$, Ca II IRT λ 8662, Hα EW, and LDR V I/Fe I.

TABLE 6.6 : Keplerian fit to the RV data of CD-78 24.

Parameter	Value	Method
Period	65.18 days	GLS
FAP	23%	GLS
Amplitude K	831.52±35 ms^{-1}	GLS
Eccentricity e	0.4±0.09	GLS
Periastron passage	4831±20 HJD	GLS
Longitude of periastron ω	22±20°	GLS
Offset RV	10.72±0.03 kms^{-1}	GLS
$m_p \sin i$	14.6±2.4 M_{jup}	GLS
a $\sin i$	0.31±0.01 AU	GLS
rms of residuals	110 ms^{-1}	GLS

only the period of S_{FEROS} (2.88 days) is significant (FAP=0.6%). The reason for the insignificant periods is the low number of observations, thus, more data are needed to verify the periods of the stellar activity indicators. However, I found that all stellar activity indicators vary on a much shorter time-scale than the RV.
I am not able to derive a stellar rotation period because of the missing photometric observations and no NIR spectroscopic observations are available either for CD-78 24.

6.2.3 Summary for CD-78 24

The RV data of CD-78 24 shows a variability with a period of 65.18 days, although with a FAP of 23%. However, nearly all stellar activity indicators vary with shorter periods in the range of 1.45–4.31 days. Only the LDR of V I/Fe I shows a period of 40 days, although with a FAP of 12%. Nevertheless, more observations are needed to verify this period, because this can also be the origin of the RV variation by rotational modulation due to a surface spot pattern. However, if I assume that the period of the RV is real, CD-78 24 is orbited by a sub-stellar companion with a mass $m \sin i$=14.6±2.4 M_{Jup}, which is in the brown dwarf mass regime. This is also supported by the positive trend in the BVS vs. RV data in Figure 6.6, which indicates that the line shape gets altered by a companion (see Section 4.1.2).
However, I have to emphasise that this is only evidence for a brown dwarf orbiting CD-78 14, because further observations must verify the long-term period found. Note that after removing two data points with RV=11.0 kms^{-1} and RV=11.1 kms^{-1} (see Figure 6.5), the most prominent period is 1.3 days. This would mean that the RV variation is most likely caused by rotational modulation due to stellar activity.

TABLE 6.7 : Basic parameters for CD-37 1123.

Parameter	Value	Method/Reference
Identifier	CD-37 1123	...
Coordinates	03 00 47.0 -37 08 02.0	SIMBAD
Spectral type	G7V	this study
V magnitude	10.5 mag	Torres *et al.* [2006]
$T_{\rm eff}$	5650±130 K	*TGV*, this study
$\log g$	5.8±0.4 cms^{-2}	*TGV*, this study
[Fe/H]	0.0±0.1	*TGV*, this study
EW of Li I	230±5 mÅ	this study
Age	30±15 Myr	Li I measurements, this study
$v \sin i$	6.9±1.2 kms^{-1}	this study
$R'_{\rm FEROS}$	-4.25	this study
Number of observations	15	...

6.3 CD-37 1123

CD-37 1123 is a star with V=10.5 mag [Torres *et al.*, 2006] and no computation of stellar parameters are available so far. I measured the effective temperature to be 5650±130 K, which yields a spectral type of G7V for this star. The metallicity is solar-like and the age interfered from the Li I measurements is 30±15 Myr. The distance to CD-37 1123 is unknown because no measurements are available. Therefore, the use of evolutionary tracks to obtain stellar age, mass, and radius is not possible. Furthermore, no observations concerning the status of a possible circumstellar disk are available.

6.3.1 Radial velocity measurements

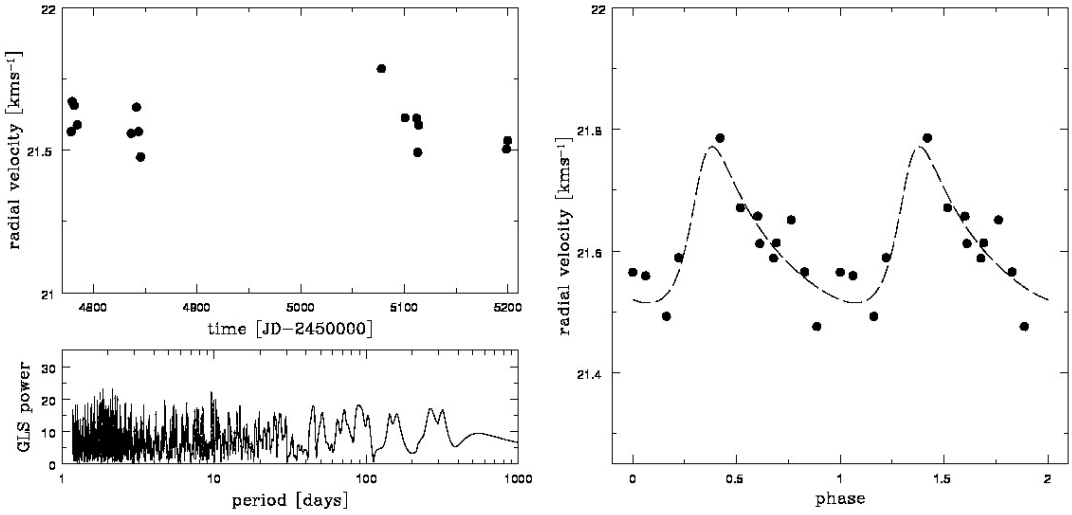

FIGURE 6.8 : Radial velocity variation of CD-37 1123 - variation over time and phase-folded with 2.32 days.

TABLE 6.8 : Periods of stellar activity indicators, photometric data, RV, the FAP of the period, and the amplitude for CD-37 1123. I list further the accuracy of a single measurement σ_{meas} and mark the significant periods.

Activity indicator	Period [days]	FAP	Significance	Semi-amplitude	σ_{meas}
Stellar activity					
BVS	3.45	3%	...	353.08 ms^{-1}	5–14 ms^{-1}
V I/Fe I LDR	1.2	29%	...	0.03	0.003
Hα	50.29	0.3%	significant	235.36 mÅ	15 mÅ
S_{FEROS}	1.44	24%	...	0.23	0.08
Ca II λ 8662	2.1	78%	...	59.47 mÅ	2 mÅ
Radial Velocity	2.32	31%	...	90.57 ms^{-1}	5–14 ms^{-1}

The RV (see Section 4.1) shows a peak-to-peak variation of 320 ms^{-1}. The variation is shown in Figure 6.8 (left panel) and its period is 2.32 days, obtained by using GLS. The FAP is 31% for this period. The number of observations should be sufficient to obtain a more significant period, thus, the variability of CD-37 1123 is probably irregular. However, more data is needed to draw a conclusion. The amplitude of the Keplerian fit to the RV data is 90.57 ms^{-1}. In Figure 6.8 (right panel) the RV is phase-folded with the 2.32 days period. The measured RV significantly scatter around the Keplerian fit (see Table 6.9), which is most likely the origin of the high FAP. However, the analysis of the RV residuals (after subtraction of the 2.32 days period) yields no significant variation.

6.3.2 Analysis of stellar activity

I have to analyse the stellar activity indicators to draw a conclusion on the source of the RV variation. For CD-37 1123, no photometric observations are available. Thus, no measurements of the the stellar rotation period and the RV jitter induced by stellar surface spots are possible.

6.3.2.1 Bisector analysis

For this analysis, the BVS, BC and BVS have been calculated and analysed for correlation with the RV data (see Section 4.1.2). All three variants of the bisector show the same behaviour with RV. The correlation of BVS on RV is shown in Figure 6.9 (left panel). The correlation coefficient is $r = 0.14$. The slope of a linear regression to the BVS vs. RV data is -0.27, which points towards a strong correlation of both measurements. However, the scatter of the data around the linear regression is high and the slope of the correlation remains inconclusive. The probability that the BVS and the RV data do not correlate is T=59% (Section 6.1.2.2), which supports that BVS and RV are uncorrelated.

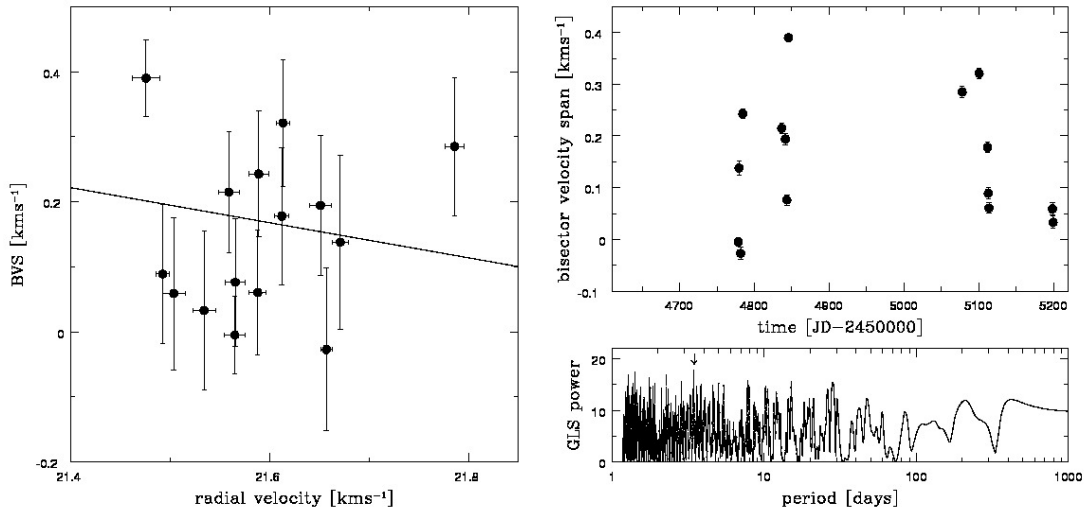

FIGURE 6.9 : Bisector velocity span for CD-37 1123 - BVS vs. RV and time variance

The analysis of the variation over time of the BVS is shown in Figure 6.6 (right panel) and yields a period of 3.45 days with FAP=3%. This period is close to the period of the RV variation and, therefore, giving evidence that the RV and the BVS variation have still the same origin.

6.3.2.2 Other stellar activity indicators

The time dependences of S_{FEROS}, EW of Ca II λ 8662, LDR of V I/Fe I, and EW of Hα are shown in Figure 6.10. The periods of nearly all indicators are in the range of 1.2–2.1 days, although with FAPs of 24–78%. The only significant period is that of Hα with 50.29 days and a FAP of 0.3%. However, this long period of the Hα line is most likely due to the low number of observations, because CD-37 1123 shows no signs of flares and accretion. As a result, I found that the periods of the stellar activity indicators are not significant, but are in the range of period of the RV variation.

6.3.3 Summary for CD-37 1123

The period of the RV variation of CD-37 1123 is 2.32 days with a FAP of 31% and a semi-amplitude of 90.57 ms^{-1}. In addition, the periods of the BVS and nearly all other stellar activity indicators are in a similar time-span of 1.44–4.2 days, giving evidence that the RV variation is caused by rotational modulation due to stellar activity. The low semi-amplitude of the RV variation of 90.57 ms^{-1} is in the typical range of RV jitter induced by stellar activity (see Section 4.2.1). However, photometric observations are needed to estimate the RV jitter due to stellar activity.
On the other hand, the BVS data does not show a strong correlation with the RV

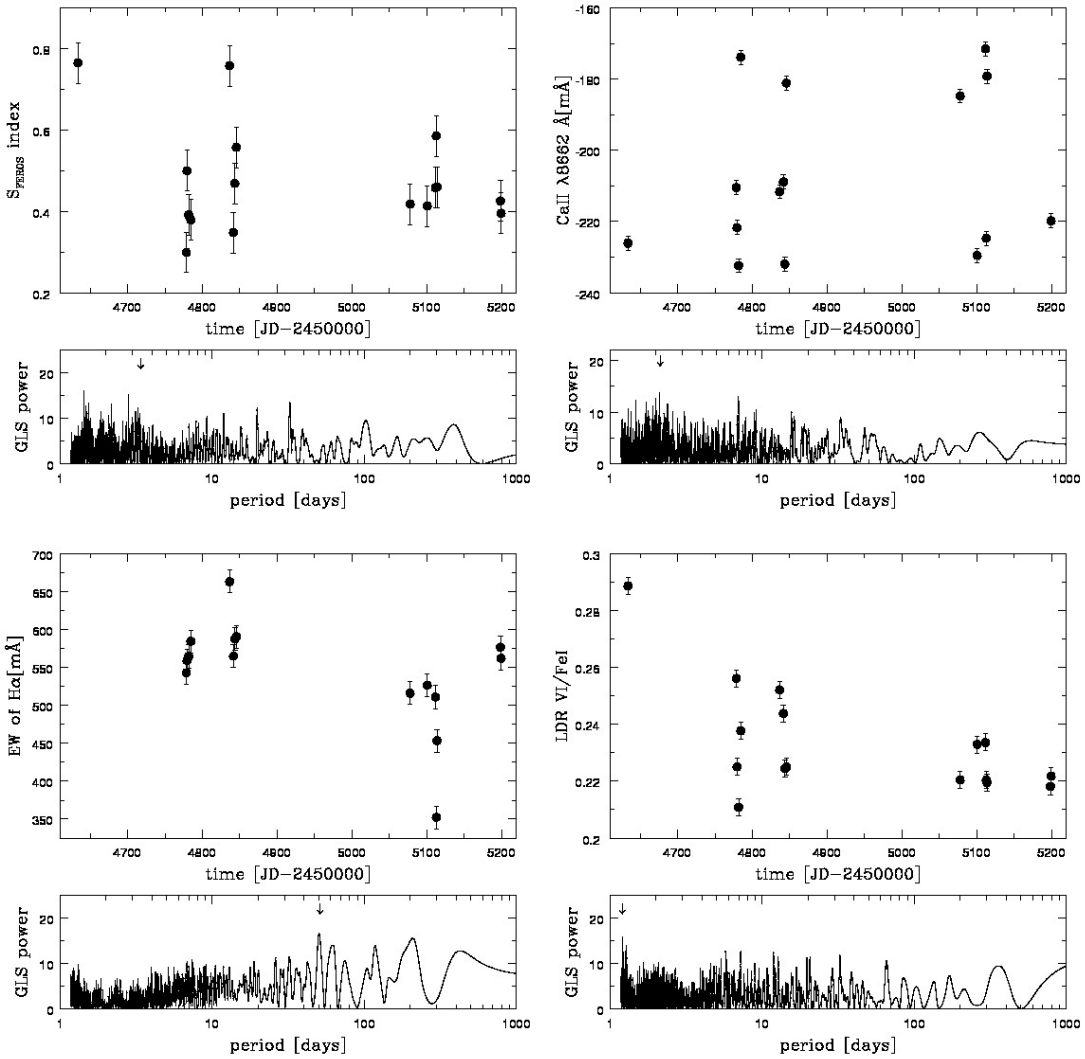

FIGURE 6.10 : Activity indicators for CD-37 1123 - S_{FEROS}, Ca II IRT λ 8662, Hα EW, and LDR V I/Fe I.

TABLE 6.9 : Keplerian fit to the RV data of CD-37 1123.

Parameter	Value	Method
Period	2.32 days	GLS
FAP	31%	GLS
Amplitude K	90.57±10 ms^{-1}	GLS
Eccentricity e	0.4±0.09	GLS
Periastron passage	4780±20 HJD	GLS
Longitude of periastron ω	106±20°	GLS
Offset RV	21.58±0.02 kms^{-1}	GLS
rms of residuals	27 ms^{-1}	GLS

data, such that there is still the chance that the RV variation is caused by a sub-stellar companion. Assuming a stellar mass of $1\,M_{\odot}$, the companion would have a minimum mass of $0.5\,M_{Jup}$ orbiting at 0.03 AU. A planet at that distance would induce stellar activity on its host star due to interactions of the magnetosphere (e.g., Shkolnik *et al.* [2007]). This gets supported by $\log R'_{FEROS}$ = -4.25, which is higher than expected for a star at the age of CD-37 1123 [Mamajek, 2009]. However, the high stellar activity can be induced by star-planet interactions (SPI). To be able to analyse this phenomenon, more data taken over several orbits are needed because stellar activity that is induced by a planet due to SPI is shifted by a quarter phase compared to the phase of the RV variation. This shift in phase is because the activity in the magnetosphere 'follows' the planet [Shkolnik *et al.*, 2007]. However, more data is needed for this scenario to be verified.

TABLE 6.10 : Basic parameters for 1RXS J033149.8-633155.

Parameter	Value	Method/Reference
Identifier	1RXS J033149.8-633155	...
optical counterpart	TYC 8870-372-1	Voges *et al.* [1999]
Coordinates	03 31 49.0 -63 31 54.0	SIMBAD
Spectral type	K0V	Torres *et al.* [2006]
V magnitude	10.9 mag	Torres *et al.* [2006]
$T_{\rm eff}$	5145±83 K	*TGV*, this study
$\log g$	4.7±0.2 cms^{-2}	*TGV*, this study
[Fe/H]	-0.15±0.05	*TGV*, this study
EW of Li I	300±3 mÅ	this study
Age	25±15 Myr	Li I measurements, this study
$v \sin i$	18.1±1.1 kms^{-1}	this study
$R'_{\rm FEROS}$	-4.53	this study
Number of observations	13	...

6.4 1RXS J033149.8-633155

1RXS J033149.8-633155 is a K0V star with V=10.9 mag [Torres *et al.*, 2006]. For this star, no measurements of basic stellar parameters are available, such that the analysis in this study is the first so far. The measurements of the basic stellar parameters are summarized in Table 6.10 and agree well with the spectral type of K0, estimated by Torres *et al.* [2006]. The age has been calculated from Li I EW measurements to be 25±15 Myr (see Section 4.3.3). However, no distance to 1RXS J033149.8-633155 is known and, therefore, no calculation of the age, stellar mass, and radius from evolutionary tracks is possible. Furthermore, the evolutionary state of a possible circumstellar disk is unknown. However, 1RXS J033149.8-633155 is slightly metal-poor compared to the sun with [Fe /H] = -0.15 ± 0.05 dex.

6.4.1 Radial velocity variation

The radial velocity of 1RXS J033149.8-633155 shows a peak-to-peak variation of 1 160 ms^{-1} and is presented in Figure 6.11 (left panel). The period obtained with GLS is 2.61 days with a FAP < 0.1%. The semi-amplitude of the Keplerian fit is only 425.96 ms^{-1} (see Table 6.12). The RV data phase-folded with the 2.62 days period, is shown in Figure 6.11 (right panel). For a few data points, the RV measurement was not as accurate as for the other RV measurements because these spectra have a lower SNR and, therefore, these data points that scatter around the Keplerian fit, are outliers. These RV measurements are not considered for further analysis.

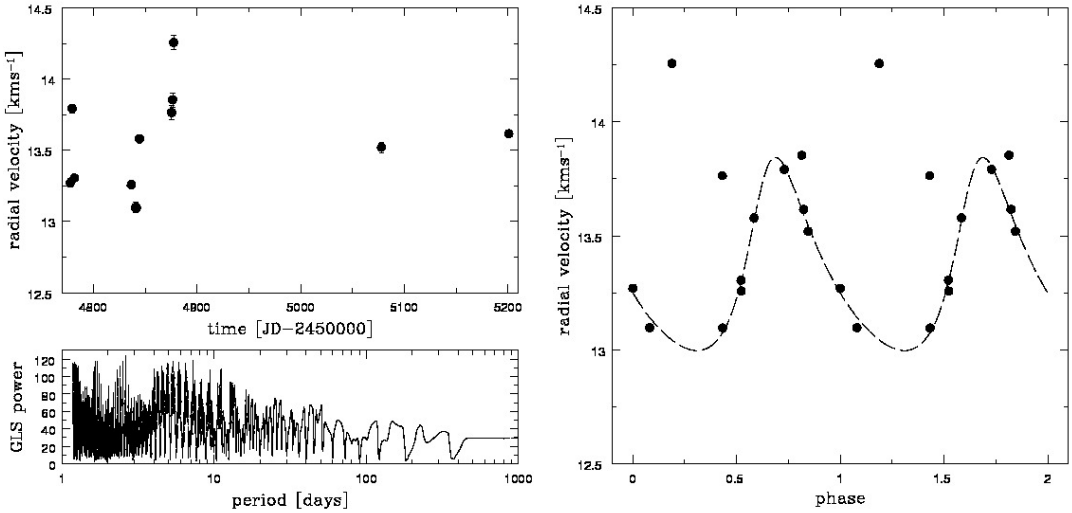

FIGURE 6.11 : Radial velocity variation of 1RXS J033149.8-633155 - variation over time and phase-folded with 2.61 days.

TABLE 6.11 : Periods of stellar activity indicators, photometric data, RV, the FAP of the period, and the amplitude for 1RXS J033149.8-633155. I list further the accuracy of a single measurement $\sigma_{\rm meas}$ and mark the significant periods.

Activity indicator	Period [days]	FAP	Significance	Semi-amplitude	$\sigma_{\rm meas}$
Stellar activity					
BVS	1.2	18%	...	1080.36 ms^{-1}	10–35 ms^{-1}
V I/Fe I LDR	4.05	1.4%	significant	0.05	0.008
Hα	14.3	1.2%	significant	52.86 mÅ	12 mÅ
$S_{\rm FEROS}$	6.7	33%	...	0.72	0.02
Ca II λ 8662	147.2	93%	...	215.68 mÅ	4 mÅ
Photometric variation	2.72	...	...	0.1 mag	...
Radial Velocity	2.61	<0.1%	significant	425.96 ms^{-1}	25–50 ms^{-1}

6.4.2 Analysis of stellar activity

For 1RXS J033149.8-633155, photometric observations are available and a period of 2.73 days with a semi-amplitude of 0.1 mag has been found for the photometric variation by Bernhard *et al.* [2009]. The rotational period can be assumed to be similar to that period. The period of the RV variation (2.61 days) is very close to the period of the stellar rotation. This gives evidence that the RV variation is caused by rotational modulation due to stellar activity. This result has to be analysed further by the analysis of the stellar activity indicators.

6.4.2.1 Bisector analysis

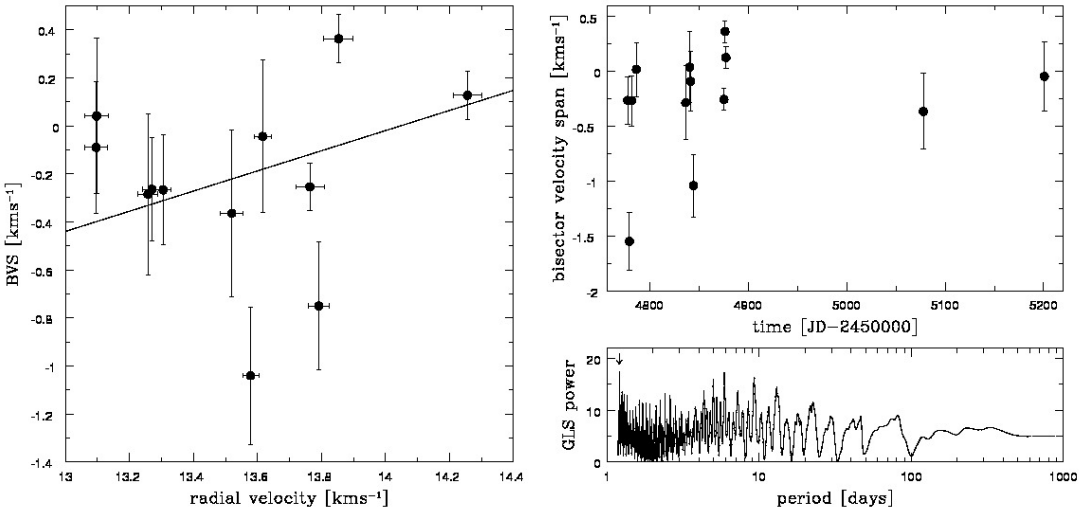

FIGURE 6.12 : Bisector velocity span for 1RXS J033149.8-633155 - BVS vs. RV and time variance

As described in Section 4.1.2, the BVS, BC, and BVD have been calculated. The correlation of BVS and RV is shown in Figure 6.12 (left panel). The BC and BVD show a similar behaviour. The correlation coefficient for the BVS vs. RV data is r=0.34 (11.6%) and the probability that both do not correlate is T=22%. In addition, the slope of a linear regression to the BVS vs. RV data is 0.42. However, the scatter around the linear regression is high and a negative slope is also possible. Therefore, no significant conclusion can be made on the correlation of BVS with RV so far because more data is needed.

The variation over time of BVS is presented in Figure 6.12 (right panel) and has a period of 1.2 days, although with a FAP of 18%. However, this period is nearly half that of the rotational period of 2.7 days and can be caused by two stellar surface spots separated by 180° on the stellar surface.

I am able to calculate the the expected RV jitter as described in Section 4.2.1 from the

photometric data. The photometric amplitude $\Delta V = 0.2$ mag yields a $f_s = 8\%$ and, with a BVS amplitude of 1 080 ms^{-1}, a RV jitter of 780–1 070 ms^{-1} can be inferred. Thus, the expected RV jitter induced by stellar activity can fully account for the peak-to-peak amplitude measured for the RV data. This gives further evidence that the RV variation is induced by stellar activity.

6.4.2.2 Other stellar activity indicators

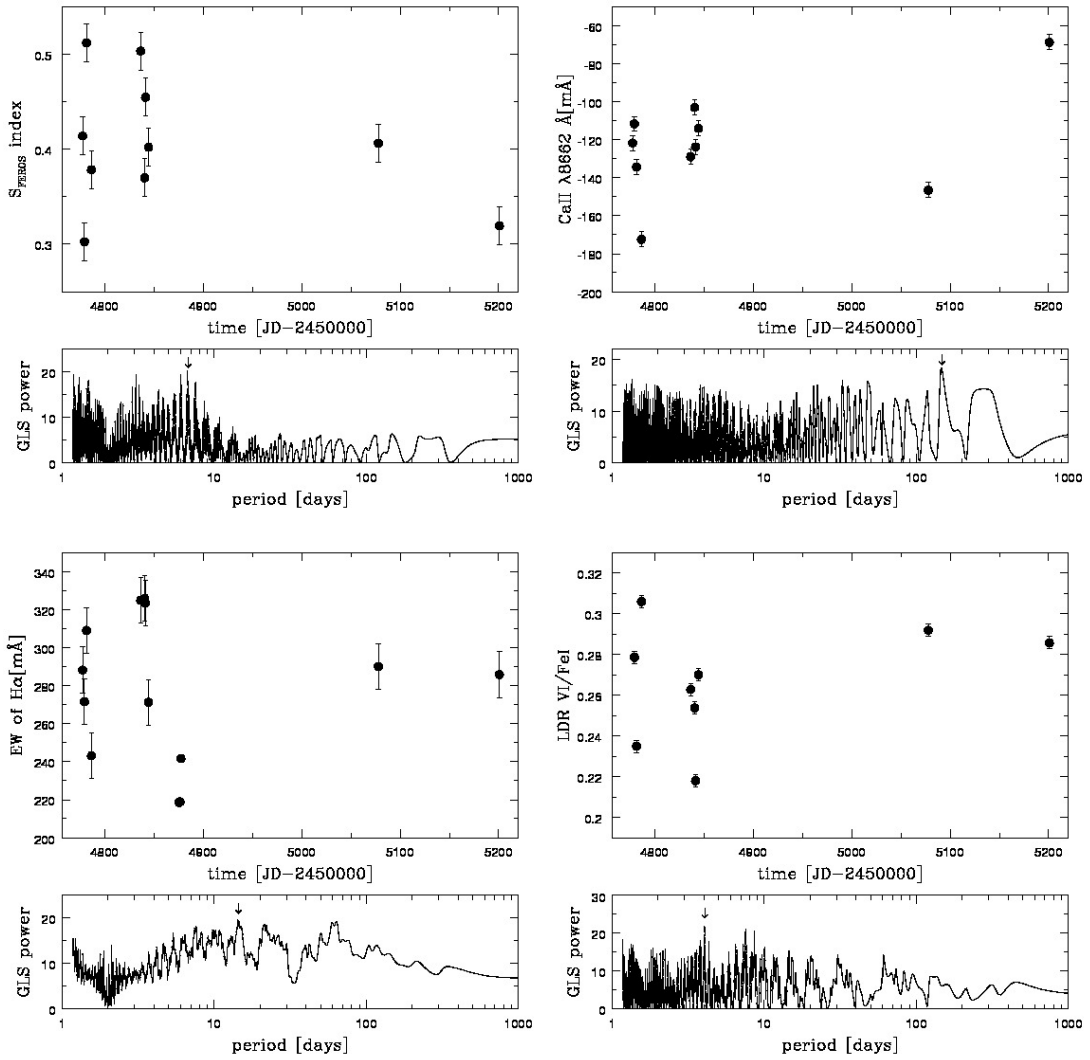

FIGURE 6.13 : Activity indicators for 1RXS J033149.8-633155 - S_{FEROS}, Ca II IRT λ 8662, Hα EW, and LDR V I/Fe I.

The other stellar activity indicators, S_{FEROS}, EW of Ca II λ 8662, LDR of V I/Fe I, and EW of Hα, are presented in Figure 6.13 and their derived periods are listed in Table 6.11. The only significant periods are that of Hα with 14.3 days and a FAP of

TABLE 6.12 : Keplerian fit to the RV data of 1RXS J033149.8-633155.

Parameter	Value	Method
Period	2.61 days	GLS
FAP	<0.1%	GLS
Amplitude K	425.96±100 ms^{-1}	GLS
Eccentricity e	0.29±0.09	GLS
Periastron passage	4779±20 HJD	GLS
Longitude of periastron ω	321±20°	GLS
Offset RV	13.32±0.02 kms^{-1}	GLS
rms of residuals	427 ms^{-1}	GLS

1.2%, and the LDR V I/Fe I with a period of 4.05 days and a FAP of 1.4%. However, these periods are longer than that of the rotational period, most likely due to irregular pattern of surface spots. The Hα variation might be induced by long-lived (longer than a rotational period of the star) plaques that do not affect the RV data.

6.4.3 Summary for 1RXS J033149.8-633155

For 1RXS J033149.8-633155, there is strong evidence that the RV variation is caused by rotational modulation due to stellar activity, because the period of the RV variation (2.61 days) is similar to the rotation period of the stars (2.72 days). Furthermore, the probability that the BVS does not correlate with the RV data is low (T=22%) and stellar surface spots can produce the observed the peak-to-peak amplitude of the RV data. Although the periods of the other stellar activity indicators are somewhat inconclusive, they are also in the range of 1.2–14 days. Thus, it is very unlikely that 1RXS J033149.8-633155 has an orbiting companion. Instead, the RV variation is most probably induced by rotational modulation due to stellar activity.

TABLE 6.13 : Basic parameters for TYC 5891-69-1

Parameter	Value	Method/Reference
Identifier	TYC 5891-69-1	...
Coordinates	04 32 43.0 -15 20 11.0	SIMBAD
Spectral type	G4V	Torres *et al.* [2006]
V magnitude	10.4 mag	Torres *et al.* [2006]
T_{eff}	5200±1203 K	*TGV*, this study
$\log g$	3.6±0.4 cms^{-2}	*TGV*, this study
[Fe/H]	-0.36±0.12	*TGV*, this study
EW of Li I	280±4 mÅ	this study
Age	10±5 Myr	Li I measurements, this study
$v \sin i$	20.5±1.3 kms^{-1}	this study
R'_{FEROS}	-4.30	this study
Circumstellar disk	none	Carpenter *et al.* [2009]
Number of observations	14	...

6.5 TYC 5891-69-1

TYC 5891-69-1 is a G4V type stars with V=10.4 mag [Torres *et al.*, 2006] and has been analysed for stellar activity and basic stellar parameters by White *et al.* [2007]. They found a slightly higher T_{eff} than I derived. As in the case of 1RXS J153328.4-665130, a different fitting method of the EWs of Fe I and Fe II is most likely the reason for this discrepancy. The parameters are summarized in Table 6.13. TYC 5891-69-1 has also been observed with *SPITZER* in the context of the *FEPS* (*Formation and Evolution of Planetary Systems*) project, thus information about a circumstellar disk is available. However, the analysis by Carpenter *et al.* [2009] yielded no signature for an existing circumstellar disk.
The age of TYC 5891-69-1 has been measured to be 10±5 Myr by the Li I EW in this study (Section 4.3.3). Carpenter *et al.* [2009] obtained an age of 4 Myr for this target. Therefore, I adopt the range 4–10 Myr as the age of TYC 5891-69-1.

6.5.1 Radial velocity data

The measured RV (see Section 4.1) is shown in Figure 6.14 (left panel). The peak-to-peak amplitude of the variation is 930 ms^{-1} and the period of the variation has been calculated by using GLS to be 3.21 days with a FAP of <0.1%. Thus, this period is significant. The semi-amplitude of the Keplerian fit to the RV data is 525 ms^{-1} (see Table 6.15). In Figure 6.14 (right panel), the RV data phase-folded with the 3.21 days period is shown.

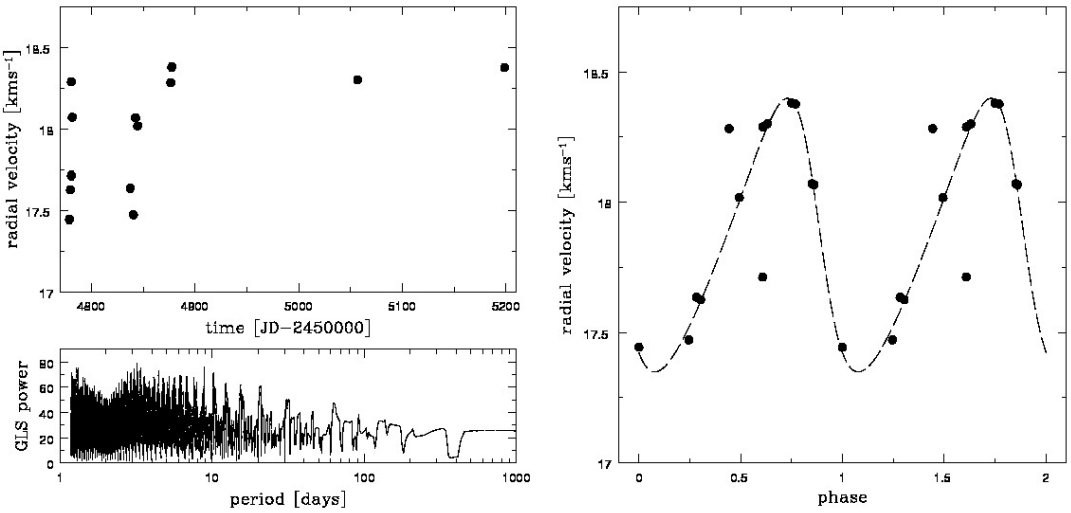

FIGURE 6.14 : Radial velocity variation of TYC 5891-69-1 - variation over time and phase-folded with 3.21 days.

TABLE 6.14 : Periods of stellar activity indicators, photometric data, RV, the FAP of the period, and the amplitude for TYC 5891-69-1. I list further the accuracy of a single measurement $\sigma_{\rm meas}$ and mark the significant periods.

Activity indicator	Period [days]	FAP	Significance	Semi-amplitude	$\sigma_{\rm meas}$
Stellar activity					
BVS	1.2	20%	...	1161.96 ms^{-1}	10–35 ms^{-1}
V I/Fe I LDR	1.37	98%	...	0.11	0.005
Hα	33.9	91%	...	63.22 mÅ	15 mÅ
$S_{\rm FEROS}$	10.1	50%	...	0.13	0.03
Ca II λ 8662	1.87	60%	...	65.97 mÅ	12 mÅ
Radial Velocity	3.21	<0.1%	significant	425.96 ms^{-1}	9–28 ms^{-1}

6.5.2 Analysis of stellar activity

Although TYC 5891-69-1 has been observed and analysed in a few projects (e.g., Carpenter *et al.* [2009]; Torres *et al.* [2006]; White *et al.* [2007]), no photometric observations are available and the stellar rotation period remains unknown. Thus, no calculation of the expected RV jitter due to stellar activity can be done. However, I analyse the stellar activity indicators to identify the source of the RV variation.

6.5.2.1 Bisector analysis

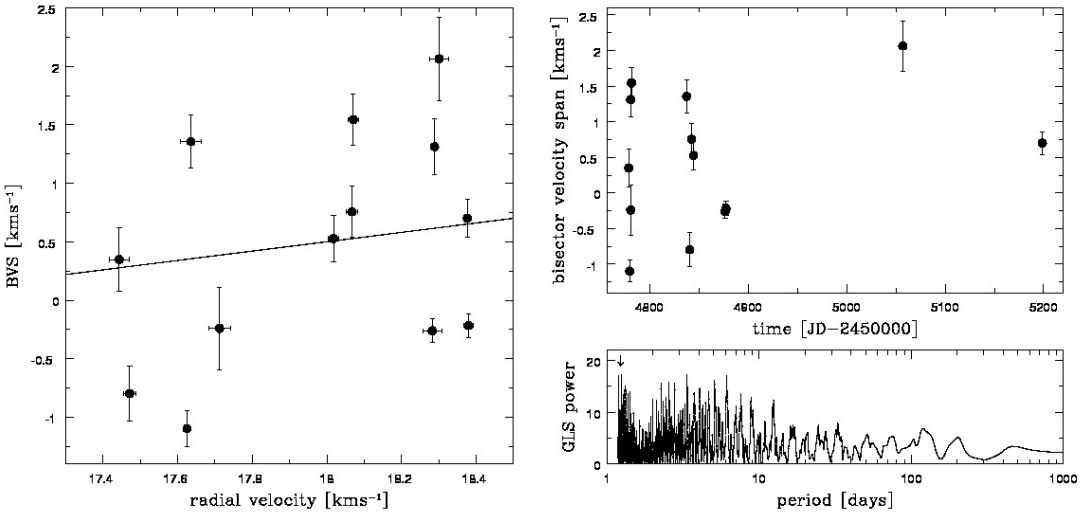

FIGURE 6.15 : Bisector velocity span for TYC 5891-69-1 - BVS vs. RV and time variance

The BVS and its dependence on RV is shown in Figure 6.15 (left panel). A correlation coefficient r=0.16 (2.6%) has been calculated. Furthermore, the probability that both data sets do not correlate is T=55%. Thus, there is no correlation between the BVS and the RV data. In addition, the slope of the linear regression to the BVS vs. RV data is 0.4. The positive slope is an indication that the RV variation is caused by a companion (see Section 4.1.2). The BC and BVD show a similar behaviour, i.e., no sign of correlation with RV.
The variation over time of the BVS is shown in Figure 6.15 (right panel). An analysis with GLS yields the period of the BVS variation to be 1.2 days, although with a FAP of 20%. However, more observations are needed because the periodogram in Figure 6.15 (right panel) shows peaks of similar height at 3.5 days and 6 days.

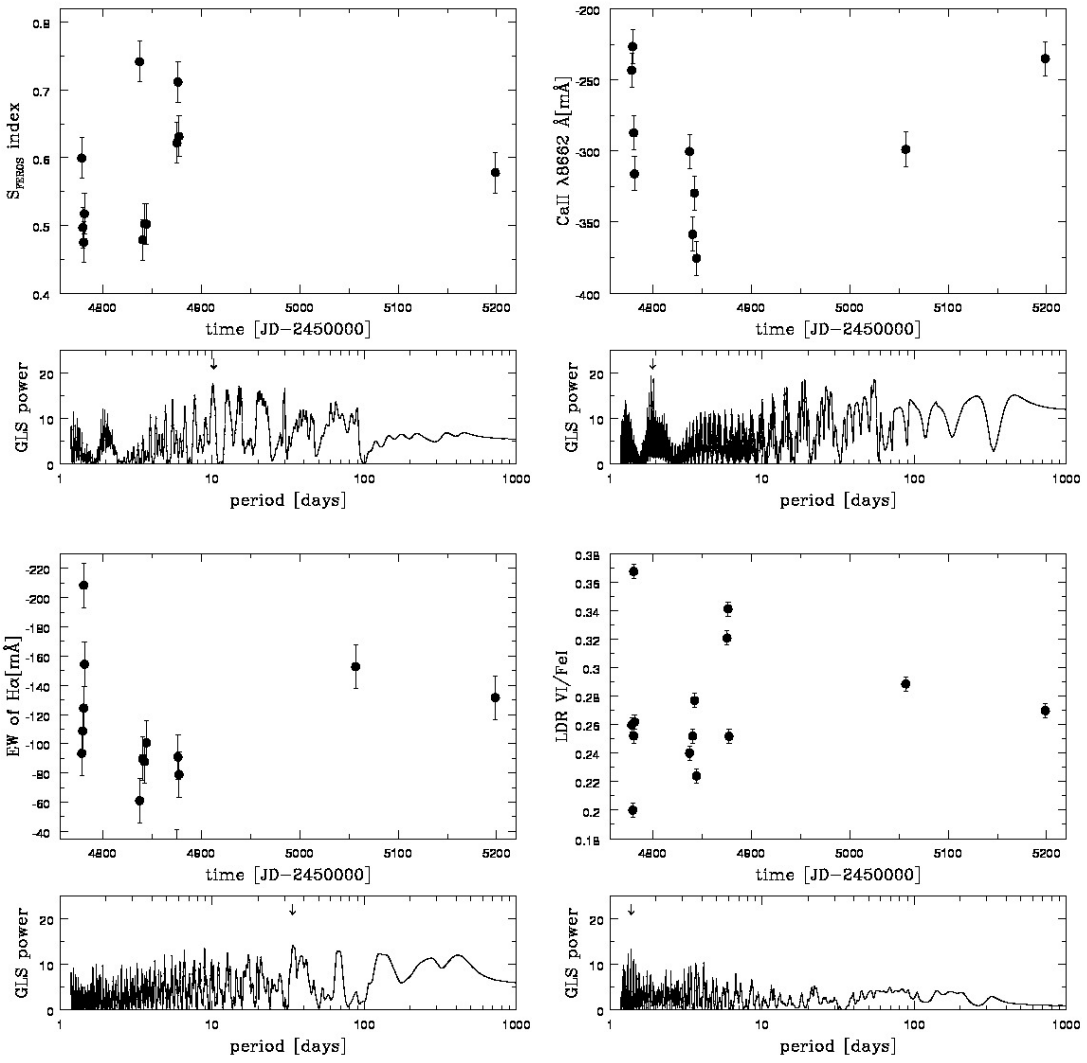

FIGURE 6.16 : Activity indicators for TYC 5891-69-1 - $S_{\rm FEROS}$, Ca II IRT λ 8662, Hα EW, and LDR V I/Fe I.

TABLE 6.15 : Keplerian fit to the RV data of TYC 5891-69-1.

Parameter	Value	Method
Period	3.21 days	GLS
FAP	<0.1%	GLS
Amplitude K	525.01±30 ms^{-1}	GLS
Eccentricity e	0.19±0.09	GLS
Periastron passage	4781±20 HJD	GLS
Longitude of periastron ω	75±20°	GLS
Offset RV	17.84±0.02 kms^{-1}	GLS
rms of residuals	192 ms^{-1}	GLS

6.5.2.2 Other stellar activity indicators

The indicators of stellar activity, S_{FEROS}, EW of Ca II λ 8662, LDR of V I/Fe I, and EW of Hα, are presented in Figure 6.16 and their derived periods in Table 6.14. All indicators show no significant periodicity. Thus, I assume that the stellar activity is not stable over the observing period (420 days). Therefore, no significant periods can be identified for the stellar activity indicators.

6.5.3 Summary for TYC 5891-69-1

TYC 5891-69-1 shows a significant variation in RV with a period of 3.21 days and a semi-amplitude of 525 ms^{-1}. The results of a Keplerian fit to the data are presented in Table 6.15. When assuming a stellar mass of 1 $M_{\odot}$, the minimum mass of a companion would be 3.74 M_{Jup}, orbiting at 0.04 AU.
The bisector is most likely not correlated with the RV data, the probability that both data sets are uncorrelated is T=55% and the slope of the correlation is positive. Furthermore, the other stellar activity indicators show no significant sign of periodicity. Thus, the RV variation is most likely induced by an orbiting companion.

TABLE 6.16 : Basic parameters for GW Ori

Parameter	Value	Method/Reference
Identifier	GW Ori	...
Coordinates	05 29 08.0 11 52 13.0	SIMBAD
Spectral type	K3V	Schegerer *et al.* [2006]
V magnitude	9.9 mag	Schegerer *et al.* [2006]
Distance	440 pc	Schegerer *et al.* [2006]
$M_\star$	3.7±0.1 $M_\odot$	Schegerer *et al.* [2006]
$R_\star$	5.6 $R_\odot$	Shevchenko *et al.* [1998]
$T_{\rm eff}$	5700±200 K	Mathieu *et al.* [1991]
EW of Li I	240±5 mÅ	this study
Age	5±2 Myr	Li I measurements, this study
Age	1 Myr	Schegerer *et al.* [2006]
$v \sin i$	43.7±2.4 kms^{-1}	this study
Circumstellar disk	mass=0.1 $M_\odot$	Schegerer *et al.* [2006]
Number of observations	38	...
double star	...	Mathieu *et al.* [1991]

6.6 GW Ori

GW Ori is a K3 type star with a well studied accretion disk and a close stellar companion. The disk has a mass of 0.1 $M_\odot$ and an outer radius of 360 AU [Schegerer *et al.*, 2006, and references therein]. An accretion rate of $1.7 \cdot 10^{-7}$ $M_\odot$/yr has been derived in Section 5.1.3. Schegerer *et al.* [2006] found a nearly gas-free gap in the circumstellar disk of GW Ori between 0.5–3.0 AU. Both components of the binary system have a circumstellar disk which get fed by a circumbinary disk that surrounds both components [Schegerer *et al.*, 2006, and references therein]. The stellar companion that has been found spectroscopically, has a mass of 0.5–1.0 $M_\odot$ and orbits at 1.08 to 1.18 AU [Mathieu *et al.*, 1991].
The temperature has been taken from Mathieu *et al.* [1991], because no EW of the Fe I and Fe II spectral lines could be measured due to the variable veiling in the spectra of GW Ori. The age of GW Ori obtained by Li I measurements in this study is 5±2 Myr. In the literature, the age is given as 1 Myr (e.g., Schegerer *et al.* [2006]). Thus, GW Ori is one of the youngest stars in our sample.

6.6.1 Radial velocity data

The RV has been measured as described in Section 4.1 and the variation of the RV is presented in Figure 6.17 (left panel). The measurement errors of the individual RV measurements are in the range of 100–680 ms^{-1}. This is due to the high $v \sin i = 43.7$ kms^{-1} and the veiling in the spectra of GW Ori.
The peak-to-peak amplitude of the RV variation is 17.83 kms^{-1} and the most significant period is 220.98 days (FAP <0.1%). The Keplerian fit (see Table 6.18) is also shown in

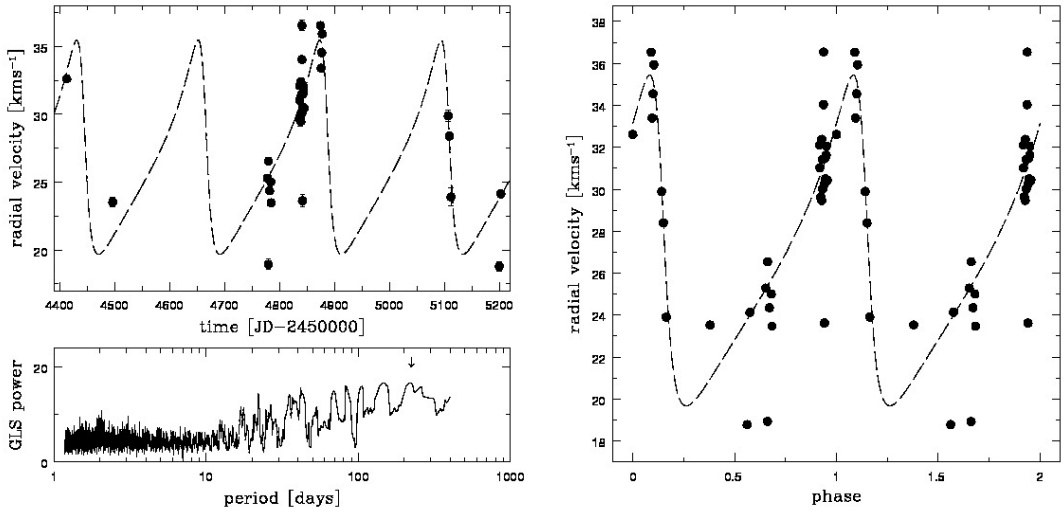

FIGURE 6.17 : Radial velocity variation of GW Ori - variation over time and phase-folded with 220.98 days. The Keplerian fit is shown by the dashed lines.

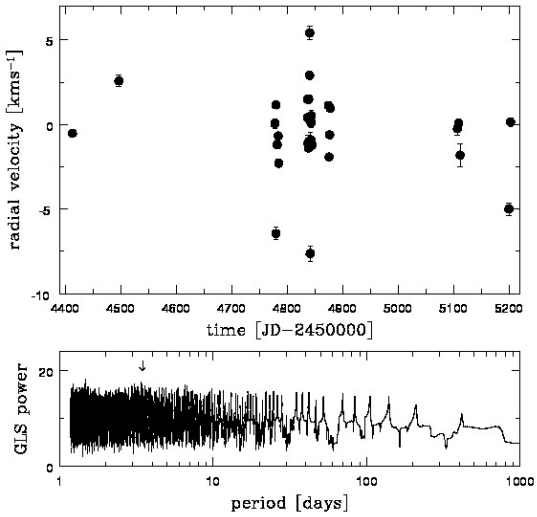

FIGURE 6.18 : Residuals of radial velocity data - Residuals after subtraction of the 220.98 days period. The period of the residuals is 3.44 days

TABLE 6.17 : Periods of stellar activity indicators, photometric data, RV, the FAP of the period, and the amplitude for GW Ori. I list further the accuracy of a single measurement $\sigma_{\rm meas}$ and mark the significant periods.

Activity indicator	Period [days]	FAP	Significance	Semi-amplitude	$\sigma_{\rm meas}$
Stellar activity					
BVS	100.8	0.4%	significant	3358.51 $\rm ms^{-1}$	10–155 $\rm ms^{-1}$
V I/Fe I LDR	69.5	0.5%	significant	0.11	0.008
Hα	63.8	<0.1%	significant	3.71 Å	0.03 Å
$S_{\rm FEROS}$	15.9	0.5%	significant	0.71	0.04
Ca II λ 8662	2.0	70%	...	204.10 mÅ	12 mÅ
Radial Velocity	220.98	<0.1%	significant	7890.93 $\rm ms^{-1}$	100–680 $\rm ms^{-1}$
RV residuals	3.44	30%	...	831.52 $\rm ms^{-1}$	100–680 $\rm ms^{-1}$

Figure 6.17 (left panel). In the right panel, the RV phase-folded with the 220.98 days period is shown. The semi-amplitude of the Keplerian fit to the RV data is 7.89 $\rm kms^{-1}$. The RV data shows also a scatter around the Keplerian fit (see Figure 6.17). Therefore, I analysed the RV residuals after subtraction of the 220.98 days period (Figure 6.18). The analysis of the RV residuals with GLS yielded a period of 3.44 days (FAP=30%). The origin of this period is discussed in the next section.

6.6.2 Analysis of stellar activity

I analyse the stellar activity indicators in this section to identify the sources of the short and long RV variation. The rotational period of GW Ori has been found to be 3.3 days and the inclination of the rotation axis is $i = 30°$ [Shevchenko *et al.*, 1998, and references therein].

6.6.2.1 Bisector analysis

I calculated the BVS, BC, and BVD as described in Section 4.1.2 and show the correlation between the BVS and RV in Figure 6.19 (left panel). The correlation coefficient is r=0.41 (16.8%) and the probability that both datasets do not correlate is 8%. However, the slope of the linear regression to the BVS vs. RV data is positive, speaking for a stellar companion as the source of the RV variation. The BC and BVD show a similar behaviour, i.e., a positive correlation with RV.
The variation over time of the BVS is shown in Figure 6.19 (right panel). The most significant period (FAP=0.4%) is 100.8 days. This period is much longer than the rotational period of 3.3 days.

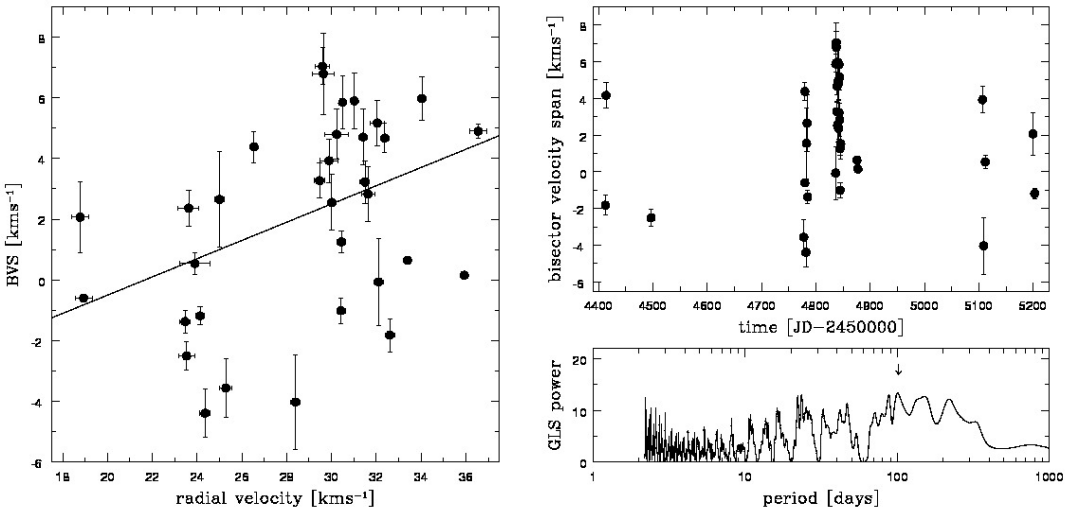

FIGURE 6.19 : Bisector velocity span for GW Ori - BVS vs. RV and time variance

6.6.2.2 Other stellar activity indicators

The other stellar activity indicators, S_{FEROS}, EW of Ca II λ 8662, LDR of V I/Fe I, and EW of Hα have been measured (see Section 4.2) and the results are presented in Figure 6.20. The derived periods for the indicators are listed in Table 6.17. Except the Ca II IRT indicator, all indicators show a significant long-term period in the range of 15–70 days. The Hα EW varies with a 63.8 days period which corresponds to a distance of 0.45 AU to the star. This distance is near the inner rim of the gas-free gap in the circumstellar disk.
Note that the Ca II IRT indicator could only be measured in spectra obtained with FEROS between JD 4832–4842. Thus, no conclusions can be drawn from Ca II IRT.

6.6.3 Summary for GW Ori

The RV data of GW Ori shows a long-term variation with a period of 220 days. The analysis of the stellar activity indicators showed that this period is not induced by stellar activity. Therefore, a stellar companion is most likely the source of the RV variation. The RV data shows also a short-term scatter around the Keplerian fit (see Table 6.18 and Figure 6.17). The short-term period is 3.44 days and has been found by the analysis of the RV residuals after subtraction of the long period. This short period is similar to the stellar rotation period of 3.3 days [Shevchenko *et al.*, 1998]. Thus, the short-term variation of the RV data is induced by rotational modulation due to surface features. However, the BVS shows still a positive correlation with the RV residuals because the effect of the stellar companion on the line shape is much stronger than the effect of stellar activity.

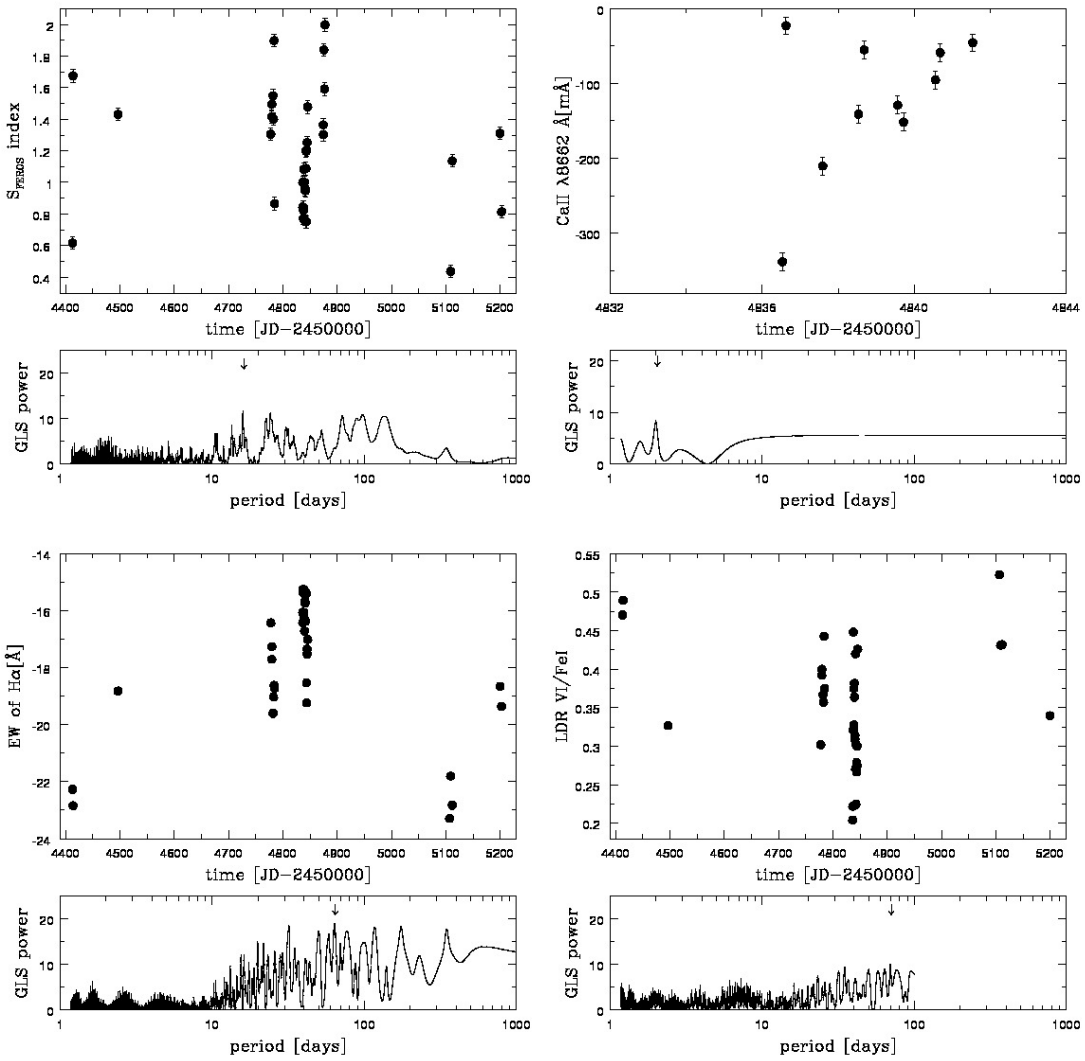

FIGURE 6.20 : Activity indicators for GW Ori - S_{FEROS}, Ca II IRT λ 8662, Hα EW, and LDR V I/Fe I.

TABLE 6.18 : Keplerian fit to the RV data of GW Ori.

Parameter	Value	Method
Period	220.98±5 days	GLS
FAP	<0.1%	GLS
Amplitude K	7890.93±120 ms^{-1}	GLS
Eccentricity e	0.55±0.09	GLS
Periastron passage	4443.97±10 HJD	GLS
Longitude of periastron ω	71±20°	GLS
Offset RV	26.19±0.08 kms^{-1}	GLS
$m_2 \sin i$	0.45±0.03 $M_\odot$	GLS
$\sin i$	0.5	[Shevchenko *et al.*, 1998]
True m_2	0.9±0.2 $M_\odot$	
$a \sin i$	1.03±0.01 AU	GLS
rms of residuals	2444.70 ms^{-1}	GLS
Period of res.	3.44 days	GLS
FAP	%	GLS
K of residuals	ms^{-1}	GLS

The long-term period of 220.98 days is close to the period of 242 days found for the orbiting stellar companion [Shevchenko *et al.*, 1998]. This supports the hypothesis of a stellar companion as the origin of the long-term RV variation. From the Keplerian fit to the RV data, I can calculate the minimum mass and the distance of the companion as $m_2 \sin i = 0.45\,M_\odot$ and 1.03 AU, respectively. With the known inclination $i = 30°$ of the rotation axis of GW Ori and the assumption that the companion orbits in the same plane, the true mass of the companion can be calculated to $m_2 = 0.9\,M_\odot$. These results agree well within the errors to the values derived by Mathieu *et al.* [1991], who found a mass of the companion of 0.5–1 $M_\odot$ at a distance of 1.08–1.18 AU [Schegerer *et al.*, 2006, and references therein]. However, due to the large error of the individual RV measurements (see Section 6.6.1), only variations induced by the stellar companion can be identified in the RV data.

Furthermore, the stellar activity indicators vary with periods around 63 days. Therefore, the distance where the variability of the Hα line originates is 0.45 AU. This is close to the inner rim of the nearly gas-free gap and shows that the variation of Hα is most likely caused by the accretion process starting at that distance. This scenario is similar as for the Hα variation of TW Hya [Setiawan *et al.*, 2008a].

TABLE 6.19 : Basic parameters for CD-84 0080

Parameter	Value	Method/Reference
Identifier	CD-84 0080	...
Coordinates	07 30 59.0 -84 19 28.0	SIMBAD
Spectral type	G9V	Torres *et al.* [2006]
V magnitude	9.96 mag	Torres *et al.* [2006]
Distance	35 pc	mean value from Zuckerman & Song [2004]
T_{eff}	5515±25 K	*TGV*, this study
$\log g$	5.2±0.1 cms^{-2}	*TGV*, this study
[Fe/H]	0.01±0.05	*TGV*, this study
EW of Li I	300±5 mÅ	this study
Age	30±15 Myr	Li I measurements, this study
Age	50±25 Myr	Zuckerman & Song [2004]
$v \sin i$	7.7±1.1 kms^{-1}	this study
R'_{FEROS}	-4.56	this study
Number of observations	34	...

6.7 CD-84 0080

CD-84 0080 is a G9V type star with V=9.96 mag [Torres *et al.*, 2006] and has been analysed in detail by Viana Almeida *et al.* [2009]. The values for T_{eff}, $\log g$, and metallicity measured in this study (see Table 6.19) agree well within the error-bars with the values obtained by Viana Almeida *et al.* [2009]. They also confirm that CD-84 0080 is a member of the AB Dor association. Thus, I adopt the mean distance of 35 pc to the AB Dor association as the distance to CD-84 0080. The mean age of the AB Dor association is given as 50±25 Myr [Zuckerman & Song, 2004] and I found an age of 30±15 Myr by the EW of Li I (see Section 4.3.3). Therefore, I adopt the range of 30-50 Myr as the age of CD-84 0080. However, estimation of the stellar mass and radius is not possible by applying evolutionary tracks because of the age of CD-84 0080. In addition, no information concerning a circumstellar disk is available.

6.7.1 Radial velocity variation

The RV has been measured (see Section 4.1) and is shown in Figure 6.21 (left panel). The Keplerian fit using GLS yields a period of 5.11 days (FAP <0.1%) and a semi-amplitude of 114.48 ms^{-1}. The peak-to-peak amplitude of the RV variation is 418 ms^{-1}. In Figure 6.21 (right panel) the RV data is shown phase-folded with the 5.11 days period. A scatter around the Keplerian fit remains, which has been analysed by computing the RV residuals after subtraction of the 5.11 days period. However, the residuals show no significant variability.

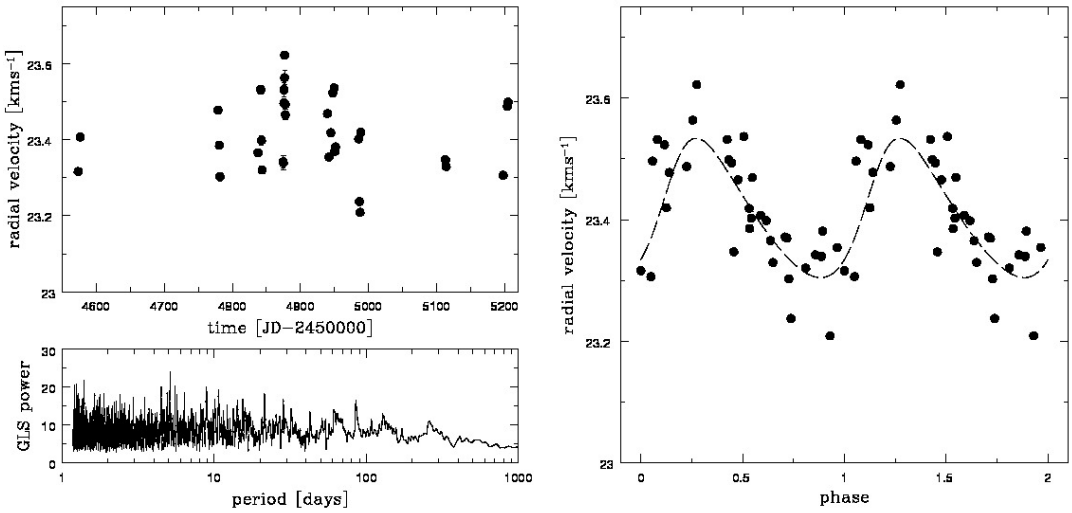

FIGURE 6.21 : Radial velocity variation of CD-84 0080 - variation over time and phase-folded with 5.11 days.

TABLE 6.20 : Periods of stellar activity indicators, photometric data, RV, the FAP of the period, and the amplitude for CD-84 0080. I list further the accuracy of a single measurement σ_{meas} and mark the significant periods.

Activity indicator	Period [days]	FAP	Significance	Semi-amplitude	σ_{meas}
Stellar activity					
BVS	5.12	57%	...	749.49 ms^{-1}	8–15 ms^{-1}
V I/Fe I LDR	3.95	99%	...	0.05	0.004
Hα	54.4	10%	...	126.11 mÅ	15 mÅ
S_{FEROS}	7.3	41%	...	0.08	0.03
Ca II λ 8662	70.3	5%	...	66.06 mÅ	12 mÅ
Radial Velocity	5.11	<0.1%	significant	114.48 ms^{-1}	6–10 ms^{-1}

6.7.2 Analysis of stellar activity

For CD-84 0080 no photometric observations are available. Therefore, no stellar rotation period could be derived for this target. However, by the analysis of stellar activity indicators the source of the RV variation can be identified.

6.7.2.1 Bisector analysis

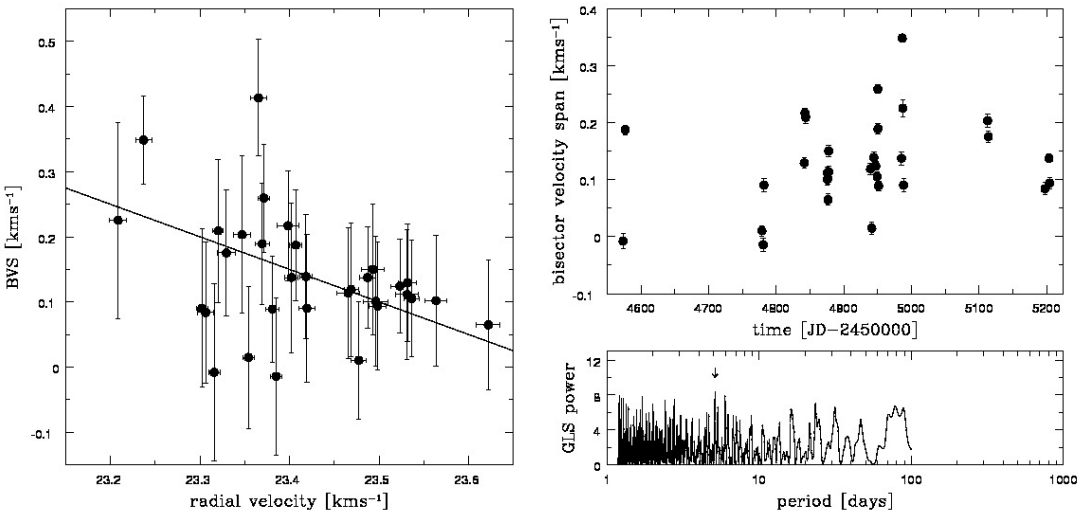

FIGURE 6.22 : Bisector velocity span for CD-84 0080 - BVS vs. RV and time variance

The BVS, BC, and BVD have been calculated (see Section 4.1.2) for CD-84 0080 and the dependence of the BVS on the RV data is shown in Figure 6.22 (left panel). A significant negative correlation can be identified with a slope of -0.5 for the linear regression to the data. In addition, the correlation coefficient yields r=0.5 (25%) and the probability that the BVS and the RV data do not correlate is T=0.02%. Therefore, the RV variation is most likely caused by changes in line shape symmetry. Note that the BC and BVD show a similar behaviour with RV. The variation of the BVS over time is shown in the right panel of Figure 6.22. The analysis with GLS yields a period of 5.12 days for the BVS variation, although with a FAP of 57%. However, this period is similar to the period of the RV variation. This supports the result that the RV variation is caused by rotational modulation due to stellar activity. Unfortunately, I was not able to estimate the RV jitter induced by stellar activity because photometric measurements are not available.

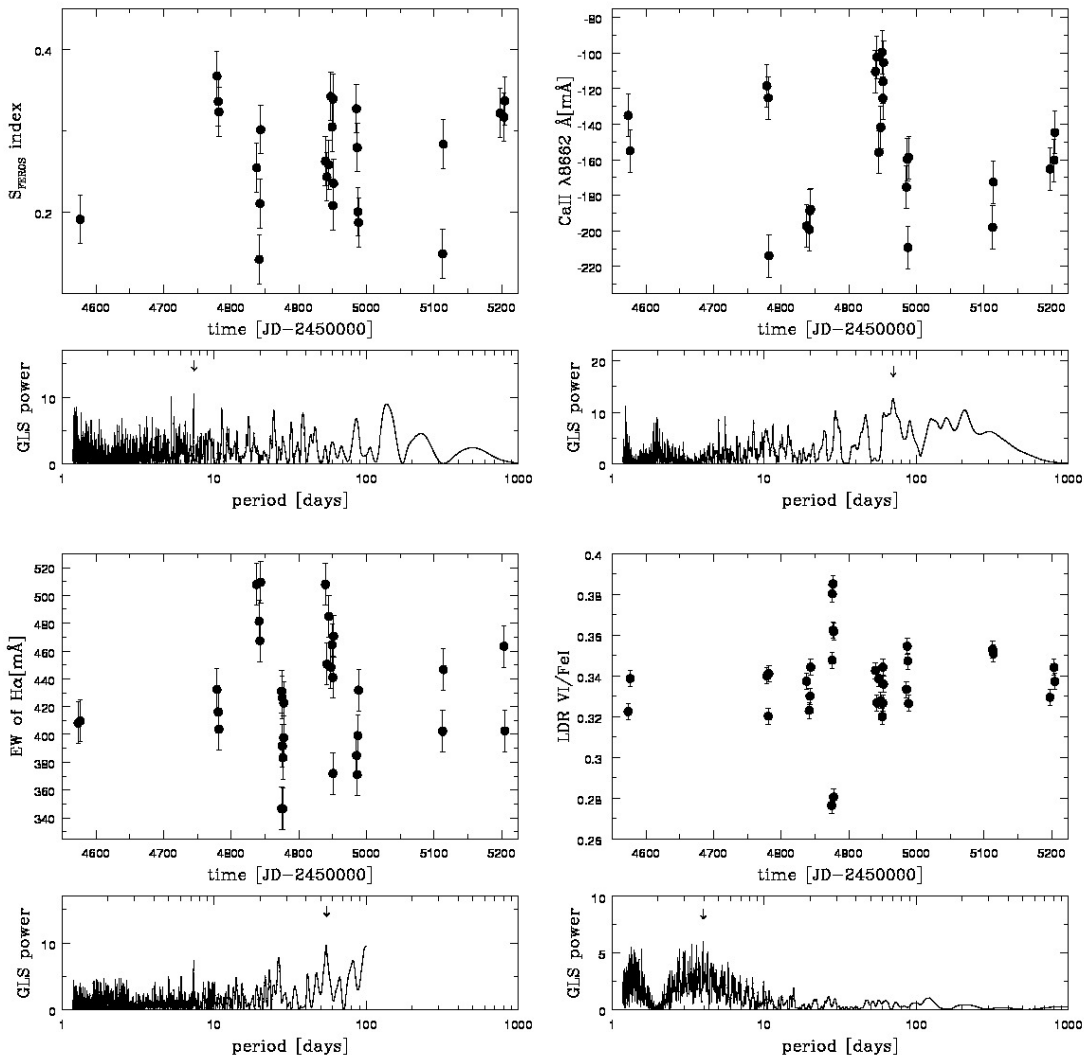

FIGURE 6.23 : Activity indicators for CD-84 0080 - S_{FEROS}, Ca II IRT λ 8662, Hα EW, and LDR V I/Fe I.

TABLE 6.21 : Keplerian fit to the RV data of CD-84 0080.

Parameter	Value	Method
Period	5.11 days	GLS
FAP	<0.1%	GLS
Amplitude K	114.48±5 ms^{-1}	GLS
Eccentricity e	0.2±0.09	GLS
Periastron passage	4574±20 HJD	GLS
Longitude of periastron ω	299±10°	GLS
Offset RV	23.41±0.02 kms^{-1}	GLS
rms of residuals	60 ms^{-1}	GLS

6.7.2.2 Other stellar activity indicators

I also analysed the other stellar activity indicators, S_{FEROS}, EW of Ca II λ 8662, LDR of V I/Fe I, and EW of Hα for periodicity. The periods derived by the analysis with GLS are listed in Table 6.23. Two indicators, S_{FEROS} and LDR V I/Fe I, show a short period in the range of 3.95–7.3 days, albeit with high FAP > 40%. The other two indicators, Ca II IRT and Hα, show longer periods in the range of 54.4–70.3 days, also with FAP = 5–10%. The periods of these indicators are not significant and no conclusions can be made concerning the source or reliability of these periods. However, S_{FEROS} and LDR V I/Fe I vary with a period similar to the RV variation. This supports the result that the RV variation is caused by stellar activity.

6.7.3 Summary for CD-84 0080

CD-84 0080 shows a RV variation with a period of 5.11 days and a semi-amplitude of 114.48 ms^{-1}. The BVS shows a significant negative correlation with the RV data and the probability that the BVS does not correlate with the RV data is below the threshold used (see Section 6.1.2.2). Furthermore, the other activity indicators vary with periods similar to the period of the RV variation. Therefore, the RV variation is caused by rotational modulation due to stellar activity and a companion as the source of the RV variation is unlikely. However, a planetary signal might hide with a smaller amplitude in the RV variation. Therefore, I analysed the residuals of the RV, but the residuals show no significant variation.

TABLE 6.22 : Basic parameters for EG Cha

Parameter	Value	Method/Reference
Identifier	EG Cha	...
Coordinates	08 36 56 -78 56 46	SIMBAD
Spectral type	K4V	Zuckerman & Song [2004]
V magnitude	10.6 mag	SIMBAD
Distance	97 pc	Zuckerman & Song [2004]
$M_\star$	1.8±0.1 $M_\odot$	Sicilia-Aguilar *et al.* [2009]
T_{eff}	5260±130 K	*TGV*, this study
log g	5.6±0.5 cms^{-2}	*TGV*, this study
[Fe/H]	-0.01±0.10	*TGV*, this study
EW of Li I	510±6 mÅ	this study
Age	5±2 Myr	Li I measurements, this study
Age	8±5 Myr	Zuckerman & Song [2004]
$v \sin i$	21.4±1.3 kms^{-1}	this study
R'_{FEROS}	-4.02	this study
Number of observations	11	...

6.8 EG Cha

EG Cha is a binary system with a system mass of 2 $M_\odot$ [Köhler & Petr-Gotzens, 2002] and a mass-ratio of 0.1 [Sicilia-Aguilar *et al.*, 2009]. Therefore, I adopt 1.8 $M_\odot$ as the mass of EG Cha. The separation between both components is 10 AU [Köhler, 2001] and the effect of this companion on the RV data is negligible for the time-span of the observations. The derived stellar parameters are listed in Table 6.22. The values for T_{eff} and log g are higher than expected for a K4-type star, which might be because both components of the binary system contribute to the EW of the Fe I and Fe II lines. The age of EG Cha has been derived to be 5±2 Myr by measurements of Li I EW and the mean age of the η Cha association is 8±5 Myr. However, these values agree within the error-bars. EG Cha has been analysed for the presence of a circumstellar disk, but no circumstellar disk has been identified (e.g., Sicilia-Aguilar *et al.* [2009]).

6.8.1 Radial velocity variation

The RV has been measured as described in Section 4.1 and is presented in Figure 6.24 (left panel). An analysis with GLS yields a period for the RV variation of 2.38 days (FAP=13%) and a semi-amplitude of 1 016.92 ms^{-1}. The peak-to-peak amplitude is 2 100 ms^{-1} and similar to the amplitude derived by the Keplerian fit. In the right panel of Figure 6.24, the RV data phase-folded with the 2.38 days period is shown.
The stellar companion does not affect the RV measurements due to the short time-span of observations compared to the period of the stellar companion.

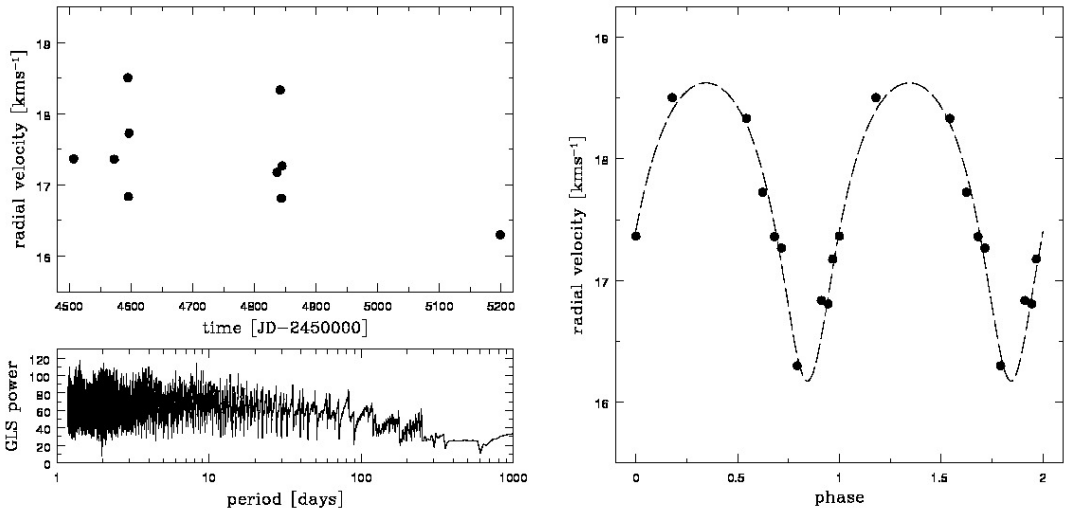

FIGURE 6.24 : Radial velocity variation of EG Cha - variation over time and phase-folded with 2.38 days.

TABLE 6.23 : Periods of stellar activity indicators, photometric data, RV, the FAP of the period, and the amplitude for EG Cha. I list further the accuracy of a single measurement σ_{meas} and mark the significant periods.

Activity indicator	Period [days]	FAP	Significance	Semi-amplitude	σ_{meas}
Stellar activity					
BVS	1.26	2.5%	...	1311 ms^{-1}	10–33 ms^{-1}
V I/Fe I LDR	5.99	1%	significant	0.03	0.01
Hα	19.5	3%	...	918.47 mÅ	15 mÅ
S_{FEROS}	2.79	9%	...	0.49	0.03
Ca II λ 8662	2.05	4%	...	126.26 mÅ	12 mÅ
Photometric variation	2.2	...	significant	0.04 mag	...
Radial Velocity	2.38	13%	...	1016.92 ms^{-1}	23–54 ms^{-1}

6.8.2 Analysis of stellar activity

For EG Cha photometric observations are available and a rotational period of 2.2 days with an amplitude of $\Delta V = 0.08$ mag has been measured by Lawson *et al.* [2001]. This period is close to the period of the RV variation. This speaks for rotational modulation due to stellar activity as the source of the RV variation.

6.8.2.1 Bisector analysis

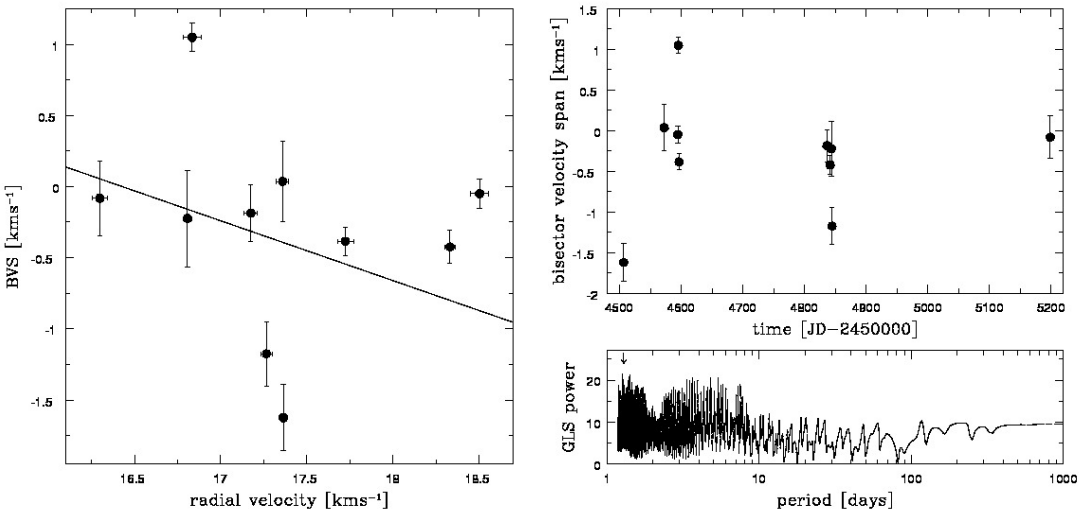

FIGURE 6.25 : Bisector velocity span for EG Cha - BVS vs. RV and time variance

The BVS, BC, and BVD have been measured as described in Section 4.1.2. The correlation between BVS and RV is shown in Figure 6.25 (left panel). The correlation coefficient yields r=0.42 (18%) and the slope of a linear regression to the data is -0.42. However, the scatter of the data around the linear regression is large and, therefore, the slope is inconclusive. In addition, the probability that both data sets do not correlate is T=15%. The BVS is altered by effects of both stellar activity and the stellar companion. Therefore, the slope of the correlation is not significant.
The variation of the BVS over time is shown in Figure 6.25 (right panel). The analysis yields a period of 1.26 days with a FAP=2.5%. This period is approximately the half of the rotational period. This effect is most likely caused by two surface spots, separated by 180°, which emerged since the photometric observations have been obtained.
I calculate the expected RV jitter due to stellar activity as described in Section 4.2.1. The spot-filling factor f_s can be calculated from the photometric amplitude to 1.6% and, therefore, the expected RV jitter can be calculated to 361 and 479 ms^{-1} by using Equations (4.11) and (4.14), respectively. Note that this is calculated for a single equatorial spot on a face-on star. This simple model can not account for the total

amplitude of the RV variation.

6.8.2.2 Other stellar activity indicators

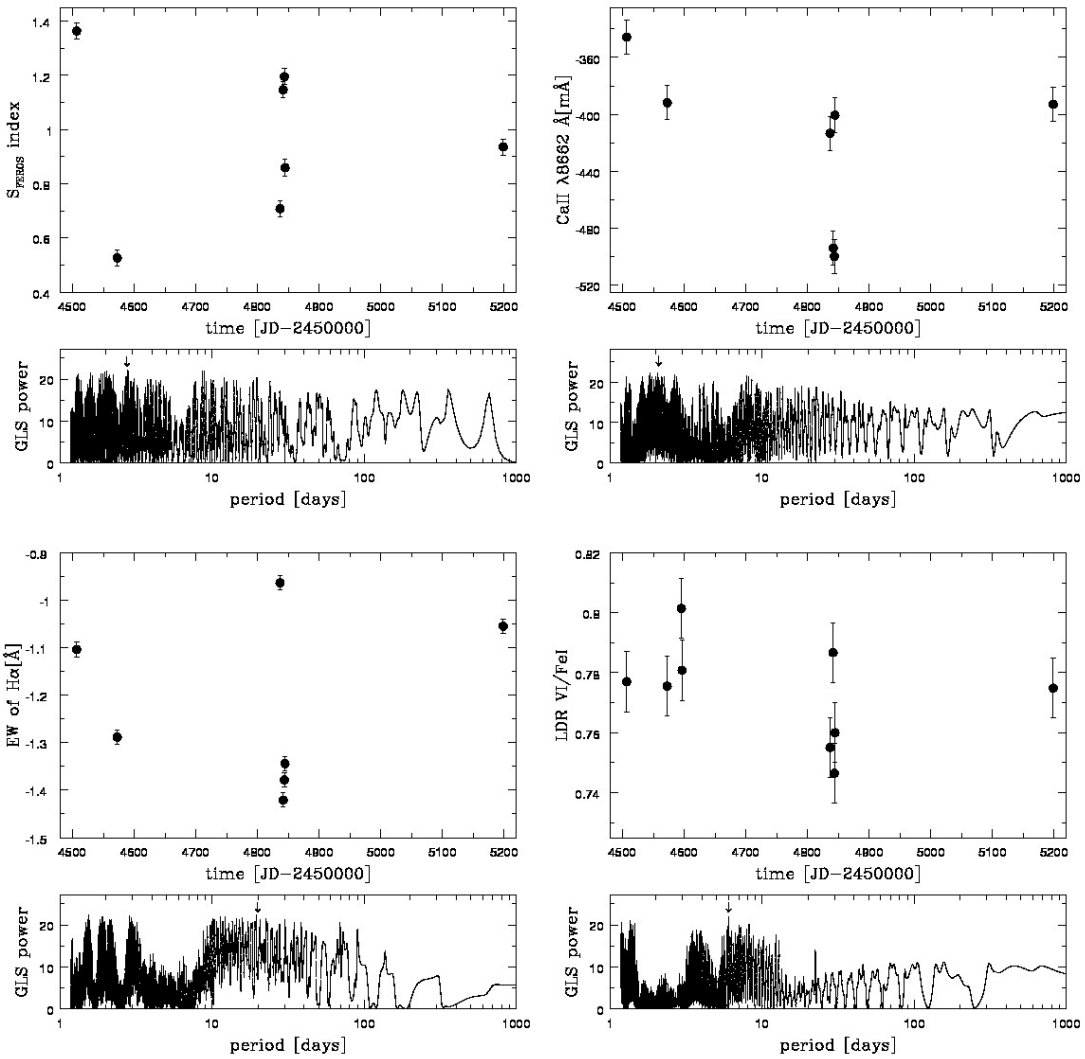

FIGURE 6.26 : Activity indicators for EG Cha - S_{FEROS}, Ca II IRT λ 8662, Hα EW, and LDR V I/Fe I.

The variation of the other activity indicators, S_{FEROS}, EW of Ca II λ 8662, LDR of V I/Fe I, and EW of Hα, is shown in Figure 6.26. The analysis with GLS yields short periods for three indicators (except Hα) in the range of 2–6 days. The longer period for Hα of 19.5 days is most likely a false detection due to the low number of observations. The periodogram also shows peaks at shorter periods. However, the short periodicity of the activity indicators show that the RV variation is most likely induced by stellar activity.

TABLE 6.24 : Keplerian fit to the RV data of EG Cha.

Parameter	Value	Method
Period	2.38 days	GLS
FAP	13%	GLS
Amplitude K	1016.92±10 ms^{-1}	GLS
Eccentricity e	0.4±0.09	GLS
Periastron passage	4508±20 HJD	GLS
Longitude of periastron ω	180±10°	GLS
Offset RV	12.25±0.02 kms^{-1}	GLS
rms of residuals	140 ms^{-1}	GLS

6.8.3 Summary for EG Cha

EG Cha shows a RV variation with a period of 2.38 days and a semi-amplitude of the Keplerian fit of 1 061.92 ms^{-1} (see Table 6.24). With the obtained data, no significant conclusion on the source of the RV variation can be made. The BVS shows an insignificant correlation on RV, which is either due to stellar activity or the stellar companion. The stellar rotation period (2.2 days) and the variability of the other stellar activity indicators are in the similar range as the period of the RV variation. However, the RV jitter amplitude induced by stellar activity is lower than the RV amplitude.
In the case of a planetary companion as the source of the RV variation, the activity of EG Cha can also be induced by star-planet-interactions (see Section 6.3.3), However, more data is needed to verify this. Therefore, I adopt rotational modulation due to stellar activity as the most likely source of the RV variation of EG Cha.

TABLE 6.25 : Basic parameters for TYC 7697-2254-1

Parameter	Value	Method/Reference
Identifier	TYC 7697-2254-1	...
Coordinates	09 47 20 -40 03 10	SIMBAD
Spectral type	K0V	Torres *et al.* [2006]
V magnitude	10.9 mag	Torres *et al.* [2006]
Distance	100 pc	Torres *et al.* [2008]
$T_{\rm eff}$	5410±40 K	*TGV*, this study
$\log g$	4.86±0.1 cms^{-2}	*TGV*, this study
[Fe/H]	0.05±0.09	*TGV*, this study
EW of Li I	240±4 mÅ	this study
Age	25±10 Myr	Li I measurements, this study
Age	40 Myr	Torres *et al.* [2008]
$v \sin i$	9.0±0.4 kms^{-1}	this study
$R'_{\rm FEROS}$	-4.21	this study
Number of observations	18	...

6.9 TYC 7697-2254-1

TYC 7697-2254-1 is a K0V type star with V=10.9 mag [Torres *et al.*, 2006] and has been analysed in detail by Viana Almeida *et al.* [2009]. The basic stellar parameters derived in this study (see Table 6.25) agree well with the values obtained by Viana Almeida *et al.* [2009]. They assign TYC 7697-2254-1 as a member of the Argus association, located at a distance of 100 pc [Torres *et al.*, 2008]. The age of this association has been set to 40 Myr [Torres *et al.*, 2008], whereas I derive an age from the Li I EW of 25±10 Myr. The stellar mass and radius can not be estimated by using evolutionary tracks because TYC 7697-2254-1 is no PMS star. Furthermore, no information about a circumstellar disk is available.

6.9.1 Radial velocity variation

The measured RV variation (see Section 4.1) is shown in Figure 6.27 (left panel). The analysis with GLS yields a period of 17.45 days with a FAP of 15%. The semi-amplitude of the Keplerian fit to the data is 255.35 ms^{-1} and the peak-to-peak amplitude of the variation is 542 ms^{-1}. The Keplerian fit (see Table 6.27) is also shown in the left panel of Figure 6.27 (dashed line). In the right panel of this figure, the RV data is shown phase-folded with the 17.45 days period. The RV measurements cover only part of the phase, which is most likely the reason for the FAP = 15% of the derived period.

6.9.2 Analysis of stellar activity

In this section, I analyse the stellar activity indicators for TYC 7697-2254-1. Unfortunately, no photometric observations are available for this star and no rotation period and estimated RV jitter can be derived.

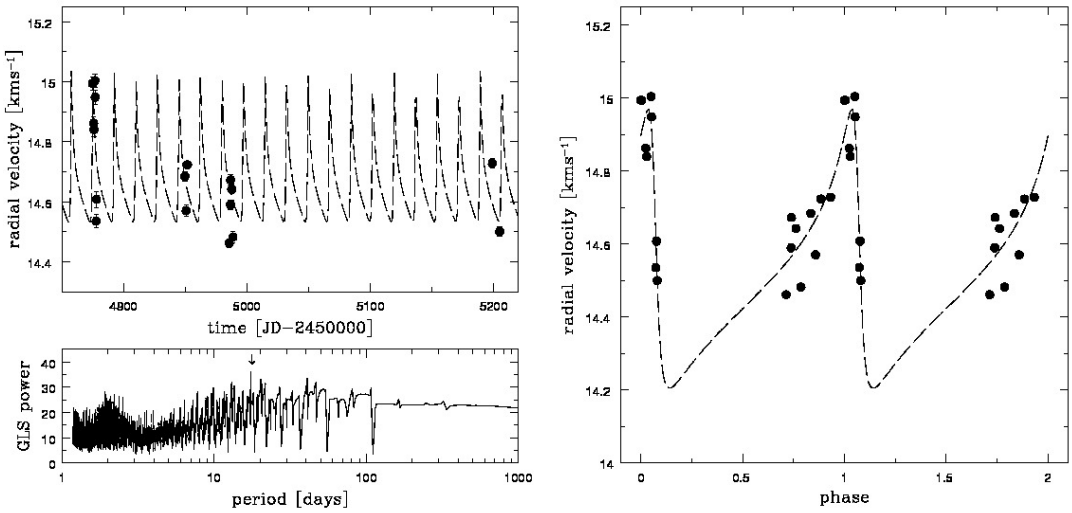

FIGURE 6.27 : Radial velocity variation of TYC 7697-2254-1 - variation over time and phase-folded with 17.45 days. The dashed line is the Keplerian fit to the data.

TABLE 6.26 : Periods of stellar activity indicators, photometric data, RV, the FAP of the period, and the amplitude for TYC 7697-2254-1. I list further the accuracy of a single measurement σ_{meas} and mark the significant periods.

Activity indicator	Period [days]	FAP	Significance	Semi-amplitude	σ_{meas}
Stellar activity					
BVS	24.7	35%	...	354.59 ms^{-1}	10–14 ms^{-1}
V I/Fe I LDR	2.7	71%	...	0.28	0.01
Hα	5.5	3%	...	156.49 mÅ	15 mÅ
S_{FEROS}	11.6	65%	...	0.43	0.03
Ca II λ 8662	2.83	32%	...	111.81 mÅ	12 mÅ
Radial Velocity	17.45	15%	...	255.35 ms^{-1}	12–24 ms^{-1}

6.9.2.1 Bisector analysis

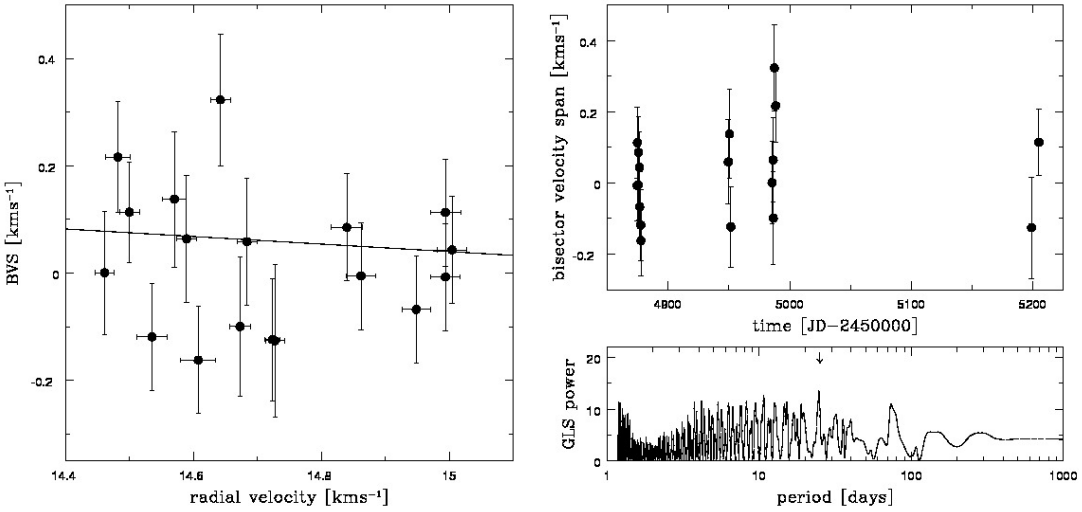

FIGURE 6.28 : Bisector velocity span for TYC 7697-2254-1 - BVS vs. RV and time variance

The BVS, BC and BVD have been calculated (Section 4.1.2) and the dependence of BVS on RV is shown in Figure 6.28 (left panel). The correlation coefficient yields r=0.11 (1.2%) and the probability that the BVS and the RV are not correlated is T=64%. The linear regression to the BVS vs. RV data shows a slope of -0.07. However, the scatter of the data around the linear regression is large and no significant conclusion on the slope can be made. The time dependence of the BVS is shown in Figure 6.28 (right panel) and the analysis yields an insignificant period of 24.7 days (FAP = 35%).

6.9.2.2 Other stellar activity indicators

The variations of the other activity indicators, S_{FEROS}, EW of Ca II λ 8662, LDR of V I/Fe I, and EW of Hα, are shown in Figure 6.26. The analysis with GLS yields periods between 2.7–11.6 days (see Table 6.26), none of which is significant (FAP = 3–71%). However, no stellar activity indicator analysed show a period comparable to that of the RV variation.

6.9.3 Summary for TYC 7697-2254-1

The RV of TYC 7697-2254-1 varies with a period of 17.45 days and a semi-amplitude of 255.25 ms^{-1} (see Table 6.27). The bisector shows no correlation with RV and no stellar activity indicator varies with a period comparable to that of the RV variation. The derived periods for the RV and stellar activity indicators are all insignificant and further observations are needed to verify the results derived here.

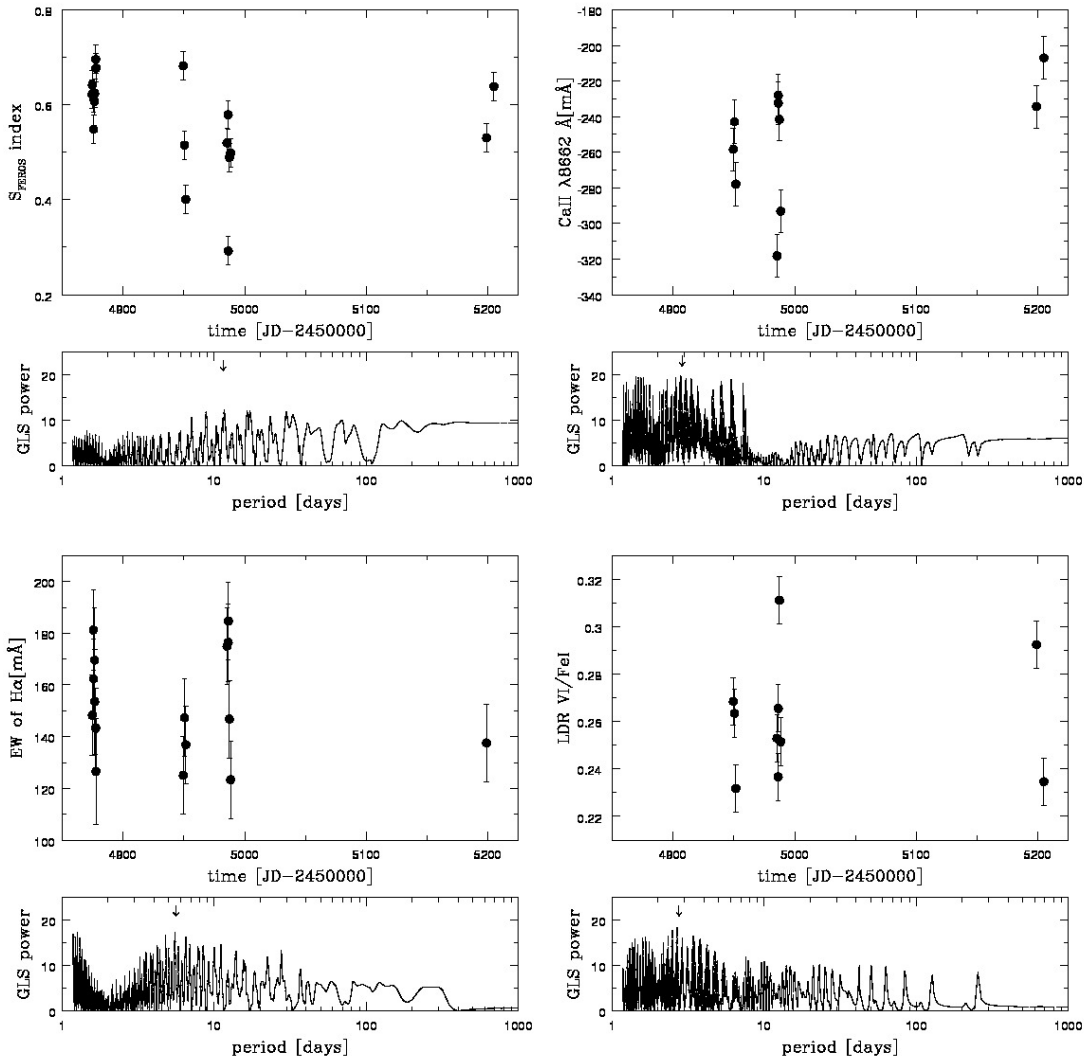

FIGURE 6.29 : Activity indicators for TYC 7697-2254-1 - $S_{\rm FEROS}$, Ca II IRT λ 8662, Hα EW, and LDR V I/Fe I.

TABLE 6.27 : Keplerian fit to the RV data of TYC 7697-2254-1.

Parameter	Value	Method
Period	17.45 days	GLS
FAP	15%	GLS
Amplitude K	255.35±10 $\rm ms^{-1}$	GLS
Eccentricity e	0.75±0.12	GLS
Periastron passage	4877±10 HJD	GLS
Longitude of periastron ω	70±5°	GLS
Offset RV	14.50±0.03 $\rm kms^{-1}$	GLS
rms of residuals	79 $\rm ms^{-1}$	GLS

I assume a stellar mass of $1\,M_{\odot}$ for TYC 7697-2254-1, which is predicted for young K0 type stars, and calculate the minimum mass of the companion. For this, I get $m_p \sin i = 2.15\,M_{\mathrm{Jup}}$ and an orbital distance of 0.13 AU to the star.

TABLE 6.28 : Basic parameters for DI Cha

Parameter	Value	Method/Reference
Identifier	Di Cha	...
Coordinates	11 07 21 -77 38 07	SIMBAD
Spectral type	G2V	Guenther *et al.* [2007]
V magnitude	10.9 mag	Guenther *et al.* [2007]
Distance	160 pc	Whittet *et al.* [1997]
$M_\star$	2.57 $M_\odot$	Lafrenière *et al.* [2008]
$T_{\rm eff}$	5820±80 K	*TGV*, this study
$\log g$	4.0±0.2 cms^{-2}	*TGV*, this study
[Fe/H]	0.18±0.13	*TGV*, this study
EW of Li I	260±1 mÅ	this study
Age	5±2 Myr	Li I measurements, this study
Age	2 Myr	Luhman [2004]
$v \sin i$	38.1±2.2 kms^{-1}	this study
$R'_{\rm FEROS}$	-4.46	this study
Number of observations	46	...

6.10 DI Cha

DI Cha is a G2 type star with V=10.9 mag [Guenther *et al.*, 2007]. It is a triple system with a separation of 4.9'' between DI Cha and its companion, which is a binary [Ghez *et al.*, 1997; Lafrenière *et al.*, 2008]. However, the period of the binary companion is ~12 000 years and the effect is not measurable in the radial velocity data. DI Cha still accretes matter from its circumstellar disk (see Section 5.1.3). The age derived by the Li I EW is 5±2 Myr (see Section 4.3.3) and the age of the Cha I association has been found to be 2 Myr [Luhman, 2004]. Thus, I adopt the range of 2–5 Myr as the age of DI Cha. The age and the derived stellar parameters are listed in Table 6.28. The stellar parameters agree well with the results from Lafrenière *et al.* [2008]. They also derive a stellar mass of 2.57 $M_\odot$ from evolutionary tracks. Note that DI Cha has a slightly enhanced metallicity compared to the Sun.

6.10.1 Radial velocity variation

The RV variation is shown in Figure 6.30 (left panel). The peak-to-peak variation is 4 140.88 ms^{-1}. The analysis with GLS yields that the RV varies with a significant period of 2.61 days (FAP<0.1%) and a semi-amplitude of 948.35 ms^{-1} (see Table 6.30). In the right panel of Figure 6.30, the RV data is shown phase-folded with the 2.61 days period. A scatter of 770 ms^{-1} around the Keplerian fit is left. The analysis of the RV residuals (after subtraction of the 2.61 days period) yields a variation with a period of 2.43 days and a semi-amplitude of 758 ms^{-1} (see Table 6.30).

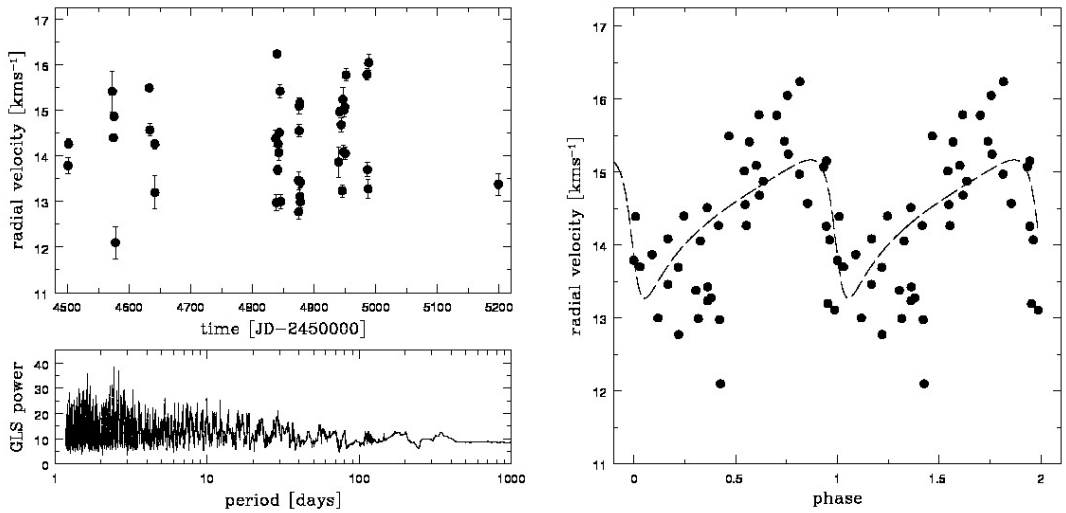

FIGURE 6.30 : Radial velocity variation of DI Cha - variation over time and phase-folded with 2.61 days.

TABLE 6.29 : Periods of stellar activity indicators, photometric data, RV, the FAP of the period, and the amplitude for DI Cha. I list further the accuracy of a single measurement $\sigma_{\rm meas}$ and mark the significant periods.

Activity indicator	Period [days]	FAP	Significance	Semi-amplitude	$\sigma_{\rm meas}$
Stellar activity					
BVS	7.1	5%	...	6789.71 ms^{-1}	10–330 ms^{-1}
V I/Fe I LDR	1.27	4%	...	0.26	0.03
Hα	10.4	80%	...	6.52 Å	0.15 Å
$S_{\rm FEROS}$	22.48	16%	...	0.27	0.03
Ca II λ 8662	1.2	5%	...	114.82 mÅ	12 mÅ
Photometric variation	1.32±0.1	<0.1%	significant	0.06 mag	0.03 mag
Radial Velocity	2.61	<0.1%	significant	948.35 ms^{-1}	77–330 ms^{-1}
RV residuals	2.43	<0.1%	significant	758 ms^{-1}	77–330 ms^{-1}

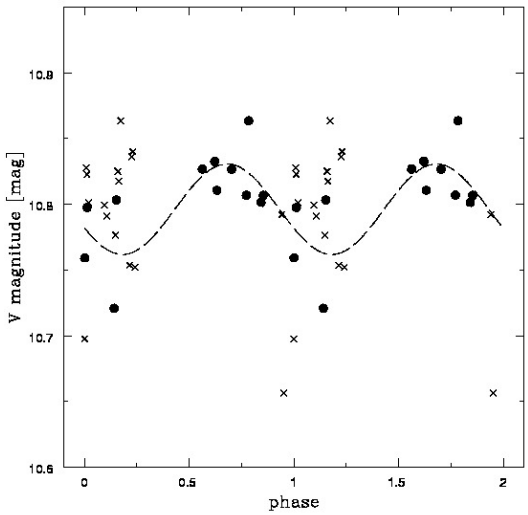

FIGURE 6.31 : Photometric variation of DI Cha - Shown is the photometric data from Hipparcos, phase-folded with 1.32 days for two different observing periods. With dots: Observations during JD 7919–7972, in crosses: observations during JD 8005–8095. Both show the same periodicity, but different phases.

6.10.2 Analysis of stellar activity

For DI Cha photometric observations are available from Hipparcos [van Leeuwen & Evans, 1998]. These observations span 1 160 days, but the analysis of the whole data set revealed no significant period for the photometric variation. This can be due to changing spot configurations over the time-span of the observations. Because new spots emerge and old spots disperse, the phase of the photometric variation gets shifted between the individual observing blocks and, therefore, the period of the variation can not be identified in the whole data set. Therefore, I analysed each observing block of ~100 days individually and found a period of 1.32±0.1 days in each of these blocks. Thus, I adopt 1.32±0.1 days as the rotation period of DI Cha with an amplitude of 0.12 mag. To illustrate the phase-shifts that occur between individual observing blocks, I show the photometric data of two observing blocks phase-folded with the 1.32 days period in Figure 6.31. To guide the eye, the sine-fit to the data of the first observing block (dots) is also shown. The data of the second observing block (crosses) is shifted by a quarter phase relative to the data of the first observing block (dots).

6.10.2.1 Bisector analysis

The dependence of the BVS on the RV data is shown in Figure 6.32 (left panel). A significant correlation can not be found. The correlation coefficient is r=0.11 (1.2%).

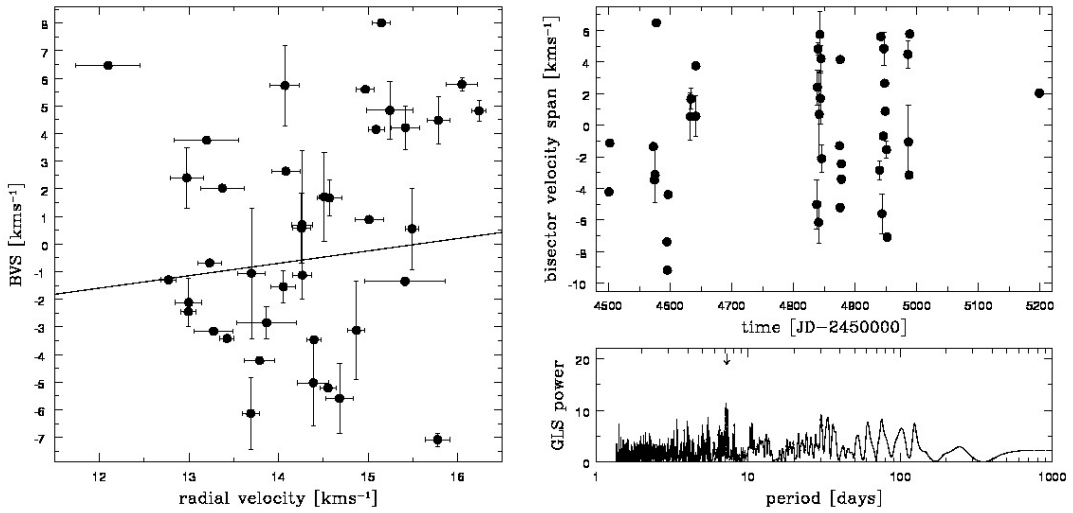

FIGURE 6.32 : Bisector velocity span for DI Cha - BVS vs. RV and time variance

The slope of the linear regression is inconclusive for the BVS vs. RV data. The best fit gives a slope of 0.45. In addition, the probability that the BVS and RV do not correlate is T=45%. Thus, the BVS is most likely not correlated with the RV. The variation over time of the BVS is shown in the right panel of Figure 6.32. An analysis with GLS yields a period of 7.1 days for the variation (FAP=5%).
I further estimate the expected RV jitter induced by stellar activity as described in Section 4.2.1. As a result, I get an expected RV jitter amplitude of 2 100 and 5 900 ms^{-1}, when using Equations (4.11) and (4.14), respectively. Thus, the simple model of a single spot can account for the measured peak-to-peak amplitude of the RV variation.

6.10.2.2 Other stellar activity indicators

The variations of the other stellar activity indicators, S_{FEROS}, EW of Ca II λ 8662, LDR of V I/Fe I, and EW of Hα, are shown in Figure 6.33. The periods and amplitudes derived by using GLS are summarized in Table 6.29. The periods of Ca II IRT and LDR V I/Fe I are in the range of 1.2–1.27 days, which is identical to the rotational period of DI Cha. The periods of Hα and S_{FEROS} are in the range of 10.4–22.5 days. The variability of these indicators is likely induced by the accretion process.

6.10.3 Summary for DI Cha

DI Cha is a young star (2–5 Myr), which shows high stellar activity. I derived a rotational period for DI Cha of 1.32 days from the photometric data taken by Hipparcos. The RV varies with a period of 2.61 days, which is twice the rotational period. Therefore, the period of the RV variation is likely an alias of the 1.32 days rotational period.

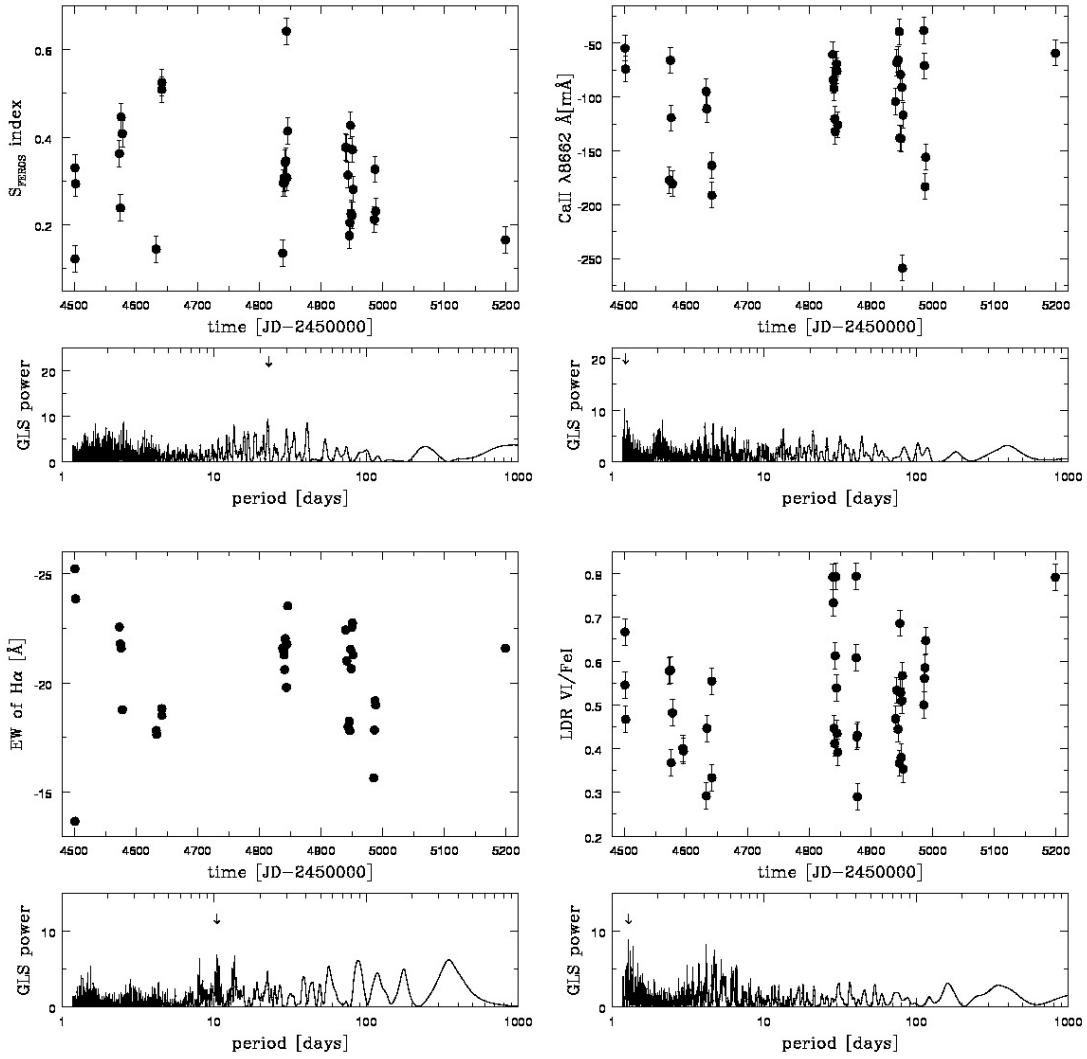

FIGURE 6.33 : Activity indicators for DI Cha - $S_{\rm FEROS}$, Ca II IRT λ 8662, Hα EW, and LDR V I/Fe I.

TABLE 6.30 : Keplerian fit to the RV data of DI Cha.

Parameter	Value	Parameter	Value	Method
Period	2.61 days	P of residuals	2.42	GLS
FAP	<0.1%	FAP	<0.1%	GLS
Amplitude K	948.35±60 ms^{-1}	K of residuals	758.71	GLS
Eccentricity e	0.55±0.08	e of residuals	0.08±0.02	GLS
Periastron passage	4869±10 HJD	T_0 of residuals	4879±10 HJD	GLS
Longitude of periastron ω	113±5°	ω of residuals	105°	GLS
Offset RV	14.42±0.03 kms^{-1}	...	...	GLS
$m_p \sin i$	10.07 $M_{\rm jup}$	$m_p \sin i$ from residuals	9.39 $M_{\rm Jup}$	GLS
a sin i	0.05 AU	a sin i from residuals	0.048 AU	GLS
rms of residuals	777 ms^{-1}	rms of residuals	566 ms^{-1}	GLS

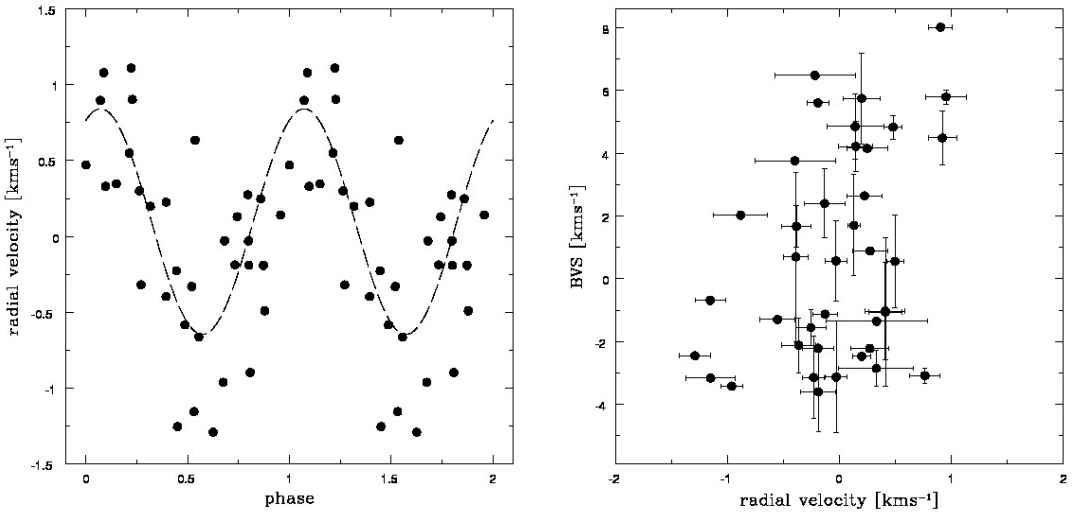

FIGURE 6.34 : Analysis of RV residuals for DI Cha - left panel: RV residuals phase-folded with 2.43 days. Right panel: BVS vs. RV residuals.

However, the correlation between BVS and RV is inconclusive, but the probability that the BVS and RV do not correlate is 45%. However, the source of the RV variation with the 2.63 days is most likely rotational modulation due to stellar activity.
The analysis of the RV variations (after subtraction of the 2.63 days period) yields a period of 2.43 days. In Figure 6.34, the RV residuals are shown phase-folded with the 2.43 days period (left panel). In the right panel, the correlation of BVS on the RV residuals is shown. A positive correlation is significant. Thus, the source of the RV residuals variation is most likely a sub-stellar companion. The mass of this companion is $m_p \sin i = 9.39\,\mathrm{M_{Jup}}$ and the orbital distance is 0.048 AU.
However, more data is needed to verify this result, but it shows that planetary companions can be detected around stars with an age of 2–5 Myr.

TABLE 6.31 : Basic parameters for T Cha.

Parameter	Value	Method/Reference
Identifier	T Cha	...
Coordinates	11 57 13 -79 21 32	SIMBAD
Spectral type	G4V	Torres *et al.* [2006]
V magnitude	11.5 mag	Torres *et al.* [2006]
Distance	100 pc	Schisano *et al.* [2009]
$M_\star$	1.5	Brown *et al.* [2007]
$R_\star$	1.0 $R_\odot$	Brown *et al.* [2007]
$T_{\rm eff}$	5695±235 K	*TGV*, this study
$\log g$	5.0±0.5 cms^{-2}	*TGV*, this study
[Fe/H]	0.15±0.13	*TGV*, this study
EW of Li I	382±1 mÅ	this study
Age	4±2 Myr	Li I measurements, this study
$v \sin i$	40.0±2.7 kms^{-1}	this study
$R'_{\rm FEROS}$	-4.55	this study
Number of observations	23	...

6.11 T Cha

T Cha is a young G4V type star with V=11.5 mag [Torres *et al.*, 2006]. It shows a strong photometric variability and variation in the Hα line ranging from pure photospheric absorption to emission [Schisano *et al.*, 2009]. Furthermore, T Cha exhibits a thick circumstellar disk with a nearly gas-free inner region of 15 AU [Brown *et al.*, 2007]. The basic stellar parameters measured in this study are summarized in Table 6.31 and agree well with the values derived by Brown *et al.* [2007].

6.11.1 Radial velocity variation

The RV variation (see Section 4.1) is shown in the left panel of Figure 6.35. The analysis with GLS yields a significant period of 3.60 days for the RV variation (FAP < 0.1%) and a semi-amplitude of 2 579.62 ms^{-1}. The peak-to-peak amplitude of the RV variation is 4 833 ms^{-1}. In the right panel of Figure 6.35, the RV data is shown phase-folded with the 3.6 days period. A small scatter around the Keplerian fit is present. However, the analysis of the variability of RV residuals (after subtraction of the 3.6 days period) yields no clear periodicity.

6.11.2 Analysis of stellar activity

The stellar rotation period of 3.2±0.2 days has been determined from photometric observations by Schisano *et al.* [2009]. The amplitude is ΔV = 1.5 mag. The derived period is close to that of the RV variation (3.6 days). Thus, the RV variation is most likely induced by rotational modulation due to stellar surface spots.
The expected RV jitter induced by stellar surface spots (see Section 4.2.1) can be es-

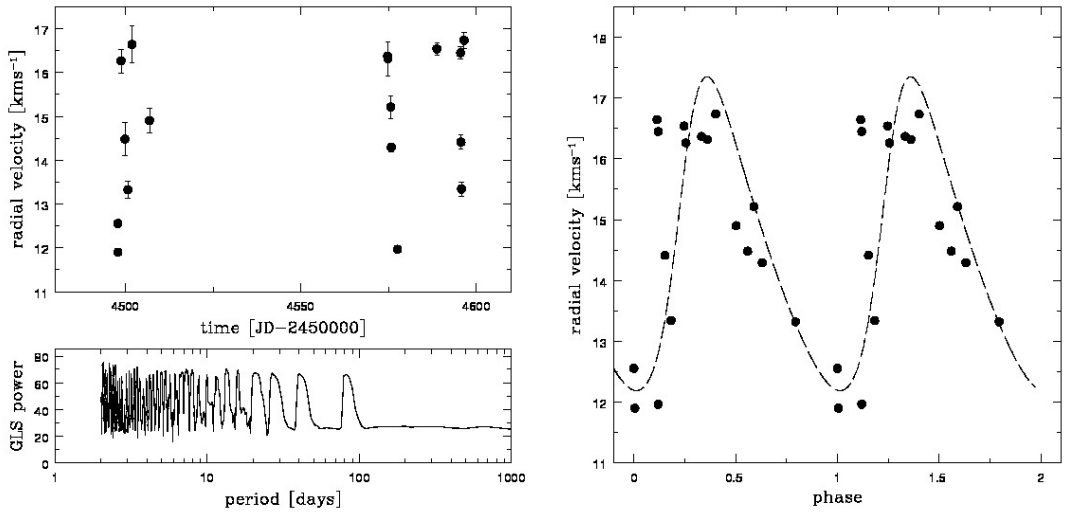

FIGURE 6.35 : Radial velocity variation of T Cha - variation over time and phase-folded with 3.60 days.

TABLE 6.32 : Periods of stellar activity indicators, photometric data, RV, the FAP of the period, and the amplitude for T Cha. I list further the accuracy of a single measurement $\sigma_{\rm meas}$ and mark the significant periods.

Activity indicator	Period [days]	FAP	Significance	Semi-amplitude	$\sigma_{\rm meas}$
Stellar activity					
BVS	1.33	2%	...	3131.65 ms^{-1}	10–170 ms^{-1}
V I/Fe I LDR	55.3	2%	...	0.09	0.02
Hα	15.98	11%	...	1866.07 mÅ	12 mÅ
$S_{\rm FEROS}$	1.28	7%	...	0.40	0.04
Ca II λ 8662	1.36	46%	...	114.56 mÅ	12 mÅ
Photometric variation	3.2±0.2	...	significant	0.75 mag	0.02 mag
Radial Velocity	3.60	<0.1%	significant	2579.62 ms^{-1}	60–430 ms^{-1}

timated to 10.39 kms^{-1} (according to Equation 4.11) and 27.77 kms^{-1}, according to Equation (4.14). This simple model of a single equatorial spot predicts a larger RV variation than it is actually measured.

6.11.2.1 Bisector analysis

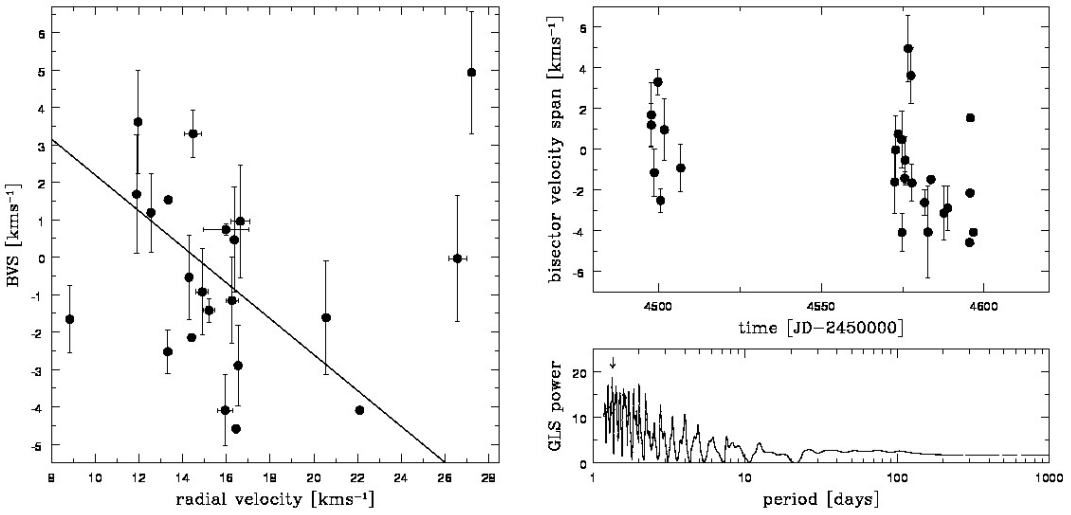

FIGURE 6.36 : Bisector velocity span for T Cha - BVS vs. RV and time variance

The correlation of BVS and RV is shown in the left panel of Figure 6.36. The correlation coefficient is r=0.3 (9%) and the probability that both do not correlate T=0.9%. Furthermore, the linear regression to the data yields a negative slope of -0.48. Thus, the bisector significantly correlates with the RV data. Note that the BC and BVD show a similar behaviour, i.e., correlate with RV.
The time dependence of the BVS is shown in Figure 6.36 (right panel). The analysis with GLS yields a period of 1.33 days for the variation (FAP = 2%). However, the CCF calculated for T Cha is noisy due to the variable veiling of this star (see Section 4.1.1). Thus, the measurement of the BVS is inaccurate, which most likely results in an irregular variation of the BVS.

6.11.2.2 Other stellar activity indicators

The variability of the other stellar activity indicators, S_{FEROS}, EW of Ca II λ 8662, LDR of V I/Fe I, and EW of Hα, is shown in Figure 6.37 and the periods, obtained from the analysis with GLS, are presented in Table 6.32. All indicators show no significant periods and no conclusions can be made. This is also most likely due to the variability of the veiling, which affects all measurements of the EW (Section 4.3.4, and yields the irregular variation of the stellar activity indicators.

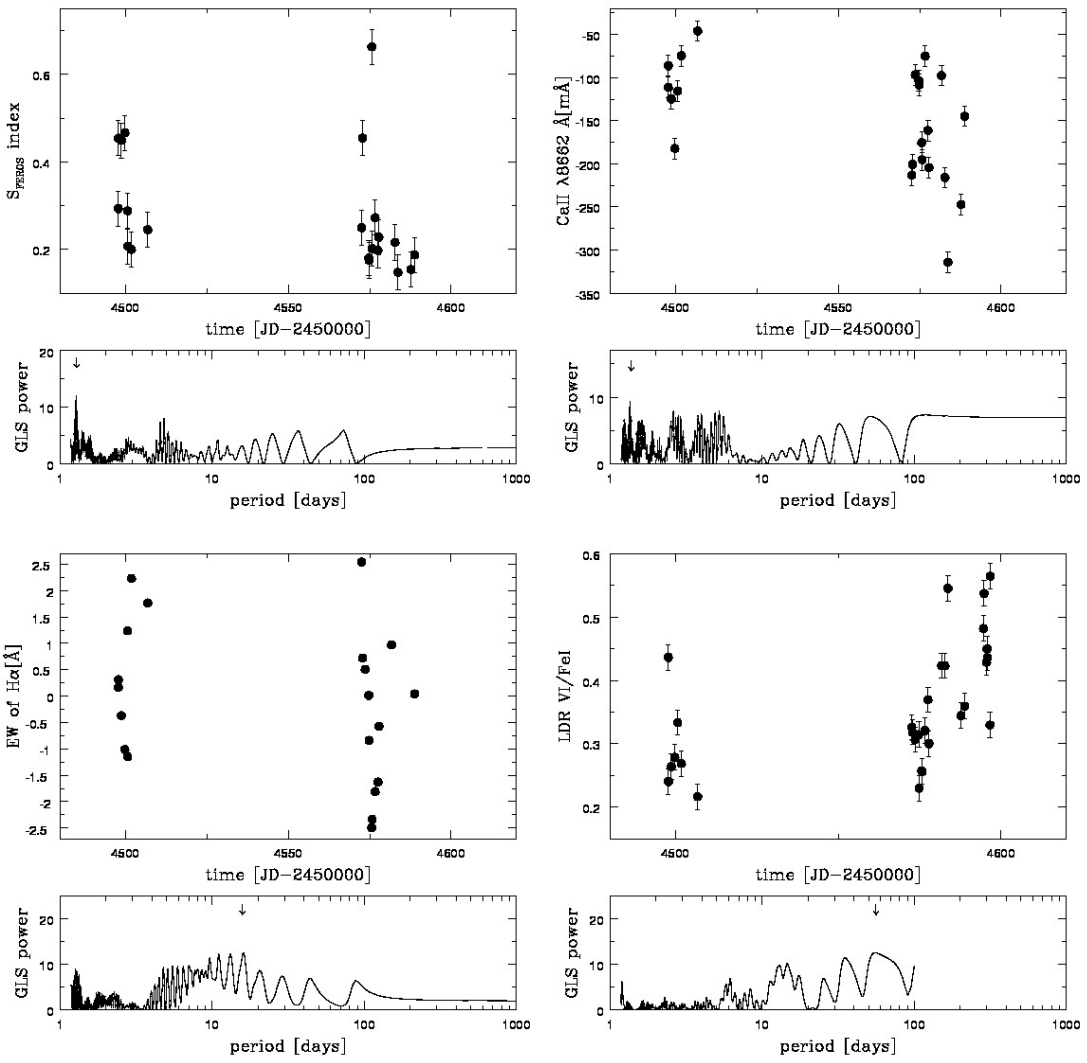

FIGURE 6.37 : Activity indicators for T Cha - S_{FEROS}, Ca II IRT λ 8662, Hα EW, and LDR V I/Fe I.

6.11.3 Summary for T Cha

T Cha shows a variability in RV data with a significant period of 3.6 days and a high semi-amplitude of 2 579 ms^{-1}. The photometric data varies with a period of 3.2 days. Furthermore, the BVS shows a negative correlation with the RV data. Thus, the source of the RV variation is most likely rotational modulation due to stellar surface spots. Schisano *et al.* [2009] also analysed RV, bisector, and photometric data for T Cha. They found similar results for the RV variation and the correlation of the bisector on RV and conclude that the RV and photometric variability of T Cha is caused by stellar surface spots and dusty clumps orbiting in the circumstellar disk, obscuring part of the star. The results derived in this analysis support the findings by Schisano *et al.* [2009]. No evidence for a sub-stellar companion orbiting T Cha can be found in the RV data.

TABLE 6.33 : Basic parameters for GQ Lup.

Parameter	Value	Method/Reference
Identifier	GQ Lup	...
Coordinates	15 49 12 -35 39 05	SIMBAD
Spectral type	K8V	Neuhäuser *et al.* [2005]
V magnitude	11.4 mag	Neuhäuser *et al.* [2005]
Distance	140±50 pc	Neuhäuser *et al.* [2005]
$M_\star$	0.7±0.1 $M_\odot$	Neuhäuser *et al.* [2005]
$T_{\rm eff}$	4650±120 K	*TGV*, this study
$\log g$	3.1±0.5 $\rm cms^{-2}$	*TGV*, this study
[Fe/H]	-0.55±0.20	*TGV*, this study
EW of Li I	644±5 mÅ	this study
Age	2±2 Myr	Li I measurements, this study
Age	1±1 Myr	Neuhäuser *et al.* [2005]
$v \sin i$	9.1±1.1 $\rm kms^{-1}$	this study
$R'_{\rm FEROS}$	-4.52	this study
Number of observations	26	...

6.12 GQ Lup

GQ Lup is a K8 type star with V=11.4 mag [Neuhäuser *et al.*, 2005]. This star is still accreting matter from its surrounding disk (see Section 5.1.3). A companion in the brown dwarf mass-regime has been found by direct imaging to orbit GQ Lup in a distance of 100-112 AU [Broeg *et al.*, 2007; Neuhäuser *et al.*, 2005]. This companion may has formed closer in and has been moved to its large separation by interaction with a massive inner companion [Boss, 2006]. Therefore, GQ Lup is an interesting target to search for additional sub-stellar companions.
The values for the basic stellar parameters derived in this study agree well within the error-bars with the values given in Neuhäuser *et al.* [2005]. Furthermore, the age inferred by Li I EW of 2±2 Myr agrees well with the mean age of 1±1 Myr derived from several evolutionary models by Neuhäuser *et al.* [2005].

6.12.1 Radial velocity variation

The RV variation (see Section 4.1) is shown in the left panel of Figure 6.38. The analysis with GLS yields a significant period of 7.75 days (FAP=0.1%) with a semi-amplitude of 955.5 $\rm ms^{-1}$. The peak-to-peak amplitude is 2 610 $\rm ms^{-1}$. A scatter around the Keplerian fit of 455 $\rm ms^{-1}$ remains. The RV data phase-folded with the 7.75 days period is presented in the right panel of Figure 6.38.
I also analysed the residuals of the RV data to search for variation in the scatter around the Keplerian fit. After subtraction of the 7.75 days period, the analysis with GLS yields a period of 3.54 days and a significant period of 220 days (FAP = 0.9%). The origin of the three periods, 7.75 days in the RV data and 3.54 days and 220 days in the residual

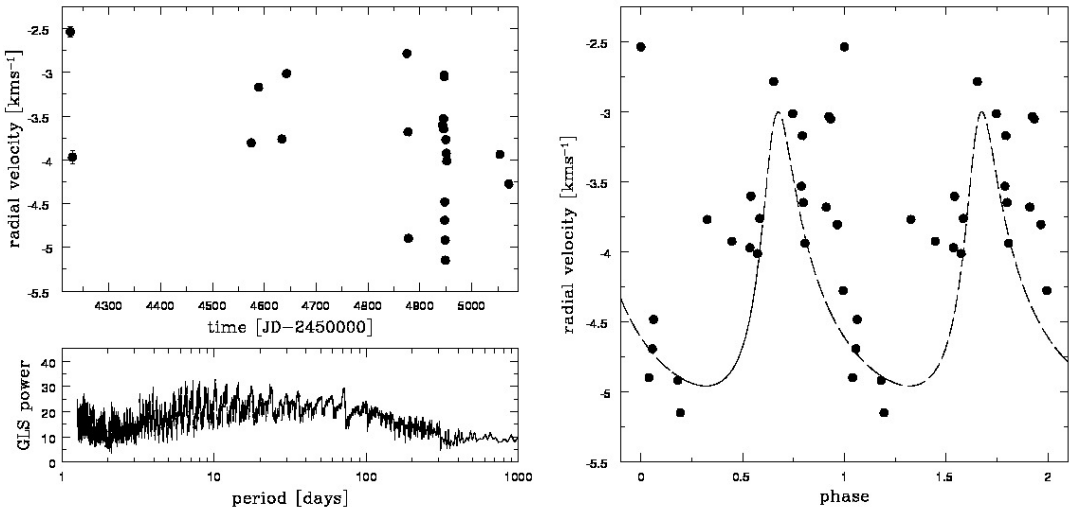

FIGURE 6.38 : Radial velocity variation of GQ Lup - variation over time and phase-folded with 7.75 days.

TABLE 6.34 : Periods of stellar activity indicators, photometric data, RV, the FAP of the period, and the amplitude for GQ Lup. I list further the accuracy of a single measurement $\sigma_{\rm meas}$ and mark the significant periods.

Activity indicator	Period [days]	FAP	Significance	Semi-amplitude	$\sigma_{\rm meas}$
Stellar activity					
BVS	2.18	19%	...	154.445 ms^{-1}	10–25 ms^{-1}
V I/Fe I LDR	5.46	32%	...	0.035	0.003
Hα	11.38	<0.1%	significant	14.02 Å	0.12 Å
$S_{\rm FEROS}$	8.54	0.4%	significant	0.399	0.03
Ca II λ 8662	1.31	20%	...	111.942 mÅ	12 mÅ
Radial Velocity	7.75	0.1%	significant	977.50 ms^{-1}	9–78 ms^{-1}
RV residuals	219.9	0.9%	significant	439.5 ms^{-1}	9–78 ms^{-1}

data, is discussed in the next section.

6.12.2 Analysis of stellar activity

Broeg *et al.* [2007] derived a stellar rotation period of 8.45±0.2 days from photometric observations of GQ Lup. They claim that this variation is caused by rotational modulation due to hot spots on the surface induced by the accretion of mass. The amplitude of the photometric variation is ΔV=0.75 mag. Broeg *et al.* [2007] showed that hot spots produce larger photometric variations than cold spots. However, if I assume that Equations (4.11) and (4.14) (Section 4.2.1) are valid for hot spots, I can derive the amplitude of the expected RV jitter of 1 265 ms^{-1} and 3 115 ms^{-1}, respectively. Thus, the RV jitter induced by stellar activity can account for the measured RV amplitude.

6.12.2.1 Bisector analysis

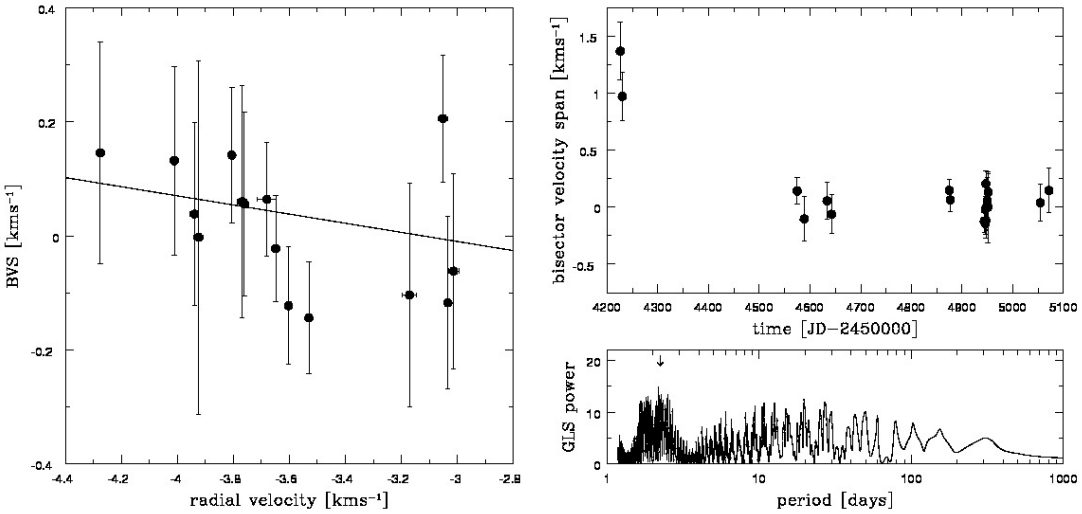

FIGURE 6.39 : Bisector velocity span for GQ Lup - BVS vs. RV and time variance

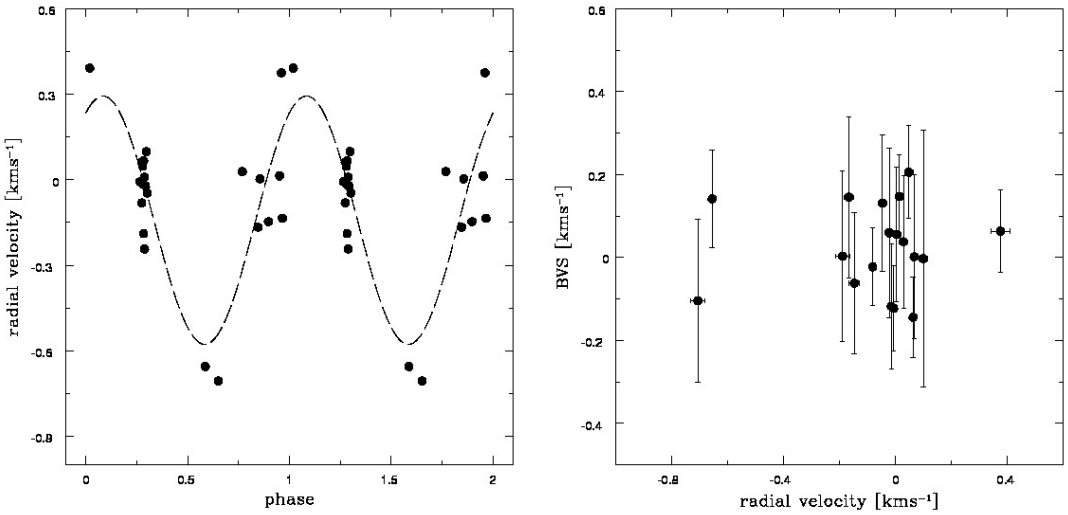

FIGURE 6.40 : Analysis of RV residuals for GQ Lup - left panel: RV residuals phase-folded with 220 days. Right panel: BVS vs. RV residuals.

The correlation of the BVS with RV is shown in the left panel of Figure 6.39. The correlation coefficient is r=0.15 (2.3%) and the probability that both data sets do not correlate is T=45%. Furthermore, the linear regression to the data shows a negative slope of -0.08. However, I analysed the correlation between the BVS and the RV residual data. For the 3.54 days period, the BVS still shows a negative correlation with the RV residuals. In contrast, the BVS does not correlate with the RV residuals data

with the 220 days period. This is presented in the right panel of Figure 6.40.
The variation of the BVS over time is shown in the right panel of Figure 6.39. The analysis with GLS yields a variability with a period of 2.18 days. Although with FAP = 19%, this period is different from the periods obtained by the analysis of the RV data.

6.12.2.2 Other stellar activity indicators

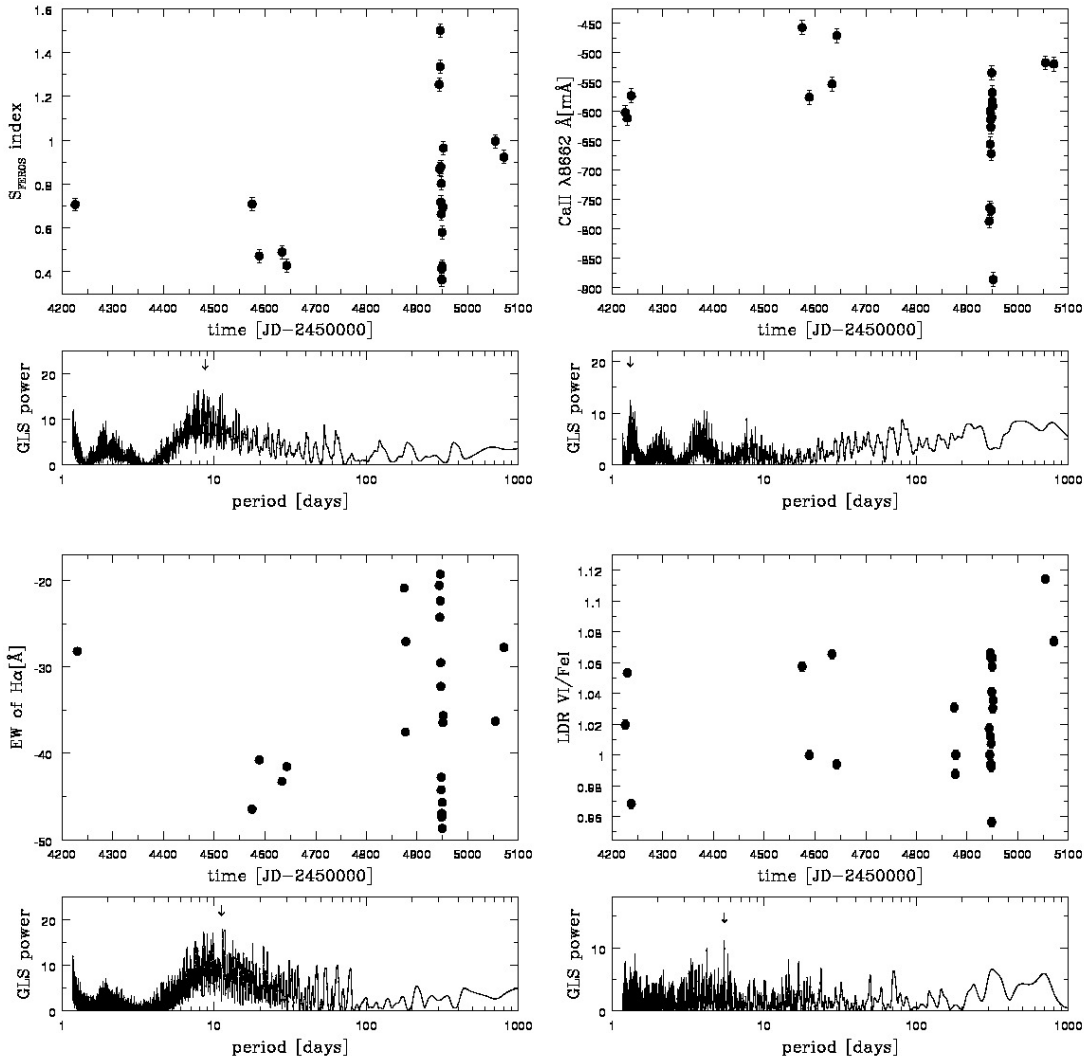

FIGURE 6.41 : Activity indicators for GQ Lup - $S_{\rm FEROS}$, Ca II IRT λ 8662, Hα EW, and LDR V I/Fe I.

The variations of the other stellar activity indicators, $S_{\rm FEROS}$, EW of Ca II λ 8662, LDR of V I/Fe I, and EW of Hα, are shown in Figure 6.41 and the periods, obtained from the analysis with GLS, are presented in Table 6.34. $S_{\rm FEROS}$ varies with a period of 8.54 days, which is similar to the rotation period of GQ Lup. The most significant period of the Hα variation is 11.38 days. However, this variation is most likely induced

TABLE 6.35 : Keplerian fit to the RV data of GQ Lup.

Parameter	Value	Parameter	Value	Method
Period	7.75 days	P of residuals	3.54 & 220 days	GLS
FAP	0.1%	FAP	0.9%	GLS
Amplitude K	977.5±60 ms^{-1}	K of residuals	729.3±60 ms^{-1}, 439.5±20 ms^{-1}	GLS
Eccentricity e	0.47±0.08	e of residuals	0.22±0.02, 0.01±0.01	GLS
Periastron passage	4944±10 HJD	T_0 of residuals	4228±10 HJD	GLS
Longitude of periastron ω	333°	ω of residuals	343°, 193°	GLS
Offset RV	-2.39±0.03 kms^{-1}	...	...	GLS
$m_p \sin i$	6.62 M_{jup}	$m_p \sin i$ from residuals	4.4 M_{Jup}, 10.2 M_{Jup}	GLS
a sin i	0.07 AU	a sin i from residuals	0.04 AU, 0.63 AU	GLS
rms of residuals	455 ms^{-1}	rms of residuals	383 ms^{-1}, 426 ms^{-1}	GLS

by the accretion process. For the other two indicators, Ca II IRT and LDR V I/Fe I, no significant periods could be derived. Thus, these two indicators vary irregular.

6.12.3 Summary for GQ Lup

GQ Lup shows a significant variation in the RV data. The period of this variation is 7.75 days. The BVS is correlated with the RV data and the period of the RV variation is close to the period derived for the stellar rotation period of 8.45 days. Therefore, the RV variation is most likely induced by rotational modulation due to hot-spots which are produced by the accretion process. The other stellar activity indicators vary with periods in the range of 7–12 days, which is in the range of the rotational period.
The analysis of the RV residuals after subtraction of the 7.75 days period, yields two periods of 3.54 days and 220 days. For the 3.54 days period, the BVS is still correlated with the RV residuals, whereas for the 220 days period, the BVS is not correlated. Furthermore, the stellar activity indicators vary with shorter periods.
As a result, I conclude that GQ Lup shows evidence for a companion orbiting with a 220 days period. This companion has a minimum mass of $m_p \sin i = 10.2\,M_{Jup}$, orbiting at a distance of 0.63 AU. The Keplerian fits to the RV and RV residual data are summarized in Table 6.35. It is probably massive enough to be responsible for the wide orbit (112 AU) of the imaged brown dwarf due to planet-planet interactions. Furthermore, this result gives evidence that giant planets can be formed in gaseous disks within 2 ± 2 Myr.

TABLE 6.36 : Basic parameters for 1RXS J223929.1-520525

Parameter	Value	Method/Reference
Identifier	1RXS J223929.1-520525	...
Coordinates	22 39 30 -52 05 17	SIMBAD
Spectral type	K0V	Torres *et al.* [2006]
V magnitude	10.9 mag	Torres *et al.* [2006]
Distance	100 pc	Torres *et al.* [2008]
T_{eff}	5500±50 K	*TGV*, this study
log g	5.3±0.2 cms^{-2}	*TGV*, this study
[Fe/H]	0.13±0.06	*TGV*, this study
EW of Li I	245±1 mÅ	this study
Age	60±15 Myr	Li I measurements, this study
Age	40 Myr	Torres *et al.* [2008]
$v \sin i$	9.4±1.0 kms^{-1}	this study
R'_{FEROS}	-4.30	this study
Number of observations	10	...

6.13 1RXS J223929.1-520525

1RXS J223929.1-520525 is a K0V type star with V=10.9 mag [Torres *et al.*, 2006]. It has been analysed in Viana Almeida *et al.* [2009]. Their measurements of basic stellar parameters agree well within the error-bars with the values obtained in this study (see Table 6.36). Viana Almeida *et al.* [2009] also allocated this target as a member of the Argus association, which is located 100 pc away with a mean age of 40 Myr [Torres *et al.*, 2008]. The age derived by Li I EW measurements is 60±15 Myr (Section 4.3.3). Therefore, I adopt 40–60 Myr as the age range for 1RXS J223929.1-520525. No information about a circumstellar disk is available because no observations with, e.g., *SPITZER*, are available.

6.13.1 Radial velocity variation

The RV variation of 1RXS J223929.1-520525 is shown in Figure 6.42 (left panel). The analysis with GLS yields a significant period of 43.38 days (FAP=1%) with a semi-amplitude of 176.50 ms^{-1}. The Keplerian fit to the RV data (see Table 6.38) is presented by the dashed line in Figure 6.42. However, because only 10 observations have been obtained, more observations are needed to verify this result. In the right panel of Figure 6.42 the RV data phase-folded with the 43.38 days period is shown.
I also calculated the residuals of the RV after subtraction of the 43.38 days period, but no significant variability of the residuals could be derived.

6.13.2 Analysis of stellar activity

In this section, I analyse the stellar activity indicators measured for 1RXS J223929.1-520525 (see Section 4.2). No photometric observations are available for this target.

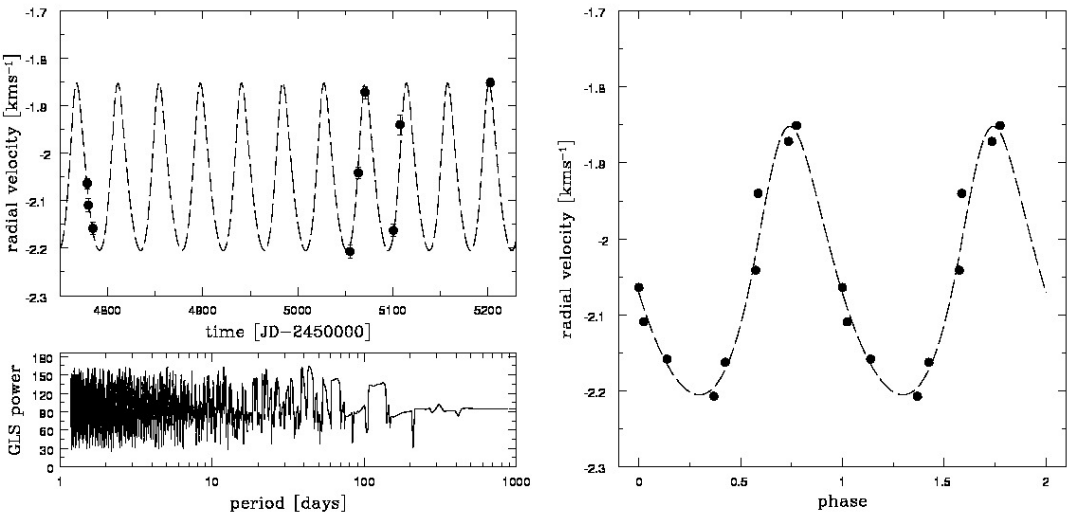

FIGURE 6.42 : Radial velocity variation of 1RXS J223929.1-520525 - variation over time and phase-folded with 43.38 days.

TABLE 6.37 : Periods of stellar activity indicators, photometric data, RV, the FAP of the period, and the amplitude for 1RXS J223929.1-520525. I list further the accuracy of a single measurement $\sigma_{\rm meas}$ and mark the significant periods.

Activity indicator	Period [days]	FAP	Significance	Semi-amplitude	$\sigma_{\rm meas}$
Stellar activity					
BVS	1.58	73%	...	102.408 ms^{-1}	90–130 ms^{-1}
V I/Fe I LDR	7.2	0.9%	significant	0.023	0.003
Hα	2.86	0.4%	significant	57.391 mÅ	15 mÅ
$S_{\rm FEROS}$	13.0	0.4%	significant	0.233	0.03
Ca II λ 8662	2.65	0.6%	significant	20.465 mÅ	12 mÅ
Radial Velocity	43.38	1%	significant	176.5 ms^{-1}	9–20 ms^{-1}

Thus, no rotation period can be identified and no expected RV jitter induced by stellar activity can be calculated.

6.13.2.1 Bisector analysis

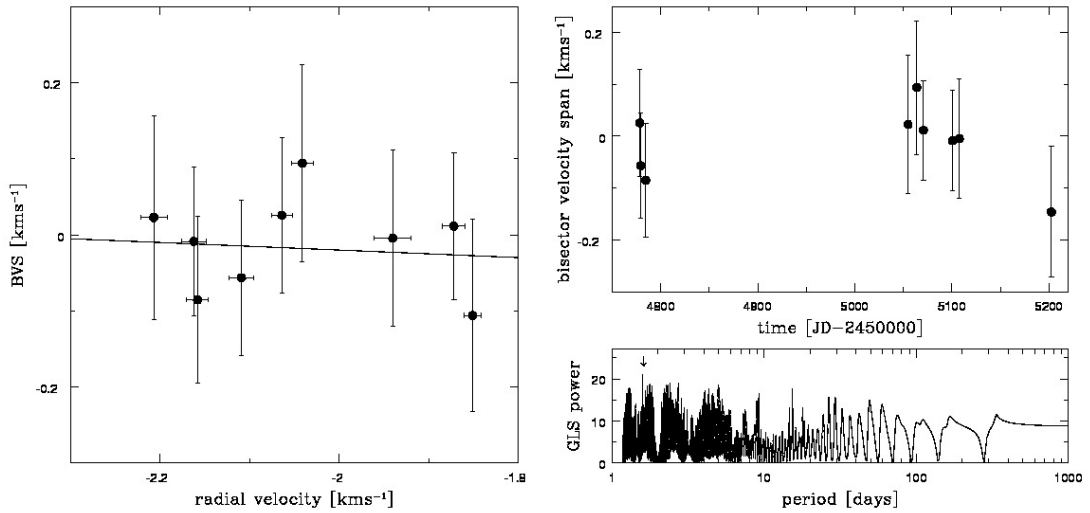

FIGURE 6.43 : Bisector velocity span for 1RXS J223929.1-520525 - BVS vs. RV and time variance

The correlation of the BVS with RV is shown in Figure 6.43 (left panel). The correlation coefficient is r=0.11 (1.2%). In addition, the probability that both data sets do not correlate is T=73%, which shows that rotational modulation due to stellar activity is unlikely the source of the RV variation. However, the slope of the linear regression to the data is -0.05, but not significant because of the scatter around the linear regression. Thus, no significant conclusion can be made for the slope of the correlation. The variation of BVS with time is shown in the right panel of Figure 6.43. The analysis with GLS yields an insignificant period of 1.58 days (FAP = 73%).

6.13.2.2 Other stellar activity indicators

The variation of the other stellar activity indicators, S_{FEROS}, EW of Ca II λ 8662, LDR of V I/Fe I, and EW of Hα, is shown in Figure 6.44 and the periods, obtained from the analysis with GLS, are presented in Table 6.37. All indicators show significant periods in the range of 2.65–13 days. No stellar activity indicator varies with a period similar to the period of 43.38 days for the RV variation.

6.13.3 Summary for 1RXS J223929.1-520525

1RXS J223929.1-520525 shows a variability in the RV data with a significant period of 43.38 days. The Keplerian fit to the RV data is presented in Table 6.38. The bisector

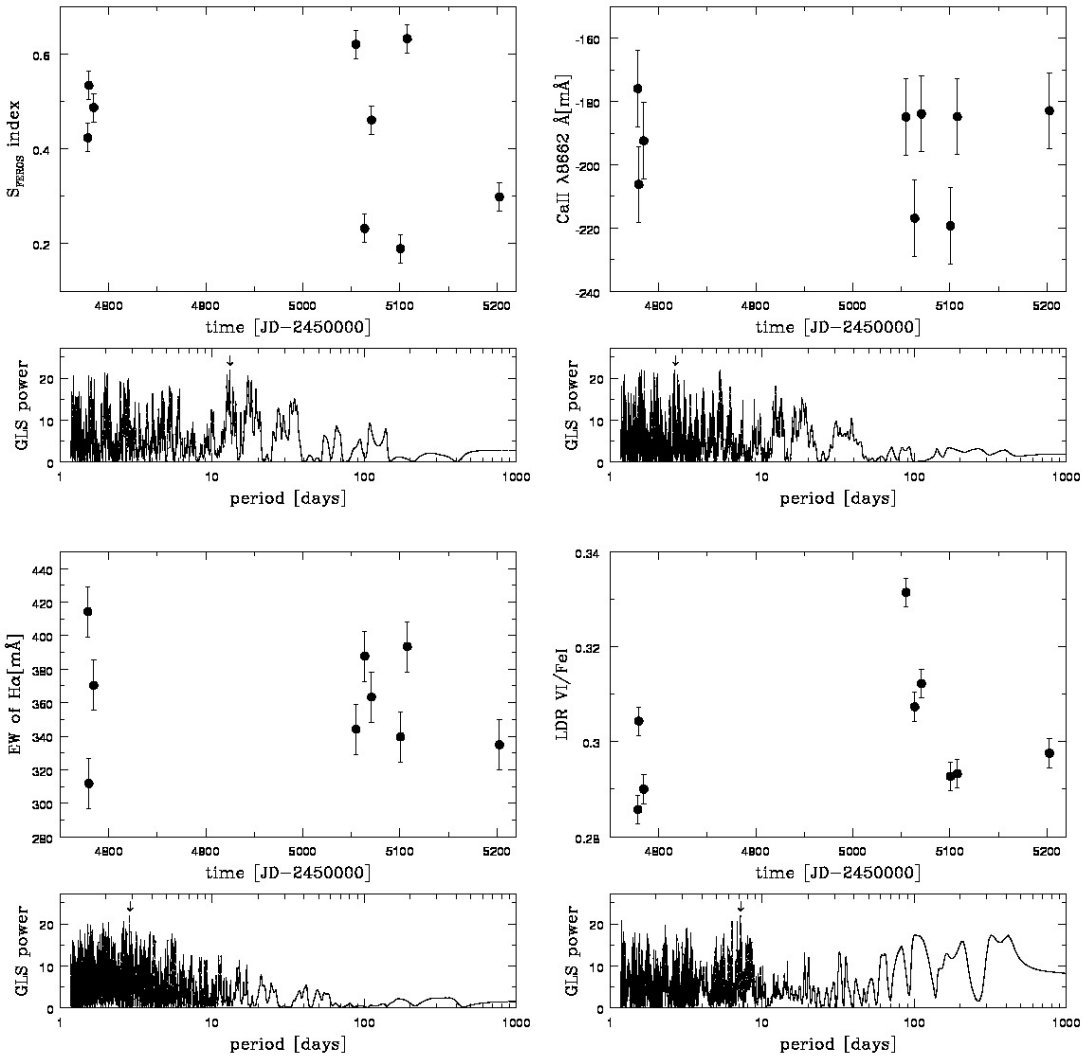

FIGURE 6.44 : Activity indicators for 1RXS J223929.1-520525 - $S_{\rm FEROS}$, Ca II IRT λ 8662, Hα EW, and LDR V I/Fe I.

TABLE 6.38 : Keplerian fit to the RV data of 1RXS J223929.1-520525.

Parameter	Value	Method
Period	43.38,days	GLS
FAP	1%	GLS
Amplitude K	176.49±10 ms^{-1}	GLS
Eccentricity e	0.2±0.03	GLS
Periastron passage	4808±10 HJD	GLS
Longitude of periastron ω	333±5°	GLS
Offset RV	-2.06±0.03 kms^{-1}	GLS
rms of residuals	26 ms^{-1}	GLS

is not correlated with the RV data. Furthermore, all other stellar activity indicators show a variability with much shorter periods in the range of 2.65–13 days. Therefore, a companion orbiting 1RXS J223929.1-520525 is most likely the source of the long RV variation. If I assume a stellar mass of $1\,M_{\odot}$ because no stellar mass could be calculated for 1RXS J223929.1-520525, the companion would have a minimum mass of $m \sin i = 3\,M_{\mathrm{Jup}}$ and orbits at a distance of 0.24 AU.

6.14 Analysis for the remaining 13 stars

For 13 stars with more than 5 observations the analysis of the RV, bisector, and stellar activity indicators is summarized in this section. For these 13 stars, either the number of observations is not sufficient enough to obtain significant periods, or the source of the RV variation is identified as rotational modulation due to stellar activity. These 13 stars are HD 51062, RX J1233.5-7523, 1RXS J123332.4-571345, TYC 9412-59-1, TYC 8654-1115-1, CD-69 1055, LT Lup, LY Lup, HBC 603, CD-37 13029, HD 217897, TYC 584-343-1, and CP-72 2713. The figures for the measured RV, the bisector analysis, and the analysis of the other stellar activity indicators are presented in Appendix D. In addition, the results for the basic stellar parameters, $T_{\rm eff}$, $\log g$, metallicity, and $R'_{\rm FEROS}$ are presented in Table B.2 in Appendix B. The results for the analysis of the RV data with GLS are presented in Table B.3, the periods of the stellar activity indicators are shown in Table B.4, and the obtained stellar age and number of observations are presented in Table B.1 in Appendix B.

HD 51062. For this star, 6 observations have been obtained and, therefore, the analysis of the RV data (Figure D.1) yielded no significant period. The correlation between the BVS and the RV data is also inconclusive (Figure D.3) due to the low number of observations. Thus, no conclusion on the source of the RV variation can be drawn from the data obtained so far.

RX J1233.5-7523. For this star, 11 observations have been obtained and the RV variation is shown in Figure D.4. The analysis yields a period of 4 days with a semi-amplitude of 75.2 $\rm ms^{-1}$. However, the negative correlation between the BVS and the RV data (see Figure D.5) indicates that the RV variation is most likely induced by rotational modulation due to stellar surface spots.

1RXS J123332.4-571345. The RV of this star varies with a period of 4.27 days and a semi-amplitude of 825.97 $\rm ms^{-1}$ (Figure D.7). The bisector shows a positive correlation with RV (Figure D.8) and all other stellar activity indicators (Figure D.9) show no significant periods in the data. These results speak for a (stellar) companion as the source of the RV variation. However, the number of observations is too low to make a conclusion on the source of the RV variation. Therefore, more observations are needed for 1RXS J123332.4-571345.

TYC 9412-59-1. For this star, the RV data (Figure D.10) shows no significant period, but I adopt the period of 1.2 days. The bisector analysis (Figure D.11) reveals a strong negative correlation between the BVS and the RV data. Furthermore, the probability that both data sets do not correlate T=0.2%. The other stellar activity indicators show

only insignificant variability. Therefore, for TYC 9412-59-1, the RV variation is most likely induced by rotational modulation due to stellar surface spots.

TYC 8654-1115-1. Only 6 observations have been obtained for TYC 8654-1115-1. Thus, the analysis for periods in the RV, bisector, and stellar activity indicators yield no significant periods. The RV data is shown in Figure D.13. The bisector in Figure D.14 shows a slight positive slope and no strong correlation with RV. However, the data obtained so far is not sufficient enough to draw a conclusion about the source of the RV variation.

CD-69 1055. This star shows an interesting variation in the RV data and, therefore, 29 spectra have been obtained. The analysis of the RV data yields a period of 1.95 days (Figure D.16). However, the the stellar activity indicators vary with periods in the range of 1.3–2.8 days and the bisector shows a strong correlation with RV (Figure D.17). Furthermore, the linear regression to the BVS vs. RV data yields a negative slope of -0.8 and the probability that both data-sets do not correlate is T=0.02%. Thus, the RV variation is most likely explanation caused by rotational modulation due to stellar activity.

LT Lup. The RV variation for this star is presented in Figure D.19. The analysis with GLS yields a period of 2.39 days. However, the variation of the stellar activity indicator LDR V I/Fe I shows a similar period (Figure D.21). In addition, the bisector is strongly correlated with the RV data (Figure D.20) and the probability that both data-sets do not correlate is T=0.2%. Thus, the RV variation is most likely caused by rotational modulation due to stellar activity.

LY Lup. The RV of this star varies with a period of 1.58 days (Figure D.22). The bisector shows a positive correlation with RV, which means that the bisector changes are induced by a stellar companion. The stellar activity indicators all vary with periods in the range of 1.2–38 days. However, no information about a stellar companion is available and more data over a longer time-span is needed to identify a possible stellar companion.

HBC 603. This star is a binary with a separation of 1''.8, which corresponds to a distance of ~340 AU [Ghez *et al.*, 1997]. Furthermore, HBC 603 exhibit a circumstellar disk in the transitional stage [Takami *et al.*, 2003]. The RV variation is shown in Figure D.25. The analysis with GLS yields no significant periods for the RV variation and all stellar activity indicators (see Figures D.26 and D.27). Thus, more data is needed for this star to be able to assign a period of the RV variation. However, the bisector

shows a positive trend with RV, which is most likely due to the stellar companion.

CD-37 13029. The RV of this star shows a variation (see Figure D.28), but no significant period could be identified because of the low number of observations. The correlation between BVS and RV is inconclusive and no significant period of the stellar activity indicators could be derived, either. Therefore, more data is needed for CD-37 13029 in order to derive a significant period and to identify the source of the RV variation.

CP-72 2713. This star shows a variation in the RV data (see Figure D.31), which can be described by a Keplerian fit with a period of 11.38 days. The dependence of BVS on RV is shown in Figure D.32 and the correlation is small. Therefore, the probability that both data-sets do not correlate is T=93%. Furthermore, the period of the RV data is higher than the periods of the variation of all stellar activity indicators (see Figure D.33). However, the time sampling of the RV data is not sufficient enough to verify the obtained solution of the Keplerian fit. Thus, more data is needed.

HD 217897. The number of observations is not sufficient enough to derive a significant period for the RV variation of HD 217897 (Figure D.34). However, the bisector correlates with RV and the linear regression has a negative slope. This yields that the source of the RV variation is rotational modulation due to stellar activity.

TYC 584-343-1. The analysis of the RV data (Figure D.37) with GLS yields an insignificant period of 3 days. The stellar activity indicators show variability with periods in the range of 1.77–4.83 days, i.e., similar to the RV variation (see Figure D.39). These results speak for rotational modulation due to stellar activity as the source of the short period in the RV data. However, the BVS is positively correlated with RV, which speaks for a stellar companion orbiting TYC 584-343-1, but more data is needed.

6.15 Stars with insufficient number of observations

From the 100 stars observed for this thesis, 26 stars with more than 5 observations have been analysed in detail in this chapter. The remaining 74 stars with 1–4 observations can be sorted into 3 groups. First, 25 of the 74 remaining stars show a $v \sin i > 30 \mathrm{kms}^{-1}$ and high precision RV measurements are very difficult to obtain (see Section 5.2.3). These stars are marked with 'high $v \sin i$' in Table B.1 in Appendix B. The second group consists of 22 stars which rotate with $v \sin i < 30 \mathrm{kms}^{-1}$, but have an error in the individual RV measurements of $\sigma_{\mathrm{RV}} > 30\,\mathrm{ms}^{-1}$. Thus, for these stars, RV measurements are possible, but stellar activity is high in these stars. The mean age in this group is

7±3 Myr. The last group consists of 27 stars, also rotating with $v \sin i < 30 \mathrm{kms}^{-1}$ and an error of the individual RV measurements of $\sigma_{\mathrm{RV}} < 30\,\mathrm{ms}^{-1}$. The mean age in this third group is 30±15 Myr. These stars are very good targets to obtain precise RV measurements. The analysis to identify the source of the RV variation yields a more significant result than for stars with will be easier as compared for the second group of targets. These targets are listed in Tables B.5 and B.6 in Appendix B, respectively.

7 Summary and conclusion

For this study, I observed 100 young stars with FEROS at the 2.2m MPG/ESO telescope and HARPS at the 3.6m telescope in La Silla, Chile, and computed radial velocities and bisectors by using the new cross-correlation tool MACS. Furthermore, other stellar activity indicators, S_{FEROS}, EW of Ca II λ 8662, LDR of V I/Fe I, and EW of Hα, have been analysed to fully characterize the stellar activity of the targets. In addition, for all observed stars, basic stellar parameters, like stellar age, T_{eff}, $\log g$, and metallicity, as well as the evolutionary stage and the projected rotational velocity, $v \sin i$, have been obtained (see Chapter 5). The age of the targets span a range from 1 Myr to 100 Myr with a mean of 15 Myr. For 27 stars more than 5 observations have been obtained during the observing period from January 2008 to May 2010. 26 of these stars show variability of the radial velocity data, which has been analysed in Chapter 6 and is summarized in Section 7.2.

7.1 Results of the spectral characterization of the targets

For the characterization of the targets, an additional sample of other SERAM targets has been added. Thus, 260 stars have been characterized. Of these, 100 targets are in sub-sample (a), which have been observed in this study, and 160 stars are in sub-sample (b), the additional SERAM sample. The results of the characterization in Chapter 5 can be summarized as:

- The mean stellar age of both sub-samples (a)+(b) is 30 Myr with a spread (width of Gaussian fit) of 20 Myr. The age distribution for the targets of sub-sample (a) shows two peaks, one at 5 Myr and a second at 30 Myr. In total, 47 stars are younger than 10 Myr.

- The stars in sub-sample (b) have a lower mean metallicity than the stars in sub-sample (a). The mean metallicities are -0.14 ± 0.02 dex and -0.02 ± 0.03 dex, respectively. However, no correlation of the metallicity with age could be identified, but the metallicity changes with T_{eff}. This trend contradicts the standard

idea that stars originated within the same cloud will show a similar abundance pattern.

- The distribution of $v \sin i$ for all 260 stars peaks at 7.8±1.2 kms^{-1}, with the vast majority having projected rotational velocities < 30 kms^{-1}.

- I found indication for rotational braking due to disk-locking, because the accreting stars in the sample rotate significantly slower ($\langle v \sin i \rangle = 10 \pm 1\,\mathrm{kms}^{-1}$) than the non-accreting stars with more evolved disks ($\langle v \sin i \rangle = 15 \pm 2\,\mathrm{kms}^{-1}$). The only 2 fast rotating ($v \sin i \sim 38\,\mathrm{kms}^{-1}$) accretors in the sample are DI Cha and CR Cha. This might point to differences in time spent for disk-braking or to different initial conditions in different star formation regions, but the significance of this statement is hampered by low number statistics.

- This $v \sin i$ evolution also provides indication that stars undergo rotational spin-up after being decoupled from their circumstellar disk and evolving along the Pre-Main-Sequence track. These stars have a mean age of 7 Myr and rotate with $\langle v \sin i \rangle = 15 \pm 2\,\mathrm{kms}^{-1}$. For more evolved stars with debris or no disks and an age > 30 Myr, $\langle v \sin i \rangle$ decreases again to $10 \pm 1\,\mathrm{kms}^{-1}$. I conclude that these stars have been rotationally braked on the ZAMS, e.g., by magnetic winds.

- I estimated the maximum rotational period of the target stars. The period distribution of the whole sample of 260 stars peaks at 2.5 ± 0.3 days, a similar result as found for young low-mass stars in the ONC and NGC 2264 by Cieza & Biliber (2007).

- Due to disk-braking, young and accreting stars can rotate sufficiently slow to serve as suitable targets for RV planet searches, since the accuracy of radial velocity measurements depends on the stellar $v \sin i$. When accretion ends after ~5–10 Myr and the stars decouple from their disk, they tend to spin up as they contract, such that they are usually no longer suitable for precise RV measurements. This changes only when the stars arrive on the ZAMS and are slowed down again by wind braking at ages of ~30 Myr.

- From these results, I can conclude that stars with disks and an age < 5 Myr and stars with an age of 30 Myr can be observed for planet search surveys because these stars rote sufficiently slow to obtain precise RV measurements. Stars with ages between 5–30 Myr are on average rotating faster and no precise RV measurements can be obtained.

7.2 Results of the radial velocity analysis

From the analysis of the RV variations and stellar activity indicators of the 26 stars with more than 5 observation, I yield the following results:

- For 6 stars the number of observations is not sufficient to identify the source and a period of the RV variation. These stars are HD 51062, 1RXS J12332.4-571345, TYC 8654-1115-1, HBC 603, CD-37 13029, and CP-72 2713.

- I found that the RV variation of 12 out of the 26 analysed stars is most likely caused by rotational modulation due to stellar activity. These 12 stars are 1RXS J033149.8-633155, CD-84 0080, EG Cha, T Cha, RX J1233.5-7523, TYC 9412-59-1, CD-69 1055, LT Lup, HD 217897, TYC 584-343-1, and LY Lup. The ages of these stars range from 2–90 Myr with a mean value of 25 Myr.
  For two of these stars, LY Lup and TYC 584-343-1, the positive correlation between the bisector and the RV data gives evidence that both stars have a stellar companion and are single-line binaries (see Section 4.1.2). However, the RV shows only a short-term variation which is due to rotational modulation of stellar activity. The variation induced by the stellar companion is probably of long-term nature and the time-span of the observations is too short to detect the stellar companion. For both stars no information about stellar companions is available.

- The RV variation of GW Ori is caused by the previously known close orbiting stellar companion. The results on stellar mass and distance of the companion derived in this study agree well with the results found by Mathieu *et al.* [1991]. No evidence could be found for an additional sub-stellar companion orbiting neither in the circumstellar disk of GW Ori, nor in the circumbinary disk.

- I found evidence for a brown dwarf with a minimum mass of $14.6 \pm 2.4\,M_{Jup}$ orbiting at 0.31 AU the 15±10 Myr old star CD-78 24. This is the only brown dwarf found in this study.

- Two planetary companions of intermediate masses have been found. One giant planet is orbiting the 15–30 Myr old 1RXS J153328.4-665130 and has a period of 292 days, thus orbiting at 0.92 AU, with a true mass of $5.2\,M_{Jup}$. The analysis of stellar activity reveals that the short-term variation of 7–11 days is produced by rotational modulation of surface features, but not the long-term period of 292 days.
  The other giant planet orbits the 40–60 Myr old 1RXS J223929.1-520525 with a minimum mass of $3\,M_{Jup}$ at 0.24 AU (with an assumed stellar mass of $1\,M_{\odot}$). In

this case, the stellar activity indicators show no correlation with the RV data and the indicators also vary with other periods.

- In addition to these two planets, two more stars are likely to be orbited by giant planets of intermediate masses. The 10 Myr old TYC 5891-69-1 might be orbited by a planet with a mass of 3.7 M_{Jup} at a distance of 0.04 AU. Furthermore, the 25–40 Myr old TYC 7697-2254-1 show a RV variation which is likely induced by a planetary companion with a mass of 2.15 M_{Jup} in a distance of 0.13 AU. However, the stellar mass of both stars is unknown and 1 $M_{\odot}$ has been assumed. Furthermore, more data are needed for both stars to verify these results because stellar activity may still account for the RV variation.

- The young stars DI Cha and GQ Lup (age ~2 Myr) show evidence for planetary companions. In both stars stellar activity is high and the signal of the companions have been found after analysis of the RV residuals (after subtraction of the variation induced by stellar activity). For DI Cha, a potential giant planet orbits at 0.05 AU with a minimum mass of 9.4 M_{Jup}. The companion of GQ Lup orbits at a higher distance of 0.63 AU with a minimum mass of 10.2 M_{Jup}. Both giant planets have minimum masses near the transition region from planet to brown dwarf and might also be of brown dwarf nature. The found companion of GQ Lup can explain the wide orbit of the brown dwarf found by Neuhäuser *et al.* [2005] by planet-planet interactions. However, more data are needed to verify the results for DI Cha and GQ Lup.

- One target remains, the 15–30 Myr old CD-37 1123, which shows significant RV variation, but where the available data do not yet allow me to distinguish between stellar activity or a planetary companion as the source of the RV variation. Therefore, CD-37 1123 might be orbited by a giant planet with a mass of 0.5 M_{Jup} at a distance of 0.03 AU which induce activity on the star by star-planet interactions. In this case, both magnetospheres would interact. However, more data is needed to verify this scenario.

7.2.1 Conclusions

I analysed the RV variability of 26 stars and for 20 of them, evidence for the source of the RV variation could be found. Of these 20 stars, 10 show no sign of an orbiting companion, but high stellar activity which can account for the observed RV variation and its period. For 6 more stars, the RV variation is either induced by stellar activity or by (stellar) companions. More data is needed for these stars. 4 stars show strong evidence that their RV variation is caused by orbiting companions. In Table 7.1, I summarize the results of this study.

TABLE 7.1 : Results of the radial velocity analysis

Source of RV	# (identified)	# (still to be verified)	percent of analysed stars
Stellar activity	10	6	50–80%
Stellar companions	1	2	5–15%
Brown dwarf companions	1	...	5%
Planetary companions	2	4	10–30%

I found evidence for 1 brown dwarf around a young star, which corresponds to 5% of the analysed stars, but evidence for 2–6 planetary companions (10–30%). Although, this is low-number statistics, this means that a brown dwarf desert is even present at an age of 15 Myr. However, this can still be due to orbital evolution of brown dwarfs, which should occur as long as a gaseous disk is present, i.e. within the disk lifetime. The frequency of giant planets around young stars (10-30%) is comparable to the frequency found around solar-like stars (5%), when I take the low number of stars into account. The found giant planets for which strong evidence is given, orbit slightly older stars with an age of 15–60 Myr, from which no conclusion on the dominant formation process can be drawn. Nevertheless, there is evidence for giant planets (or brown dwarfs, because the minimum mass is near the transition to brown dwarfs) orbiting stars, DI Cha and GQ Lup, with an age of ~2 Myr. Although, the age is known only to an accuracy of 50–100%, these are the youngest giant planets found by the RV technique so far. To yield constraints on the dominant process in planet formation, the number of planets is too low. However, the detection of very young sub-stellar companions is possible.

7.3 Limitations of the radial velocity technique

An additional goal of this thesis was to identify limitations to the use of the RV technique to search for planets around young stars. One important limitation does not only affect the serch for planets around young stars, but for all stars. This is the time-coverage of the observations. The time-coverage is important to derive significant periods and to identify the short-term variability (mostly induced by stellar activity), but also to find long-term periods of potential companions. For this study, the targets should have been observed 2–3 times each night during an observing run. However, due to bad weather and interruptions at the telescope, this strategy could only be applied to a few stars. Since these stars also showed an interesting RV variation, these few have been observed more often and other stars only have been observed 5–10 times, which complicated the analysis of the RV variation. From this, a good observing strategy can be inferred, which consists of 2–3 observations on a single night, repeated nightly during a 10-14 days observing block, which will again be

repeated every 2–3 months over 3–5 years for each star. This is a good strategy to analyse the data for short and long-term periods. Also important is the time interval between the individual observations on one night. Because constant intervals can give false periods during the analysis, the time intervals should differ. However, this strategy costs a lot of observing time, more than available for this study. Nevertheless, I was able to analyse 26% of the targets for periodicity.

From the characterization of the targets and the analysis of the RV data, four obstacles can be identified which prevent the computation of high-precision RVs. Even with the use of MACS, which was designed to handle the spectra of young stars, not all features can be removed. These features are:

- High $v \sin i$ can produce large uncertainties on the individual RV measurements because the CCF can no longer be described by a Gaussian (see Section 4.1.2). MACS can also use an analytical function of a broadened Gaussian to fit the CCF, but the accuracy of the fit is still hampered by the effect that higher $v \sin i$ means fewer lines to be used during cross-correlation due to blending. This results in badly sampled CCFs for stars rotating faster than $30\,\mathrm{kms}^{-1}$, which can either not be fitted or the accuracy of the fit is bad. No solution to the problem of high stellar rotation is found so far.

- For stars with strong accretion, the computation of RVs with the cross-correlation is also very difficult. The reason for this is not the presence of strong emission lines in the spectrum (MACS is able to mask out these features), but the spectral veiling induced by the accretion process. It changes the depth and shape of all spectral lines. Therefore, the template used for cross-correlation no longer matches the spectral lines exactly and the CCF is noisy (which results in a bad fit) or cannot be calculated at all. Furthermore, the correlation of the veiled stellar spectra with itself did not yield a significant increase in the accuracy of the fit to the CCF. However, I was not able to unveil the spectra of the veiled stars because the veiling is variable and changes across the spectrum. Furthermore, appropriate theoretical spectra are needed to derive the veiling in the observed spectra (e.g., Hartigan *et al.* [1989]).

- Finally, the accuracy of the RV measurement is restricted by the signal-to-noise ratio (SNR) of the obtained spectra. A low SNR also affects directly the spectral lines used for cross-correlation, thus, the CCF is noisy and the Gaussian fit inaccurate. The CCF is improved when applying a smooth filter on the data, like it is applicable in MACS.

- Rotational modulation due to stellar activity can produce a effective radial velocity variation which can mimic the orbital motion of a companion (Chapter 2.3).

However, this effect can be filtered out by a careful analysis of the spectral line shape (bisector), periodicity of stellar activity indicators, photometric variability and, in an ideal case, by spectroscopic observations in the near-Infrared (see analysis in Chapter 6.1.2.3). This is especially important when the signal induced by rotational modulation due to stellar activity hides the signal of a real orbiting companion. In this case, the analysis of RV residuals (after subtracting the amplitude and period of the rotational modulation of stellar activity) can probably reveal the planetary signal.

7.4 Future prospects

This thesis attempts to search for young giant planets with the radial velocity technique. This technique has been widely used to search for planets around Main-Sequence stars. Unfortunately, young stars with an age of 1–100 Myr have often been excluded from RV surveys due to the high stellar activity and rotation. However, in this thesis, I have shown that it is possible to measure RV variability of young stars and by analysing the RV variation and stellar activity, it is possible to detect signals from orbiting companions. Therefore, the radial velocity technique will still play an important role to identify companions around very young stars. Especially, when measurements of RVs in the near-infraread becomes possible with a reasonable accuracy, the contribution of stellar surface spots to the RV variation can be measured and companions be identified.

Appendix

A Target list

Here, I present the target list of all 200 targets selected by the selection criteria listed in Section 3.1. The numbering of the stars has been set arbitrarily, but it is fixed for this study. In the next column, the ID of the star is listed followed by its coordinates. In column 5, the magnitude in V-band is given and in the following column the spectral type of the targets. In column 7, the stellar age taken from the literature is given and finally the reference of the source catalogue for the target. References: SACY: Torres *et al.* [2006]; FEPS: Silverstone *et al.* [2006]; c2dL: Lahuis *et al.* [2007]; c2dP: Padgett *et al.* [2006]; Rodm: Rodmann *et al.* [2006]; Sche: Schegerer *et al.* [2006]; Guen: Guenther *et al.* [2007]; JMSB: James *et al.* [2006].

TABLE A.1 : Compiled list of all targets selected by the selection criteria. Note that the stellar age listed in this table is taken from the literature (see text.

#	ID	Name	RA	DEC	V mag	SpT	Age	Reference
			h:m:s	deg:m:s	mag		Myr	
1	HD	224725	00:00:12.100	01:46:17.000	10.78	G9IV	9	SACY
2	CD-78	24	00:42:20.300	-77:47:40.000	10.21	K3Ve	75	SACY
4	CD-31	571	01:24:51.800	-30:44:45.000	10.34	K2V(e)	95	SACY
5	CCDM	J01377+1836	01:37:39.419	18:35:32.910	9.9	K2	5	FEPS
18	CD-37	1123	03:00:46.900	-37:08:02.000	10.52	G9V	75	SACY
31	HD	21955	03:31:20.800	-30:30:59.000	9.93	G7IV	10	SACY
32	1RXS	J033149.8-633155	03:31:48.900	-63:31:54.000	10.93	K0V	10	SACY
36	HD	23208	03:42:39.800	-20:32:44.000	9.16	G8V	15	SACY
44	LkHA	330	03:45:48.300	32:24:11.900	10.97	G3	5.7	c2dL
54	TYC	1258-338-1	04:05:19.590	20:09:25.830	10.38	K1	<10	c2dP
56	CD-31	1688	04:05:52.200	-31:38:38.000	10.02	G6IV	10	SACY
63	CD-58	860	04:11:55.700	-58:01:47.000	10.01	G6V	55	SACY
65	HD	26980	04:14:22.600	-38:19:02.000	9.08	G3V	75	SACY
71	CD-43	1395	04:21:48.700	-43:17:33.000	10.18	G7V	10	SACY
72	RY	Tau	04:21:57.420	28:26:35.500	10.21	K1	0.2	Rodm
75	V1201	Tau	04:24:49.110	26:43:09.800	10.9	K0	<10	c2dP
79	CD-43	1451	04:30:27.300	-42:48:47.000	10.75	G9V(e)	15	SACY
86	TYC	5891-69-1	04:32:43.509	-15:20:11.268	10.39	G4V	5	FEPS
88	1RXS	J043451.0-354715	04:34:50.800	-35:47:21.000	10.84	K1Ve	75	SACY
91	V1204	Tau	04:38:39.000	15:46:13.200	10.72	K2	<10	c2dP
99	SU	Aur	04:55:59.385	30:34:01.525	9.42	G2IIIev	9	Sche
103	V1407	Ori	04:57:17.700	15:25:09.000	10.4	K1	<10	c2dP
104	TYC	1289-513-1	04:57:30.662	20:14:29.680	11.11	K3	<10	c2dP
106	HD	286264	05:00:49.280	15:26:59.900	11	G0	20	FEPS
107	HD	32372	05:00:51.900	-41:01:07.000	9.5	G5V	45	SACY
131	HD	274576	05:28:51.400	-46:28:19.000	10.57	G6V	20	SACY

Table A.1 – continued from previous page

#	ID	Name	RA	DEC	V mag	SpT	Age	Reference
			h:m:s	deg:m:s	mag		Myr	
132	GW	Ori	05:29:08.391	11:52:12.700	9.92	K3V:e	1	Sche
135	HD	36329	05:29:24.100	-34:30:56.000	9.18	G3V	15	SACY
136	HD	269620	05:29:27.100	-68:52:05.000	9.56	G6V	55	SACY
151	HD	37551	05:37:12.900	-42:42:56.000	9.55	G7V	85	SACY
161	HD	42270	05:53:29.300	-81:56:53.000	9.14	K0V	10	SACY
164	CD-34	2676	06:08:33.900	-34:02:55.000	10.17	G9Ve	65	SACY
165	1RXS	J061155.8-352910	06:11:55.700	-35:29:13.000	10.57	K1Ve	100	SACY
167	HD	44748	06:21:57.300	-34:30:44.000	9.12	G6V	75	SACY
169	TYC	7617-549-1	06:26:06.900	-41:02:54.000	10	K0V	10	SACY
170	HD	49078	06:42:07.400	-64:31:26.000	8.11	A9V	10	SACY
171	HD	51062	06:53:47.400	-43:06:51.000	9.19	G5V	75	SACY
172	HD	51797	06:56:23.500	-46:46:55.000	9.84	K0V(e)	9	SACY
173	1RXS	J070153.4-422759	07:01:53.400	-42:27:56.000	10.61	K1V	85	SACY
174	TYC	8558-1148-1	07:10:50.600	-57:36:46.000	10.44	G2V	75	SACY
175	TYC	8559-1016-1	07:21:23.700	-57:20:37.000	10.72	K0V	75	SACY
176	CD-84	80	07:30:59.500	-84:19:28.000	9.96	G9V	9	SACY
177	TYC	8911-2430-1	07:43:42.900	-61:07:17.000	10.82	K0V(e)	75	SACY
178	TYC	8142-1112-1	07:47:26.000	-49:02:51.000	10.61	G7V	25	SACY
179	CD-38	4458	08:26:10.000	-39:02:05.000	10.31	G9V	40	SACY
180	EG	Cha	08:36:56.200	-78:56:46.000	10.58	K4Ve	8	SACY
182	TYC	8577-1672-1	08:50:08.100	-57:45:59.000	10.21	K3Ve	70	SACY
183	1RXS	J090929.2-553825	09:09:29.400	-55:38:27.000	10.2	G8V	80	SACY
185	HD	81544	09:23:35.000	-61:11:36.000	10.86	K1V(e)	10	SACY
186	TYC	8584-2642-1	09:32:26.100	-52:37:40.000	10.86	G8V(e)	30	SACY
187	HD	84075	09:36:17.800	-78:20:42.000	8.59	G2	75	Guen
188	BD-20	2977	09:39:51.400	-21:34:17.000	10.22	G9V	35	SACY
189	TYC	7697-2254-1	09:47:19.900	-40:03:10.000	10.89	K0V	60	SACY
190	HD	86588	09:53:13.700	-79:33:28.000	9.61	F6	75	Guen
191	HD	86021	09:54:11.000	-53:38:28.000	10.73	G5V	9	SACY
192	HD	309851	09:55:58.300	-67:21:22.000	9.9	G1V	75	SACY
193	HD	310316	10:49:56.100	-69:51:22.000	10.82	G8V	70	SACY
194	CR	Cha	10:59:07.000	-77:01:40.000	11.37	K2	8	Guen
195	HD	310308	10:59:40.900	-69:17:04.000	10.45	G6V	75	SACY
196	DI	Cha	11:07:20.700	-77:38:07.000	10.9	G2	9	Guen
197	CV	Cha	11:12:27.700	-76:44:22.000	10.98	G8	9	Guen
199	HD	98800	11:22:05.300	-24:46:40.000	9.42	K5V	10	SACY
200	1RXS	J112755.0-662558	11:27:55.400	-66:26:4.000	10.82	K1V(e)	9	SACY
201	CD-54	4320	11:45:51.800	-55:20:46.000	10.24	K5Ve	75	SACY
202	1RXS	J115554.5-525332	11:55:57.700	-52:54:01.000	11	K4V	10	SACY
203	T	Cha	11:57:13.500	-79:21:32.000	11.5	G4V	3	Guen
204	RX	J1159.7-7601	11:59:42.300	-76:01:26.000	11	K2	8	Guen
205	TYC	8640-2515-1	12:06:13.500	-57:02:17.000	10.55	G8IV(e)	10	SACY
206	CD-42	7422	12:06:32.900	-42:47:51.000	10.66	K0V	60	SACY
207	TYC	8978-4572-1	12:07:42.400	-62:27:28.000	10.9	K3Ve	8	SACY
209	CD-57	4328	12:11:31.400	-58:16:53.000	10.19	G9V(e)	8	SACY
210	HD	105923	12:11:38.100	-71:10:36.000	9.16	G8V	10	SACY
211	CPD-55	4937	12:14:52.300	-55:47:04.000	9.53	G9V(e)	8	SACY
212	HD	106538	12:15:28.300	-62:32:21.000	9.09	F7V	75	SACY
213	HD	106725	12:16:27.800	-50:08:36.000	10.05	G3V	25	SACY
214	HD	106772	12:17:26.900	-80:35:06.000	8.54	G2	25	Guen
215	TYC	8645-1339-1	12:18:27.600	-59:43:13.000	10.92	K2Ve	10	SACY
216	CP-64	1859	12:19:21.600	-64:54:10.000	9.87	K3V	9	SACY

Table A.1 – continued from previous page

#	ID	Name	RA	DEC	V mag	SpT	Age	Reference
			h:m:s	deg:m:s	mag		Myr	
217	CD-49	7027	12:21:55.700	-49:46:12.000	10.02	G9V	10	SACY
219	RX	J1233.5-7523	12:33:30.600	-75:23:11.500	9.47	K1	0.5	JMSB
220	1RXS	J123332.4-571345	12:33:33.800	-57:14:07.000	10.92	K1V(e)	7	SACY
221	TYC	9412-59-1	12:39:21.300	-75:02:39.000	10.3	K3Ve	8	SACY
222	TYC	8654-1115-1	12:39:38.000	-57:31:41.000	10.12	G9V	9	SACY
223	CD-39	7793	12:43:51.800	-39:46:16.000	10.8	K0V	8	SACY
224	HD	110817	12:45:06.800	-47:42:58.000	10.4	K1Ve	10	SACY
225	HD	111170	12:47:51.866	-51:26:38.146	9.53	G9V	20	FEPS
226	TYC	8655-149-1	12:48:48.200	-56:35:38.000	10.4	G8IV	10	SACY
227	CD-69	1055	12:58:25.600	-70:28:49.000	9.95	K0Ve	8	SACY
229	HD	117524	13:31:53.614	-51:13:33.192	9.92	G5/G6V	20	FEPS
231	HD	118072	13:34:57.400	-29:55:24.000	9.26	G3V	15	SACY
232	CPD-75	902	13:49:12.900	-75:49:48.000	9.67	G1V	20	SACY
233	HD	120812	13:52:47.797	-46:44:09.214	9.59	F9V	20	FEPS
234	TYC	9243-1332-1	13:54:07.400	-67:33:45.000	10.93	G6V	65	SACY
235	1RXS	J140602.3-583246	14:06:02.800	-58:32:45.000	10.8	K1Ve	75	SACY
237	HD	124784	14:16:57.900	-49:56:42.000	9.09	G0V	100	SACY
239	HD	125896	14:23:56.400	-50:29:58.000	9.95	G1V	90	SACY
240	HD	126670	14:28:09.302	-44:14:17.432	9.81	G7III/IV	20	FEPS
241	HD	129181	14:42:43.600	-48:47:59.000	8.48	F8V	75	SACY
244	TYC	7833-2037-1	15:00:51.890	-43:31:21.130	11.26	K1	20	FEPS
248	LQ	Lup	15:08:37.800	-44:23:17.000	10.63	G8	10	Guen
253	LT	Lup	15:15:45.400	-33:32:00.000	10.69	K0e	8	SACY
254	LX	Lup	15:18:52.838	-40:50:52.670	11.01	G8	<10	c2dP
255	LY	Lup	15:19:15.990	-40:56:07.700	11.2	K0	<10	c2dP
256	MP	Lup	15:24:32.400	-36:52:02.000	11.3	K1	8	Guen
257	CD-35	10273	15:25:03.600	-36:04:45.000	10.92	K1IV(e)	9	SACY
259	MS	Lup	15:25:59.600	-45:01:16.000	10.87	G7IV	9	SACY
260	TYC	7326-928-1	15:29:38.600	-35:46:51.000	10.43	K1IVe	9	SACY
261	1RXS	J153328.4-665130	15:33:27.500	-66:51:25.000	10.99	K2V(e)	75	SACY
263	RX	J1538.6-3916	15:38:38.300	-39:16:54.000	11.47	K4	8	Guen
264	CD-43	10072	15:38:43.100	-44:11:47.000	10.56	G6IV(e)	8	SACY
265	MU	Lup	15:40:41.200	-37:56:18.000	4.27	K6	8	Guen
266	GSC	06785-00476	15:41:06.800	-26:56:26.000	11.33	G7	9	Guen
267	GSC	06781-01046	15:42:49.900	-25:36:41.000	10.7	G5	65	Guen
268	HT	Lup	15:45:12.900	-34:17:30.500	10.4	K2	1	c2dL
269	HD	327427	15:45:42.700	-46:32:33.000	9.98	G5IV	70	SACY
270	HD	140637	15:45:47.600	-30:20:56.000	9.28	K2V	8	SACY
271	TYC	7845-1174-1	15:45:52.245	-42:22:16.431	10.6	K1	20	FEPS
272	RX	J1546.6-3618	15:46:41.000	-36:18:47.500	11.28	K1	8.5	JMSB
273	RX	J1547.6-4018	15:47:41.800	-40:18:26.700	11.08	K1	7	JMSB
274	GQ	Lup	15:49:12.100	-35:39:05.000	11.4	K8	1	c2dL
276	HD	141521	15:51:13.733	-42:18:51.336	9.57	G8V	20	FEPS
277	HBC	603	15:51:47.000	-35:56:43.000	11	M0	5	Guen
278	RU	Lup	15:56:42.312	-37:49:15.474	11.4	G5V	1	Sche
279	GSC	06195-00768	15:57:02.400	-19:50:41.000	11.5	K7	5	Guen
280	HD	142987	15:58:20.600	-18:37:25.000	10.1	G3	9	Guen
282	RY	Lup	15:59:28.400	-40:21:51.000	11.1	G0	2	Guen
283	CD-36	10569	15:59:49.500	-36:28:28.000	10.88	K3e	8	SACY
284	MZ	Lup	16:01:09.000	-33:20:14.000	10.95	G5IVe	6	SACY
286	EX	Lup	16:03:05.500	-40:18:25.000	11	M0	9	Guen
288	TYC	7855-1106-1	16:03:52.499	-39:39:00.910	11.02	K3	<10	c2dP

Table A.1 – continued from previous page

#	ID	Name	RA	DEC	V mag	SpT	Age	Reference
			h:m:s	deg:m:s	mag		Myr	
289	TYC	7334-429-1	16:04:30.600	-32:07:29.000	10.88	K2e	10	SACY
291	GSC	06784-01219	16:05:50.600	-25:33:14.000	10.93	K1V(e)	10	SACY
292	GSC	06784-00039	16:08:43.400	-26:02:17.000	10.24	G7	8	Guen
294	V1096	Sco	16:10:04.869	-40:16:11.060	11.2	K2	<10	c2dP
295	V1002	Sco	16:12:40.500	-18:59:28.000	11	K0	6	Guen
296	BD-21	4301	16:13:18.600	-22:12:49.000	10.95	K1IV(e)	8	SACY
297	TYC	7355-317-1	16:13:58.000	-36:18:13.000	11	K0V(e)	9	SACY
298	GSC	06793-00994	16:14:02.100	-23:01:01.000	11.5	G4	9	Guen
299	TYC	6793-819-1	16:14:11.100	-23:05:36.000	10.66	K2IV	8	SACY
300	CD-50	10271	16:14:52.000	-50:26:18.000	10.24	K1V	10	SACY
301	GSC	06801-00186	16:14:59.251	-27:50:21.760	11	G5	5	FEPS
302	GSC	06801-00186	16:14:59.300	-27:50:22.000	11.5	G5	9	Guen
303	GSC	06793-01406	16:16:18.000	-23:39:47.000	10.8	G7	9	Guen
305	GSC	06214-02384	16:19:34.000	-22:28:29.000	11.5	K0	9	Guen
306	CD-33	11099	16:19:50.600	-33:54:45.000	10.11	G6V	10	SACY
307	HD	147048	16:21:12.200	-40:30:21.000	10.38	G9IV	9	SACY
309	GSC	06798-00035	16:23:32.300	-25:23:48.000	11.1	G1	9	Guen
312	HD	147808	16:24:51.400	-22:39:33.000	9.66	G9IVe	9	SACY
313	CD-24	12683	16:25:19.200	-24:26:53.000	10.55	G9V	15	SACY
315	GSC	06794-00337	16:27:39.600	-22:45:22.000	11.5	K1	8	Guen
316	V2129	Oph	16:27:40.300	-24:22:03.000	11.38	K3	5	Guen
317	HD	148440	16:29:20.200	-30:57:40.000	9.87	G9V(e)	15	SACY
318	V2505	Oph	16:29:48.700	-21:52:12.000	11.06	K0	<10	c2dP
319	1RXS	J162950.1-272834	16:29:49.900	-27:28:50.000	11.01	K1V(e)	7	SACY
320	CD-29	12588	16:30:38.000	-29:54:22.000	10.94	K2Ve	8	SACY
322	ROX	43	16:31:20.100	-24:30:05.000	10.57	G0	12.2	c2dL
323	TYC	7353-2640-1	16:31:42.000	-35:05:17.000	10.73	K0V	10	SACY
324	1RXS	J163349.9-511908	16:33:50.400	-51:19:01.000	10.75	K2V(e)	10	SACY
325	1RXS	J163743.5-335703	16:37:43.400	-33:56:53.000	10.79	G8V	10	SACY
326	HD	321857	16:39:59.300	-39:24:59.000	10.32	G8V	10	SACY
327	CD-30	13383	16:42:07.700	-30:38:38.000	10.6	G8V	10	SACY
329	HD	321958	16:46:40.300	-38:08:51.000	10.97	G9V	20	SACY
330	Wa	Oph6	16:48:45.600	-14:16:35.800	11.4	K7	0.9	c2dL
331	V1121	Oph	16:49:15.300	-14:22:08.800	11.5	K5	0.5	c2dL
332	1RXS	J164935.8-272810	16:49:36.000	-27:28:08.000	10.65	K0Ve	85	SACY
333	AK	Sco	16:54:44.849	-36:53:18.572	9.14	F5Ve	6	Sche
334	TYC	8726-57-1	16:59:55.300	-52:46:20.000	10.75	G9V	40	SACY
335	HD	153481	17:00:49.900	-25:47:07.000	10.02	G3V	25	SACY
336	CD-31	13486	17:02:27.800	-32:04:36.000	10.13	G8V	40	SACY
337	HD	153888	17:03:33.200	-32:36:51.000	9.15	G0V	60	SACY
338	BD-18	4452	17:13:11.600	-18:34:25.000	10.86	M0Ve	75	SACY
339	CD-27	11535	17:15:03.600	-27:49:40.000	10.66	K5Ve	8	SACY
340	TYC	6812-348-1	17:16:18.100	-23:10:47.000	10.97	K3Ve	8	SACY
341	CD-28	12998	17:17:21.400	-28:36:41.000	10.21	G6V	40	SACY
342	HD	155915	17:18:14.600	-60:27:28.000	9.48	G8V	65	SACY
343	1RXS	J172228.9-372657	17:22:29.000	-37:26:56.000	10.95	K2V(e)	9	SACY
344	HD	317637	17:27:25.500	-33:16:49.000	10.88	K2V	9	SACY
347	HD	160682	17:42:30.400	-28:44:56.000	9.03	G5V	9	SACY
348	HD	161460	17:48:33.700	-53:06:43.000	9.61	K0IV	9	SACY
351	HD	173148	18:45:34.800	-37:50:20.000	9.17	G5	9	Guen
352	RX	J1853.1-3609	18:53:05.900	-36:10:22.800	9.6	K2	9	JMSB
353	CrAPMS	4SE	18:57:20.700	-36:43:00.300	10.95	G5	20	JMSB

Table A.1 – continued from previous page

#	ID	Name	RA	DEC	V mag	SpT	Age	Reference
			h:m:s	deg:m:s	mag		Myr	
355	S	CrA	19:01:08.600	-36:57:20.000	10.7	K6	30	Guen
357	V709	CrA	19:01:34.900	-37:00:57.000	11.24	K0	8	Guen
358	CD-37	13029	19:02:02.000	-37:07:44.000	10.53	G5e	6	SACY
359	HD	178085	19:10:57.900	-60:16:20.000	8.34	G1V	80	SACY
360	CD-26	13904	19:11:44.700	-26:04:09.000	10.27	K4V(e)	25	SACY
361	CD-38	13398	19:17:23.800	-37:56:50.000	9.99	K0IVe	5	SACY
362	TYC	7952-273-1	20:11:12.600	-40:32:04.000	10.71	G2V	70	SACY
363	HD	195289	20:33:13.300	-58:06:44.000	7.85	F8V	10	SACY
364	CD-33	15436	21:11:55.200	-32:58:37.000	10.58	K2V(e)	100	SACY
365	HD	207278	21:48:48.500	-39:29:09.000	9.66	G7V	80	SACY
366	CD-47	14100	22:13:16.700	-47:13:56.000	10.37	K0V	60	SACY
367	HD	211087	22:15:35.200	-39:00:51.000	9.32	K0V	80	SACY
368	HD	211712	22:20:07.500	-48:37:38.000	10.07	G4V	10	SACY
369	1RXS	J223929.1-520525	22:39:30.300	-52:05:17.000	10.85	K0V	75	SACY
370	CP-72	2713	22:42:48.900	-71:42:21.000	10.6	K7Ve	9	SACY
371	CD-40	14901	22:46:33.500	-39:28:45.000	9.42	G5V	80	SACY
372	HD	217897	23:05:52.000	-35:51:11.000	7.35	M2V	60	SACY
373	BD-03	5579	23:09:37.100	-02:25:55.000	10.99	K4Ve	100	SACY
374	HD	220054	23:21:52.500	-69:42:12.000	9.91	G8V	15	SACY
375	TYC	584-343-1	23:21:56.400	07:21:33.000	10.97	K0V	10	SACY
376	BD-13	6424	23:32:30.900	-12:15:52.000	10.54	M0Ve	10	SACY
377	HD	25457	04:02:36.744	00:16:08.123	5.38	F5V	100	SACY

B Results on stellar parameter, activity and radial velocity variation

In this Appendix, I present the results for the observed and analysed stars.
The first table lists all 100 observed stars. Listed are the ID, star name, coordinates, V magnitude and spectral type. In the Notes column, *qualified* shows that enough observations are available to analyse the RV variation in Chapter 6, otherwise the reason for disqualification is given. In addition, the number of observations and the age inferred by the analysis in Section 5.1.1 is listed.

TABLE B.1 : List of stars from Table A.1 that have been observed for this study.

#	ID	Name	RA	DEC	V mag	SpT	Notes	# obs	Age	σ_{age}
			h:m:s	deg:m:s	mag				Myr	Myr
1	HD	224725	00:00:12.0	01:46:17.0	11.0	G9V	high $v \sin i$	2	30	15
2	CD	78 24	00:42:20.0	-77:47:40.0	10.2	K3V	qualified	13	15	10
4	CD	31 571	01:24:52.0	-30:44:45.0	10.3	K2V	no variation	5	30	10
5	CCDM	J01377+1836	01:37:39.0	18:35:33.0	9.9	K2	less obs	1	8	3
9	HD	17662	02:50:30.0	11:52:12.0	8.5	G5	less obs	1	250	50
18	CD	37 1123	03:00:47.0	-37:08:02.0	10.5	G9V	qualified	15	30	15
31	HD	21955	03:31:21.0	-30:30:59.0	9.9	G7IV	high $v \sin i$	3	30	10
32	1RXS	J033149.8-633155	03:31:49.0	-63:31:54.0	10.9	K0V	qualified	13	25	15
36	HD	23208	03:42:40.0	-20:32:44.0	9.2	G8V	less obs	3	25	10
56	CD	31 1688	04:05:52.0	-31:38:38.0	10.0	G6IV	high $v \sin i$	4	30	10
63	CD	58 860	04:11:56.0	-58:01:47.0	10.0	G6V	high $v \sin i$	1	30	15
65	HD	26980	04:14:23.0	-38:19:02.0	9.0	G3V	less obs	1	75	15
71	CD	43 1395	04:21:49.0	-43:17:33.0	10.2	G7V	high $v \sin i$	3	30	10
79	CD	43 1451	04:30:27.0	-42:48:47.0	10.8	G9V	less obs	3	15	5
86	TYC	5891-69-1	04:32:43.0	-15:20:11.0	10.4	G4V	qualified	14	10	5
88	1RXS	J043451.0-354715	04:34:51.0	-35:47:21.0	10.8	K1V	less obs	2	20	15
91	V1204	Tau	04:38:39.0	15:46:13.0	10.7	K2	activity	1	3	2
105	HD	31950	05:00:24.0	15:05:25.0	9.9	G	less obs	1	30	15
106	HD	286264	05:00:49.0	15:26:60.0	11.0	G0	less obs	1	3	2
107	HD	32372	05:00:52.0	-41:01:07.0	9.5	G5V	less obs	1	30	15
121	HD	34700	05:19:44.0	05:39:39.0	9.2	G	multiple	1	100	50
132	GW	Ori	05:29:08.0	11:52:13.0	9.9	K3V	qualified	38	5	2
135	HD	36329	05:29:24.0	-34:30:56.0	9.2	G3V	less obs	1	20	10

Table B.1 – continued from previous page

#	ID	Name	RA	DEC	V mag	SpT	Notes	# obs	Age	σ_{age}
			h:m:s	deg:m:s	mag				Myr	Myr
136	HD	269620	05:29:27.0	-68:52:05.0	9.6	G6V	less obs	1	75	15
151	HD	37551	05:37:13.0	-42:42:56.0	9.6	G7V	less obs	1	100	20
161	HD	42270	05:53:29.0	-81:56:53.0	9.1	K0V	less obs	1	20	10
167	HD	44748	06:21:57.0	-34:30:44.0	9.1	G6V	less obs	1	80	15
170	HD	49078	06:42:07.0	-64:31:26.0	8.1	A9V	less obs	1	100	30
171	HD	51062	06:53:47.0	-43:06:51.0	9.2	G5V	qualified	6	200	50
172	HD	51797	06:56:23.0	-46:46:55.0	9.8	K0V	less obs	4	30	15
173	1RXS	J070153.4-422759	07:01:53.0	-42:27:56.0	10.6	K1V	less obs	1	30	15
174	TYC	8558-1148-1	07:10:51.0	-57:36:46.0	10.4	G2V	high $v \sin i$	1	75	15
175	TYC	8559-1016-1	07:21:24.0	-57:20:37.0	10.7	K0V	less obs	1	55	15
176	CD	84 0080	07:30:59.0	-84:19:28.0	10.0	G9V	qualified	34	30	15
177	TYC	8911-2430-1	07:43:43.0	-61:07:17.0	10.8	K0V	less obs	1	30	15
178	TYC	8142-1112-1	07:47:26.0	-49:02:51.0	10.6	G7V	high $v \sin i$	1	80	15
179	CD	38 4458	08:26:10.0	-39:02:05.0	10.3	G9V	less obs	1	30	15
180	EG	Cha	08:36:56.0	-78:56:46.0	10.6	K4V	qualified	11	5	2
185	HD	81544	09:23:35.0	-61:11:36.0	10.9	K1V	qualified	3	8	3
189	TYC	7697-2254-1	09:47:20.0	-40:03:10.0	10.9	K0V	qualified	18	25	10
194	CR	Cha	10:59:06.9	-77:01:40.3	11.4	K4V	less obs	2	5	3
196	DI	Cha	11:07:21.0	-77:38:07.0	10.9	G2	qualified	46	5	2
203	T	Cha	11:57:13.0	-79:21:32.0	11.5	G4V	qualified	23	4	2
219	RX	J1233.5-7523	12:33:31.0	-75:23:11.0	11.5	K1	qualified	11	90	15
220	1RXS	J123332.4-571345	12:33:34.0	-57:14:07.0	10.9	K1V	qualified	10	8	5
221	TYC	9412-59-1	12:39:21.0	-75:02:39.0	10.2	K3V	qualified	9	5	3
222	TYC	8654-1115-1	12:39:38.0	-57:31:41.0	10.1	G9V	qualified	6	5	3
227	CD	69 1055	12:58:26.0	-70:28:49.0	10.0	K0V	qualified	29	5	3
237	HD	124784	14:16:58.0	-49:56:42.0	9.1	G0	less obs.	4	200	50
241	HD	129181	14:42:44.0	-48:47:59.0	8.5	F8V	high $v \sin i$	3	110	30
248	LQ	Lup	15:08:38.0	-44:23:17.0	10.6	G8	high $v \sin i$	2	20	15
253	LT	Lup	15:15:45.0	-33:32:00.0	10.7	K0	qualified	12	8	3
254	LX	Lup	15:18:53.0	-40:50:53.0	11.0	G8	high $v \sin i$	1	...	...
255	LY	Lup	15:19:16.0	-40:56:08.0	11.2	K0	qualified	16	3	2
256	MP	Lup	15:24:32.0	-36:52:02.0	11.3	K1	less obs	4	5	3
259	MS	Lup	15:25:60.0	-45:01:16.0	10.9	G7IV	less obs	2	5	3
261	1RXS	J153328.4-665130	15:33:27.0	-66:51:25.0	11.0	K2V	qualified	66	30	15
263	RX	J1538.6-3916	15:38:38.0	-39:16:54.0	11.5	K4	less obs	1	8	4
264	CD	43 10072	15:38:43.0	-44:11:47.0	10.6	G6IV	less obs	1	7	3
265	MU	Lup	15:40:41.0	-37:56:18.0	4.3	K6	less obs	2	3	2
268	HT	Lup	15:45:13.0	-34:17:30.0	10.4	K2	high $v \sin i$	1	5	2
270	HD	140637	15:45:47.0	-30:20:56.0	9.3	K2	less obs	2	5	2
273	RX	J1547.6-4018	15:47:42.0	-40:18:27.0	11.1	K1	less obs	1	8	3
274	GQ	Lup	15:49:12.0	-35:39:05.0	11.4	K8	qualified	26	2	1
277	IM	Lup	15:56:09.0	-37:56:06.0	10.0	M0	less obs	4	5	3
277B	HBC	603	15:51:47.0	-35:56:43.0	11.0	M0	qualified	7	5	3
278	RU	Lup	15:56:42.0	-37:49:15.0	11.4	G5V	high $v \sin i$	2	2	1
279	GSC	06195-00768	15:57:02.0	-19:50:41.0	11.5	K7	less obs	1	5	2
282	RY	Lup	15:59:28.0	-40:21:51.0	11.1	G0	less obs	1	2	1
283	CD	36 10569	15:59:49.0	-36:28:28.0	10.9	K3	less obs	1	3	2
284	MZ	Lup	16:01:09.0	-33:20:14.0	11.0	G5IV	less obs	1	5	2
286	EX	Lup	16:03:05.0	-40:18:25.0	11.0	M0	less obs	4	5	2
289	TYC	7334-429-1	16:04:31.0	-32:07:29.0	10.9	K2	less obs	1	10	3
295	V1002	Sco	16:12:40.0	-18:59:28.0	11.0	K0	high $v \sin i$	2	4	2
307	HD	147048	16:21:12.0	-40:30:21.0	10.4	G9IV	less obs	1	30	15

Table B.1 – continued from previous page

#	ID	Name	RA	DEC	V mag	SpT	Notes	# obs	Age	σ_{age}
			h:m:s	deg:m:s	mag				Myr	Myr
315	EM*	SR21	16:27:10.0	-24:19:13.0	14.1	M	high $v \sin i$	3	...	...
316	V2129	Oph	16:27:40.0	-24:22:03.0	11.4	K3	less obs	4	3	2
319	1RXS	J162950.1-272834	16:29:50.0	-27:28:50.0	11.0	K1	less obs	1	5	2
322	DoAr	44	16:31:33.0	-24:27:37.0	11.0	K3	less obs	3	5	3
330	Wa	Oph6	16:48:46.0	-14:16:36.0	11.4	K7	less obs	2	1	1
331	V1121	Oph	16:49:15.0	-14:22:09.0	11.5	K5	less obs	2	8	3
334	TYC	8726-57-1	16:59:55.0	-52:46:20.0	10.8	G9	less obs	3	25	15
339	CD	27 11535	17:15:04.0	-27:49:40.0	10.7	K5V	less obs	1	6	3
340	TYC	6812-348-1	17:16:18.0	-23:10:47.0	11.0	K3V	less obs	2	5	2
345	HD	319896	17:31:06.0	-35:08:29.0	11.0	F8	high $v \sin i$	1	...	...
348	HD	161460	17:48:34.0	-53:06:43.0	9.6	K0IV	less obs	1	30	15
357	V709	CrA	19:01:35.0	-37:00:57.0	11.2	K0	high $v \sin i$	4	5	2
358	CD	37 13029	19:02:02.0	-37:07:44.0	10.5	G5	qualified	6	5	2
361	CD	38 13398	19:17:24.0	-37:56:50.0	10.0	K0	less obs	1	3	2
365	HD	207278	21:48:48.0	-39:29:09.0	9.7	G7V	less obs	1	50	10
369	1RXS	J223929.1-520525	22:39:30.0	-52:05:17.0	10.9	K0V	qualified	10	60	15
370	CP	72 2713	22:42:49.0	-71:42:21.0	10.6	K7V	qualified	6	8	1
371	CD	40 14901	22:46:33.0	-39:28:45.0	9.4	G5V	less obs	3	75	15
372	HD	217897	23:05:52.0	-35:51:11.0	7.4	M2	qualified	7	30	15
373	BD	03 5579	23:09:37.0	-02:25:55.0	11.0	K4V	less obs	1	50	15
374	HD	220054	23:21:52.0	-69:42:12.0	9.9	G8V	less obs	1	30	10
375	TYC	584-343-1	23:21:56.0	07:21:33.0	11.0	K0V	qualified	7	30	15
376	BD	13 6424	23:32:31.0	-12:15:52.0	10.5	M0V	less obs	1	30	15
377	HD	25457	04:02:37.0	00:16:08.0	5.4	F5	less obs	3	50	15

B.1 Stellar parameters of target stars

In this table, the results for T_{eff}, $\log g$, microturbulence, metallicity, $(b-v)$, mean stellar activity index $\langle S_{\mathrm{FEROS}} \rangle$, and the corrected stellar activity index $\log R'_{\mathrm{FEROS}}$ are listed for all observed targets. In the last column, the 16 stars observed with HARPS are marked. For these stars no measurements of the stellar parameter are available because not all Fe I lines needed for the calculation are included in the wavelength range of HARPS. For some other stars, no measurements of stellar parameters was also not possible because of high $v \sin i$ that blends the spectral lines.

TABLE B.2 : Results for the basic stellar parameter of the 100 observed targets.

#	Name	$T_{\rm eff}$ K	$\sigma_{T_{\rm eff}}$ K	$\log g$ cms^{-2}	$\sigma_{\log g}$ cms^{-2}	v_t kms^{-1}	σ_{v_t} kms^{-1}	[Fe/H] $\odot$	$\sigma_{\rm [Fe/H}$ $\odot$	$(b-v)$ mag	$\langle S_{\rm FEROS}\rangle$	$\log R'_{\rm FEROS}$	Note
1	HD 224725	...	...	...	...	...	...	...	...	...	0.36	...	
2	CD 78 24	4845	120	5.2	0.3	1.50	0.50	-0.07	0.08	1.00	0.50	-4.65	
4	CD 31 571	4915	85	4.5	0.3	1.73	0.43	-0.14	0.11	0.96	0.84	-4.33	
5	CCDM J01377+1836	4430	140	4.5	0.3	1.62	0.50	-0.15	0.13	1.23	1.20	-4.62	
9	HD 17662	7140	110	4.7	0.3	2.16	0.25	0.77	0.07	0.34	0.57	-4.21	
18	CD 37 1123	5650	130	5.8	0.4	1.50	0.50	0.00	0.10	0.67	0.48	-4.25	
31	HD 21955	5309	38	5.2	0.3	0.88	0.25	-0.25	0.04	0.79	0.30	-4.63	
32	1RXS J033149.8-633155	5145	83	4.7	0.2	1.48	0.30	-0.15	0.05	0.86	0.42	-4.53	
36	HD 23208	...	...	...	...	...	...	...	...	...	...	...	HARPS
56	CD 31 1688	5190	100	4.9	0.3	1.41	0.25	-0.33	0.06	0.84	0.50	-4.41	
63	CD 58 860	5280	90	5.0	0.3	0.27	0.25	-0.23	0.06	0.80	0.47	-4.40	
65	HD 26980	5689	100	5.2	0.3	1.69	0.25	-0.02	0.06	0.66	0.30	-4.51	
71	CD 43 1395	5471	75	5.2	0.3	1.62	0.25	-0.07	0.06	0.73	0.47	-4.31	
79	CD 43 1451	5172	50	4.8	0.1	1.65	0.32	-0.12	0.08	0.84	0.60	-4.32	
86	TYC 5891-69-1	5200	120	3.6	0.4	2.00	0.30	-0.36	0.12	0.83	0.61	-4.30	
88	1RXS J043451.0-354715	5382	40	5.3	0.1	1.70	0.32	0.14	0.06	0.76	0.84	-4.06	
91	V1204 Tau	5149	90	4.5	0.3	1.81	0.50	0.10	0.17	0.85	0.27	-4.77	
105	HD 31950	...	...	...	...	...	...	...	...	...	...	...	HARPS
106	HD 286264	5980	110	8.7	0.5	2.78	0.50	0.32	0.08	0.57	0.66	-4.03	
107	HD 32372	5952	43	5.5	0.2	1.56	0.34	0.20	0.06	0.58	...	...	
121	HD 34700	...	...	...	...	...	...	...	...	...	0.08	...	
132	GW Ori	...	...	...	...	...	...	...	...	...	1.35	...	
135	HD 36329	5869	140	5.1	0.5	1.99	0.50	-0.30	0.13	0.61	0.41	-4.30	
136	HD 269620	5592	50	4.6	0.2	1.05	0.37	0.08	0.11	0.69	0.37	-4.41	
151	HD 37551	5833	25	5.5	0.1	0.61	0.25	0.33	0.04	0.61	0.49	-4.20	
161	HD 42270	5192	100	4.7	0.3	1.73	0.25	-0.17	0.06	0.84	0.70	-4.25	
167	HD 44748	5857	100	5.5	0.3	0.11	0.25	0.23	0.06	0.61	0.19	-4.78	
170	HD 49078	...	...	...	...	...	...	...	...	...	0.09	...	
171	HD 51062	5470	60	4.7	0.2	2.00	0.30	-0.33	0.03	0.73	0.26	-4.65	
172	HD 51797	...	...	...	...	...	...	...	...	...	...	...	HARPS
173	1RXS J070153.4-422759	5415	53	5.0	0.2	1.25	0.31	0.13	0.07	0.75	0.62	-4.20	
174	TYC 8558-1148-1	5859	65	4.9	0.2	0.36	0.31	0.19	0.07	0.61	0.33	-4.43	

Table B.2 – continued from previous page

#	Name	$T_{\rm eff}$ K	$\sigma_{T_{\rm eff}}$ K	$\log g$ cms^{-2}	$\sigma_{\log g}$ cms^{-2}	v_t kms^{-1}	σ_{v_t} kms^{-1}	[Fe/H]	$\sigma_{\rm [Fe/H}$	$(b-v)$ mag	$\langle S_{\rm FEROS}\rangle$	$\log R'_{\rm FEROS}$	Note
175	TYC 8559-1016-1	5433	28	5.1	0.1	0.81	0.27	0.17	0.05	0.74	0.87	-4.02	
176	CD 84 0080	5515	25	5.2	0.1	1.00	0.30	0.01	0.05	0.71	0.29	-4.56	
177	TYC 8911-2430-1	5179	125	4.5	0.3	1.23	0.50	0.04	0.17	0.84	0.79	-4.19	
178	TYC 8142-1112-1	5506	100	3.8	0.5	1.31	0.50	0.04	0.10	0.72	0.25	-4.66	
179	CD 38 4458	5959	100	5.6	0.5	0.68	0.25	0.31	0.03	0.58	0.50	-4.18	
180	EG Cha	5260	130	5.6	0.5	2.60	0.50	-0.01	0.10	0.81	1.05	-4.02	
185	HD 81544	5501	100	5.4	0.2	0.17	0.25	0.35	0.03	0.72	0.22	-4.73	
189	TYC 7697-2254-1	5410	40	4.8	0.1	1.40	0.40	0.05	0.09	0.75	0.61	-4.21	
194	CR Cha	...	...	...	...	...	...	...	...	...	...	...	HARPS
196	DI Cha	5820	80	4.0	0.2	1.80	0.30	0.18	0.13	0.62	0.31	-4.46	
203	T Cha	5695	235	5.0	0.5	2.10	0.50	0.15	0.13	0.66	0.28	-4.55	
219	RX J1233.5-7523	5660	35	5.2	0.1	0.20	0.40	0.17	0.04	0.67	0.32	-4.47	
220	1RXS J123332.4-571345	4810	90	5.0	0.2	1.70	0.30	-0.04	0.07	1.02	1.13	-4.29	
221	TYC 9412-59-1	4890	120	5.0	0.3	1.50	0.50	0.02	0.10	0.98	0.71	-4.45	
222	TYC 8654-1115-1	5235	25	3.7	0.2	1.72	0.25	-0.10	0.09	0.82	...	...	
227	CD 69 1055	4835	105	4.8	0.3	1.67	0.41	-0.01	0.11	1.01	0.72	-4.49	
237	HD 124784	5674	108	4.4	0.3	0.48	0.28	-0.39	0.10	0.66	0.20	-4.79	
241	HD 129181	...	...	...	...	...	...	...	...	...	0.16	...	
248	LQ Lup	...	...	...	...	...	...	...	...	...	0.61	...	
253	LT Lup	5400	105	5.6	0.4	2.00	0.50	0.07	0.11	0.76	0.64	-4.19	
254	LX Lup	...	...	...	...	...	...	...	...	...	0.35	...	
255	LY Lup	4800	90	4.1	0.3	1.84	0.37	-0.08	0.14	1.02	0.68	-4.53	
256	MP Lup	4992	65	4.5	0.2	1.17	0.38	-0.03	0.11	0.93	0.47	-4.57	
259	MS Lup	5263	93	4.9	0.3	1.84	0.40	-0.10	0.11	0.81	0.70	-4.21	
261	1RXS J153328.4-665130	4770	50	4.4	0.2	1.90	0.50	-0.10	0.08	1.04	1	-4.34	
263	RX J1538.6-3916	4781	80	4.4	0.2	1.52	0.25	-0.04	0.07	1.03	0.41	-4.81	
264	CD 43 10072	5461	188	5.0	0.5	2.84	0.50	-0.16	0.15	0.73	0.81	-4.05	
265	MU Lup	5290	100	5.3	0.5	2.78	0.50	0.04	0.10	0.80	0.24	-4.77	
268	HT Lup	...	...	...	...	...	...	...	...	...	...	...	HARPS
270	HD 140637	5001	45	4.8	0.1	1.95	0.25	0.04	0.05	0.92	1.32	-4.06	
273	RX J1547.6-4018	5121	53	4.9	0.2	1.44	0.25	0.13	0.03	0.87	0.49	-4.46	
274	GQ Lup	4650	120	3.1	0.5	1.10	0.40	-0.55	0.20	1.11	0.96	-4.52	
277	IM Lup	...	...	...	...	...	...	...	...	...	...	...	HARPS

Table B.2 – continued from previous page

#	Name	$T_{\rm eff}$ K	$\sigma_{T_{\rm eff}}$ K	$\log g$ cms^{-2}	$\sigma_{\log g}$ cms^{-2}	v_t kms^{-1}	σ_{v_t} kms^{-1}	[Fe/H]	$\sigma_{\rm [Fe/H}$	$(b-v)$ mag	$\langle S_{\rm FEROS}\rangle$	$\log R'_{\rm FEROS}$	Note
277B	HBC 603	...	...	...	...	...	...	...	...	...	...	...	HARPS
278	RU Lup	...	...	...	...	...	...	...	...	...	...	...	HARPS
279	GSC 06195-00768	4674	100	3.6	0.5	1.68	0.50	-0.11	0.10	1.09	0.73	-4.61	
282	RY Lup	...	...	...	...	...	...	...	...	...	...	...	HARPS
283	CD 36 10569	4916	100	4.4	0.3	2.65	0.50	-0.23	0.13	0.96	0.48	-4.61	
284	MZ Lup	4944	70	3.2	0.3	1.68	0.24	-0.40	0.12	0.95	0.49	-4.59	
286	EX Lup	4930	175	4.0	0.5	1.48	0.50	-0.69	0.18	0.95	0.89	-4.29	
289	TYC 7334-429-1	...	...	...	...	...	...	...	...	...	...	...	HARPS
295	V1002 Sco	...	...	...	...	...	...	...	...	...	...	...	HARPS
307	HD 147048	5171	78	4.8	0.2	1.69	0.38	-0.04	0.11	0.84	...	...	
315	EM* SR21	...	...	...	...	...	...	...	...	...	...	...	HARPS
316	V2129 Oph	4476	55	3.4	0.2	1.89	0.24	-0.39	0.14	1.20	1.28	-4.53	
319	1RXS J162950.1-272834	4767	45	4.1	0.1	1.74	0.25	-0.12	0.10	1.04	0.64	-4.59	
322	DoAr 44	...	...	...	...	...	...	...	...	...	...	...	HARPS
330	Wa Oph6	...	...	...	...	...	...	...	...	...	...	...	HARPS
331	V1121 Oph	6504	100	5.9	0.5	2.01	0.50	0.72	0.10	0.45	0.18	-5.01	
334	TYC 8726-57-1	5299	55	4.6	0.2	1.07	0.35	0.12	0.11	0.79	0.47	-4.38	
339	CD 27 11535	4500	70	3.6	0.2	2.05	0.25	-0.57	0.11	1.19	0.93	-4.67	
340	TYC 6812-348-1	4703	120	4.4	0.3	1.75	0.46	0.01	0.15	1.08	0.72	-4.61	
345	HD 319896	...	...	...	...	...	...	...	...	...	...	...	HARPS
348	HD 161460	5405	95	4.6	0.3	0.84	0.34	-0.37	0.09	0.75	0.72	-4.12	
357	V709 CrA	...	...	...	...	...	...	...	...	...	...	...	
358	CD 37 13029	5570	80	5.1	0.3	2.10	0.50	0.00	0.11	0.70	0.68	-4.10	
361	CD 38 13398	4881	140	5.4	0.4	0.97	0.50	-0.03	0.09	0.98	1.26	-4.18	
365	HD 207278	5919	100	5.7	0.2	0.50	0.25	0.28	0.03	0.59	0.21	-4.70	
369	1RXS J223929.1-520525	5500	50	5.3	0.2	1.30	0.30	0.13	0.06	0.72	0.48	-4.30	
370	CP 72 2713	5150	170	5.1	0.4	2.00	0.50	0.11	0.12	0.85	1.35	-3.95	
371	CD 40 14901	5539	83	4.9	0.5	0.99	0.50	-0.11	0.07	0.71	0.29	-4.56	
372	HD 217897	5620	215	5.0	0.5	4.00	0.50	-0.18	0.15	0.68	0.63	-4.12	
373	BD 03 5579	4971	110	5.1	0.3	1.20	0.50	0.10	0.08	0.94	1.81	-3.95	
374	HD 220054	5503	140	5.4	0.4	1.03	0.50	-0.11	0.13	0.72	0.41	-4.38	
375	TYC 584-343-1	5325	80	4.9	0.2	1.60	0.40	0.05	0.11	0.78	0.39	-4.47	
376	BD 13 6424	5302	125	4.5	0.1	1.20	0.50	-0.27	0.10	0.79	1.48	-3.83	

Table B.2 – continued from previous page

#	Name	$T_{\rm eff}$ K	$\sigma_{T_{\rm eff}}$ K	$\log g$ cms^{-2}	$\sigma_{\log g}$ cms^{-2}	v_t kms^{-1}	σ_{v_t} kms^{-1}	[Fe/H]	$\sigma_{\rm [Fe/H]}$	$(b-v)$ mag	$\langle S_{\rm FEROS}\rangle$	$\log R'_{\rm FEROS}$	Note
377	HD 25457	6470	160	5.2	0.5	0.86	0.48	0.25	0.14	0.47	0.16	-5.10	

B.2 Radial velocity periods of qualified stars

In this Section, I list the values for period P, semi-amplitude K, the false alarm probability (FAP), the eccentricity e, and the χ^2 for the Sine fit and Keplerian fit obtained with GLS.

TABLE B.3 : Periods obtained by GLS for the radial velocity data of the qualified stars.

#	ID	Name	P	K	FAP	P	K	e	χ^2
				Sine-fit			Keplerian fit		
			days	ms^{-1}	0.01%	days	ms^{-1}		
2	CD	78 24	65.21	876.27	0.23	65.18	831.52	0.4	117.27
18	CD	37 1123	2.31	79.94	0.31	2.32	90.57	0.4	97.26
32	1RXS	J033149.8-633155	2.61	476.73	<0.001	2.61	425.96	0.29	5.92
86	TYC	5891-69-1	3.21	431.52	<0.001	3.21	525.01	0.19	11.99
132	GW	Ori	140.44	5900.28	<0.001	154.11	7890.93	0.55	969.87
171	HD	51062	8.25	715.21	0.38	3.54	696.48	0.48	4.126
176	CD	84 0080	5.11	100.53	<0.001	5.11	114.48	0.2	198.58
180	EG	Cha	1.41	1122.5	0.13	2.38	1016.92	0.4	92.50
189	TYC	7697-2254-1	2.35	142.5	0.15	17.45	255.35	0.75	75.82
196	DI	Cha	2.44	758.72	<0.001	2.61	948.35	0.55	13.39
203	T	Cha	7.39	2201.89	<0.001	3.60	2579.62	0.27	14.99
219	RX	J1233.5-7523	3.56	58.52	0.07	4.01	75.2	0.5	20.99
220	1RXS	J123332.4-571345	2.3	867.4	0.73	4.27	825.97	0.5	23.19
221	TYC	9412-59-1	1.2	1256.1	1	1.20	680.6	0.7	24.20
222	TYC	8654-1115-1	4.31	1026.9	0.96	1.93	1376.97	0.7	50.63
227	CD	69 1055	2.03	1720.63	<0.001	1.95	2042.5	0.6	167.31
253	LT	Lup	1.65	1621.19	0.04	2.39	1640.69	0.36	49.47
255	LY	Lup	2.99	726.04	<0.001	1.58	881.88	0.4	244.47
261	1RXS	J153328.4-665130	292.03	143.3	<0.001	292.1	157.21	0.38	110.13
274	GQ	Lup	3.54	759.14	0.1	7.75	977.50	0.47	95.86
277B	HBC	603	5.88	757.74	1	2.87	1928.96	0.5	10.39
358	CD	37 13029	2.24	1380.22	0.09	3.06	41145.32	0.8	21.27
369	1RXS	J223929.1-520525	43.83	181.72	0.01	43.38	176.5	0.2	19.27
370	CP	72 2713	3.98	358.61	0.71	11.38	305.01	0.7	20.25
372	HD	217897	1.98	136.78	0.68	1.62	120.03	0.5	21.47
375	TYC	584-343-1	2.85	512.98	0.14	3.01	767.14	0.7	15.06

B.3 Periods of stellar activity indicators of qualified stars

In this table, the periods of the stellar activity indicators for the 26 stars analysed are listed. The periods and the corresponding false-alarm probabilities (FAP) are listed for the BVS, Ca II IRT, S_{FEROS}, Hα, LDR V I/Fe I are listed. Furthermore, in the last 5 columns the correlation coefficient, as r and in percent, the slope of the linear regression to the BVS vs. RV data and the probability T that the BVS and RV data do not correlate are given. See Section 4.1 for details.

TABLE B.4 : Resulting periods for the stellar activity indicators of qualified stars.

#	ID	Name	BVS period days	FAP 0.01%	Ca II IRT period days	FAP 0.01%	S_{FEROS} period days	FAP 0.01%	Hα period days	FAP 0.01%	LDR V I/Fe I period days	FAP 0.01%	r corr. coef.	corr. coef. %	slope kms^{-1}	Correlation	T %
2	CD	78 24	2.14	0.57	4.31	0.56	2.88	0.006	1.45	0.16	39.99	0.12	0.05	0.25	0.11	no	87
18	CD	37 1123	3.45	0.03	2.1	0.78	1.44	0.24	50.29	0.004	1.2	0.29	0.14	1.96	-0.27	yes	59
32	1RXS	J033149.8-633155	1.2	0.18	147.2	0.93	6.7	0.33	14.3	0.012	4.05	0.014	0.34	11.56	0.42	...	22
86	TYC	5891-69-1	1.2	0.2	1.87	0.6	10.1	0.5	33.9	0.91	1.37	0.98	0.16	2.56	0.4	...	55
132	GW	Ori	100.8	0.004	2	0.7	15.9	0.005	63.8	<0.01	69.5	0.005	0.41	16.81	0.3	...	0.08
171	HD	51062	5.2	0.7	21.2	0.95	4.4	0.99	2.2	0.6	1.34	0.15	0.14	1.96	0.04	...	70
176	CD	84 0080	5.12	0.57	70.3	0.05	7.3	0.41	54.4	0.1	3.95	0.99	0.5	25	-0.5	yes	0.02
180	EG	Cha	1.26	0.025	2.05	0.04	2.79	0.087	19.5	0.03	5.99	0.01	0.42	17.64	-0.42	yes	15
189	TYC	7697-2254-1	24.7	0.35	2.83	0.32	11.6	0.65	5.5	0.03	2.7	0.71	0.11	1.21	-0.07	no	64
196	DI	Cha	7.1	0.05	1.2	0.05	22.48	0.16	10.4	0.8	1.27	0.04	0.11	1.21	0.45	no	45
203	T	Cha	1.33	0.02	1.36	0.46	1.28	0.07	15.98	0.11	55.3	0.02	0.30	9	-0.48	yes	0.9
219	RX	J1233.5-7523	1.96	0.47	2.29	0.01	10.5	0.99	90.7	0.66	1.5	0.21	0.46	21.16	-0.32	yes	11
220	1RXS	J123332.4-571345	2.1	0.9	...	...	13.2	0.74	8.4	0.005	1.96	0.99	0.7	49	2.83	...	0.1
221	TYC	9412-59-1	1.18	0.82	2.36	1	...	...	1.52	0.17	1.22	1	0.67	44.89	-0.97	yes	0.2
222	TYC	8654-1115-1	1.7	0.18	...	...	...	...	21.6	1	1.2	1	0.75	56.25	0.04	...	0.3
227	CD	69 1055	1.5	0.05	2.8	0.93	4.53	0.79	53.01	0.03	1.33	0.48	0.54	29.16	-0.8	yes	0.02
253	LT	Lup	3.14	0.006	1.3	0.12	19.84	0.94	10.31	0.009	2.34	0.02	0.63	39.69	-0.29	yes	0.2
255	LY	Lup	1.5	0.26	37.66	0.12	3.39	0.12	1.2	0.9	1.2	0.16	0.37	13.69	0.73	...	13
261	1RXS	J153328.4-665130	7.5	0.007	11.8	0.01	2	0.6	8.8	0.002	25	0.12	0.1	1	-0.06	no	42
274	GQ	Lup	2.18	0.19	1.31	0.2	8.54	0.004	11.38	<0.001	5.46	0.32	0.15	2.25	-0.08	...	45
277B	HBC	603	1.3	1	...	...	2.92	0.09	17.7	0.5	1.7	1	0.69	47.61	0.098	yes	0.4
358	CD	37 13029	2.87	1	4.59	0.07	77.9	0.1	3.122	0.85	1.5	0.57	0.05	0.25	-0.21	yes	91
369	1RXS	J223929.1-520525	1.58	0.73	2.65	0.006	13.02	0.004	2.86	0.004	7.2	0.009	0.11	1.21	-0.05	no	73
370	CP	72 2713	1.99	0.14	4.57	0.82	2.23	0.72	3.35	0.55	5.58	0.5	0.04	0.16	-0.02	no	93
372	HD	217897	1.21	0.71	5.26	0.26	1.29	0.58	1.97	0.78	9.72	0.82	0.3	9	-0.3	yes?	43
375	TYC	584-343-1	4.83	1	2.88	0.02	1.77	0.27	3.26	0.14	3.61	0.01	0.37	13.69	0.39	no?	33

B.4 Interesting targets for further observations

In Table B.5, all stars with $v \sin i$<30 kms^{-1} and an error of the RV measurement of <30 ms^{-1} are listed. For these stars, RV measurements are precise enough to identify a variation and analyse this. Unfortunately, these stars have been observed only 1–3 times.

In Table B.6, I list those stars with $v \sin i$<30 kms^{-1} that show an error of the RV measurement of >30 ms^{-1}, For these stars, the analysis of the RV is difficult and stellar activity is probably very high.

TABLE B.5 : Targets for which precise RV measurements are possible.

#	Star	RA	DEC	V mag
		h:m:s	deg:m:s	mag
9	HD 17662	02:50:30.0	11:52:12.0	8.5
36	HD 23208	03:42:40.0	-20:32:44.0	9.2
65	HD 26980	04:14:23.0	-38:19:02.0	9.0
88	1RXS J043451.0-354715	04:34:51.0	-35:47:21.0	10.8
106	HD 286264	05:00:49.0	15:26:60.0	11.0
107	HD 32372	05:00:52.0	-41:01:07.0	9.5
135	HD 36329	05:29:24.0	-34:30:56.0	9.2
136	HD 269620	05:29:27.0	-68:52:05.0	9.6
151	HD 37551	05:37:13.0	-42:42:56.0	9.6
167	HD 44748	06:21:57.0	-34:30:44.0	9.1
172	HD 51797	06:56:23.0	-46:46:55.0	9.8
173	1RXS J070153.4-422759	07:01:53.0	-42:27:56.0	10.6
175	TYC 8559-1016-1	07:21:24.0	-57:20:37.0	10.7
179	CD 38 4458	08:26:10.0	-39:02:05.0	10.3
185	HD 81544	09:23:35.0	-61:11:36.0	10.9
263	RX J1538.6-3916	15:38:38.0	-39:16:54.0	11.5
270	HD 140637	15:45:47.0	-30:20:56.0	9.3
273	RX J1547.6-4018	15:47:42.0	-40:18:27.0	11.1
316	V2129 Oph	16:27:40.0	-24:22:03.0	11.4
348	HD 161460	17:48:34.0	-53:06:43.0	9.6
365	HD 207278	21:48:48.0	-39:29:09.0	9.7
371	CD 40 14901	22:46:33.0	-39:28:45.0	9.4
373	BD 03 5579	23:09:37.0	-02:25:55.0	11.0
376	BD 13 6424	23:32:31.0	-12:15:52.0	10.5
377	HD 25457	04:02:37.0	00:16:08.0	5.4

TABLE B.6 : Targets for which precise RV measurements are possible.

#	Star	RA	DEC	V mag
		h:m:s	deg:m:s	mag
5	CCDM J01377+1836	01:37:39.0	18:35:33.0	9.9
105	HD 31950	05:00:24.0	15:05:25.0	9.9
170	HD 49078	06:42:07.0	-64:31:26.0	8.1
237	HD 124784	14:16:58.0	-49:56:42.0	9.1
256	MP Lup	15:24:32.0	-36:52:02.0	11.3
259	MS Lup	15:25:60.0	-45:01:16.0	10.9
264	CD 43 10072	15:38:43.0	-44:11:47.0	10.6
265	MU Lup	15:40:41.0	-37:56:18.0	4.3
277	IM Lup	15:56:09.0	-37:56:06.0	10.0
279	GSC 06195-00768	15:57:02.0	-19:50:41.0	11.5
283	CD 36 10569	15:59:49.0	-36:28:28.0	10.9
284	MZ Lup	16:01:09.0	-33:20:14.0	11.0
289	TYC 7334-429-1	16:04:31.0	-32:07:29.0	10.9
307	HD 147048	16:21:12.0	-40:30:21.0	10.4
319	1RXS J162950.1-272834	16:29:50.0	-27:28:50.0	11.0
322	DoAr 44	16:31:33.0	-24:27:37.0	11.0
330	Wa Oph6	16:48:46.0	-14:16:36.0	11.4
331	V1121 Oph	16:49:15.0	-14:22:09.0	11.5
334	TYC 8726-57-1	16:59:55.0	-52:46:20.0	10.8
339	CD 27 11535	17:15:04.0	-27:49:40.0	10.7
340	TYC 6812-348-1	17:16:18.0	-23:10:47.0	11.0
361	CD 38 13398	19:17:24.0	-37:56:50.0	10.0

C Results for $v \sin i$, Li I and disk status

Table of results for $v \sin i$, equivalent width measurements of Hα, He I, and Li I, veiling, stellar age, and evolutionary state of a circumstellar disk. Also appeared in Weise *et al.* [2010]. In Column (1) star identifier, column (2) the spectral type (from SIMBAD). The EW of Hα (col. 5) is negative when in emission, "a" for absorption, and "fi" for filled up Hα. The evolutionary state of the circumstellar disk (col. 14) is represented by "accr." for accretion disk, "non-accr." for non-accreting and optically thick disks, and "debris" for disks with cold dust only, "none" for verified absence of a circumstellar disk. No entry means no data is available. Stars marked with † are from this study, the others from Weise [2007].

References: ^{a}: Brown et al. (2007), ^{b}: Carpenter et al. (2009), ^{c}: Chen et al. (2005), ^{d}: Gautier et al. (2008), ^{e}: Kessler-Silacci et al. (2006), ^{f}: Köhler (2001), ^{g}: Lommen et al. (2007), ^{h}: López-Santiago et al. (2006), ^{i}: Low et al. (2005), ^{k}: Makarov & Fabricius (2001), ^{l}: Mamajek et al. (2002), ^{m}: Mamajek et al. (2004), ^{n}: Neuhäuser et al. (2003), ^{o}: Padgett et al. (2006), ^{p}: Rebull et al. (2008), ^{r}: Soderblom et al. (1998), ^{s}: Torres et al. (2000), ^{t}: Wichmann et al. (2003), ^{u}: Zuckerman & Song (2004), ^{v}: SIMBAD, ^{w}: Weise [2007]

TABLE C.1 : Results for $v \sin i$, equivalent width measurements of Hα, He I, and Li I, veiling, stellar age, and evolutionary state of a circumstellar disk.

(1) Star ID	(2) SpT[v,w]	(3) $v \sin i$ kms^{-1}	(4) $\sigma_{v \sin i}$ kms^{-1}	(5) EW(Hα) Å	(6) $\sigma_{EW(H\alpha)}$ Å	(7) $W_{H\alpha}$ Å	(8) EW(He I) Å	(9) Veiling	(10) EW(Li I) mÅ	(11) $\sigma_{EW(Li\,I)}$ mÅ	(12) Age Myr	(13) σ_{Age} Myr	(14) disk[b]	(15) YSA[v]
HD 105	G1	14.7	1.0	a	...	...	...	...	145	4	50	15	debris	Tuc/Hor[u]
HD 225213	M1.5	5.8	1.7	a	...	...	...	...	n/a	...	...	...	...	field
HD 377	G6	14.2	1.0		...	...	...	...	131	10	90	15	debris	field[b]
HD 987	G5	7.3	1.1	a	...	...	...	...	191	5	30	15	none[p]	Tuc/Hor[u]
HD 984	F6	41.8	5.1	a	...	...	...	...	131	5	25	10	none	field[b]
HD 1466	F8	22.7	2.2	a	...	...	...	...	117	3	30	10	debris[m]	Tuc/Hor[u]
HD 3221	K4.5	146.6	11.5	-2.03	0.05	10.2	...	...	174	5	30	10	debris[m]	Tuc/Hor[u]
CD-78 24[†]	K3	30.7	2.3	-0.1	0.01	1.5	...	...	291	8	30	10	...	Tuc/Hor[s]
HD 4944	F8.5	33.5	1.9	a	...	...	...	...	132	5	30	10	...	field[t]
TYC 8852-264-1	G9	31.7	1.8	-0.21	0.03	2.4	...	...	287	5	20	10	none	Tuc/Hor[u]
HD 7661	G7.5	3.8	1.9	a	...	...	...	...	34	5	300	50	none	field[b]
HIP 6276	G6	4.2	1.7	a	...	...	...	...	141	5	50	10	debris	AB Dor[u]
HD 8813	G3.5	6.7	1.2	a	...	...	...	...	120	4	120	20	...	field[t]
HD 8558	G5.5	13.6	0.9	a	...	...	...	...	189	3	30	15	debris[m]	Tuc/Hor[u]
CD-31 571[†]	K2	22.3	1.5	fi	...	...	...	...	260	5	30	10	...	field
HD 9054	K1	3.9	1.9	a	...	...	...	...	182	7	30	10	...	Tuc/Hor[u]
TYC 8047-232-1	K2.5	20.6	1.2	-0.11	0.01	1.8	...	...	333	5	30	10	...	Tuc/Hor[u]
HD 12039	G2.5	15.8	1.0	a	...	...	...	...	173	4	30	15	debris	Tuc/Hor[u]
1RXS J020154.6-523453	K3.5	19.9	1.2	-0.18	0.02	2.0	...	...	298	5	20	10	...	Tuc/Hor[u]
HD 13246	F7.5	43.3	2.7	a	...	...	...	...	125	5	30	15	...	Tuc/Hor[u]
HD 14706	G0	7.9	1.0	a	...	...	...	...	99	5	90	10	...	field
HD 15526	G4	8.9	1.0	a	...	...	...	...	155	3	60	15	none	field[b]
GSC 08056-00482	M2.5	29.3	1.7	-4.98	0.6	3.5	...	...	350	5	20	10	none[p]	Tuc/Hor[u]
V* AF Hor	M2.5	19.0	1.3	-4.07	0.2	2.1	...	...	16	5	20	10	debris[m]	Tuc/Hor[u]
HIP 12545	K9.5	9.0	1.0	-1.07	0.05	3.0	...	...	427	5	10	3	none[p]	β Pic[u]
TYC 8497-995-1	K9	5.9	1.4	-0.64	0.05	2.0	...	...	98	5	30	10	...	Tuc/Hor[u]
HD 17662[†]	G5	17.0	1.2	a	...	...	...	...	42	2	250	50	...	field
HD 17925	K0	4.8	1.6	a	...	...	...	...	206	5	90	10	...	field[b]
CD-37 1123[†]	G9	6.9	1.2	a	...	...	...	...	230	5	30	15	...	field
HD 19330	F9	7.0	1.1	a	...	...	...	...	18	5	400	50	...	...
HD 19491	G1	5.2	1.5	a	...	...	...	...	33	5	600	50	...	...

Table C.1 – continued from previous page

(1) Star ID	(2) SpT[v,w]	(3) $v \sin i$ kms^{-1}	(4) $\sigma_{v \sin i}$ kms^{-1}	(5) EW(Hα) Å	(6) $\sigma_{EW(H\alpha)}$ Å	(7) $W_{H\alpha}$ Å	(8) EW(He I) Å	(9) Veiling	(10) EW(Li I) mÅ	(11) $\sigma_{EW(Li\,I)}$ mÅ	(12) Age Myr	(13) σ_{Age} Myr	(14) disk[b]	(15) YSA[v]
HD 19668	G5.5	7.1	1.1		...	...	...	...	165	5	90	10	debris	field[b]
HD 21411	G6	4.1	1.8	a	...	...	...	...	<2	...	>600	...	none	field[b]
TYC 5879-490-1	G4	14.7	1.0	a	...	...	...	...	188	4	30	15	none	field[b]
RX J 0329.1+0118	F9	65.1	4.0	a	...	...	...	...	82	5	200	50	none	field[b]
1RXS J033149.8-633155[†]	G9	18.1	1.1	a	...	...	...	...	300	3	25	15	...	field
HD 21955[†]	G7	27.7	1.7	a	...	...	...	...	230	1	30	10	...	field
HD 23208[†]	G8	9.3	0.4	a	...	...	...	...	252	3	25	10	...	...
RX J 0354.4+0535	G2	69.6	5.6	a	...	...	...	...	118	5	90	10	none	field[b]
HD 25300	K4	13.0	1.0	-0.62	0.05	4.0	...	...	108	5	90	10	none	field[b]
TYC 5882-1169-1	K2	6.5	1.3	a	...	...	...	...	221	5	30	15	...	Tuc/Hor[u]
HD 25457[†]	F6.5	18.5	1.1	a	...	...	...	...	112	3	50	15	...	AB Dor[u]
CD-31 1688[†]	G6	30.0	1.8	a	...	...	...	...	240	4	30	10	...	field
HD 26990	G2	7.1	1.1	a	...	...	...	...	47	<1	300	50	none	field[r]
CD-43 1395[†]	G7	28.1	1.7	a	...	...	...	...	270	4	30	10	...	field
CD-43 1451[†]	G9	21.3	1.4	fi	...	...	...	...	280	4	15	5	...	field
TYC 5891-69-1[†]	G4	20.5	1.3	fi	...	...	...	...	280	4	10	5	none	field
1RXS J043451.0-354715[†]	K1	11.3	1.0	-0.24	0.03	1.9	...	...	300	5	20	15	...	field
RX J 0434.3+0226	K5.5	5.7	1.4	-0.67	0.03	2.2	...	...	233	3	30	10	none	field[b]
HD 29623	G2	8.8	1.0	a	...	...	...	...	96	1	90	10	...	field[t]
RX J 0442.5+0906	K0	12.1	0.9	a	...	...	...	...	240	5	60	15	none	field[b]
HIP 23309	K7	5.8	1.5	-1.21	0.03	2.3	...	...	341	3	10	3	none[p]	β Pic[u]
HD 31950[†]	G	29.2	0.8	a	...	...	...	...	181	6	30	15	none[b]	field
GJ 3323	M1.5	10.1	3.8	-5.43	0.2	2.7	...	...	11	5	12	15	...	β Pic[u]
GJ 3323B	...	11.3	1.5	...	...	...	...	...	...	...	...	...	...	...
HD 35114	F7	73.8	5.7	a	...	...	...	...	108	1	30	10	...	Tuc/Hor[u]
HD 35850	G0	71.6	9.6	a	...	...	...	...	149	10	12	15	...	β Pic[u]
V* AB Dor	K1	104.5	10.9	a	...	...	...	...	233	19	50	15	none[c]	AB Dor[u]
V* GW Ori[†]	K3	43.7	2.4	-20.76	0.2	9.9	0.05	0.95	240	5	5	2	accr.[e]	Ori
TYC 7600-0516-1	K0.5	18.6	1.1	a	...	...	...	...	248	5	30	15	...	Tuc/Hor[u]
HD 37484	F3	48.4	4.0	a	...	...	...	...	92	3	30	15	...	field[b]
V* AI Lep	G0	27.9	1.6	a	...	...	...	...	200	7	30	15	...	field[b]
HD 38397	G1	15.9	1.0	a	...	...	...	...	151	4	60	15	...	field[t]

Table C.1 – continued from previous page

(1) Star ID	(2) SpT[v,w]	(3) $v \sin i$ kms^{-1}	(4) $\sigma_{v \sin i}$ kms^{-1}	(5) EW(Hα) Å	(6) $\sigma_{EW(H\alpha)}$ Å	(7) $W_{H\alpha}$ Å	(8) EW(He I) Å	(9) Veiling	(10) EW(Li I) mÅ	(11) $\sigma_{EW(Li\,I)}$ mÅ	(12) Age Myr	(13) σ_{Age} Myr	(14) disk[b]	(15) YSA[v]
HD 38207	F2	70.7	4.2	a	...	...	...	...	75	5	55	15	...	field[b]
HD 38949	G1	7.2	1.1	a	...	...	...	...	82	<1	250	50	...	field[b]
HD 42270†	K0	32.6	2.3	a	...	...	...	...	305	1	20	10	...	field
HD 40216	F7	32.2	1.8	a	...	...	...	...	115	2	30	10	...	Tuc/Hor[u]
HD 41700	F8.5	16.6	1.0	a	...	...	...	...	78	5	200	50	...	field[r]
CD-34 2676†	K1	18.1	1.1	...	...	...	...	...	240	5	65	15	...	field
HD 45081	K3.5	15.9	1.0	-0.79	0.02	2.1	...	...	398	3	10	5	none	β Pic[u]
V* AB Pic	K0.5	11.5	0.9	a	...	...	...	...	287	4	30	15	none	Tuc/Hor[u]
HD 43989	G0.5	42.3	5.0	...	...	...	...	...	n/a	...	...	...	debris	Tuc/Hor[u]
HD 45270	G0	17.2	1.1	a	...	...	...	...	139	5	50	10	...	AB Dor[u]
HD 47875	G3	11.6	0.9	a	...	...	...	...	198	3	30	15	none	field[b]
HD 48189	G0	16.5	1.0	a	...	...	...	...	132	3	50	10	none[c]	AB Dor[u]
HD 51062†	G5	14.2	0.9	a	...	...	...	...	180	2	200	50	...	Carina-Vela
TYC 8545-1758-1	F9	46.7	6.8	a	...	...	...	...	136	5	25	10	...	field[b]
HD 51797†	K0	14.5	0.5	a	...	...	...	...	288	5	30	15	...	...
HD 55279	K2	9.4	1.0	a	...	...	...	...	271	4	30	15	...	Tuc/Hor[u]
CD-84 80†	G9	7.7	1.1	a	...	...	...	...	300	5	30	15	...	field
HD 61005	G5.5	9.9	0.9	a	...	...	...	...	169	3	30	15	debris	field[r]
HD 62850	F9.5	14.4	1.0	a	...	...	...	...	122	1	90	10	...	field[r]
HD 70573	G2	13.5	0.9	a	...	...	...	...	148	4	70	15	...	field[b]
V* EG Cha†	K4	21.4	1.3	-0.96	0.05	2.9	...	...	510	6	5	2	none[d]	Cha
RX J 0849.2-7735	K2	6.0	1.4	a	...	...	...	...	120	4	90	10	none	Cha[f]
HD 75393	F9	4.7	1.6	a	...	...	...	...	9	2	>600	50	none	field[b]
RX J 0850.1-7554	G7	47.7	3.6	a	...	...	...	...	210	5	60	15	none	Cha[f]
RX J 0917.2-7744	G4.5	76.5	8.9	a	...	...	...	...	165	5	30	10	none	Cha[f]
HD 81544†	G9	12.9	0.5	fi	...	...	...	...	331	5	8	3	...	...
HD 84323	F9	...	...	a	...	...	...	...	197	5	30	15	...	field
TYC 7697-2254-1†	G8	9.0	0.4	fi	...	...	...	...	240	4	25	10	...	...
HD 86356	G8	136.4	10.8	-0.04	0.01	1.5	...	...	265	5	10	5	none	Cha[f]
HD 86021†	G7	24.3	1.6	a	...	...	...	...	78	10	200	100	...	...
TYC 6604-118-1	K1	18.3	1.1	-0.11	0.01	1.5	...	...	72	5	8	5	...	TWA[k]
TYC 6604-118-1B	...	65.4	6.0	...	...	...	...	...	...	...	...	...	...	...

Table C.1 – continued from previous page

(1) Star ID	(2) SpT[v,w]	(3) $v \sin i$ kms^{-1}	(4) $\sigma_{v \sin i}$ kms^{-1}	(5) EW(Hα) Å	(6) $\sigma_{EW(H\alpha)}$ Å	(7) W$_{H\alpha}$ Å	(8) EW(He I) Å	(9) Veiling	(10) EW(Li I) mÅ	(11) $\sigma_{EW(Li I)}$ mÅ	(12) Age Myr	(13) σ_{Age} Myr	(14) disk[b]	(15) YSA[v]
HD 88201	G0	10.3	0.9	a	...	...	...	...	71	4	300	50	none	field[b]
TWA 21	K2	8.2	1.0	a	...	...	...	...	357	3	8	3	...	TWA[u]
TWA 6	K6	94.7	9.1	-3.55	0.6	5.1	...	...	500	5	7	3	non-accr.[i]	TWA[u]
HD 90712	G1.5	11.2	0.9	a	...	...	...	...	99	1	250	50	none	field[b]
RX J 1029.5-6349	K1.5	24.3	1.5	a	...	...	...	...	251	5	40	15	none	IC 2602[b]
RX J 1040.0-6315	G2.5	13.9	0.9	a	...	...	...	...	177	6	30	15	none	IC 2602[b]
HD 307938	F9	81.1	5.0	a	...	...	...	...	161	1	30	15	...	IC 2602[b]
TWA 7	M1	5.0	2.1	-4.64	0.5	2.1	...	...	465	10	8	3	non-accr.[i]	TWA[u]
RX J 1046.2-6402	G3	35.2	2.0	a	...	...	...	...	187	5	40	10	none	IC 2602[b]
2MASS J10574936-6913599	K3	26.8	4.2	a	...	...	...	...	404	8	5	3	none	ScoCen/LCC[b]
V* CR Cha[†]	K2	36.5	4.4	-26.94	1.24	10.55	0.06	0.07	380	3	5	3	accr.	Cha
V* TW Hya	M0	6.2	1.3	-116.78	5	9.5	1.94	0.8	361	<1	8	3	accr.[e]	TWA[u]
HD 96064	G7	6.1	1.3	a	...	...	...	...	106	2	90	10	...	field[t]
V* DI Cha[†]	G2	38.1	2.2	-26.07	0.5	9.8	0.03	0.05	260	1	5	2	accr.[g]	Cha
TWA 2	M0.5	11.8	1.0	-1.89	0.07	2.2	...	...	509	11	8	3	non-accr.[i]	TWA[u]
HD 98553	G2	4.0	1.9	a	...	...	...	...	21	1	300	50	none	field[b]
TWA 4	K1	5.0	1.6	-0.09	0.01	1.5	...	...	312	5	8	5	non-accr.[i]	TWA[u]
TWA 4B	...	8.0	1.1	...	...	...	...	...	...	...	...	...	...	...
HD 99409	G6	17.6	1.1	a	...	...	...	...	95	<1	125	20	...	field[t]
TWA 5	M1.5	63.2	9.5	-8.5	0.3	8.8	...	...	564	5	8	3	none[i]	TWA[u]
TWA 8	M1	7.1	1.2	-6.43	0.5	2.8	...	...	475	5	8	3	non-accr.[i]	TWA[u]
RX J 1140.3-8321	K1	9.3	1.1	-0.18	0.02	2.1	...	...	195	1	15	10	none	Cha[f]
HD 101472	F8.5	5.8	1.3	a	...	...	...	...	112	2	90	10	none	field[b]
TWA 19	G7	30.1	1.7	a	...	...	...	...	197	5	8	5	non-accr.[i]	TWA[u]
V* GQ Leo	K8	7.2	1.6	-0.63	0.02	2.2	...	...	83	2	12	4	none	field
TWA 9	K4	10.4	1.0	-1.57	0.07	2.1	...	...	506	5	7	3	non-accr.[i]	TWA[u]
V* T Cha[†]	G4	40.0	2.7	fi	...	...	...	...	382	1	4	2	non-accr.[a]	Cha
HD 104576	G1	3.5	2.1	a	...	...	...	...	52	2	300	50	none	field[b]
RX J 1203.7-8129	K2	2.7	2.7	a	...	...	...	...	69	6	250	50	none	Cha[f]?
TWA 24	K1.5	15.5	1.0	-0.6	0.02	2.8	...	...	383	5	7	3	...	TWA[u]
HD 105690	G4	8.5	1.0	a	...	...	...	...	149	1	8	15	...	TWA[k]
2MASS J12123577-5520273	K4	28.5	1.6	-0.2	0.02	1.5	...	...	358	2	5	3	debris	ScoCen/LCC[b]

Table C.1 – continued from previous page

(1) Star ID	(2) SpT[v,w]	(3) $v \sin i$ kms^{-1}	(4) $\sigma_{v \sin i}$ kms^{-1}	(5) EW(Hα) Å	(6) $\sigma_{EW(H\alpha)}$ Å	(7) W$_{H\alpha}$ Å	(8) EW(He I) Å	(9) Veiling	(10) EW(Li I) mÅ	(11) $\sigma_{EW(Li\,I)}$ mÅ	(12) Age Myr	(13) σ_{Age} Myr	(14) disk[b]	(15) YSA[v]
2MASS J12143410-5110124	K0	17.9	1.1	a	...	...	...	...	311	5	25	10	...	ScoCen/LCC[b]
TWA 25	M0	11.6	1.1	-1.87	0.6	2.8	...	...	531	13	8	3	...	TWA[u]
RX J 1220.6-7539	K2.5	6.3	1.3	-0.2	0.03	2.1	...	...	208	2	15	10	none	Cha[f]
HD 107441	K2	41.5	2.7	a	...	...	...	...	226	4	30	10	none	ScoCen/LCC[b]
2MASS J12223322-5333489	G1	70.9	7.3	a	...	...	...	...	191	5	30	10	debris	ScoCen/LCC[b]
RX J 1225.3-7857	G7	8.2	1.0	a	...	...	...	...	119	5	125	20	none	Cha[f]
HD 108799	G0	7.2	1.1	a	...	...	...	...	94	2	125	20	none	field[b]
HD 109138[†]	K0	6.4	0.4	a	...	...	...	...	129	3	90	15	...	...
1RXS J123332.4-571345[†]	K1	18.2	0.8	fi	...	...	...	...	424	8	8	5	...	...
TYC 9412-59-1[†]	K3	18.0	0.8	fi	...	...	...	...	429	8	5	3	...	Cha
TYC 8654-1115-1[†]	G9	19.4	0.4	a	...	...	...	...	298	7	5	3	...	...
HD 111170	G9	133.2	7.7	a	...	...	...	...	4	1	>600	50	none	ScoCen/LCC[b]
TYC 8655-149-1	G7.5	28.0	1.6	a	...	...	...	...	235	5	30	10	none	ScoCen/LCC[b]
CD-69 1055[†]	K0	26.0	1.5	fi	...	...	...	...	400	6	5	3	...	LCC
2MASS J13015069-5304581	K1.5	8.9	1.0	a	...	...	...	...	367	5	8	3	debris	ScoCen/LCC[b]
HD 113553	G4	11.6	0.9	a	...	...	...	...	139	1	90	10	...	field[r]
TYC 8649-251-1	F9.5	115.8	10.2	a	...	...	...	...	208	5	30	15	none	ScoCen/LCC[b]
V* MP Mus	K2	12.9	1.0	-42.11	3	10.5	0.5	0.1	410	5	7	3	accr.	ScoCen/LCC[b]
HD 117524	G7	32.1	1.9	a	...	...	...	...	210	3	30	10	none	ScoCen/LCC[b]
2MASS J13375730-4134419	K1	13.7	1.0	a	...	...	...	...	312	3	30	10	debris	ScoCen/UCL[b]
HD 119269	G5	24.2	1.4	a	...	...	...	...	211	4	30	10	...	ScoCen/LCC[b]
TYC 8270-2015-1	K0	69.6	8.7	-0.17	0.02	1.8	...	...	232	5	30	10	...	ScoCen/UCL[b]
HD 120812	F9.5	25.9	1.5	a	...	...	...	...	94	5	30	15	none	ScoCen/UCL[b]
TYC 7811-2909-1	K1	17.5	1.1	a	...	...	...	...	329	5	25	10	none	ScoCen[b]
HD 124784[†]	G0	17.3	1.1	a	...	...	...	...	140	1	200	50	...	UCL
HD 124784B	...	17.5	1.1	...	...	...	...	...	...	...	...	...	...	...
TYC 8282-516-1	G9	10.3	0.9	a	...	...	...	...	290	5	30	10	debris	ScoCen/UCL[b]
HD 126670	G7	13.4	0.9	a	...	...	...	...	275	2	30	10	none	ScoCen/UCL[b]
HD 128242	G1	115.8	6.7	a	...	...	...	...	60	12	300	50	none	ScoCen/UCL[b]
RX J 1457.3-3613	G5	31.9	1.8	a	...	...	...	...	280	3	20	10	none	ScoCen/UCL[b]
HD 132173	F9	9.6	0.9	a	...	...	...	...	117	2	30	10	...	field[b]
TYC 8297-1613-1	G4	17.9	1.1	a	...	...	...	...	192	5	30	10	...	ScoCen/UCL[b]

Table C.1 – continued from previous page

(1) Star ID	(2) SpT[v,w]	(3) $v \sin i$ kms^{-1}	(4) $\sigma_{v \sin i}$ kms^{-1}	(5) EW(Hα) Å	(6) $\sigma_{EW(H\alpha)}$ Å	(7) W$_{H\alpha}$ Å	(8) EW(He I) Å	(9) Veiling	(10) EW(Li I) mÅ	(11) $\sigma_{EW(Li I)}$ mÅ	(12) Age Myr	(13) σ_{Age} Myr	(14) disk[b]	(15) YSA[v]
RX J 1507.2-3505	K0.5	12.2	0.9	a	...	...	...	...	320	5	30	10	none	ScoCen/UCL[b]
HD 133938	G7.5	24.9	1.4	a	...	...	...	...	223	4	45	15	none	ScoCen/UCL[b]
V* LT Lup[†]	K0	27.8	1.7	fi	...	...	...	...	385	5	8	3	none[o]	Lup
RX J 1518.4-3738	K2.5	25.2	1.5	a	...	...	...	...	321	5	30	15	none	ScoCen/UCL[b]
V* LY Lup[†]	K0	17.2	1.1	-0.5	0.05	2.5	...	...	401	10	3	2	none[o]	Lup
V* MP Lup[†]	K0	18.0	1.3	fi	...	...	...	...	360	2	5	3	none[o]	Lup
V* MS Lup[†]	G7	28.9	1.8	a	...	...	...	...	308	6	5	3	none[o]	Lup
RX J 1531.3-3329	G9	15.6	1.0	a	...	...	...	...	281	5	30	15	none	ScoCen/UCL[l]
1RXS J153328.4-665130[1†]	K2	9.1	1.1	fi	...	...	...	...	295	1	30	15	...	field
HD 139084	G8	18.2	1.1	a	...	...	...	...	278	4	50	15	none	β Pic[u]
HD 139498	G7	32.6	3.2	a	...	...	...	...	149	5	30	10	none	ScoCen/UCL[b]
HD 139498B	...	17.4	1.1		...	...	...	...	...	...	...	...	...	...
HD 140374	G7.5	5.1	1.5	a	...	...	...	...	124	5	30	10	none	ScoCen/UCL[b]
HD 140374B	...	8.1	1.1		...	...	...	...	...	...	...	...	...	...
RX J 1544.0-3311	K1	10.3	1.0	-1.25	0.03	3.7	...	...	357	3	12	3	none	ScoCen/UCL[b]
V* HT Lup[†]	K2	44.8	3.0	-7.02	0.2	11.0	...	...	442	5	5	2	non-accr.	Lup
V* GQ Lup[†]	K8	9.1	1.1	-39.53	0.5	13.2	0.6	0.5	644	5	2	3	accr.	Lup
HD 141521	G3.5	7.1	1.1	a	...	...	...	...	149	2	30	10	none	ScoCen/UCL[b]
HD 141521B	...	8.1	1.1	...	...	...	...	...	...	...	...	...	...	...
HBC 603[†]	M0	5.9	0.6	-16.08	2.5	7.71	0.1	0.05	566	10	5	3	accr.	...
HD 141943	G4	36.3	2.1	a	...	...	...	...	198	2	30	15	debris	field[b]
HD 142229	G0	5.6	1.4	a	...	...	...	...	116	5	90	10	none	field[b]
HD 142361	G3	79.4	4.6	a	...	...	...	...	195	5	30	10	none	ScoCen/UCL[b]
V* IM Lup[†]	M0	12.6	0.6	-5.71	0.51	5.5	0.03	0.1	598	10	5	3	accr.	Lup
HD 143358	G1	72.5	4.4	a	...	...	...	...	166	3	30	10	...	ScoCen/UCL[b]
EM* SR 9[†]	K5	13.4	0.7	-20.38	1.42	7.82	0.3	0.15	567	8	5	3	accr.	...
V* V2129 Oph[†]	K3	13.5	1.0	-14.6	2	6.5	0.25	0.15	530	5	3	2	accr.	Oph
DoAr 44[†]	K3	14.6	1.1	-22.87	4.42	9.98	0.6	0.15	507	8	5	3	accr.	...
V* V1121 Oph[†]	K5	8.4	0.5	-20.81	2.48	8.28	0.3	0.25	550	6	8	3	accr.	Oph
HD 151798	G1	11.3	0.9	a	...	...	...	...	131	2	90	10	none	field[b]

[1]TYC 9034-968-1

Table C.1 – continued from previous page

(1) Star ID	(2) SpT[v,w]	(3) $v \sin i$ kms^{-1}	(4) $\sigma_{v \sin i}$ kms^{-1}	(5) EW(Hα) Å	(6) $\sigma_{EW(H\alpha)}$ Å	(7) $W_{H\alpha}$ Å	(8) EW(He I) Å	(9) Veiling	(10) EW(Li I) mÅ	(11) $\sigma_{EW(Li\,I)}$ mÅ	(12) Age Myr	(13) σ_{Age} Myr	(14) disk[b]	(15) YSA[v]
HD 152555	F9	17.8	1.1	a	...	...	...	...	123	2	50	10	none	AB Dor[u]
TYC 8726-57-1†	G9	22.1	1.4	a	...	...	...	...	250	4	25	15	...	field
CD-27 11535†	K5	12.3	1.1	-1.06	0.07	3.1	...	...	490	1	6	3	...	field
TYC 6812-348-1†	K3	19.1	1.4	-0.27	0.05	2.0	...	...	455	4	5	2	...	field
HD 155555	K2	39.9	2.3	a	...	...	...	...	170	5	12	3	none[p]	β Pic[u]
HD 155555B	...	8.8	0.9	...	...	...	...	...	169	5	...	...	...	...
HD 161460†	K0	10.1	1.0	fi	...	...	...	...	320	4	30	15	...	field
RX J 1841.8-3525	G7	41.2	2.3	a	...	...	...	...	248	1	30	15	none	Cor Aus[b]
HD 174656	G4	27.8	1.9	a	...	...	...	...	338	5	8	3	none	Cor Aus[b]
HD 181327	F5.5	19.4	1.2	a	...	...	...	...	108	<1	15	10	debris[p]	β Pic[u]
HD 183414	G3	9.6	0.9	a	...	...	...	...	142	3	75	15	...	field[r]
HD 191089	F9	48.8	3.0	a	...	...	...	...	101	5	125	20	...	field[b]
HD 193464	F9	15.0	1.0	a	...	...	...	...	92	2	300	50	...	field[t]
HD 197481	M0.5	8.2	1.2	-3.16	0.05	2.8	...	...	56	3	15	10	debris[p]	β Pic[u]
HD 199143	F9.5	161.5	11.8	a	...	...	...	...	60	5	300	50	none	β Pic[u]
HD 200746	G1.5	6.4	1.2	a	...	...	...	...	78	5	300	50	none	field[b]
HD 201219	G2.5	3.5	2.1	a	...	...	...	...	n/a	...	...	...	debris	field[b]
HD 201989	G2	5.0	1.5	...	...	...	...	...	n/a	...	...	...	none	field[b]
HD 202917	G4.5	14.9	1.0	a	...	...	...	...	211	1	30	15	...	Tuc/Hor[u]
HD 202947	K1	12.9	0.9	a	...	...	...	...	161	11	30	10	debris[m]	Tuc/Hor[u]
HD 205905	K1	4.8	1.6	...	...	...	...	...	n/a	...	...	...	none	field[b]
HD 207278†	G7	11.2	0.9	a	...	...	...	...	190	1	50	10	...	AB Dor
HD 207575	F9	36.5	2.1	a	...	...	...	...	111	7	30	10	debris[m]	Tuc/Hor[u]
HD 209253	F8	16.9	1.0	...	...	...	...	...	n/a	...	...	...	...	field[b]
HD 209779	G0	5.5	1.4	a	...	...	...	...	n/a	...	...	...	none	field[b]
HD 212291	G4	1.5	4.4	a	...	...	...	...	n/a	...	...	...	none	field[b]
1RXS J223929.1-520525†	K0	9.4	1.0	a	...	...	...	...	245	1	60	15	...	field
CP-72 2713†	K7	6.6	1.4	-12.5	0.6	2.3	...	...	440	4	8	1	...	field
CD-40 14901†	G5	14.9	1.0	a	...	...	...	...	175	2	75	15	...	field
HD 216803	K3	4.5	1.8	a	...	...	...	...	26	5	400	50	...	field[b]
HD 217343	G3	12.2	0.9	a	...	...	...	...	163	1	45	10	none	AB Dor[u]
HD 217897†	M2.5	8.5	1.2	a	...	...	...	...	50	3	30	15	...	field

Table C.1 – continued from previous page

(1) Star ID	(2) SpT[v,w]	(3) $v \sin i$ kms^{-1}	(4) $\sigma_{v \sin i}$ kms^{-1}	(5) EW(Hα) Å	(6) $\sigma_{EW(H\alpha)}$ Å	(7) $W_{H\alpha}$ Å	(8) EW(He I) Å	(9) Veiling	(10) EW(Li I) mÅ	(11) $\sigma_{EW(Li\,I)}$ mÅ	(12) Age Myr	(13) σ_{Age} Myr	(14) disk[b]	(15) YSA[v]
BD-03 5579	K4	14.0	1.0	-0.7	0.02	1.3	...	...	200	3	50	15	...	field
TYC 9129-1361-1	K1	86.1	9.8	a	...	...	...	...	<2	5	>600	50	...	field
TYC 9129-1361-1B	...	119.5	10.0	...	...	...	...	...	...	...	...	...	...	...
HD 220054	G8	31.8	1.9	a	...	...	...	...	259	4	30	10	...	field
TYC 584-343-1[†]	K0	14.0	1.0	fi	...	...	...	...	300	2	30	15	...	field
BD-13 6424[†]	M0	9.6	1.2	-1.2	0.03	1.9	...	...	185	8	30	15	...	field
HD 222259	G4	17.5	1.1	a	...	...	...	...	204	5	30	10	debris[m]	Tuc/Hor[u]
HD 224228	K2	2.7	2.8	a	...	...	...	...	60	5	50	20	...	AB Dor[u]

D Figures to Section 6.14

In this Appendix, the figures of radial velocity variation (over time and phase-folded), of the BVS analysis and for the analysis of the other stellar activity indicators for the 10 stars in Section 6.14 are presented.

D.1 HD 51062

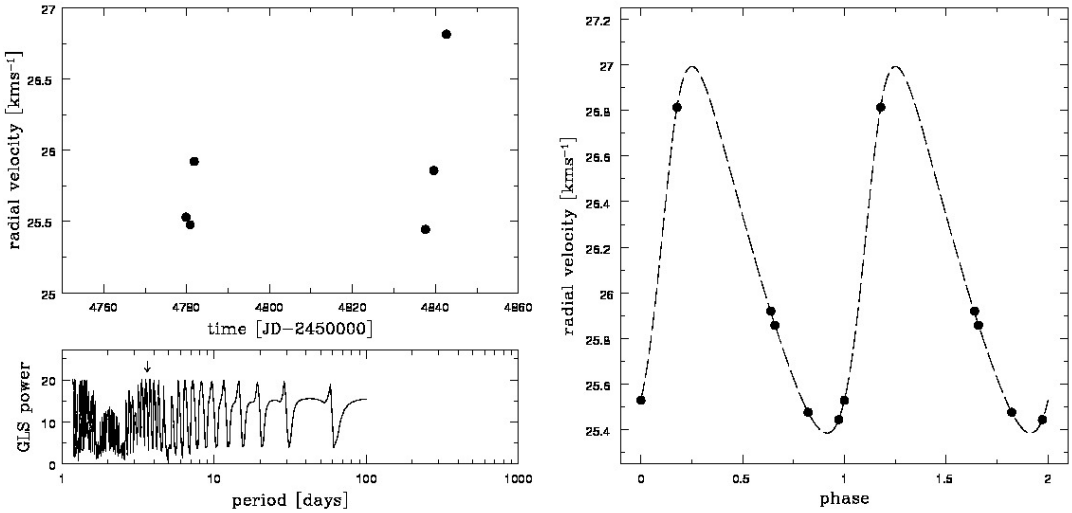

FIGURE D.1 : Radial velocity variation of HD 51062 - variation over time and phase-folded with 3.54 days.

D.2 RX J1233.5-7523

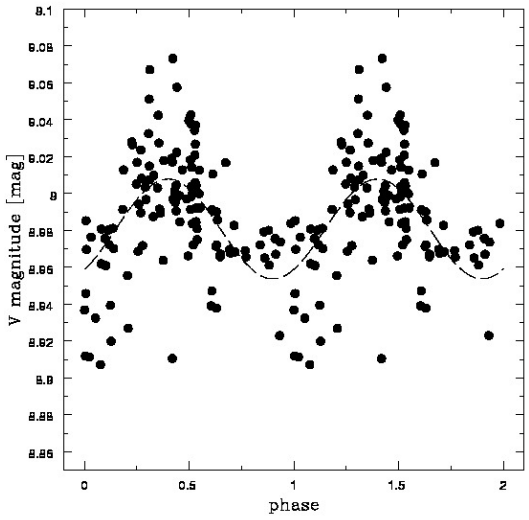

FIGURE D.2 : Photometric variation of HD 51062 - Photometric data obtained with Hipparcos and phase-folded with 4.1 days.

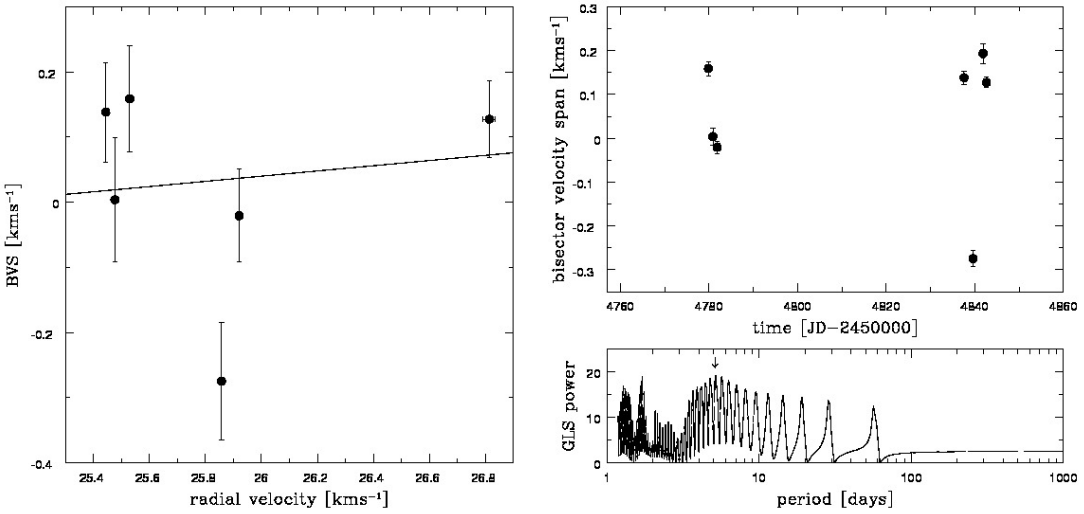

FIGURE D.3 : Bisector velocity span for CHD 51062 - BVS vs. RV and time variance

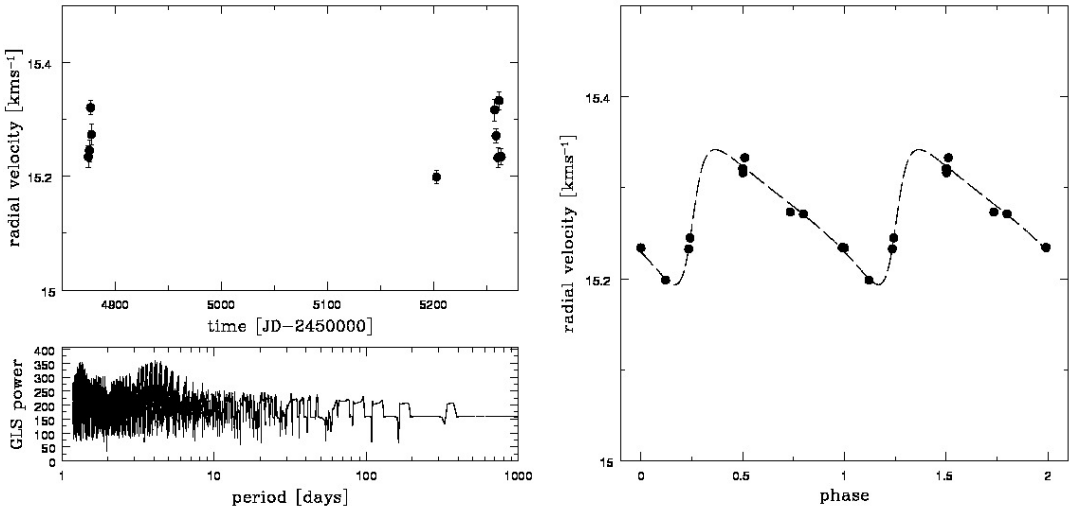

FIGURE D.4 : Radial velocity variation of RX J1233.5-7523 - variation over time and phase-folded with 4.10 days.

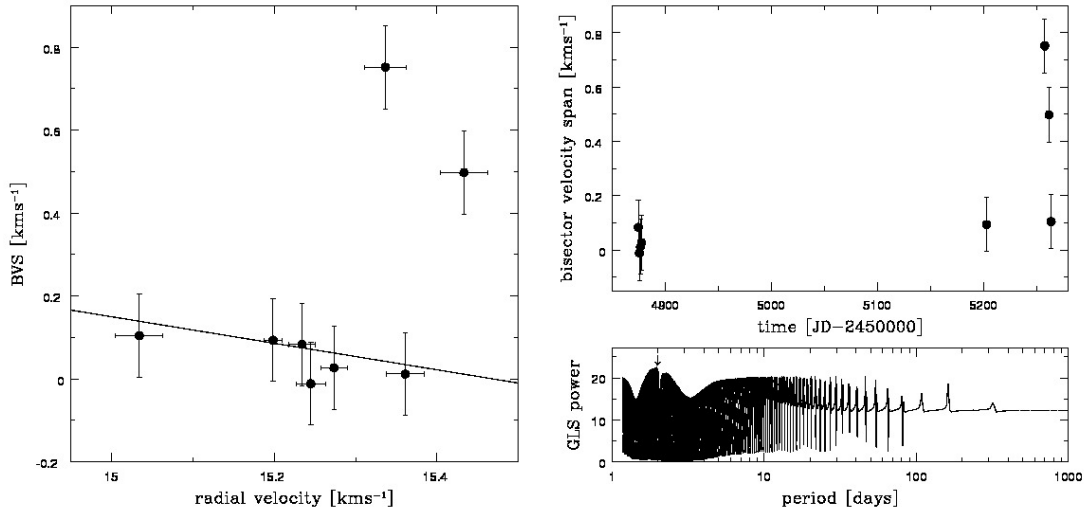

FIGURE D.5 : Bisector velocity span for RX J1233.5-7523 - BVS vs. RV and time variance

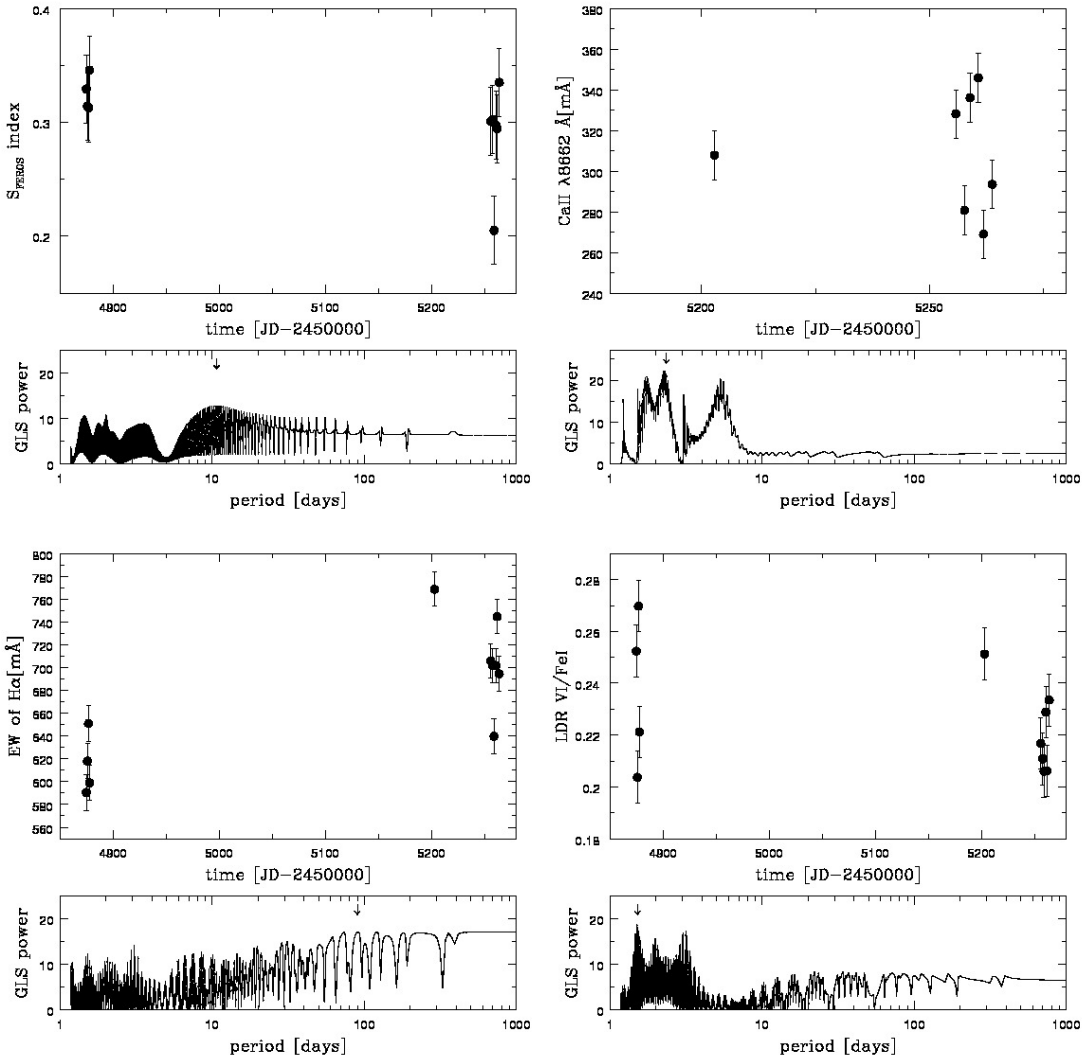

FIGURE D.6 : Activity indicator for RX J1233.5-7523 - S_{FEROS}, Ca II IRT λ 8662, Hα EW, and LDR V I/Fe I.

D.3 1RXS J123332.4-571345

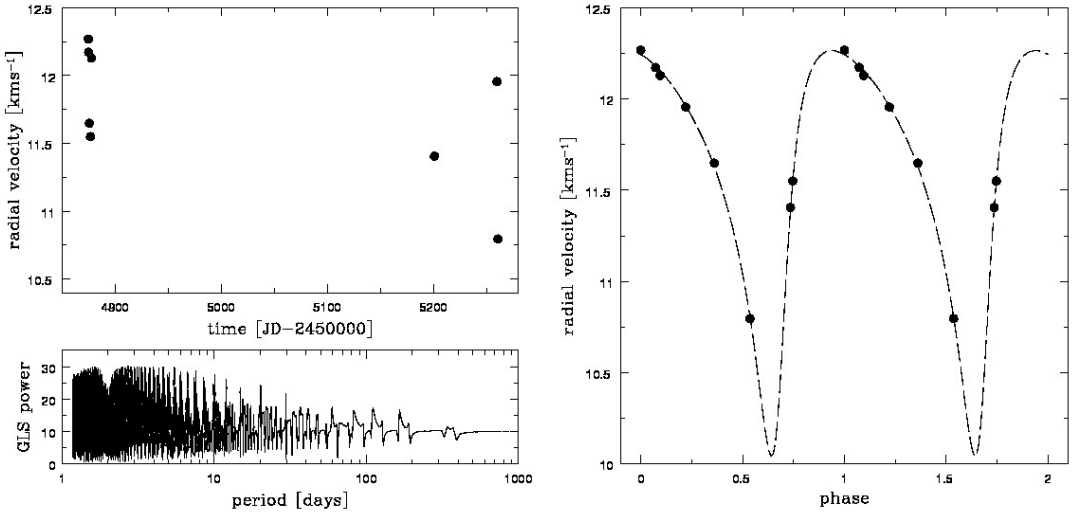

FIGURE D.7 : Radial velocity variation of 1RXS J123332.4-571345 - variation over time and phase-folded with 4.27 days.

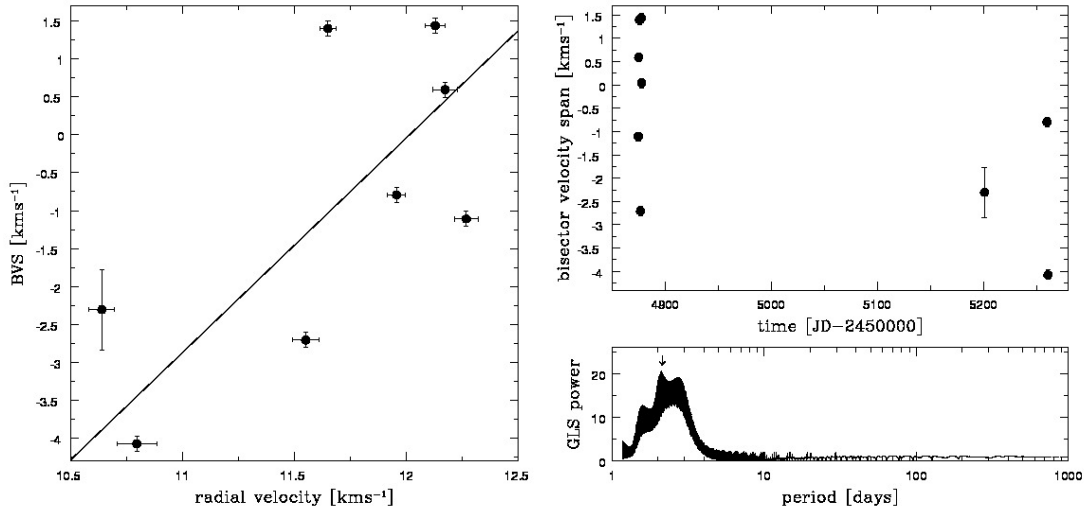

FIGURE D.8 : Bisector velocity span for 1RXS J123332.4-571345 - BVS vs. RV and time variance

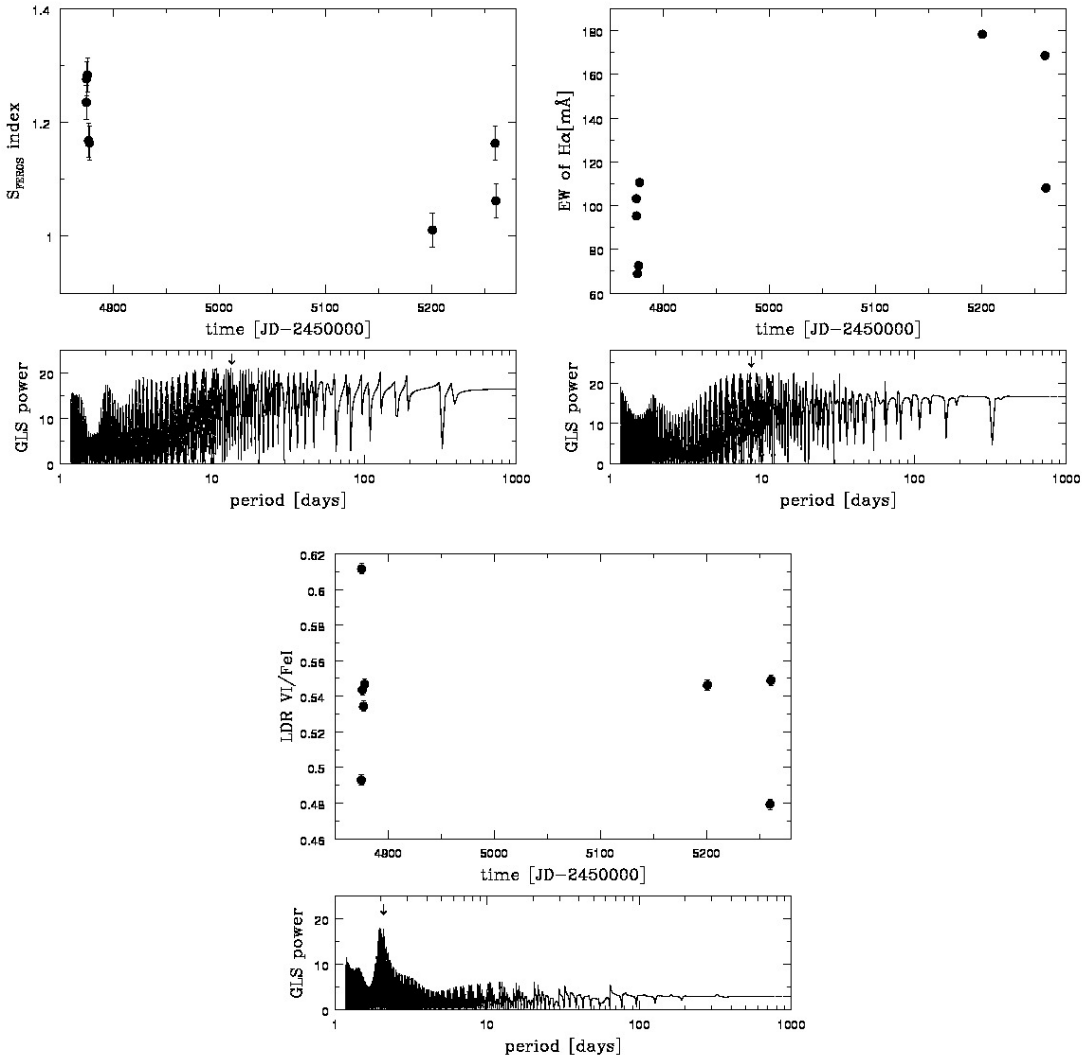

FIGURE D.9 : Activity indicators for 1RXS J123332.4-571345 - S_{FEROS}, Hα EW, and LDR V I/Fe I.

D.4 TYC 9412-59-1

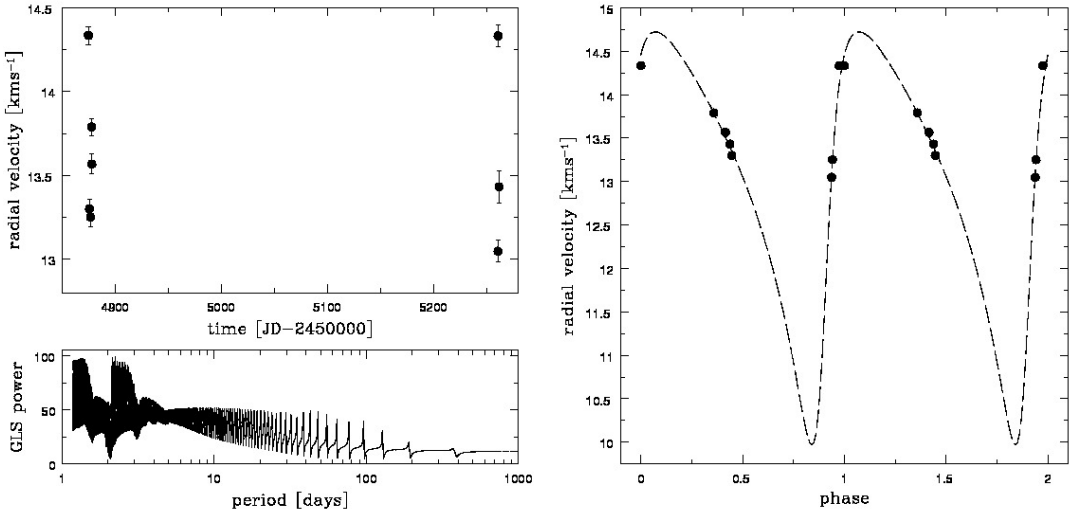

FIGURE D.10 : Radial velocity variation of TYC 9412-59-1 - variation over time and phase-folded with 1.20 days.

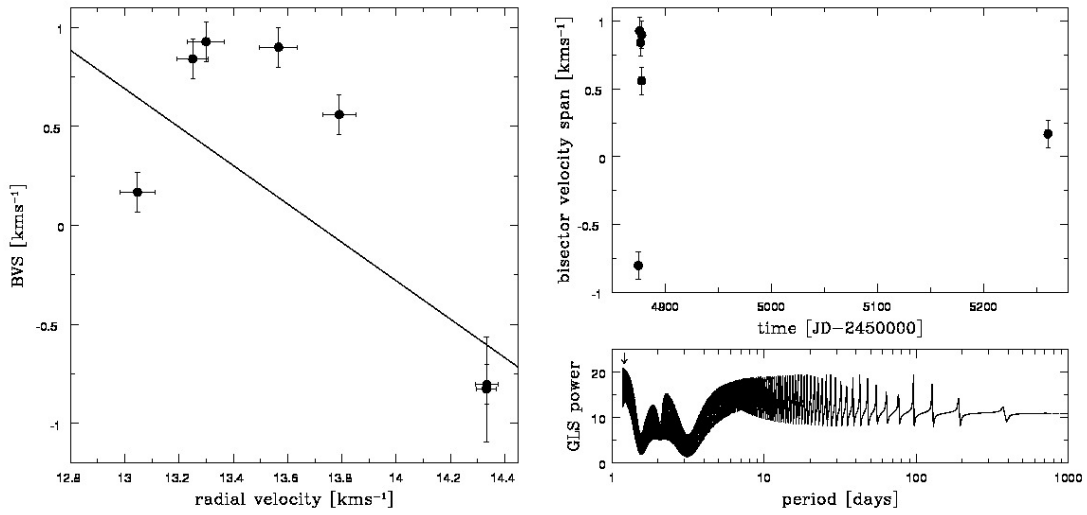

FIGURE D.11 : Bisector velocity span for TYC 9412-59-1 - BVS vs. RV and time variance

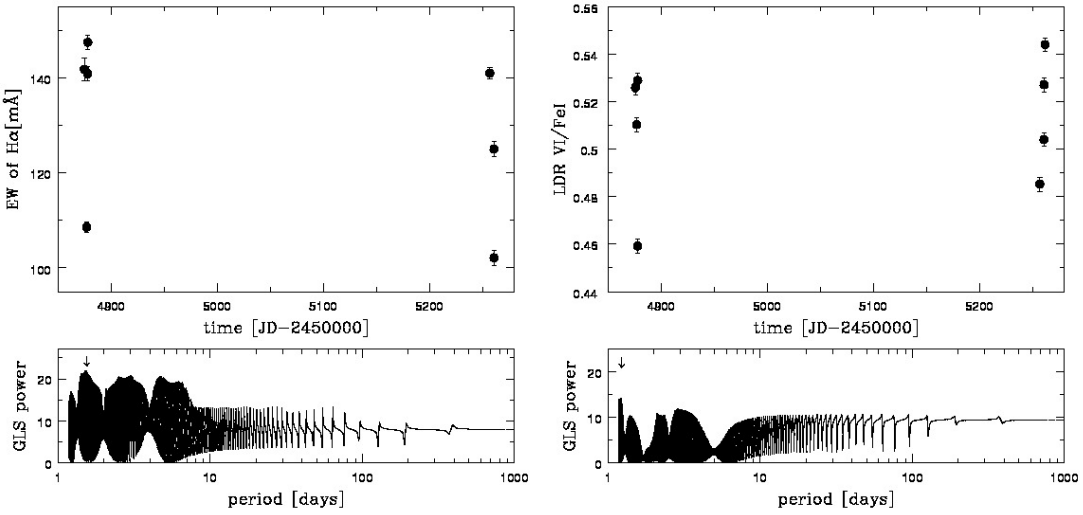

FIGURE D.12 : Activity indicators for TYC 9412-59-1 - Hα EW and LDR V I/Fe I.

D.5 TYC 8654-1115-1

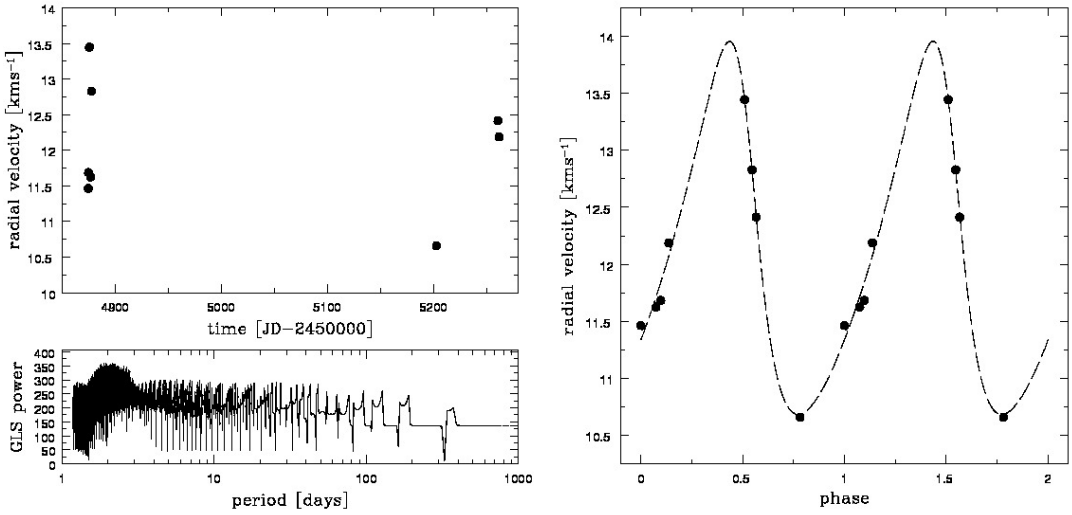

FIGURE D.13 : Radial velocity variation of TYC 8654-1115-1 - variation over time and phase-folded with 1.93 days.

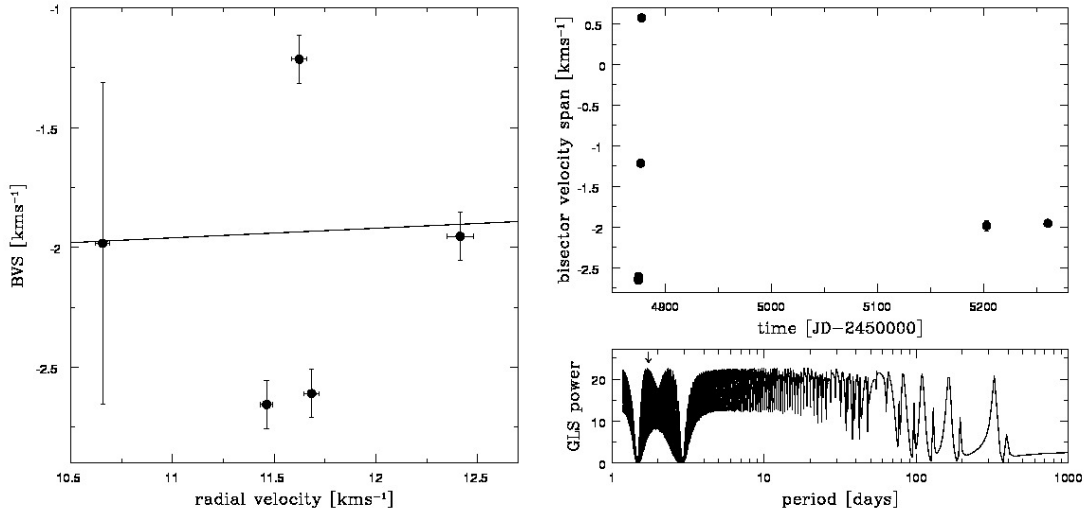

FIGURE D.14 : Bisector velocity span for TYC 8654-1115-1 - BVS vs. RV and time variance

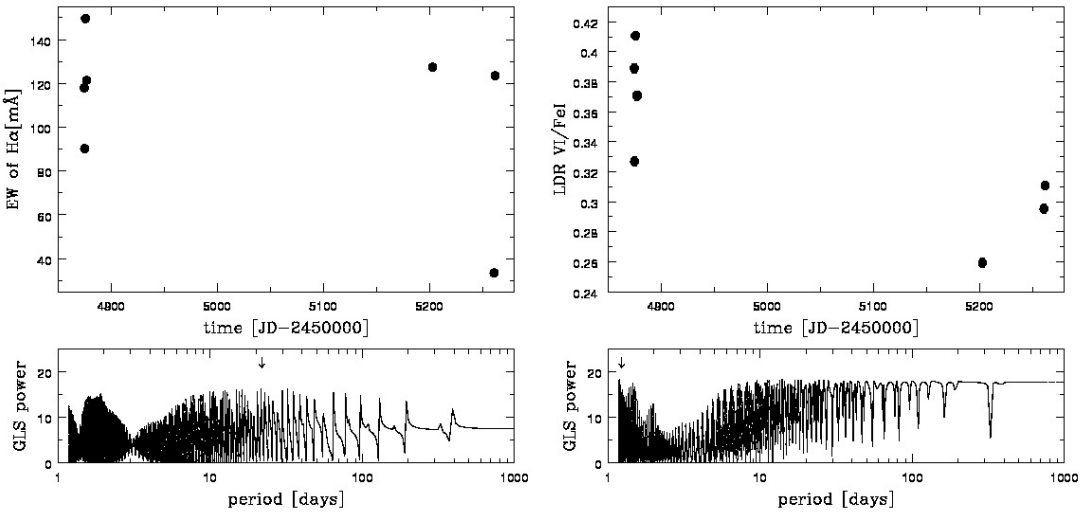

FIGURE D.15 : Activity indicators for TYC 8654-1115-1 - Hα EW and LDR V I/Fe I.

D.6 CD-69 1055

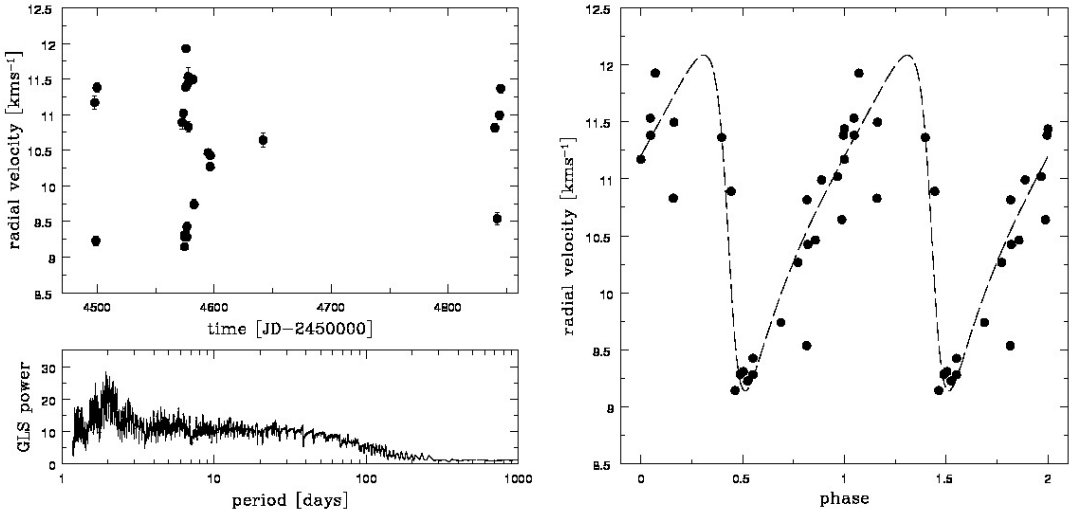

FIGURE D.16 : Radial velocity variation of CD-69 1055 - variation over time and phase-folded with 1.95 days.

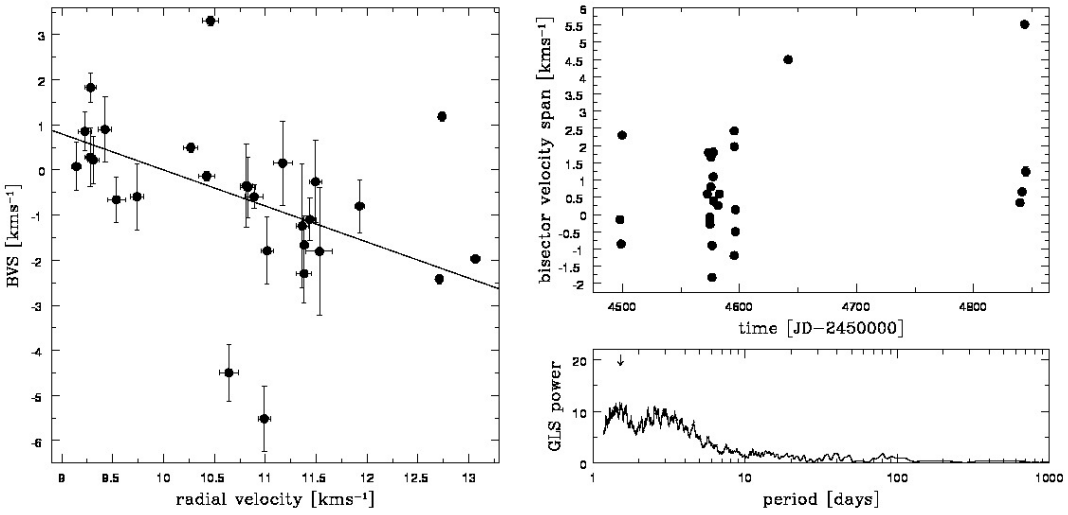

FIGURE D.17 : Bisector velocity span for CD-69 1055 - BVS vs. RV and time variance

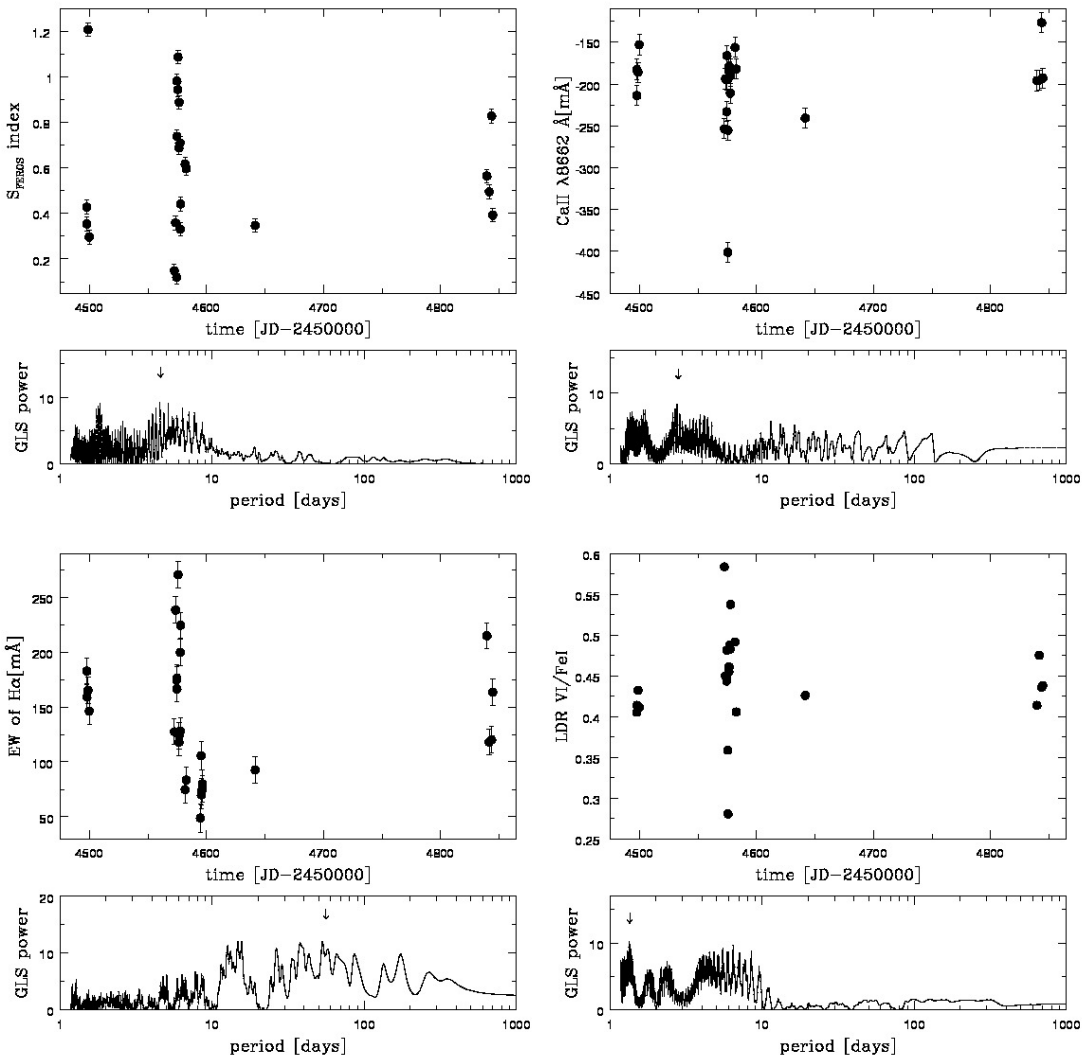

FIGURE D.18 : Activity indicators for CD-69 1055 - $S_{\rm FEROS}$, Ca II IRT λ 8662, Hα EW, and LDR V I/Fe I.

D.7 LT Lup

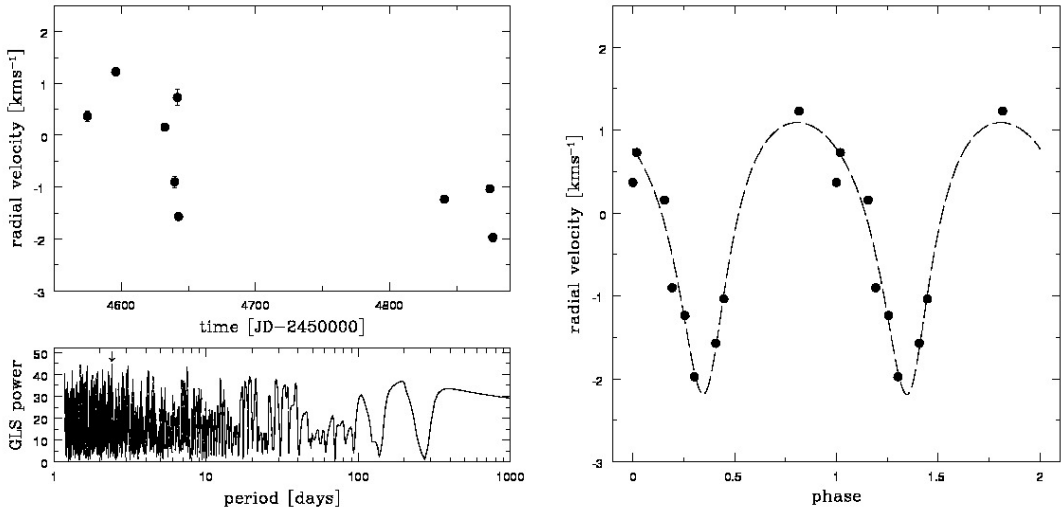

FIGURE D.19 : Radial velocity variation of LT Lup - variation over time and phase-folded with 2.39 days.

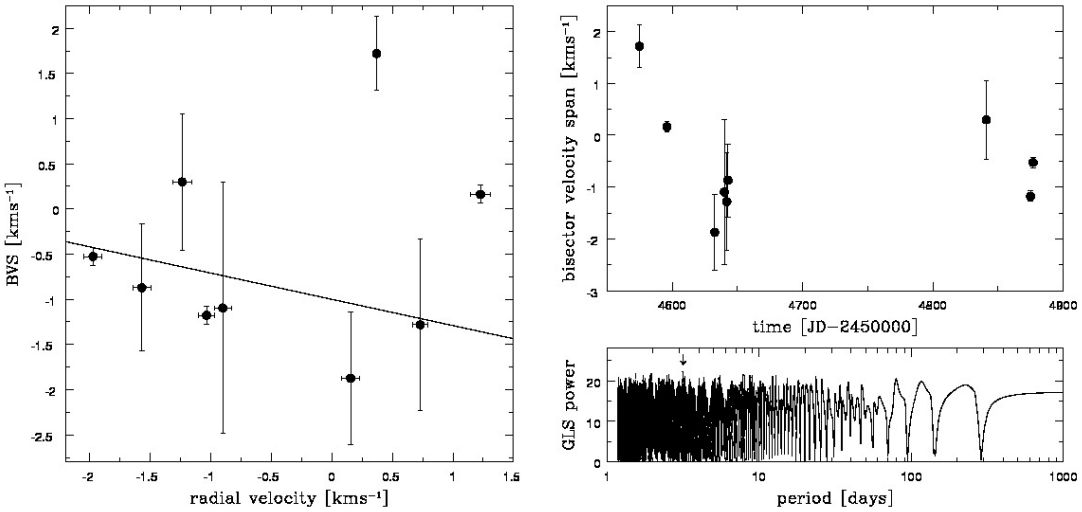

FIGURE D.20 : Bisector velocity span for LT Lup - BVS vs. RV and time variance

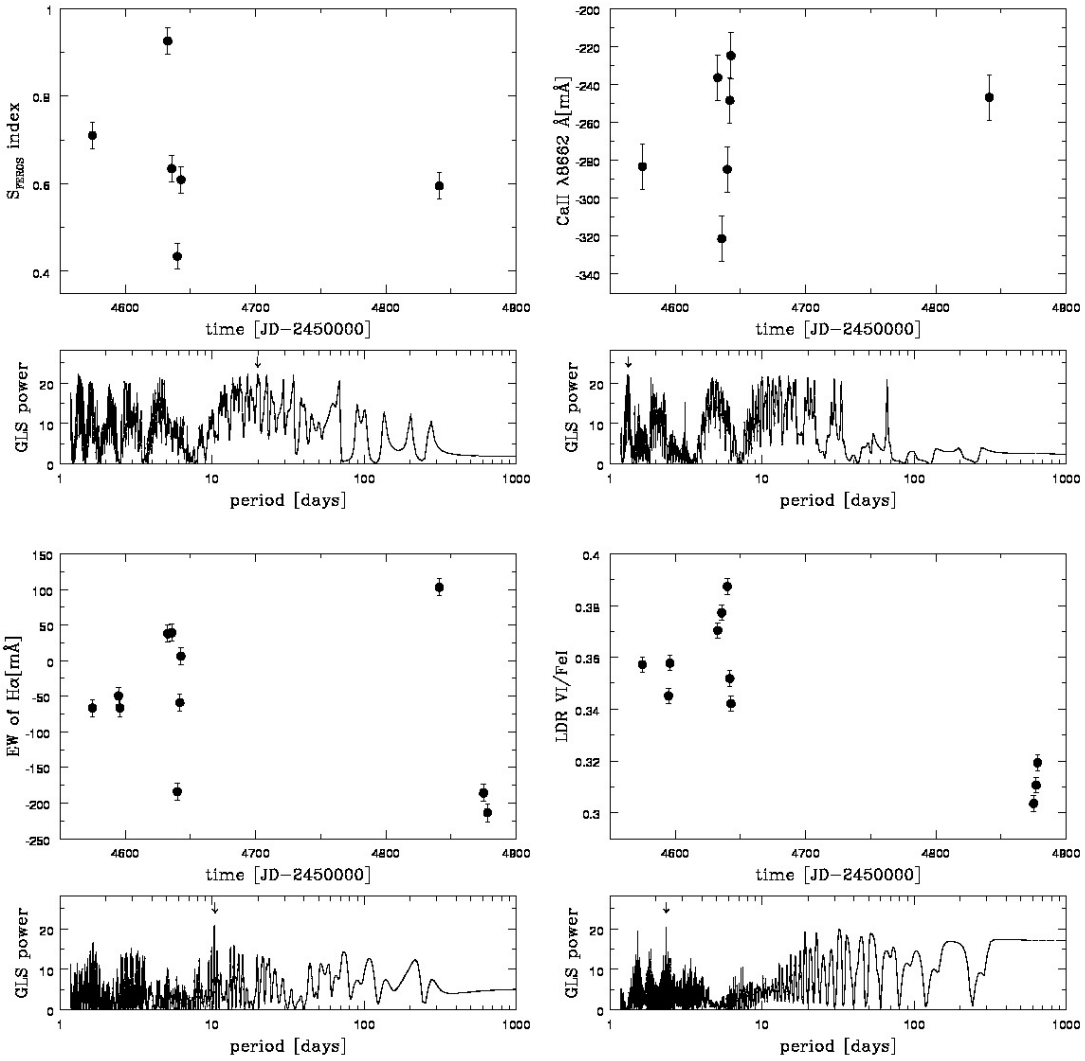

FIGURE D.21 : Activity indicators for LT Lup - S_{FEROS}, Ca II IRT λ 8662, Hα EW, and LDR V I/Fe I.

D.8 LY Lup

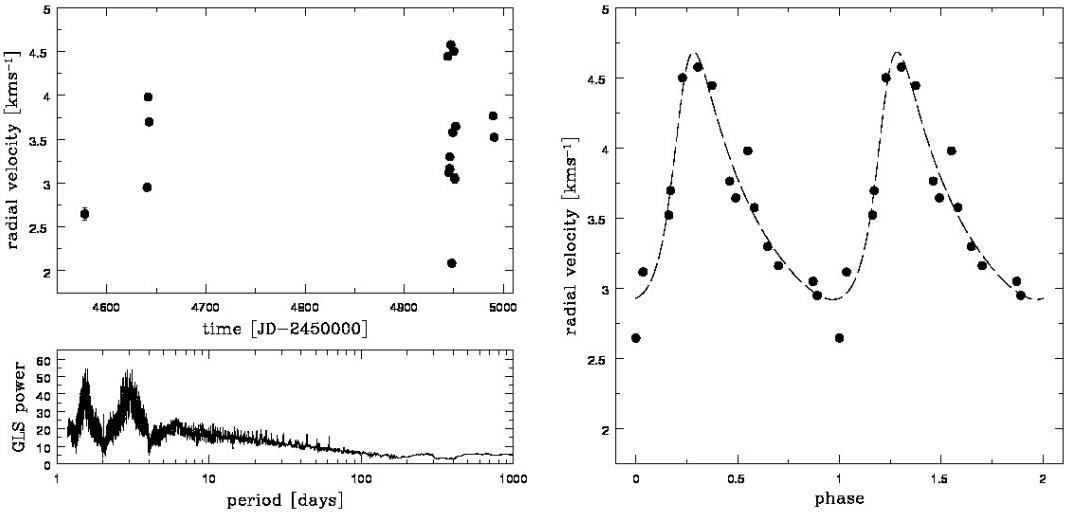

FIGURE D.22 : Radial velocity variation of LY Lup - variation over time and phase-folded with 1.58 days.

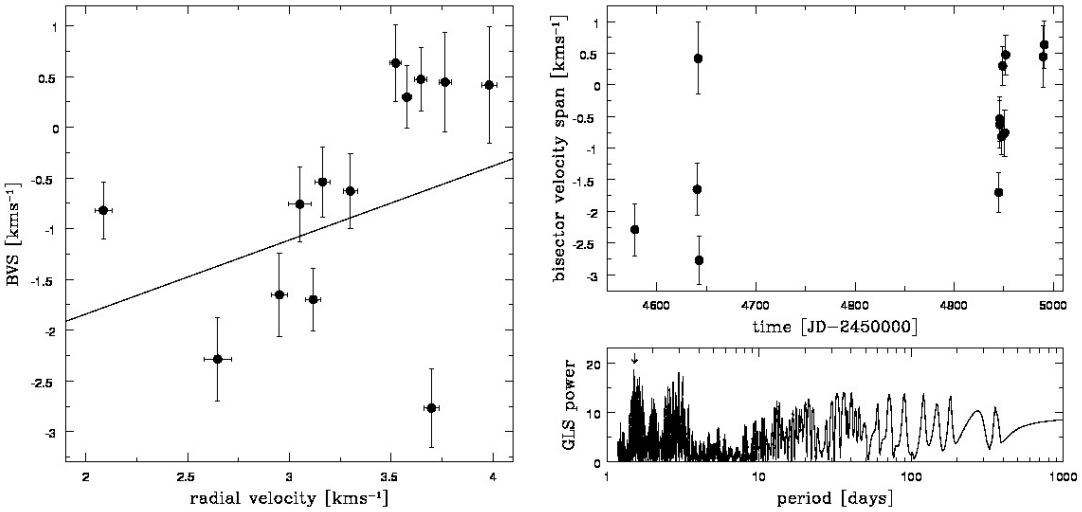

FIGURE D.23 : Bisector velocity span for LY Lup - BVS vs. RV and time variance

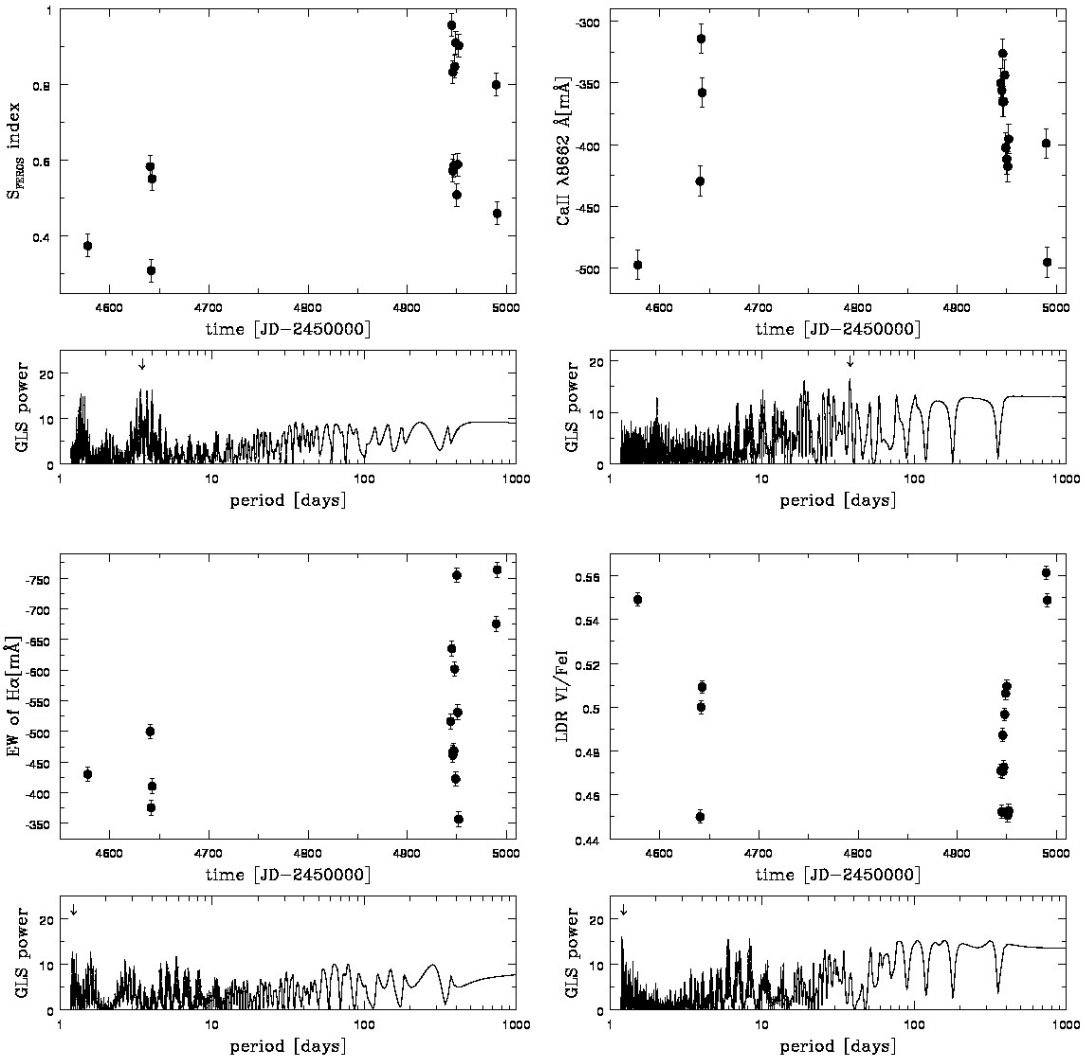

FIGURE D.24 : Activity indicators for LY Lup - S_{FEROS}, Ca II IRT λ 8662, Hα EW, and LDR V I/Fe I.

D.9 HBC 603

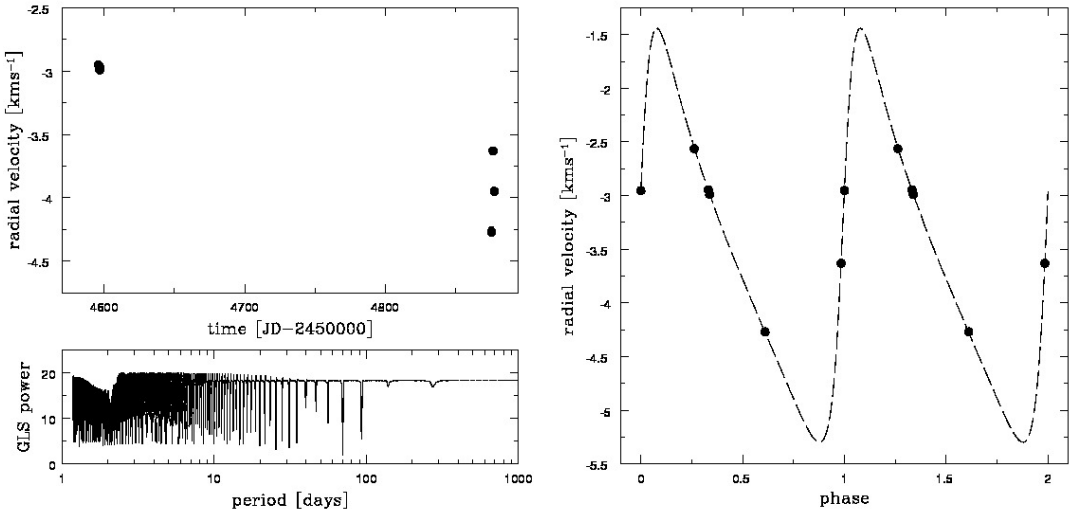

FIGURE D.25 : Radial velocity variation of HBC 603 - variation over time and phase-folded with 2.87 days.

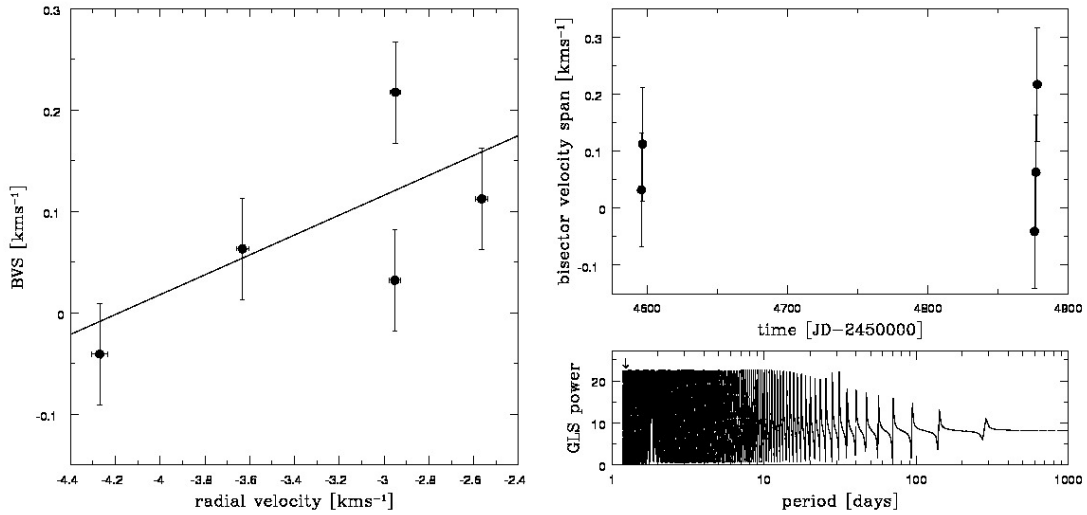

FIGURE D.26 : Bisector velocity span for HBC 603 - BVS vs. RV and time variance

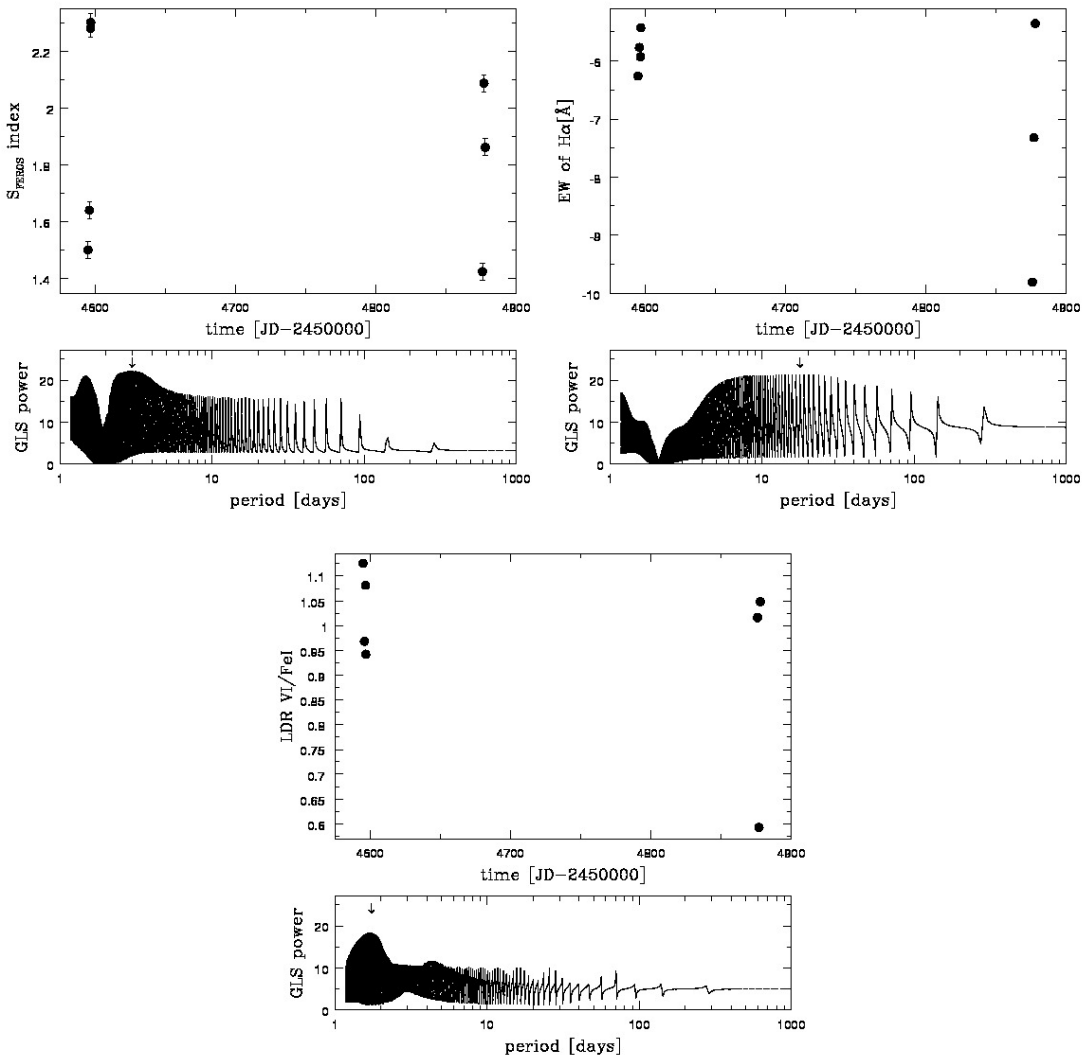

FIGURE D.27 : Activity indicators for HBC 603 - S_{FEROS}, Hα EW, and LDR V I/Fe I.

D.10 CD-37 13029

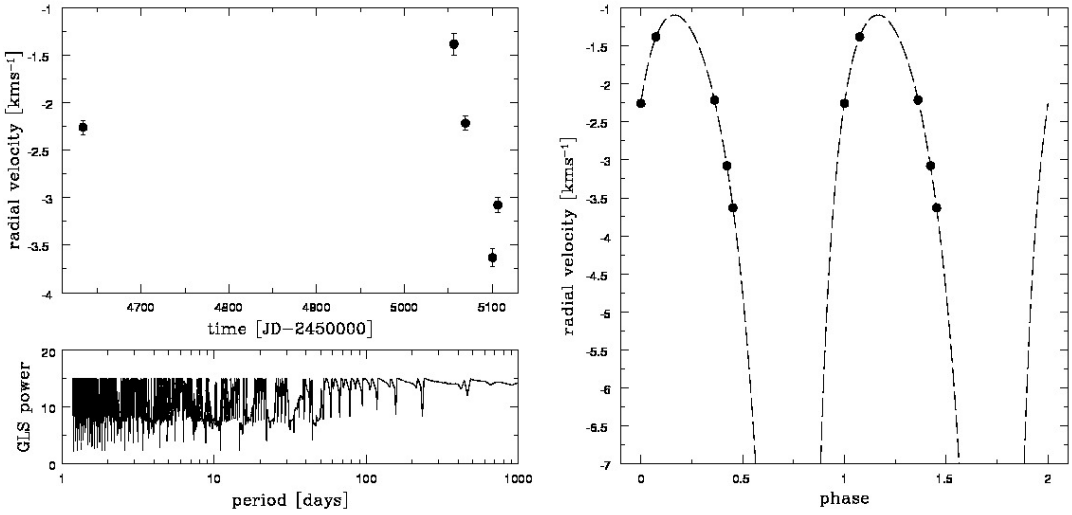

FIGURE D.28 : Radial velocity variation of CD-37 13029 - variation over time and phase-folded with 3.06 days.

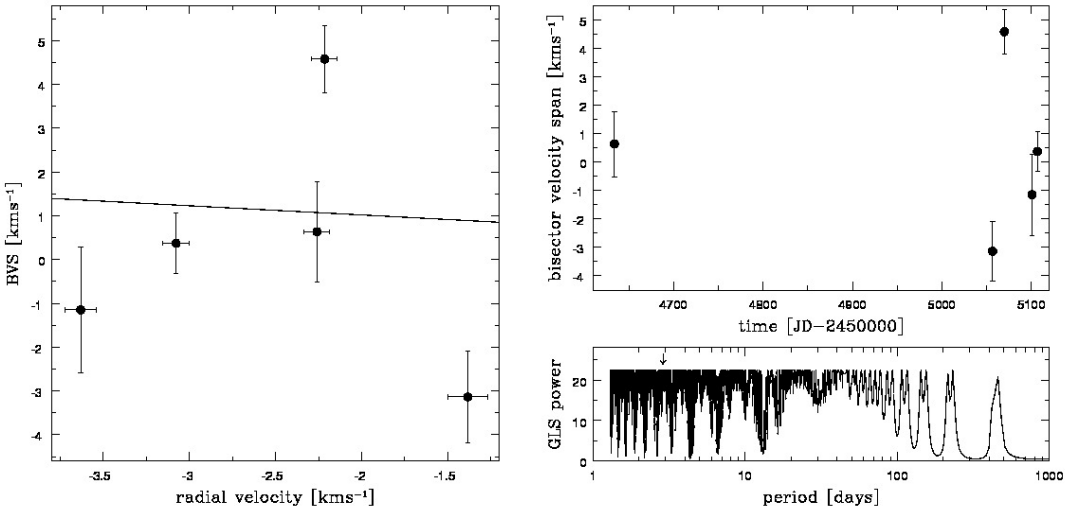

FIGURE D.29 : Bisector velocity span for CD-37 13029 - BVS vs. RV and time variance

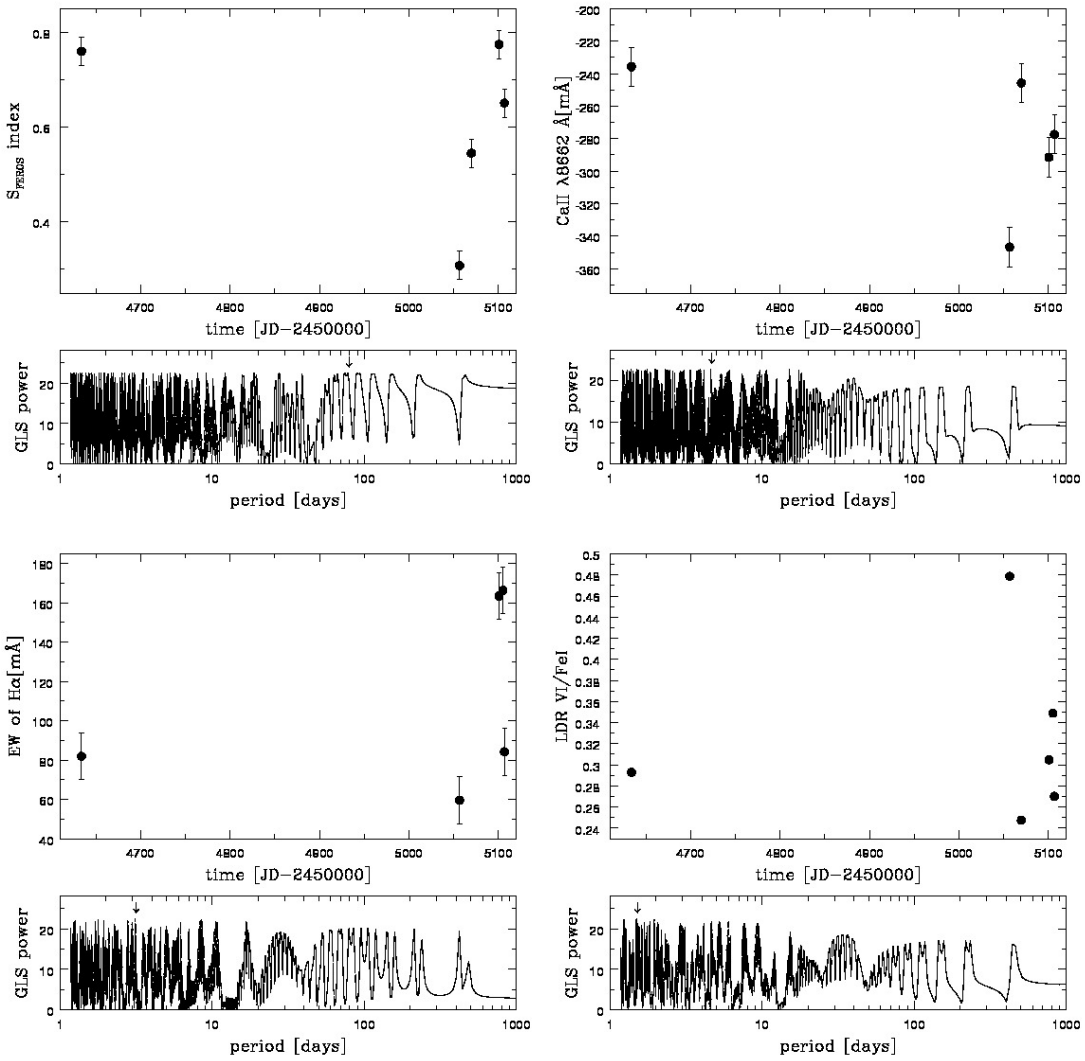

FIGURE D.30 : Activity indicators for CD-37 13029 - S_{FEROS}, Ca II IRT λ 8662, Hα EW, and LDR V I/Fe I.

D.11 CP-72 2713

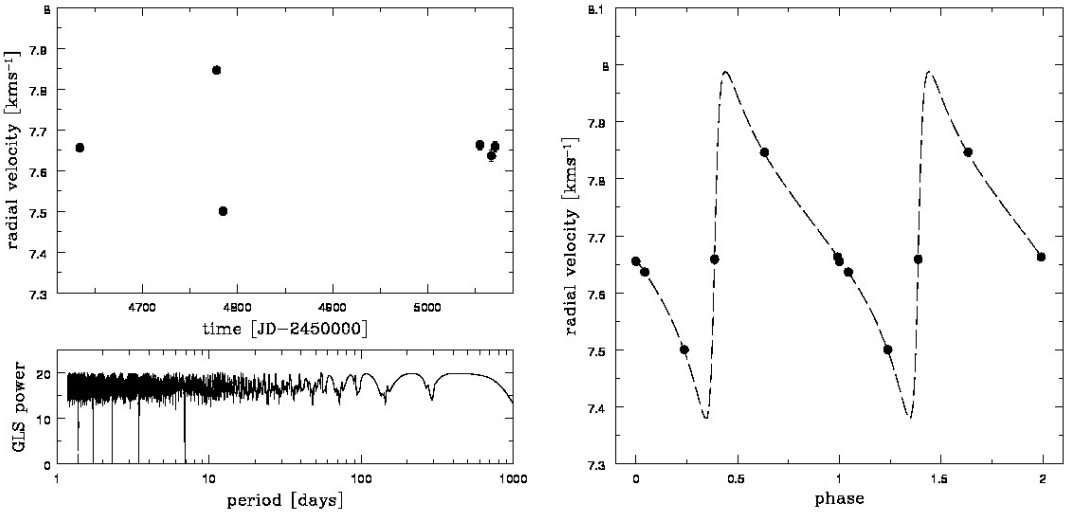

FIGURE D.31 : Radial velocity variation of CP-72 2713 - variation over time and phase-folded with 11.38 days.

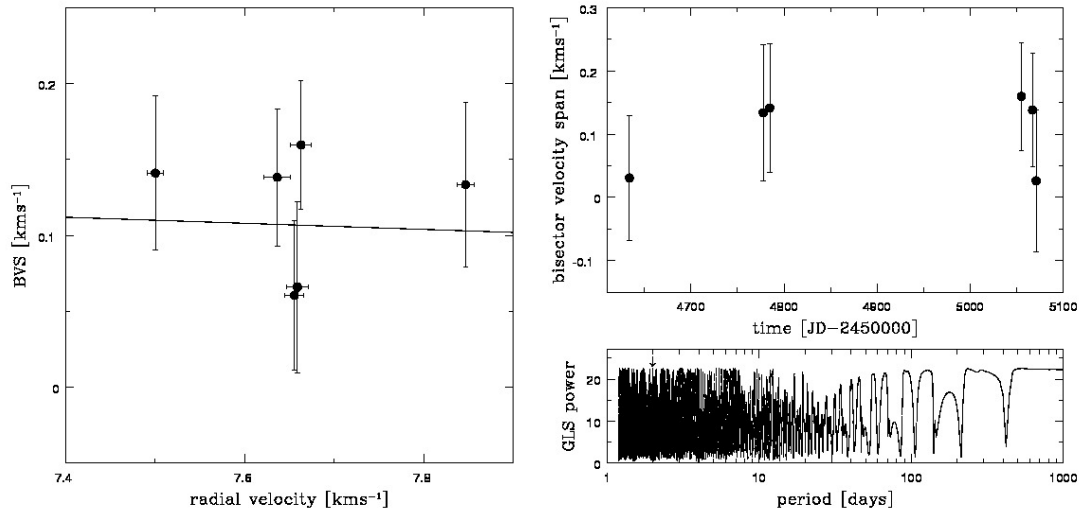

FIGURE D.32 : Bisector velocity span for CP-72 2713 - BVS vs. RV and time variance

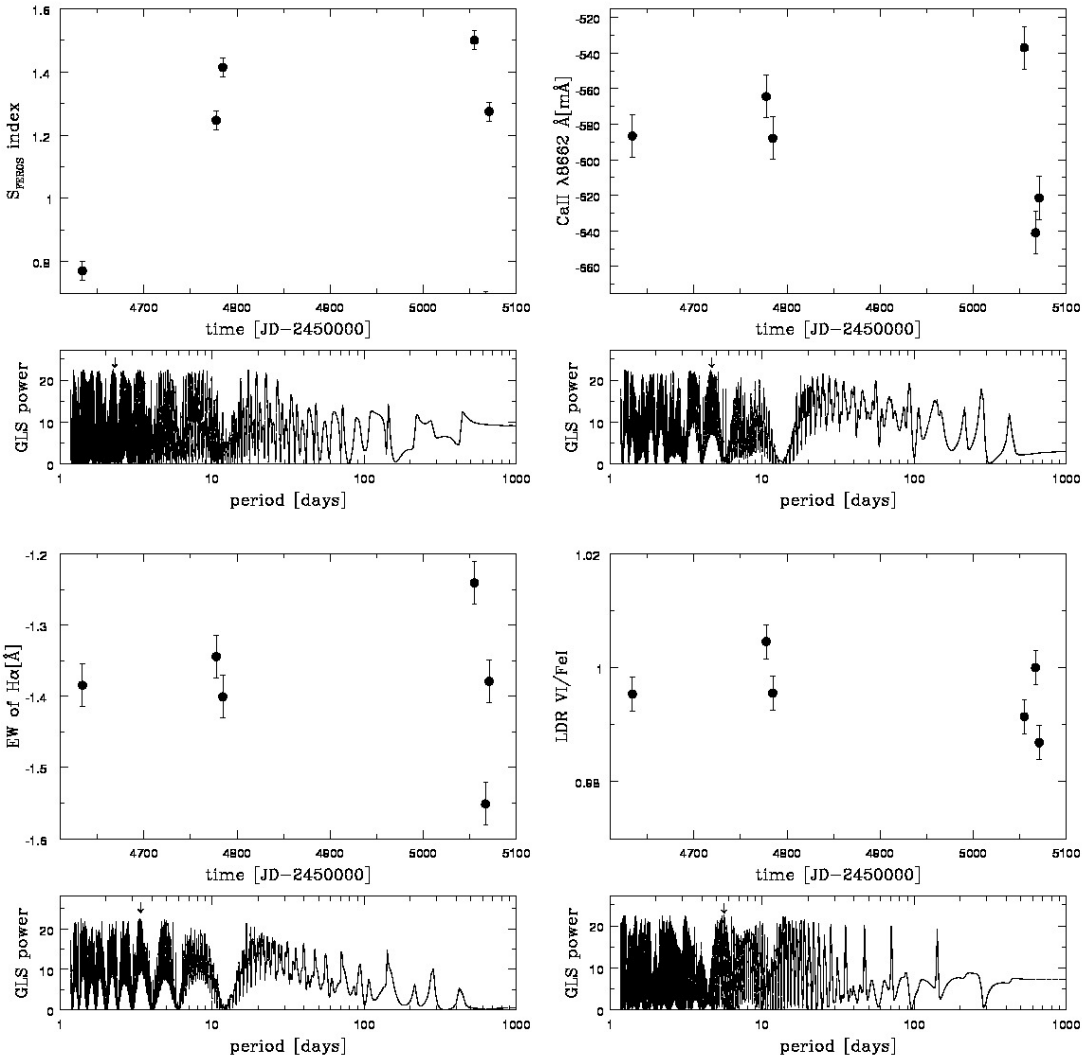

FIGURE D.33 : Activity indicators for CP-72 2713 - S_{FEROS}, Ca II IRT λ 8662, Hα EW, and LDR V I/Fe I.

D.12 HD 217897

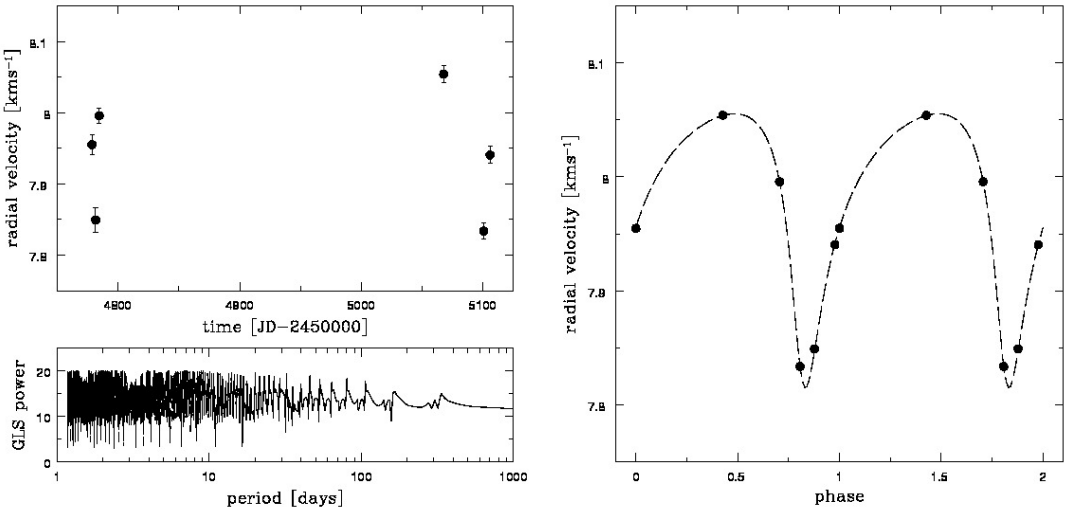

FIGURE D.34 : Radial velocity variation of HD 217897 - variation over time and phase-folded with 1.62 days.

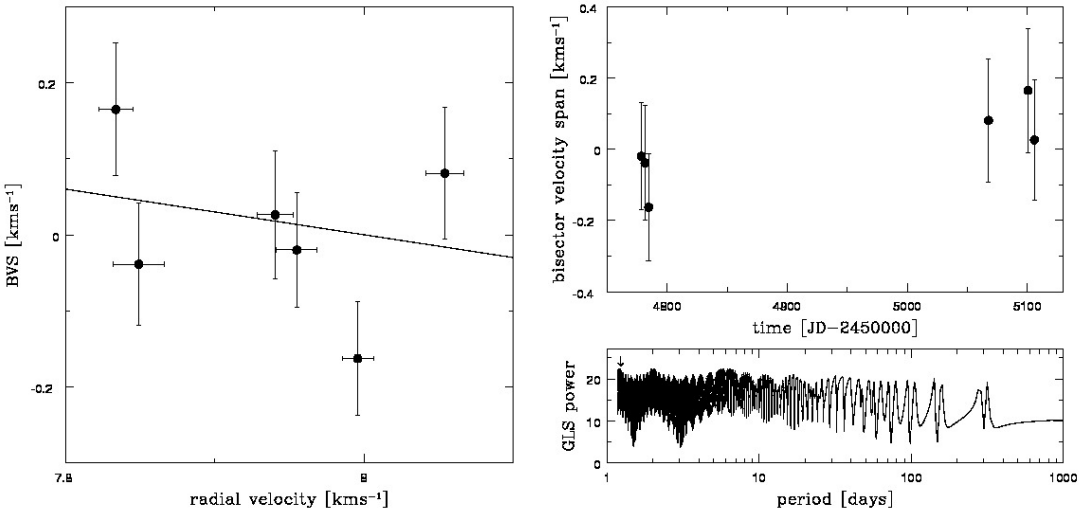

FIGURE D.35 : Bisector velocity span for HD 217897 - BVS vs. RV and time variance

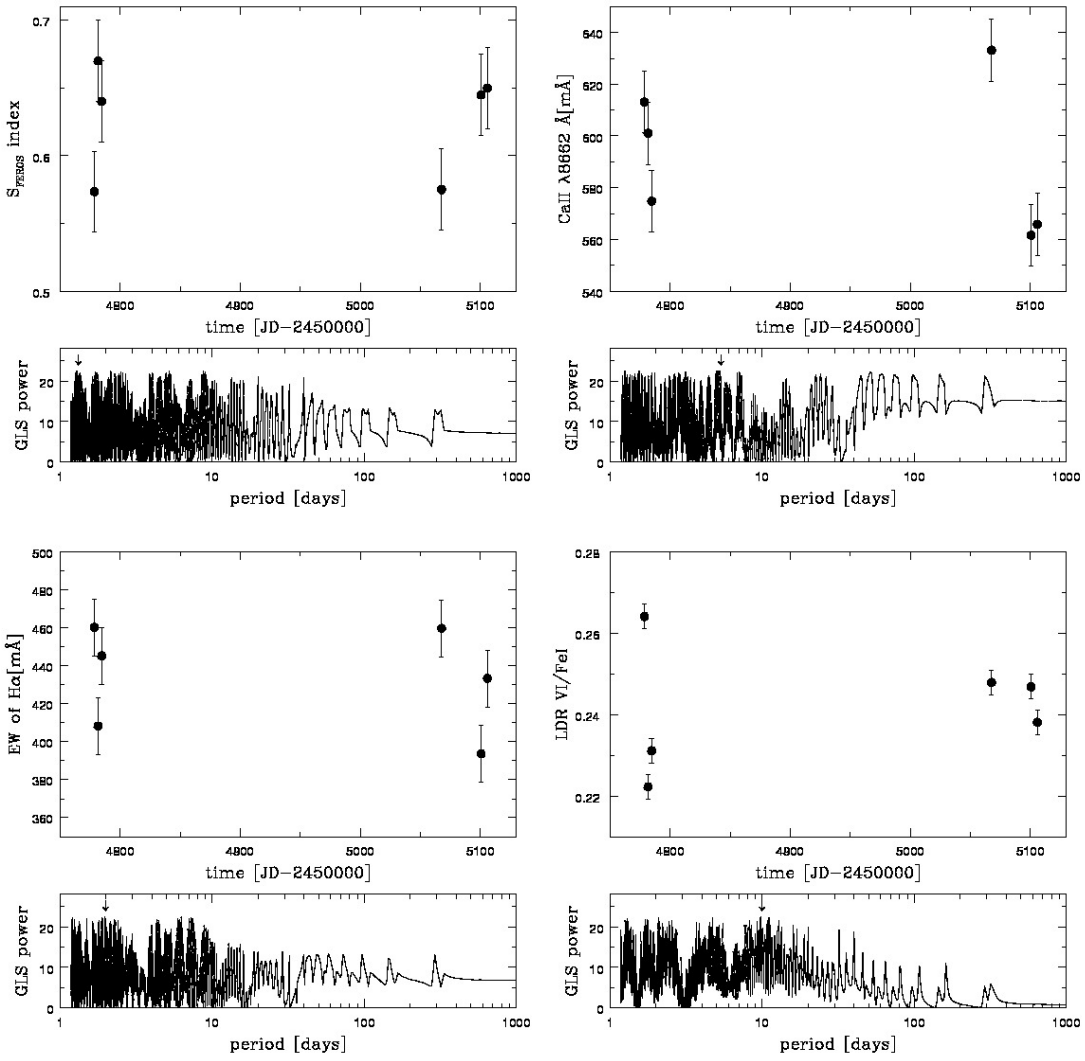

FIGURE D.36 : Activity indicators for HD 217897 - S_{FEROS}, Ca II IRT λ 8662, Hα EW, and LDR V I/Fe I.

D.13 TYC 584-343-1

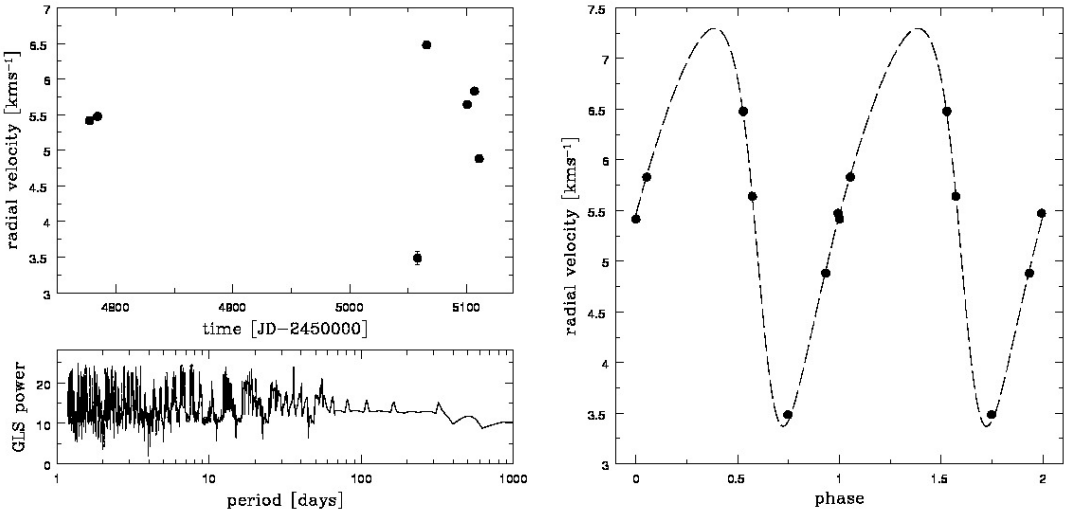

FIGURE D.37 : Radial velocity variation of TYC 584-343-1 - variation over time and phase-folded with 3.01 days.

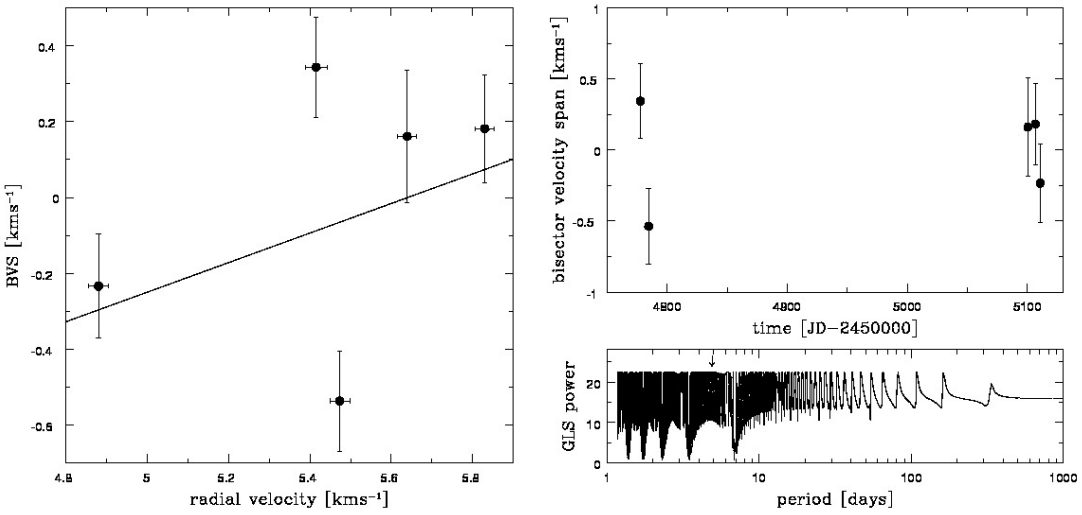

FIGURE D.38 : Bisector velocity span for TYC 584-343-1 - BVS vs. RV and time variance

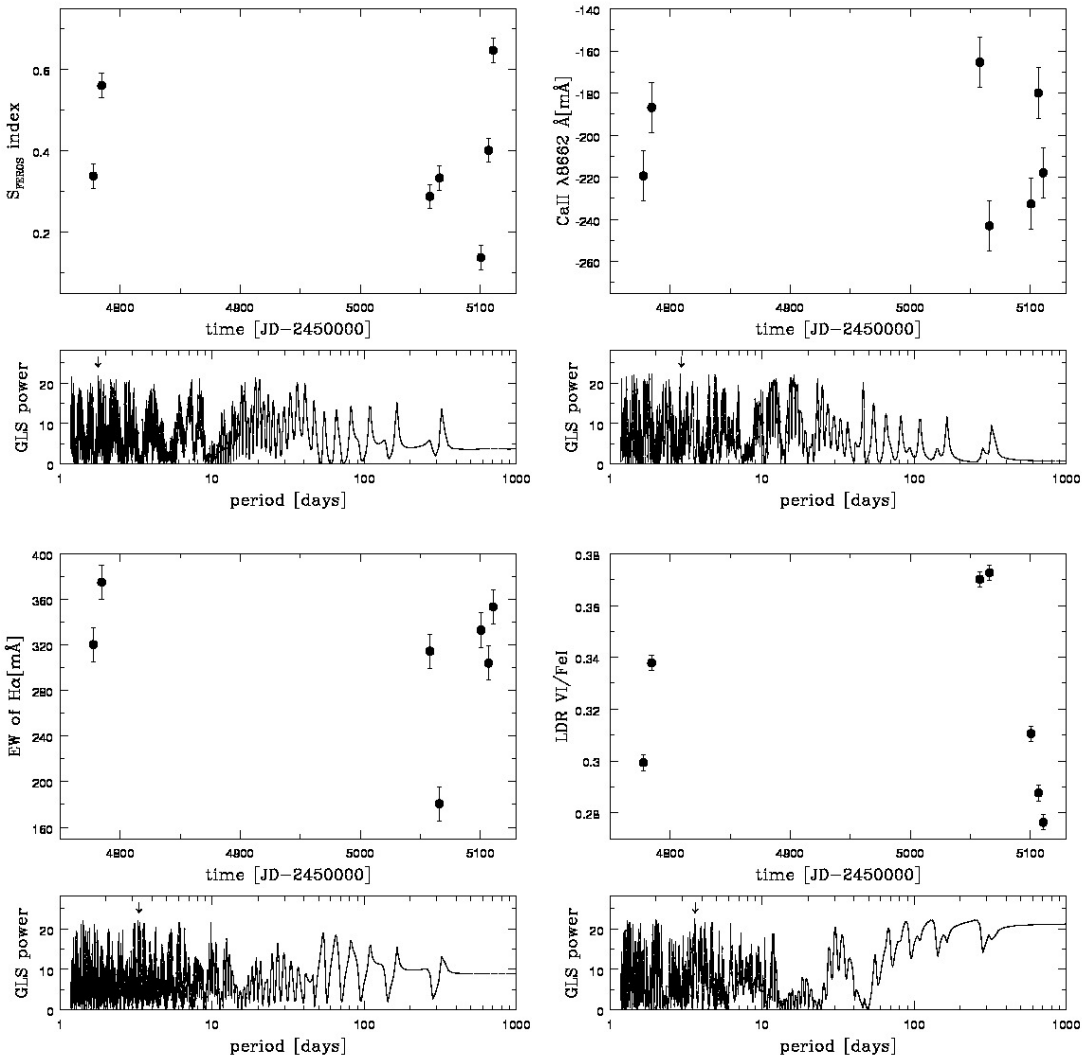

FIGURE D.39 : Activity indicators for TYC 584-343-1 - S_{FEROS}, Ca II IRT λ 8662, Hα EW, and LDR V I/Fe I.

E Calibration of $v \sin i$

In this Appendix, the calibration for the $v \sin i$ measurements in Section 4.3.2 is presented. The $v \sin i$ can be calculated from the width of the CCF $\sigma_{\rm CCF}$ by using

$$v \sin i = A \sqrt{\sigma_{\rm CCF}^2 - \sigma_0^2}, \tag{E.1}$$

where A is a coupling constant and σ_0 is a quantity for intrinsic stellar line-broadening effects (see Section 4.3.2).

The coupling constant A and σ_0 can be calibrated independently of each other, since the quantity A only depends on instrumental and numerical parameters and the quantity σ_0 depends on intrinsic stellar effects. On the other hand, each is needed to calibrate the other variable. To be able to calibrate A, σ_0 has been taken as the width of the unbroadenend artificial spectra (see Section E.1). The resulting A has been used to calibrate σ_0 (Section E.2) with spectra of slow rotating stars with different effective temperatures. As a cross-check, σ_0 computed in Section E.2 has been iteratively used to recalculate A (Section E.1), which yielded the same results for A.

E.1 Calibration of the coupling constant A

The coupling constant A has been derived in a similar way as described by Queloz *et al.* [1998]. For this analysis, theoretical spectra have been cross-correlated with an appropriate template. A synthetic stellar spectrum with effective temperature of 5750 K and $\log g = 4.5$ dex has been produced from Kurucz models [Kurucz, 1993], using the program SPECTRUM [Gray & Corbally, 1994]. This has been done to have the best agreement with the used template for G-type stars. In a first step, the theoretical spectrum has been convolved with a Gaussian-shape instrumental profile matching that of FEROS or HARPS, respectively. Then, the theoretical spectrum with the instrumental profile has been broadened to $v \sin i = 0$, 5, 10, 15, 20, 25 and 30 kms^{-1} and the respective CCF has been calculated by using MACS. The widths of the CCF obtained by a Gaussian fit, $\sigma_{\rm CCF}$, are listed in Table E.1. The effective line width of a non-rotating star, σ_0, has been adopted to be equal to the width of the CCF with $v \sin i = 0\,\mathrm{kms}^{-1}$.

The coupling constant A was then determined as the weighted mean of the A-values derived for the CCFs with different $v \sin i$, using Equation E.1. We derive

$$A_{\mathrm{FEROS}} = 1.8 \pm 0.1 \tag{E.2}$$

and

$$A_{\mathrm{HARPS}} = 1.88 \pm 0.05 \,. \tag{E.3}$$

In both cases, the cross-check by using the σ_0 from Section E.2 yielded the same result for A.

TABLE E.1 : Calibration of A

$v \sin i$ kms^{-1}	σ_{CCF} kms^{-1}	$\sqrt{\sigma^2_{\mathrm{CCF}} - \sigma^2_0}$ kms^{-1}	A
		FEROS	
0	4.47 ± 0.01	...	...
5	5.47 ± 0.02	3.15 ± 0.02	1.59 ± 0.02
10	6.85 ± 0.04	5.15 ± 0.04	1.96 ± 0.03
15	9.69 ± 0.07	8.60 ± 0.08	1.75 ± 0.05
20	11.07 ± 0.10	10.13 ± 0.09	1.98 ± 0.03
25	14.01 ± 0.25	13.28 ± 0.27	1.88 ± 0.16
30	17.34 ± 0.44	16.75 ± 0.48	1.79 ± 0.30
		HARPS	
0	3.86 ± 0.01	...	...
5	4.56 ± 0.02	2.45 ± 0.02	2.05 ± 0.02
10	6.54 ± 0.03	5.28 ± 0.02	1.89 ± 0.01
15	9.02 ± 0.07	8.15 ± 0.06	1.84 ± 0.05
20	11.81 ± 0.13	11.16 ± 0.12	1.79 ± 0.09
25	13.85 ± 0.23	13.30 ± 0.22	1.88 ± 0.15
30	16.62 ± 0.39	16.17 ± 0.37	1.86 ± 0.33

The scatter of A around the adopted weighted mean value is due to the fact that the shape of rotationally broadened spectral lines is no longer well represented by a Gaussian (e.g., Gray [1992]). Thus, the scatter has been introduced by the imperfect matching of the Gaussian fitting function. This behaviour only affects the measurement of the width of the CCF but not the determination of the minimum position, since the CCF of the theoretical spectra is symmetric. In order to test, whether other fitting functions describe the resulting CCF better, several line-profile functions have been used, like an additionally broadened Gaussian. This function has been adopted from Hirano *et al.* [2010]. They describe the stellar rotation profile by a Gaussian, which is then convolved with the first Gaussian used to describe the unbroadened spectral line.

As a result, measurements with all fitting functions yielded the same mean value for A and the scatter around it is not significantly reduced compared to a single Gaussian fit. Thus, an ideal fitting function for a rotationally broadened CCF is not yet existent.

E.2 Calibration of σ_0

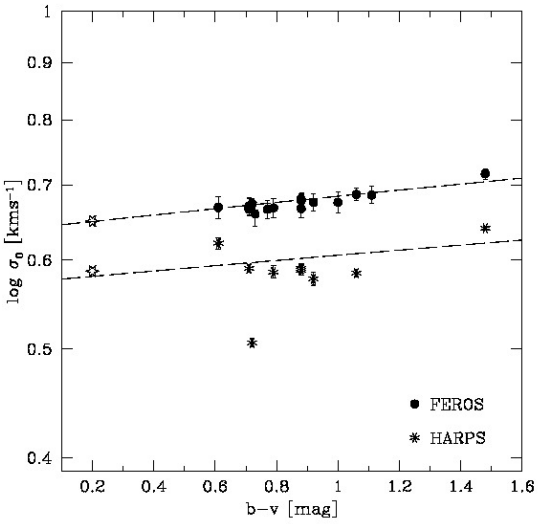

FIGURE E.1 : Calibration of σ_0 - By using slowly rotating stars listed in Table E.2. Also shown at $(b-v) = 0.2$ (open stars) is the σ_0 measured in Section E.1. The dashed lines show the fit to the data.

In order to correctly measure the projected rotational velocity $v \sin i$ of a target and to disentangle it from the intrinsic and instrumental broadening effects, σ_0 has to be known. The instrumental broadening effects should be independent of stellar properties of the observed star, while the intrinsic stellar line broadening depends strongly on $T_{\rm eff}$, due to Doppler broadening. From the Maxwellian most likely velocity of atoms in thermal motion, $v_0^2 \propto T$, and from the relation of the Doppler wavelength shift to this velocity, $\Delta\lambda = v_0\lambda/c$, it follows that

$$\Delta\lambda \propto \sqrt{T_{\rm eff}}. \tag{E.4}$$

Here $\Delta\lambda$ is equivalent to $\sigma_0 = \sigma_{0,\star}$.

Since not all stars have reliable measurements of $T_{\rm eff}$, but colours, like (b − v) are available and can directly be linked to $T_{\rm eff}$, the relation of line broadening with (b − v) has been investigated. According to Flower [1996], the relation between (b − v) and $\log T$ for main-sequence stars and giants is linear within the region of interest of $0 < (b-v) < 1.6$, such that

$$(b-v) \propto \log T_{\rm eff}\ [\rm K] \tag{E.5}$$

holds.

Hence, we can use

$$\log \sigma_0 = a_0 + a_1 \cdot (\mathrm{b} - \mathrm{v}) \tag{E.6}$$

to fit the data. In order to determine this relation, slowly rotating stars have been observed with FEROS at the 2.2m MPG/ESO telescope in La Silla, Chile in 2003 and 2004 and with HARPS at the 3.6m telescope in La Silla, Chile in 2008 and 2009, see Table E.2.

TABLE E.2 : Calibration stars for σ_0, sorted by (b − v)

Identifier	(b − v) mag	$v \sin i_{\mathrm{Valenti}}$ km s^{-1}	Instrument	σ_{CCF} km s^{-1}	σ_0 km s^{-1}
HD 76932	0.53	2.6[a]	FEROS	4.97 ± 2.77	4.76 ± 2.89
HD 1581	0.61	3.0	FEROS	4.95 ± 0.04	4.66 ± 0.11
HD 1581	0.61	3.0	HARPS	4.47 ± 0.04	4.18 ± 0.05
HD 20794	0.71	1.5	FEROS	4.71 ± 0.03	4.63 ± 0.06
HD 20794	0.71	1.5	HARPS	3.97 ± 0.03	3.89 ± 0.03
HD 115617	0.71	2.2	FEROS	4.82 ± 0.04	4.66 ± 0.08
HD 128620	0.71	2.3	FEROS	4.85 ± 0.03	4.68 ± 0.08
HD 10700	0.72	1.3	FEROS	4.77 ± 0.02	4.72 ± 0.05
HD 10700	0.72	1.3	HARPS	3.28 ± 0.03	3.21 ± 0.03
HD 73752	0.73	3.3[a]	FEROS	4.92 ± 0.02	4.63 ± 0.11
HD 13445	0.77	2.4	FEROS	4.82 ± 0.03	4.63 ± 0.09
HD 72673	0.79	2.7[a]	FEROS	4.89 ± 0.02	4.65 ± 0.09
HD 72673	0.79	2.7[a]	HARPS	4.10 ± 0.03	3.85 ± 0.05
HD 4628	0.88	2.0	FEROS	4.89 ± 0.03	4.76 ± 0.07
HD 4628	0.88	2.0	HARPS	4.01 ± 0.02	3.87 ± 0.04
HD 22049	0.88	2.4	FEROS	4.83 ± 0.02	4.64 ± 0.09
HD 22049	0.88	2.4	HARPS	4.09 ± 0.02	3.89 ± 0.04
HD 128621	0.88	0.9	FEROS	4.81 ± 0.03	4.78 ± 0.04
HD 23249	0.92	2.6	FEROS	4.95 ± 0.02	4.74 ± 0.09
HD 23249	0.92	2.6	HARPS	4.02 ± 0.02	3.78 ± 0.05
HD 82106	1.00	3.1	FEROS	5.04 ± 0.02	4.74 ± 0.11
HD 32147	1.06	1.7	FEROS	4.95 ± 0.03	4.86 ± 0.06
HD 32147	1.06	1.7	HARPS	3.94 ± 0.02	3.84 ± 0.03
HD 131977	1.11	2.6	FEROS	5.06 ± 0.02	4.85 ± 0.09
HD 81797	1.48	1.4[b]	FEROS	5.26 ± 0.06	5.20 ± 0.08
HD 81797	1.48	1.4[b]	HARPS	4.43 ± 0.02	4.37 ± 0.02

The error for $v \sin i$ is 0.5 km s^{-1}
References:
Valenti & Fischer [2005]
[a] Reiners & Schmitt [2003]
[b] Gray & Toner [1986]

For FEROS data, the coefficients in Equation E.6 are $a_0 = 0.641 \pm 0.001$, $a_1 = 0.043 \pm 0.003$, and for HARPS data the coefficients are $a_0 = 0.574 \pm 0.001$ and $a_1 = 0.032 \pm 0.002$.

F MACS User Guide

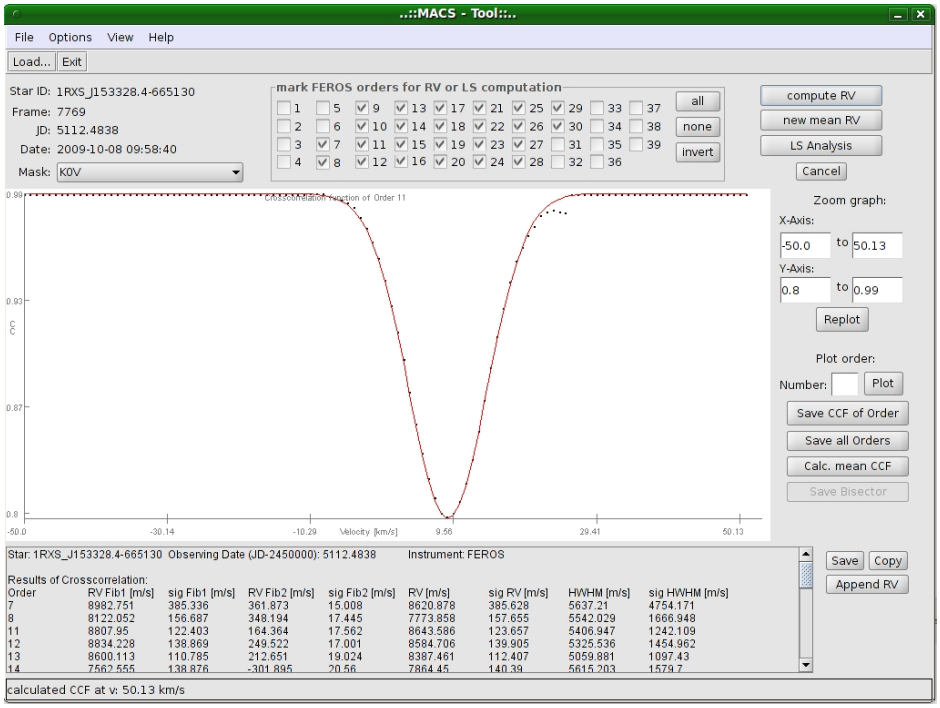

FIGURE F.1 : MACS - The GUI.

F.1 Introduction

MACS is the Max-Planck Institute for Astronomy Cross-correlation and Spectral analysis Tool developed by Patrick Weise. It's purpose is to cross-correlate stellar spectra with template spectra (binary mask or standard-star spectrum) to obtain the stellar radial velocity (RV).

The MACS is written in JAVA and needs Java Runtime Environment 1.5 or higher. It was tested on Linux, Solaris and Windows operating systems. It makes use of the *org.eso.fits* library by Preben Grosbøl[1] to deal with the FITS files. MACS also uses the

[1] `http://www.hq.eso.org/~pgrosbol/fits_java/jfits.html`

scientific library *flanagan* by Dr Michael Thomas Flanagan[1] for the regression method.

F.1.1 Computation of the cross-correlation

For an introduction to the cross-correlation method see Section 4.1. MACS follows very closely Baranne *et al.* [1996] and calculates the cross-correlation function (CCF) $C_o(v)$ as follows

$$C_o(v) = \sum_l \sum_x p_{l,x}(v)\, f_x, \tag{F.1}$$

where f_x is the value of the stellar spectrum at pixel x and $p_{l,x}$ is the value of l^{th} line of the template spectrum at pixel x. The sum is calculated for every given v and then the CCF is normalized. This procedure is done for every order o of the echelle spectrum.
The RV of the order is then obtained by a Gaussian fit to the CCF. If a calibration frame exposure has been taken (e.g. simultaneous ThArNe exposures with FEROS), the procedure described above will be used for the calibration frame too. The RV of an order is then (e.g. Setiawan *et al.* [2003])

$$\mathrm{RV}_o = O_o - C_o, \tag{F.2}$$

where O_o is the RV of the stellar exposure in order o and C_o the corresponding order of the calibration exposure.
The RV of all orders is given in two values. The *weighted mean RV* and the *mean RV* values are given. The *weighted mean RV* is calculated with the errors of the Gaussian fit as the weights of the measurements. The *mean RV* value is calculated without including the errors of each individual measurement.
In both cases the error of RV is calculated as

$$\sigma_{\mathrm{RV}} = \sum_o \sqrt{\frac{(\mathrm{RV}_o - \bar{\mathrm{RV}})^2}{2 \cdot N \cdot (N-1)}}, \tag{F.3}$$

where N is the number of measurements.
In addition to the RV, the Half-Width at Half-Maximum (HWHM) of the CCF is given, calculated as the weighted mean of the individual measurements. With the HWHM of the CCF and the calibration given by Weise *et al.* [2010], one can calculate the $v \sin i$ of the target.

F.1.1.1 Line Shape Analysis

To characterize magnetic activity of stars, the Bisector of the CCF is calculated and analysed (e.g., Queloz *et al.* [2001]). MACS is able to calculate the Bisector Velocity

[1] `http://www.ee.ucl.ac.uk/~mflanaga`

Span (BVS), Bisector Curvature (BC) and Bisector Velocity Displacement (BVD) of the CCF (see Section F.5). Furthermore, the dependence of RV with wavelength is calculated by MACS (see Launhardt et al. 2010, in preparation). This can be used to rule out surface spots as the source of the RV variation. MACS calculates the slope of the RV over the mean wavelength of each FEROS order used, such that the unit of this correlation coefficient is $ms^{-1}nm^{-1}$.

F.2 Install

Install MACS by

```
> tar -xvfz macs.tar.gz
```

and start it by

```
> java -jar macs.jar
```

F.3 How to start

To start you have to load a spectral file. MACS can handle FEROS spectra (.mt) or HARPS spectra (.fits), each processed with the ESO Data Reduction System. Furthermore, ascii-files can be used, which have two columns of wavelength and flux. In

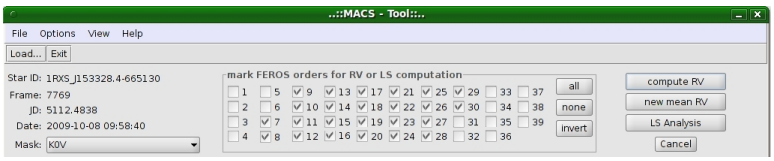

FIGURE F.2 : MACS GUI - Upper part of MACS

the upper part of the MACS window (see Figure F.2), the information retrieved from the data file, like the ID of the target, frame number (FEROS only), JD, and observing date is presented. In the drop-list *Mask*, the template for the cross-correlation has to be changed according to the spectral type of the target.
Next to this information the panel *mark FEROS orders for RV or LS computation* is located, where one selects the FEROS orders to be used in the calculation. The calculation of the RV will start by clicking the *compute RV* button.
The button *new mean RV* can be used to calculate a new mean RV after deselecting some orders without re-calculating each individual CCF.
Calculation of the Bisector starts by clicking on the button *LS analysis* (see Section F.5). Each calculation can be stopped by clicking on the *cancel* button, but no results will be displayed.

After finishing the calculations, results will be displayed below the plot-area. You can now save these results in a file (*save* button), which is essential for the results of the line-shape analysis. One can select some parts of the results and copy them to the clipboard (*copy* button) or append the results for the mean RV, HWHM and color dependence to an existing file with the *append RV* button.

F.4 The plot-area

After loading a stellar spectrum one can zoom into this by entering a new range in the *X-Axis* and *Y-Axis* text-fields on the right to the plot-area.

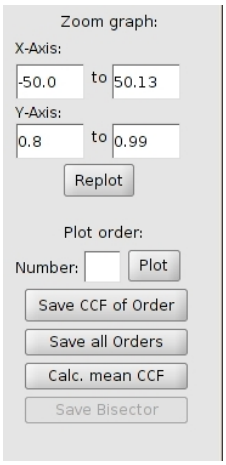

FIGURE F.3 : MACS GUI - Plot area.

Another order of the loaded exposure can be plotted (without loading a new file) by entering the number of the order in the *plot order* text-field and pressing the *plot* button.
The CCF of the selected order can be saved by clicking on the *Save CCF of order* button. This will provide a plain ascii-file of the CCF, which can then be used in any other application. *Save all orders* will save each CCF of the selected orders in a separate file. *Calc. mean CCF* will calculate the mean CCF of all selected orders, plot it and fit the mean CCF with a Gaussian. This can be used to reduce the noise of a CCF.
The *Save Bisector* button is available after calculating the Bisector for each order and saves the shape of the bisector in individual ascii-files.

F.5 Line Shape analysis

MACS can also calculate the *Bisector Velocity Span*, *Bisector Curvature* and the *Bisector Velocity Displacement*. All of them can be used as an indicator of stellar activity.

The Line Shape analysis starts by clicking on the *LS Analysis* button at the top right of MACS.
After the computation of an individual CCF, one has to give the positions of the the left and right border of the CCF (see figure). When done, proceed with the right mouse button.

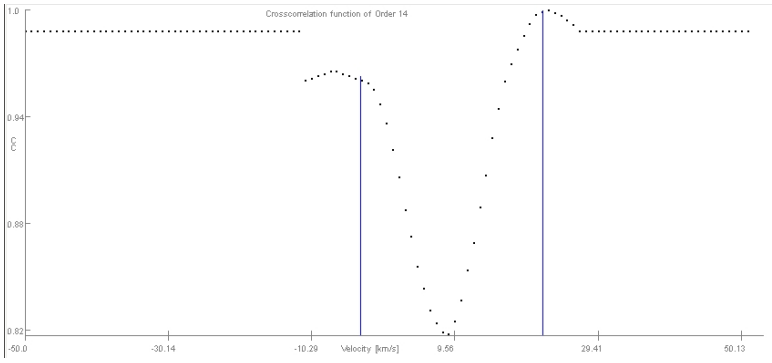

FIGURE F.4 : MACS GUI - Example of Line shape analysis.

The BVS, BC and BVD are then calculated. For this, the CCF is interpolated to get a very high resolution and the corresponding points on each side of the CCF are connected. At which height these points are can be changed in the *preferences* (see section F.6.6). The values for BC and BVD are calculated as described in Section 4.1.2. The resulting shape of the Bisector can be shown in the plot-area by selecting *View - View Bisector results* in the menu-bar. The results can be saved by clicking on *Save Bisector*.

F.6 Preferences dialogue

Some adjustments to the calculations can be found in the *Options - Preferences* window in the menu-bar.

F.6.1 General appearance

On the *General preferences* tab, one can enter the length of a pause between two calculations, so that there is time to look at the resulting CCF. The value has to be entered in nanoseconds.
By clicking on the check-box *Stop between CCF plotting*, MACS stops calculating after each order until one proceeds with the right mouse button. This is useful to check whether the mask is appropriate or has to be changed.

The use of the *Savitzky-Golay filter* is highly recommended to increase the accuracy of the RV measurement. The Savitzky-Golay filter simply sets the noise next to the

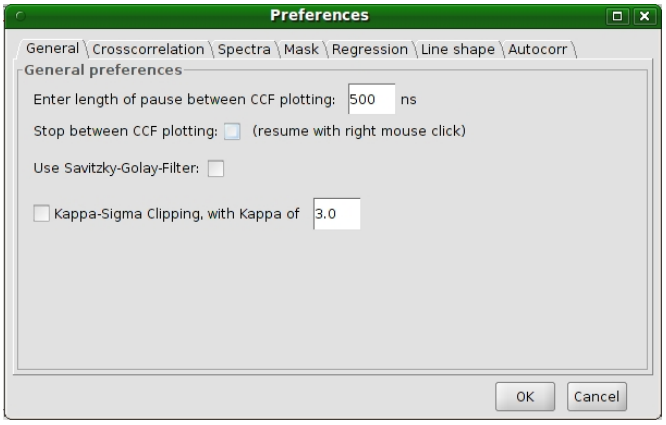

FIGURE F.5 : MACS preferences - The general appearance tab.

CCF to unity, which increases the accuracy of the Gaussian fit.
Finally, the $\kappa\sigma$ *clipping* can be activated. This removes the RV of all orders which is higher or lower than $\kappa\sigma$ of the mean RV, where σ is the error of the mean RV and κ the value specified in the test-field.

F.6.2 Cross-correlation

The tab titled *Cross-correlation* allows one to change the range and the velocity step used in the CCF calculation.
As a default the range of the cross-correlation is set to [-100,100] kms^{-1}, but one can enter any range in which the CCF should to be calculated. The value in the left text-field has to be lower than the value in the right text-field.

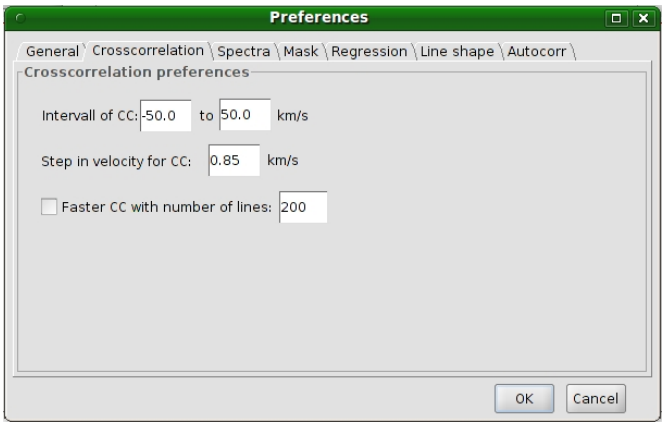

FIGURE F.6 : MACS preferences - The cross-correlation tab

Another possibility to gain more resolution in the CCF is to set a lower velocity step, *vstep*. As default a *vstep* of 0.85 kms^{-1} is set (these are 235 calculations for the default range). The higher resolution leads to a higher accuracy in the Gaussian fit.

In addition to these two, one has the possibility to restrict the number of lines to be used during cross-correlation. This can be used for merged spectra (like HARPS). This may save computation time, but increases the noise in the CCF.

F.6.3 Spectra

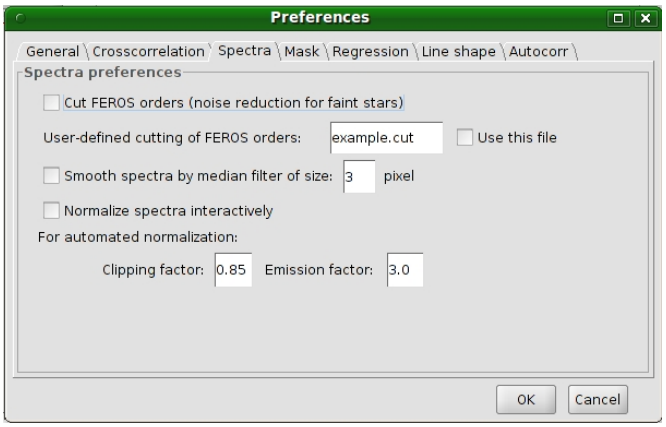

FIGURE F.7 : MACS preferences - The spectra tab

The (mostly) noisy beginning and ending of the FEROS orders can be cut by activating *Cut FEROS orders*. This will truncate the order by a few pixel and results in a more de-noised CCF. If this is not enough one has the possibility to provide a *file* in which the amount of pixel to be cut are noted.
This file must consists of two columns per line, with each line representing an order. The first column is the left pixel border, all pixels left to this one will be cut away. The second column is the right pixel border (counted from the start), all pixel on the right are cut away. To use this file, one has to activate the check-box.
If the CCF is still too noisy, smooth the spectrum with a *median* filter by activating the check-box and enter a (odd) number of pixel to be used to determine the median value.
Each spectrum is automatically normalized, but the parameters can be changed. The clipping factor is multiplied with σ of the residuals of the polynomial fit and each value of the spectra below this value is replaced by the fit. With this method the fit comes closer to the real continuum. The emission factor is used to remove emission line features in the spectrum. Each value higher than the emission factor times the mean of the spectral data is replaced by the mean. This leads to vanishing emission line features after some iterations, thus, these features do not disturb the fitting of the continuum.
In case of very broad emission lines or if one is not satisfied with the normalized spectrum, the spectrum can be normalized interactively. Check the corresponding box on this panel. During the computation of the CCF one will be asked to select points for

the normalization of the spectra by clicking at the spectra. These points will be used to calculate a cubic spline, which is used to normalize the spectra. Proceed with the right mouse-button.

F.6.4 Provide a new mask

If a user-created mask should be used, one can enter the file-name in the *Mask* tab.

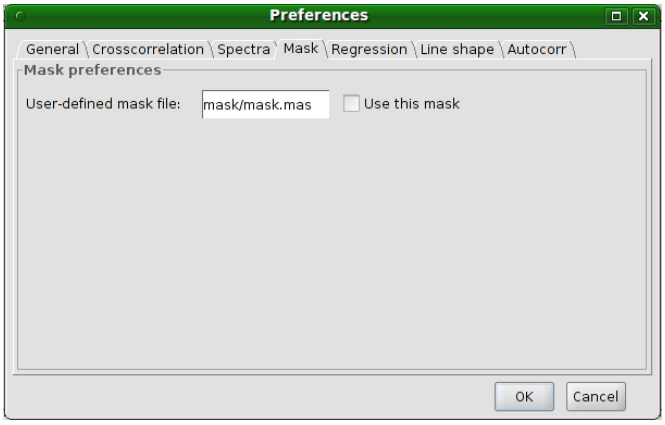

FIGURE F.8 : MACS preferences - Provide a new mask.

The template must consists of two columns. The first column gives the starting point of the line in Angstroms, the second column the endpoint in Angstroms.
To use the file, the check-box has to be activated.

F.6.5 Regression

On the *Regression* panel, one can select the desired fitting function to fit the CCF. The fitting functions are shown in the figure. The *broadened Gaussian* is a convolution of two Gaussians, one broad and one narrow Gaussian. The Lorentz and Voigt functions have been taken from Origin. One can also switch of the fit.

MACS has the ability to fit more than one Gaussian to a CCF. To do this, this option on the *Regression* tab has to be activated and the number of Gaussian entered. When the CCF has been calculated, one has to indicate the center and the left and right border for each Gaussian within the CCF. The first mouse click must be the center of the first Gaussian, followed by the left and right border. After this, proceed with the center of the second Gaussian and so on. After providing all values for all Gaussian one can proceed with the right mouse button.
The fit of more than one Gaussian is still in a testing phase and the resulting Gaussian still strongly depends on the point of your provided center and the depth of the CCF at that point.

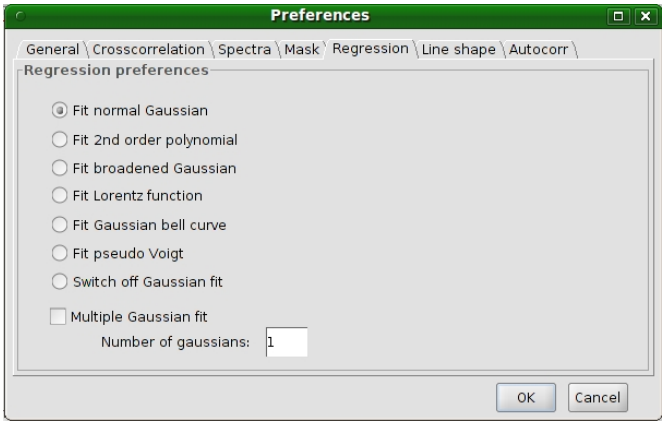

FIGURE F.9 : MACS preferences - The regression tab.

F.6.6 Line shape

In the panel *Line shape*, the automated calculation of the Bisector can be activated. In this case, the left and right border are set automatically.

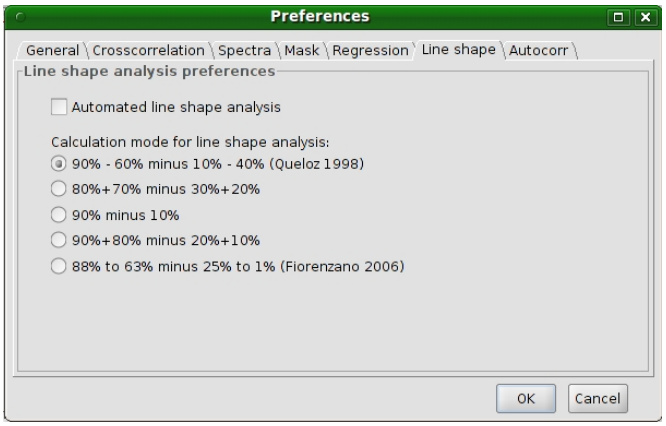

FIGURE F.10 : MACS preferences - Adjustments for for the calculation of line shape.

Furthermore, the computation of the Bisector can be changed as stated in the figure.

F.6.7 Autocorrelation

The Autocorrelation in MACS is still not fully tested, but one can select a file (FEROS, HARPS or ascii-file) which will then be correlated with the data. To use the autocorrelation the check-box has to be activated.

For the Autocorrelation, the data and the template will be split in chunks of a given width and then each chunk will be correlated with the corresponding chunk of the template. The resulting CCF per order is the mean of all chunks of this order. The width of the chunks can be set in the text-field.

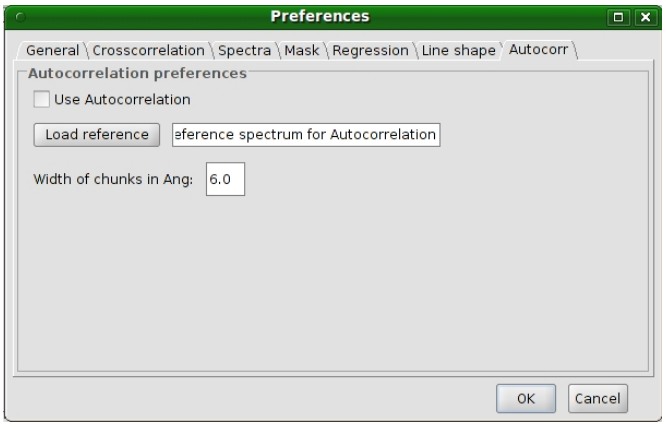

FIGURE F.11 : MACS preferences - Adjustments for auto-correlation.

References

Allain, S. (1998). Modelling the angular momentum evolution of low-mass stars with core-envelope decoupling. *A&A*, **333**, 629–643. 40

Appenzeller, I. & Mundt, R. (1989). T Tauri stars. *A&A Rev.*, **1**, 291–334. 4, 27, 28

Armitage, P.J. & Bonnell, I.A. (2002). The brown dwarf desert as a consequence of orbital migration. *MNRAS*, **330**, L11–L14. 9

Armitage, P.J. & Clarke, C.J. (1996). Magnetic braking of T Tauri stars. *MNRAS*, **280**, 458–468. 36

Attridge, J. & Herbst, W. (1992). CCD Photometry of T Tauri Variables in Orion. In *Bulletin of the American Astronomical Society*, vol. 24 of *Bulletin of the American Astronomical Society*, 798–+. 38, 39

Baade, D., Meisenheimer, K., Iwert, O., Alonso, J., Amico, P., Augusteijn, T., Beletic, J., Bellemann, H., Benesch, W., Böhm, H., Böhnhardt, H., Deiries, S., Delabre, B., Donaldson, R., Dupuy, C., Franke, O., Gerdes, R., Gilmozzi, R., Grimm, B., Haddad, N., Hess, G., Klein, H., Lenzen, R., Lizon, J., Mancini, D., Münch, N., Rahmer, G., Reyes, J., Robledo, E. & Silber, A. (1998). The wide field imager for the 2.2-m MPG/ESO telescope: a preview. *The Messenger*, **93**, 13–15. 49

Baranne, A., Queloz, D., Mayor, M., Adrianzyk, G., Knispel, G., Kohler, D., Lacroix, D., Meunier, J., Rimbaud, G. & Vin, A. (1996). ELODIE: A spectrograph for accurate radial velocity measurements. *A&AS*, **119**, 373–390. 17, 19, 20, 192

Benz, W. & Mayor, M. (1984). Photoelectric rotational velocities of late-type dwarfs. *A&A*, **138**, 183–188. 20, 25

Bernhard, K., Bernhard, C. & Bernhard, M. (2009). Chromospherically active stars in the ASAS-3 database: Paper 1. 25 new variables. *Open European Journal on Variable Stars*, **98**, 1–+. 66

Bevington, P.R. & Robinson, D.K. (2003). *Data reduction and error analysis for the physical sciences*. 43, 49, 50

Bodenheimer, P. (1989). Formation and Evolution of the Solar Nebula. In F. Meyer, ed., *NATO ASIC Proc. 290: Theory of Accretion Disks*, 75–+. 4

Boss, A.P. (2006). On the Formation of Gas Giant Planets on Wide Orbits. *ApJ*, **637**, L137–L140. 106

Boss, A.P. (2008). Rapid formation of gas giants, ice giants and super-Earths. *Physica Scripta Volume T*, **130**, 014020–+. 6, 7, 9

Bouvier, J. (1995). The rotational history of solar-type stars: does it affect Lithium abundances? *Memorie della Societa Astronomica Italiana*, **66**, 341–+. 27

Bouwman, J., Lawson, W.A., Dominik, C., Feigelson, E.D., Henning, T., Tielens, A.G.G.M. & Waters, L.B.F.M. (2006). Binarity as a Key Factor in Protoplanetary Disk Evolution: Spitzer Disk Census of the η Chamaeleontis Cluster. *ApJ*, **653**, L57–L60. 36, 37

Brauer, F., Henning, T. & Dullemond, C.P. (2008). Planetesimal formation near the snow line in MRI-driven turbulent protoplanetary disks. *A&A*, **487**, L1–L4. 7

Broeg, C., Schmidt, T.O.B., Guenther, E., Gaedke, A., Bedalov, A., Neuhäuser, R. & Walter, F.M. (2007). Rotational period of GQ Lupi. *A&A*, **468**, 1039–1044. 106, 107

Brown, J.M., Blake, G.A., Dullemond, C.P., Merín, B., Augereau, J.C., Boogert, A.C.A., Evans, N.J., II, Geers, V.C., Lahuis, F., Kessler-Silacci, J.E., Pontoppidan, K.M. & van Dishoeck, E.F. (2007). Cold Disks: Spitzer Spectroscopy of Disks around Young Stars with Large Gaps. *ApJ*, **664**, L107–L110. 101

Burrows, A., Marley, M., Hubbard, W.B., Lunine, J.I., Guillot, T., Saumon, D., Freedman, R., Sudarsky, D. & Sharp, C. (1997). A Nongray Theory of Extrasolar Giant Planets and Brown Dwarfs. *ApJ*, **491**, 856–+. 9

Camenzind, M. (1990). Magnetized Disk-Winds and the Origin of Bipolar Outflows. In G. Klare, ed., *Reviews in Modern Astronomy*, vol. 3 of *Reviews in Modern Astronomy*, 234–265. 36

Cameron, A.G.W. (1973). Formation of the Outer Planets (Article published in the Space Science Reviews special issue on 'Outer Solar System Exploration - An Overview', ed. by J. E. Long and D. G. Rea.). *Space Science Reviews*, **14**, 383–391. 6

Carpenter, J.M., Bouwman, J., Mamajek, E.E., Meyer, M.R., Hillenbrand, L.A., Backman, D.E., Henning, T., Hines, D.C., Hollenbach, D., Kim, J.S., Moro-Martin, A., Pascucci, I., Silverstone, M.D., Stauffer, J.R. & Wolf, S. (2009). Formation and Evolution of Planetary Systems: Properties of Debris Dust Around Solar-Type Stars. *ApJS*, **181**, 197–226. 34, 69, 71

Catalano, S., Biazzo, K., Frasca, A. & Marilli, E. (2002). Measuring starspot temperature from line depth ratios. I. The method. *A&A*, **394**, 1009–1021. 13, 24

Chauvin, G., Lagrange, A., Bonavita, M., Zuckerman, B., Dumas, C., Bessell, M.S., Beuzit, J., Bonnefoy, M., Desidera, S., Farihi, J., Lowrance, P., Mouillet, D. & Song, I. (2010). Deep imaging survey of young, nearby austral stars . VLT/NACO near-infrared Lyot-coronographic observations. *A&A*, **509**, A52+. 54

Cieza, L. & Baliber, N. (2007). Testing the Disk Regulation Paradigm with Spitzer Observations. II. A Clear Signature of Star-Disk Interaction in NGC 2264 and the Orion Nebula Cluster. *ApJ*, **671**, 605–615. 42

Desort, M., Lagrange, A., Galland, F., Udry, S. & Mayor, M. (2007). Search for exoplanets with the radial-velocity technique: quantitative diagnostics of stellar activity. *A&A*, **473**, 983–993. 11, 24, 50, 52

Devillard, N. (1997). The eclipse software. *The Messenger*, **87**, 19–20. 49

Dullemond, C.P., Durisen, R.H. & Papaloizou, J.C.B. (2009). *Structure and dynamics of protoplanetary disks*, 350–+. Cambridge University Press. 5

Eggenberger, A. & Udry, S. (2010). Detection and Characterization of Extrasolar Planets through Doppler Spectroscopy. In T. Montmerle, D. Ehrenreich, & A.-M. Lagrange, ed., *EAS Publications Series*, vol. 41 of *EAS Publications Series*, 27–75. 10, 11, 20

Fallscheer, C. & Herbst, W. (2006). Testing the Disk-locking Paradigm: An Association between U - V Excess and Rotation in NGC 2264. *ApJ*, **647**, L155–L158. 37

Fang, M., van Boekel, R., Wang, W., Carmona, A., Sicilia-Aguilar, A. & Henning, T. (2009). Star and protoplanetary disk properties in Orion's suburbs. *A&A*, **504**, 461–489. 29, 35

Figueira, P., Marmier, M., Bonfils, X., di Folco, E., Udry, S., Santos, N.C., Lovis, C., Megevand, D., Melo, C.H.F., Pepe, F., Queloz, D., Segransan, D., Triaud, A.H.M.J. & Almeida, P.V. (2010). Evidence against the young hot-jupiter around bd +20 1790. 1

Flower, P.J. (1996). Transformations from Theoretical Hertzsprung-Russell Diagrams to Color-Magnitude Diagrams: Effective Temperatures, B-V Colors, and Bolometric Corrections. *ApJ*, **469**, 355–+. 42, 189

Ghez, A.M., McCarthy, D.W., Patience, J.L. & Beck, T.L. (1997). The Multiplicity of Pre-Main-Sequence Stars in Southern Star-forming Regions. *ApJ*, **481**, 378–+. 35, 95, 117

Gray, D.F. (1992). *The observation and analysis of stellar photospheres.*. 12, 13, 21, 25, 188

Gray, D.F. & Toner, C.G. (1986). Rotation and macroturbulence in bright giants. *ApJ*, **310**, 277–283. 190

Gray, R.O. & Corbally, C.J. (1994). The calibration of MK spectral classes using spectral synthesis. 1: The effective temperature calibration of dwarf stars. *AJ*, **107**, 742–746. 28, 187

Grether, D. & Lineweaver, C.H. (2006). How Dry is the Brown Dwarf Desert? Quantifying the Relative Number of Planets, Brown Dwarfs, and Stellar Companions around Nearby Sun-like Stars. *ApJ*, **640**, 1051–1062. 9

Griffin, R.F. (1967). A Photoelectric Radial-Velocity Spectrometer. *ApJ*, **148**, 465–+. 20

Guenther, E.W., Esposito, M., Mundt, R., Covino, E., Alcalá, J.M., Cusano, F. & Stecklum, B. (2007). Pre-main sequence spectroscopic binaries suitable for VLTI observations. *A&A*, **467**, 1147–1155. 15, 95, 131

Hall, J.C. (2008). Stellar Chromospheric Activity. *Living Reviews in Solar Physics*, **5**, 2–+. 11, 12

Hartigan, P., Hartmann, L., Kenyon, S., Hewett, R. & Stauffer, J. (1989). How to unveil a T Tauri star. *ApJS*, **70**, 899–914. 28, 126

Henning, T. (2008). Early phases of planet formation in protoplanetary disks. *Physica Scripta Volume T*, **130**, 014019–+. 6

Herbig, G.H. (1962). The properties and problems of T Tauri stars and related objects. *Advances in Astronomy and Astrophysics*, **1**, 47–103. 4

Herbst, W., Herbst, D.K., Grossman, E.J. & Weinstein, D. (1994). Catalogue of UBVRI photometry of T Tauri stars and analysis of the causes of their variability. *AJ*, **108**, 1906–1923. 5

Herbst, W., Bailer-Jones, C.A.L., Mundt, R., Meisenheimer, K. & Wackermann, R. (2002). Stellar rotation and variability in the Orion Nebula Cluster. *A&A*, **396**, 513–532. 36

Herbst, W., Eislöffel, J., Mundt, R. & Scholz, A. (2007). The Rotation of Young Low-Mass Stars and Brown Dwarfs. *Protostars and Planets V*, 297–311. 36

Hernán-Obispo, M., Gálvez-Ortiz, M.C., Anglada-Escudé, G., Kane, S.R., Barnes, J.R., de Castro, E. & Cornide, M. (2010). Evidence of a massive planet candidate orbiting the young active K5V star BD+20 1790. *A&A*, **512**, A45+. 1, 53

Hillenbrand, L.A., Bauermeister, A. & White, R.J. (2008). An Assessment of HR Diagram Constraints on Ages and Age Spreads in Star-Forming Regions and Young Clusters. In G. van Belle, ed., *14th Cambridge Workshop on Cool Stars, Stellar Systems, and the Sun*, vol. 384 of *Astronomical Society of the Pacific Conference Series*, 200–+. 27

Hirano, T., Suto, Y., Taruya, A., Narita, N., Sato, B., Johnson, J.A. & Winn, J.N. (2010). Analytic Description of the Rossiter-Mclaughlin Effect for Transiting Exoplanets: Cross-Correlation Method and Comparison with Simulated Data. *ApJ*, **709**, 458–469. 22, 188

Hoaglin, D.C., Mosteller, F. & Tukey, J.W. (1983). *Understanding robust and exploratory data anlysis*. 20

Hogerheijde, M.R. (2010). Structure and life time of circumstellar disks. In T. Montmerle, D. Ehrenreich, & A.-M. Lagrange, ed., *EAS Publications Series*, vol. 41 of *EAS Publications Series*, 113–132. 4, 5, 6, 8

Huélamo, N., Figueira, P., Bonfils, X., Santos, N.C., Pepe, F., Gillon, M., Azevedo, R., Barman, T., Fernández, M., di Folco, E., Guenther, E.W., Lovis, C., Melo, C.H.F., Queloz, D. & Udry, S. (2008). TW ;Hydrae: evidence of stellar spots instead of a Hot Jupiter. *A&A*, **489**, L9–L13. 1

Ida, S. (2010). Planet formation from planetesimals and diversity of planetary systems. In T. Montmerle, D. Ehrenreich, & A.-M. Lagrange, ed., *EAS Publications Series*, vol. 41 of *EAS Publications Series*, 339–354. 6, 7, 9

James, D.J., Melo, C., Santos, N.C. & Bouvier, J. (2006). Fundamental properties of pre-main sequence stars in young, southern star forming regions: metallicities. *A&A*, **446**, 971–983. 15, 131

Jayawardhana, R., Coffey, J., Scholz, A., Brandeker, A. & van Kerkwijk, M.H. (2006). Accretion Disks around Young Stars: Lifetimes, Disk Locking, and Variability. *ApJ*, **648**, 1206–1218. 28, 29, 37, 41

Joergens, V. & Guenther, E. (2001). UVES spectra of young brown dwarfs in Cha I: Radial and rotational velocities. *A&A*, **379**, L9–L12. 41

Johansen, A., Oishi, J.S., Mac Low, M., Klahr, H., Henning, T. & Youdin, A. (2007). Rapid planetesimal formation in turbulent circumstellar disks. *Nature*, **448**, 1022–1025. 6

Johns-Krull, C.M. & Basri, G. (1997). The Spectral Variability of the T Tauri Star DF Tauri. *ApJ*, **474**, 433–+. 28

Joy, A.H. (1945). T Tauri Variable Stars. *ApJ*, **102**, 168–+. 4

Kaufer, A., Stahl, O., Tubbesing, S., Nørregaard, P., Avila, G., Francois, P., Pasquini, L. & Pizzella, A. (1999). Commissioning FEROS, the new high-resolution spectrograph at La-Silla. *The Messenger*, **95**, 8–12. 11, 16

Kaufer, A., Stahl, O., Tubbesing, S., Norregaard, P., Avila, G., Francois, P., Pasquini, L. & Pizzella, A. (2000). Performance report on FEROS, the new fiber-linked echelle spectrograph at the ESO

1.52-m telescope. In M. Iye & A. F. Moorwood, ed., *Society of Photo-Optical Instrumentation Engineers (SPIE) Conference Series*, vol. 4008 of *Society of Photo-Optical Instrumentation Engineers (SPIE) Conference Series*, 459–466. 16

Koenigl, A. (1991). Disk accretion onto magnetic T Tauri stars. *ApJ*, **370**, L39–L43. 36

Köhler, R. (2001). Multiplicity of X-Ray-selected T Tauri Stars in Chamaeleon. *AJ*, **122**, 3325–3334. 85

Köhler, R. & Petr-Gotzens, M.G. (2002). Close Binaries in the η Chamaeleontis Cluster. *AJ*, **124**, 2899–2904. 85

Kurucz, R. (1993). ATLAS9 Stellar Atmosphere Programs and 2 km/s grid. *ATLAS9 Stellar Atmosphere Programs and 2 km/s grid. Kurucz CD-ROM No. 13. Cambridge, Mass.: Smithsonian Astrophysical Observatory, 1993.*, **13**. 28, 187

Lada, C.J. & Kylafis, N.D., eds. (1999). *The Origin of Stars and Planetary Systems*, Kluwer Academic Publishers. 3

Lafrenière, D., Jayawardhana, R., Brandeker, A., Ahmic, M. & van Kerkwijk, M.H. (2008). A Multiplicity Census of Young Stars in Chamaeleon I. *ApJ*, **683**, 844–861. 95

Lahuis, F., van Dishoeck, E.F., Blake, G.A., Evans, N.J., II, Kessler-Silacci, J.E. & Pontoppidan, K.M. (2007). c2d Spitzer IRS Spectra of Disks around T Tauri Stars. III. [Ne II], [Fe I], and H_2 Gas-Phase Lines. *ApJ*, **665**, 492–511. 15, 131

Lamm, M.H., Mundt, R., Bailer-Jones, C.A.L. & Herbst, W. (2005). Rotational evolution of low mass stars: The case of NGC 2264. *A&A*, **430**, 1005–1026. 4, 36, 37, 40, 41

Larson, A.M., Irwin, A.W., Yang, S.L.S., Goodenough, C., Walker, G.A.H., Walker, A.R. & Bohlender, D.A. (1993). A low-amplitude periodicity in the radial velocity and chromospheric emission of Beta Geminorum. *PASP*, **105**, 825–831. 23, 24

Lawson, W.A., Crause, L.A., Mamajek, E.E. & Feigelson, E.D. (2001). The η Chamaeleontis cluster: photometric study of the ROSAT-detected weak-lined T Tauri stars. *MNRAS*, **321**, 57–66. 87

Linsky, J.L., Hunten, D.M., Sowell, R., Glackin, D.L. & Kelch, W.L. (1979). Stellar model chromospheres. XI - A survey of CA II lambda 8542 line profiles in late-type stars of differing chromospheric activity. *ApJS*, **41**, 481–500. 23

Luhman, K.L. (2004). A Census of the Chamaeleon I Star-forming Region. *ApJ*, **602**, 816–842. 95

Mac Low, M. & Klessen, R.S. (2004). Control of star formation by supersonic turbulence. *Reviews of Modern Physics*, **76**, 125–194. 3

Makarov, V.V. (2007). Unraveling the Origins of Nearby Young Stars. *ApJS*, **169**, 105–119. 44

Makidon, R.B., Rebull, L.M., Strom, S.E., Adams, M.T. & Patten, B.M. (2004). Periodic Variability of Pre-Main-Sequence Stars in the NGC 2264 OB Association. *AJ*, **127**, 2228–2245. 36

Mamajek, E.E. (2009). How accurately can we age-date solar-type dwarfs using activity/rotation diagnostics? In E. E. Mamajek, D. R. Soderblom, & R. F. G. Wyse, ed., *IAU Symposium*, vol. 258 of *IAU Symposium*, 375–382. 23, 50, 63

Martínez Fiorenzano, A.F., Gratton, R.G., Desidera, S., Cosentino, R. & Endl, M. (2005). Line bisectors and radial velocity jitter from SARG spectra. *A&A*, **442**, 775–784. 21

Mathieu, R.D., Adams, F.C. & Latham, D.W. (1991). The T Tauri spectroscopic binary GW Orionis. *AJ*, **101**, 2184–2198. 74, 79, 123

Matt, S. & Pudritz, R.E. (2005). Accretion-powered Stellar Winds as a Solution to the Stellar Angular Momentum Problem. *ApJ*, **632**, L135–L138. 36

Matt, S. & Pudritz, R.E. (2008). Accretion-powered Stellar Winds. II. Numerical Solutions for Stellar Wind Torques. *ApJ*, **678**, 1109–1118. 36

Mayor, M. & Queloz, D. (1995). A Jupiter-mass companion to a solar-type star. *Nature*, **378**, 355–359. 1

Mayor, M., Pepe, F., Queloz, D., Bouchy, F., Rupprecht, G., Lo Curto, G., Avila, G., Benz, W., Bertaux, J., Bonfils, X., Dall, T., Dekker, H., Delabre, B., Eckert, W., Fleury, M., Gilliotte, A., Gojak, D., Guzman, J.C., Kohler, D., Lizon, J., Longinotti, A., Lovis, C., Megevand, D., Pasquini, L., Reyes, J., Sivan, J., Sosnowska, D., Soto, R., Udry, S., van Kesteren, A., Weber, L. & Weilenmann, U. (2003). Setting New Standards with HARPS. *The Messenger*, **114**, 20–24. 11, 17

Melo, C.H.F., Pasquini, L. & De Medeiros, J.R. (2001). Accurate Vsin i measurements in M 67: The angular momentum evolution of 1.2 $M_{\odot}$ stars. *A&A*, **375**, 851–862. 25, 26

Mordasini, C., Alibert, Y., Benz, W. & Naef, D. (2009). Extrasolar planet population synthesis. II. Statistical comparison with observations. *A&A*, **501**, 1161–1184. 1

Morel, T., Micela, G., Favata, F. & Katz, D. (2004). The photospheric abundances of active binaries. III. Abundance peculiarities at high activity levels. *A&A*, **426**, 1007–1020. 34

Neuhäuser, R., Guenther, E.W., Wuchterl, G., Mugrauer, M., Bedalov, A. & Hauschildt, P.H. (2005). Evidence for a co-moving sub-stellar companion of GQ Lup. *A&A*, **435**, L13–L16. 106, 124

Nguyen, D.C., Jayawardhana, R., van Kerkwijk, M.H., Brandeker, A., Scholz, A. & Damjanov, I. (2009). Disk Braking in young Stars: Probing Rotation in Chamaeleon i and Taurus-Auriga. *ApJ*, **695**, 1648–1656. 36, 39, 40, 41

Noyes, R.W., Hartmann, L.W., Baliunas, S.L., Duncan, D.K. & Vaughan, A.H. (1984). Rotation, convection, and magnetic activity in lower main-sequence stars. *ApJ*, **279**, 763–777. 23, 50

Padgett, D.L., Cieza, L., Stapelfeldt, K.R., Evans, N.J., II, Koerner, D., Sargent, A., Fukagawa, M., van Dishoeck, E.F., Augereau, J., Allen, L., Blake, G., Brooke, T., Chapman, N., Harvey, P., Porras, A., Lai, S., Mundy, L., Myers, P.C., Spiesman, W. & Wahhaj, Z. (2006). The SPITZER c2d Survey of Weak-Line T Tauri Stars. I. Initial Results. *ApJ*, **645**, 1283–1296. 15, 131

Palla, F. (2002). Pre-main-sequence evolution of stars and young clusters. In F. Palla, H. Zinnecker, A. Maeder, & G. Meynet, ed., *Physics of Star Formation in Galaxies*, 9–133. 3, 4, 27, 36, 38

Papaloizou, J.C.B. & Terquem, C. (2006). Planet formation and migration. *Reports on Progress in Physics*, **69**, 119–180. 6, 7, 8

Papaloizou, J.C.B., Nelson, R.P. & Terquem, C. (2004). On the Eccentricities of the Extrasolar Planets. In J. Beaulieu, A. Lecavelier Des Etangs, & C. Terquem, ed., *Extrasolar Planets: Today and Tomorrow*, vol. 321 of *Astronomical Society of the Pacific Conference Series*, 379–+. 53

Pollack, J.B., Hubickyj, O., Bodenheimer, P., Lissauer, J.J., Podolak, M. & Greenzweig, Y. (1996). Formation of the Giant Planets by Concurrent Accretion of Solids and Gas. *Icarus*, **124**, 62–85. 6

Povich, M.S., Giampapa, M.S., Valenti, J.A., Tilleman, T., Barden, S., Deming, D., Livingston, W.C. & Pilachowski, C. (2001). Limits on Line Bisector Variability for Stars with Extrasolar Planets. *AJ*, **121**, 1136–1146. 21

Prato, L., Huerta, M., Johns-Krull, C.M., Mahmud, N., Jaffe, D.T. & Hartigan, P. (2008). A Young-Planet Search in Visible and Infrared Light: DN Tauri, V836 Tauri, and V827 Tauri. *ApJ*, **687**, L103–L106. 51

Queloz, D., Allain, S., Mermilliod, J., Bouvier, J. & Mayor, M. (1998). The rotational velocity of low-mass stars in the Pleiades cluster. *A&A*, **335**, 183–198. 25, 187

Queloz, D., Henry, G.W., Sivan, J.P., Baliunas, S.L., Beuzit, J.L., Donahue, R.A., Mayor, M., Naef, D., Perrier, C. & Udry, S. (2001). No planet for HD 166435. *A&A*, **379**, 279–287. 21, 192

Raymond, S.N., O'Brien, D.P., Morbidelli, A. & Kaib, N.A. (2009). Building the terrestrial planets: Constrained accretion in the inner Solar System. *Icarus*, **203**, 644–662. 7

Rebull, L.M., Wolff, S.C. & Strom, S.E. (2004). Stellar Rotation in Young Clusters: The First 4 Million Years. *AJ*, **127**, 1029–1051. 36, 37

Rebull, L.M., Stauffer, J.R., Megeath, S.T., Hora, J.L. & Hartmann, L. (2006). A Correlation between Pre-Main-Sequence Stellar Rotation Rates and IRAC Excesses in Orion. *ApJ*, **646**, 297–303. 36, 37

Reid, I.N. & Hawley, S.L. (2005). *New light on dark stars : red dwarfs, low-mass stars, brown dwarfs*. 11, 12

Reiners, A. & Schmitt, J.H.M.M. (2003). Rotation and differential rotation in field F- and G-type stars. *A&A*, **398**, 647–661. 190

Rodmann, J., Henning, T., Chandler, C.J., Mundy, L.G. & Wilner, D.J. (2006). Large dust particles in disks around T Tauri stars. *A&A*, **446**, 211–221. 15, 131

Saar, S.H. & Donahue, R.A. (1997). Activity-related Radial Velocity Variation in Cool Stars. *ApJ*, **485**, 319–+. 1, 24, 50

Safronov, V.S. (1969). *Evoliutsiia doplanetnogo oblaka.*. 6

Santos, N.C., Mayor, M., Naef, D., Pepe, F., Queloz, D., Udry, S., Burnet, M., Clausen, J.V., Helt, B.E., Olsen, E.H. & Pritchard, J.D. (2002). The CORALIE survey for southern extra-solar planets. IX. A 1.3-day period brown dwarf disguised as a planet. *A&A*, **392**, 215–229. 26

Savitzky, A. & Golay, M.J.E. (1964). Smoothing and differentiation of data by simplified least squares procedures. *Analytical Chemistry*, **36**, 1627–1639. 22

Schegerer, A., Wolf, S., Voshchinnikov, N.V., Przygodda, F. & Kessler-Silacci, J.E. (2006). Analysis of the dust evolution in the circumstellar disks of T Tauri stars. *A&A*, **456**, 535–548. 15, 74, 79, 131

Schisano, E., Covino, E., Alcalá, J.M., Esposito, M., Gandolfi, D. & Guenther,

E.W. (2009). Variability of the transitional T Tauri star T Chamaeleontis. *A&A*, **501**, 1013–1030. 101, 105

Schneider, J. (2010). The Extrasolar Planets Encyclopaedia. 1, 53

Scholz, A., Coffey, J., Brandeker, A. & Jayawardhana, R. (2007). Rotation and Activity of Pre-Main-Sequence Stars. *ApJ*, **662**, 1254–1267. 38

Seifahrt, A. & Käufl, H.U. (2008). High precision radial velocity measurements in the infrared. A first assessment of the RV stability of CRIRES. *A&A*, **491**, 929–939. 51

Setiawan, J., Pasquini, L., da Silva, L., von der Lühe, O. & Hatzes, A. (2003). Precise radial velocity measurements of G and K giants. First results. *A&A*, **397**, 1151–1159. 192

Setiawan, J., Weise, P., Henning, T., Launhardt, R., Müller, A. & Rodmann, J. (2007). Evidence for a Planetary Companion around a Nearby Young Star. *ApJ*, **660**, L145–L148. 1, 15, 16, 20, 22

Setiawan, J., Henning, T., Launhardt, R., Müller, A., Weise, P. & Kürster, M. (2008a). A young massive planet in a star-disk system. *Nature*, **451**, 38–41. 1, 6, 50, 79

Setiawan, J., Weise, P., Henning, T., Hatzes, A.P., Pasquini, L., Silva, L.D., Girardi, L., von der Lühe, O., Döllinger, M.P., Weiss, A. & Biazzo, K. (2008b). Planets Around Active Stars. In N. C. Santos, L. Pasquini, A. C. M. Correia, & M. Romaniello , ed., *Precision Spectroscopy in Astrophysics*, 201–204. 15

Shevchenko, V.S., Grankin, K.N., Mel'Nikov, S.Y. & Lamzin, S.A. (1998). The quasi-Algol GW Ori: The nature of eclipses and estimation of the component masses. *Astronomy Letters*, **24**, 528–534. 74, 76, 77, 79

Shkolnik, E., Bohlender, D.A., Walker, G.A. & Gu, P. (2007). New Insights into Star-Planet Interactions (SPI). In *Bulletin of the American Astronomical Society*, vol. 38 of *Bulletin of the American Astronomical Society*, 105–+. 63

Sicilia-Aguilar, A., Hartmann, L.W., Hernández, J., Briceño, C. & Calvet, N. (2005). Cepheus OB2: Disk Evolution and Accretion at 3-10 Myr. *AJ*, **130**, 188–209. 36, 40, 41

Sicilia-Aguilar, A., Bouwman, J., Juhász, A., Henning, T., Roccatagliata, V., Lawson, W.A., Acke, B., Feigelson, E.D., Tielens, A.G.G.M., Decin, L. & Meeus, G. (2009). The Long-Lived Disks in the η Chamaeleontis Cluster. *ApJ*, **701**, 1188–1203. 85

Siess, L., Dufour, E. & Forestini, M. (2000). An internet server for pre-main sequence tracks of low- and intermediate-mass stars. *A&A*, **358**, 593–599. 27, 44, 54

Silverstone, M.D., Meyer, M.R., Mamajek, E.E., Hines, D.C., Hillenbrand, L.A., Najita, J., Pascucci, I., Bouwman, J., Kim, J.S., Carpenter, J.M., Stauffer, J.R., Backman, D.E., Moro-Martin, A., Henning, T., Wolf, S., Brooke, T.Y. & Padgett, D.L. (2006). Formation and Evolution of Planetary Systems (FEPS): Primordial Warm Dust Evolution from 3 to 30 Myr around Sun-like Stars. *ApJ*, **639**, 1138–1146. 15, 131

Skumanich, A. (1972). Time Scales for CA II Emission Decay, Rotational Braking, and Lithium Depletion. *ApJ*, **171**, 565–+. 36

Soderblom, D.R., Jones, B.F., Balachandran, S., Stauffer, J.R., Duncan, D.K., Fedele,

S.B. & Hudon, J.D. (1993). The evolution of the lithium abundances of solar-type stars. III - The Pleiades. *AJ*, **106**, 1059–1079. 31

Takami, M., Bailey, J. & Chrysostomou, A. (2003). A spectro-astrometric study of southern pre-main sequence stars. Binaries, outflows, and disc structure down to AU scales. *A&A*, **397**, 675–691. 117

Takeda, Y., Ohkubo, M. & Sadakane, K. (2002). Spectroscopic Determination of Atmospheric Parameters of Solar-Type Stars: Description of the Method and Application to the Sun. *PASJ*, **54**, 451–462. 25, 26

Terquem, C.E.J.M.L.J. (2010). Disk dynamics and planet migration. In T. Montmerle, D. Ehrenreich, & A.-M. Lagrange, ed., *EAS Publications Series*, vol. 41 of *EAS Publications Series*, 209–218. 8

Torres, C.A.O., Quast, G.R., da Silva, L., de La Reza, R., Melo, C.H.F. & Sterzik, M. (2006). Search for associations containing young stars (SACY). I. Sample and searching method. *A&A*, **460**, 695–708. ix, 15, 16, 43, 44, 54, 59, 64, 69, 71, 80, 90, 101, 111, 131

Torres, C.A.O., Quast, G.R., Melo, C.H.F. & Sterzik, M.F. (2008). *Young Nearby Loose Associations*, 757–+. 90, 111

Unsöld, A. & Baschek, B. (2002). *Der neue Kosmos. Einführung in die Astronomie und Astrophysik*. 11

Valenti, J.A. & Fischer, D.A. (2005). Spectroscopic Properties of Cool Stars (SPOCS). I. 1040 F, G, and K Dwarfs from Keck, Lick, and AAT Planet Search Programs. *ApJS*, **159**, 141–166. 42, 190

van Leeuwen, F. & Evans, D.W. (1998). On the use of the HIPPARCOS intermediate astrometric data. *A&AS*, **130**, 157–172. 97

Vaughan, A.H., Preston, G.W. & Wilson, O.C. (1978). Flux measurements of CA II H and K emission. *PASP*, **90**, 267–274. 12, 23

Viana Almeida, P., Santos, N.C., Melo, C., Ammler-von Eiff, M., Torres, C.A.O., Quast, G.R., Gameiro, J.F. & Sterzik, M. (2009). Search for associations containing young stars (SACY). II. Chemical abundances of stars in 11 young associations in the solar neighborhood. *A&A*, **501**, 965–971. 33, 34, 43, 44, 80, 90, 111

Voges, W., Aschenbach, B., Boller, T., Bräuninger, H., Briel, U., Burkert, W., Dennerl, K., Englhauser, J., Gruber, R., Haberl, F., Hartner, G., Hasinger, G., Kürster, M., Pfeffermann, E., Pietsch, W., Predehl, P., Rosso, C., Schmitt, J.H.M.M., Trümper, J. & Zimmermann, H.U. (1999). The ROSAT all-sky survey bright source catalogue. *A&A*, **349**, 389–405. 44, 64

Weise, P. (2007). *Charakterisierung naher junger Sterne*. Diploma thesis, University of Heidelberg. 15, 23, 31, 42, 151

Weise, P., Launhardt, R., Setiawan, J. & Henning, T. (2010). Rotational velocities of nearby young stars. *ArXiv:1005.0984*. 151, 192

White, R.J. & Basri, G. (2003). Very Low Mass Stars and Brown Dwarfs in Taurus-Auriga. *ApJ*, **582**, 1109–1122. 28, 29

White, R.J., Gabor, J.M. & Hillenbrand, L.A. (2007). High-Dispersion Optical Spectra of Nearby Stars Younger Than the Sun. *AJ*, **133**, 2524–2536. 69, 71

Whittet, D.C.B., Prusti, T., Franco, G.A.P., Gerakines, P.A., Kilkenny, D., Larson,

K.A. & Wesselius, P.R. (1997). On the distance to the Chamaeleon I and II associations. *A&A*, **327**, 1194–1205. 95

Wilson, O.C. (1976). Absolute magnitudes of stars from widths of chromospheric Ca II emission lines. *ApJ*, **205**, 823–840. 23

Wolff, S.C., Strom, S.E. & Hillenbrand, L.A. (2004). The Evolution of Angular Momentum of Intermediate Mass Stars: From the Birthline to the Main Sequence. In A. Maeder & P. Eenens, ed., *Stellar Rotation*, vol. 215 of *IAU Symposium*, 431–+. 36

Zechmeister, M. & Kürster, M. (2009). The generalised Lomb-Scargle periodogram. A new formalism for the floating-mean and Keplerian periodograms. *A&A*, **496**, 577–584. 16, 29

Zhao, J., Zhao, G., Chen, Y., Shi, J., Liu, Y. & Zhang, J. (2006). Automatic Normalization and Equivalent-Width Measurement of High-Resolution Stellar Spectra. *Chinese Journal of Astronomy and Astrophysics*, **6**, 689–696. 19

Zuckerman, B. & Song, I. (2004). Young Stars Near the Sun. *ARA&A*, **42**, 685–721. 27, 31, 80, 85

Danksagung

Diese Arbeit wäre nicht ohne die tatkräftige Unterstützung zahlreicher Menschen möglich gewesen.
Ich danke vor Allem Dr. Ralf Launhardt und Dr. Johny Setiawan für ihre Unterstützung, Lehrbereitschaft, Lesebereitschaft und Geduld. Herrn Prof. Thomas Henning danke ich für die Möglichkeit diese Studie am Max-Planck-Institut für Astronomie durchführen zu können. Meinen Büro-Genossen, Min, Mario, Bhargav und Javier, danke ich für ihre Geschichten und Ablenkung, aber auch Ruhe im richtigen Moment. Mathias und André für Diskussionen, Hilfe und Beobachtungen. Ich danke auch allen anderen Beobachtern, Tim, Eva, Christina, Markus, Monika, Juliet, Davide, Joe and Viki (auch für zwei Spektren von GQ Lup). Ganz besonderer Dank gilt auch Prof. Reinhardt Mundt, nicht nur für Korrekturen an der ersten Publikation, sondern auch für Tipps zur Gesundheit und Heilung.
Neben der Welt der Wissenschaft gibt es auch die private Welt, in der ich meinen Freunden zu Dank verpflichtet bin. Vielen Dank für eure Geduld mit mir wenn mal wieder kein anderes Thema als diese Arbeit möglich war oder ich mich wieder hinter den Büchern verschanzte. Danke an Iria, die sich die Zeit genommen hat, sprachliche Fehler in dieser Arbeit zu korrigieren. Noch viel mehr Danken muss ich meinen Eltern, meiner Schwester und meinen Schwiegereltern ohne deren Unterstützung vieles so nicht möglich gewesen wäre.
Ganz besonderen Dank spreche ich meinem liebsten Menschen aus. Danke, Sabrina, dass du für mich da bist und Verständnis aufgebracht hast, dass diese Arbeit doch irgendwie mein Leben mitbestimmte. Du hast mir sehr geholfen, wie auch unsere Hunde, beim Rauskommen und neu auftanken.

Declaration

I herewith declare that I have produced this thesis without the prohibited assistance of third parties and without making use of aids other than those specified; notions taken over directly or indirectly from other sources have been identified as such. This thesis has not previously been presented in identical or similar form to any other German or foreign examination board.

The thesis work was conducted from June 2007 to August 2010 under the supervision of Prof. Dr. Thomas Henning at Max-Planck Institute for Astronomy, Heidelberg.

Heidelberg, August 2nd, 2010